Keele UNIVERSITY

A study of mechanical and capillary bifurcation phenomena in soft elastic materials

Dominic Robert Emery

School of Computer Science and Mathematics

Keele University

A thesis submitted for the degree of

Doctor of Philosophy

June 2023

This thesis is dedicated to
Mum and Dad.
Thank you for everything.

Declaration

I, Dominic Emery, certify that this thesis, submitted for the degree of Doctor of Philosophy, is the result of my own research, except where otherwise acknowledged, and has not been submitted for a higher degree to any other university or institution.

D. K. Emery

Signature

April 19, 2023

Date

Acknowledgements

I'll first take this opportunity to thank my PhD supervisor, Professor Yibin Fu, whose constant support, guidance and encouragement has undoubtedly made me a better researcher.

I'd also like to offer special thanks to Professor John Chapman, Dr Danila Prikazchikov, Dr Mike Nieves and Dr Peter Wootton for many helpful discussions and words of advice, as well as Dr Lishuai Jin, University of Pennsylvania, for carrying out the supplementary finite element method simulations presented in chapter 5.

I acknowledge the School of Computing and Mathematics, Keele University, for funding my PhD studies through a faculty scholarship. In addition, I am thankful to have been afforded the opportunity to attend the following in-person international research events:

- 25th CISM-IUTAM International Summer School on "*Instability and Bifurcation of Solids Including Coupled Field Phenomena*" held in Udine, Italy from June 13 2022 to June 17 2022.

- 11th European Solid Mechanics Conference held in Galway, Ireland from July 4 2022 to July 8 2022.

I am highly grateful to friends within and outside of the Keele Mathematics postgraduate community who have made the experience an incredibly enjoyable one in spite of a sizeable period of lockdown and isolation.

Lastly, I am extremely appreciative of my parents, Lynn and Rob, and my brother, Owen, for their unwavering support.

Abstract

Stress-induced pattern formations in soft elastic materials are bifurcation phenomena which can be *localized* or *periodic*. Certain localized pattern formations such as necking or bulging are associated with zero wavenumber, whereas periodic pattern formations such as wrinkling or buckling are associated with a strictly positive wavenumber. Whilst the near-critical behaviour of the periodic case is well understood, studies of the localized case have only recently gathered momentum, and are conceptually more challenging to undertake. Despite this, a remarkable amount of analytical progress can be made. We will highlight this generally under-appreciated fact by studying theoretically the complete bifurcation behaviour of localized patterns, as well as the competition from periodic patterns, in elastic materials under various effects.

Firstly, the bifurcation behaviour of soft *incompressible* hollow tubes under elasto-capillary effects is studied. Analytical bifurcation conditions for localized pattern formation are initially derived using established results from a prototypical problem. A linear bifurcation analysis then shows that an axi-symmetric zero wavenumber bifurcation mode is favoured over periodic modes for a range of boundary conditions and loading scenarios. A weakly non-linear analysis provides an explicit connection between this zero wavenumber mode and localized necking or bulging, and a *phase-separation-like* evolution of these localized patterns into a final Maxwell state is described analytically. The effect of material *compressibility* on localized pattern formation in soft cylinders is also studied analytically, and comparisons with recently published numerical simulation results are made.

We then consider the formation of a self-contacting crease on the free surface of a compressed elastic half-space. This is a highly unique localized pattern since its inception is an inherently non-linear bifurcation phenomenon. Therefore, unlike localized bulging or necking, it is undetectable through a linear analysis. We derive a new analytical bifurcation condition for creasing by reformulating the analysis of a recent ground-breaking study.

Contents

List of Figures

1
Introduction

Contents

1.1 Context

The theory of non-linear elasticity provides a mathematical description of soft elastic material bodies which can undergo *large deformations*. The development of the theory in notable works such as Mooney (1940) and Rivlin (1948) was largely motivated by the popularity of rubber in World War II for applications such as vehicle and aircraft tyres, medical equipment, gas and oxygen masks and clothing. In more recent times, interest in soft materials such as hydrogels and biological tissue has intensified, and a knowledge of the response to stress and the *bifurcation behaviour* of such materials has become highly desirable. In particular, localized or periodic pattern formation is a bifurcation phenomena in soft materials which has many useful applications, from the optimization of surface wettability and adhesion properties to the determination of material properties through buckling-based metrology. It can also play a prominent role in many biological and physiological processes; for instance, localized pattern formation has been observed in tunnelling nanotubes connecting migrating cells (Veranič et al., 2008), and in nerve fibres as part of the overall neurodegeneration associated with traumatic brain injuries (Kilinc et al., 2009) and disorders such as Alzheimer's and Parkinson's diseases (Datar et al., 2019). The attainment of a fundamental understanding of pattern formation and other bifurcation phenomena in a wide range of soft materials will therefore facilitate many advancements in the scientific, technological and medical communities. To this end, there have been many extensions of the classical theory which couple elasticity with additional effects due to electric fields (Dorfmann and Ogden, 2005), biological growth (Goriely, 2017) and surface tension (Liu and Feng, 2012), among others.

A unifying theme of this thesis is the theoretical analysis of *localized* pattern formation in soft materials using non-linear elasticity theory and advanced mathematical techniques. We will study the competition between localized and periodic pattern formation, as well as the near-critical and fully non-linear post-bifurcation behaviour of localized patterns, in different contexts.

1.2 Localized pattern formation with zero wavenumber

1.2.1 A prototypical problem

The treatment of localized pattern formation in soft materials as a bifurcation mode with *zero wavenumber* has become increasingly prevalent over the last 15 years. This particular mode is not sinusoidal or constant; the correct spatial variation of the associated eigenfunction can only be determined through a weakly non-linear, near-critical analysis (Fu, 2001). A problem which serves as the foundation for this area of research is the localized bulging of a hollow tube subject to the combined effects of axial loading and internal inflation. Despite many experimental observations in the past (Mallock, 1891; Kyriakides and Yu-Chung, 1990), this was only recognized as a bifurcation phenomenon with zero wavenumber under the membrane assumption relatively recently (Fu et al., 2008).

The phenomenon is now well understood to consist of three stages: bulge initiation, radial growth and axial propagation (i.e. lengthening); see Fig. 1.1. There has been significant attention towards the so-called limiting-point instability

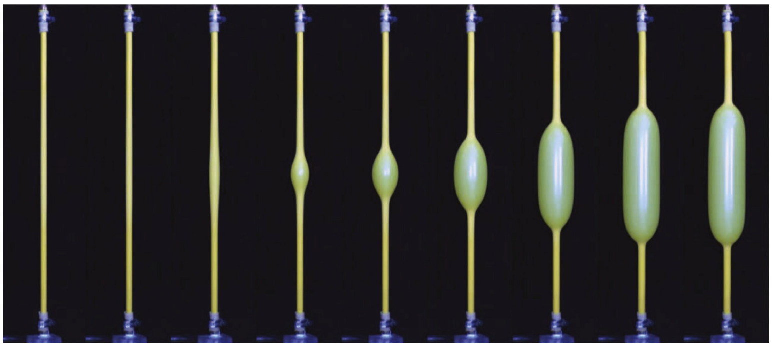

Figure 1.1: Experimental observations of the bulge initiation, radial growth and axial propagation (lengthening) states in an internally inflated tube of fixed length (Wang et al., 2019).

which occurs at the maximum of the pressure – volume loading curve. Historically, the explicit nature of this instability had not been associated with bulging, and some thought that it corresponded to snap-through (i.e. instantaneous) buckling (Alexander, 1971). Interpretations of the bulge propagation stage as a *phase-separation-like* phenomenon have also been constructed (Yin, 1977). To elaborate, the far right configuration in Fig. 1.1 can be viewed as two coexisting solid states with distinct but uniform amplitude connected by a smooth transition region. Thus, the process emulates more commonly known phase separation phenomena such as the formation of gas bubbles in a liquid body, say. Fu et al. (2016) demonstrated that, for a tube of arbitrary thickness under any type of end conditions, the bifurcation condition for localized bulging is that the Jacobian determinant of the inflation pressure P and the resultant axial force $\mathcal{N}$ as functions of the axial stretch and the circumferential stretch on the inner surface must vanish. This condition has exceptional agreement with experimental results (Wang et al., 2019), and was shown by Yu and Fu (2022) to be analytically equivalent to the condition for an axi-symmetric bifurcation mode with zero wavenumber to exist. A connection between the zero wavenumber bifurcation mode and localized static solitary wave bifurcation solutions has been established previously through the general theory of dynamical systems (Kirchgässner, 1982; Haragus and Iooss, 2010), and more recently for the inflation problem through a weakly non-linear analysis (Ye et al., 2020). Earlier linear bifurcation analyses (Haughton and Ogden, 1979a,b) focussed, however, on periodic axi-symmetric modes, and the zero wavenumber mode was thought to correspond to an alternate uniformly inflated state (as is incorrectly predicted by a linear analysis). Since the revelation of Fu et al. (2016), many additional effects such as rotation (Wang et al., 2017), double fibre-reinforcement (Wang and Fu, 2018), bi-layering (Liu et al., 2019) and torsion (Althobaiti, 2022) have been incorporated into the analysis.

The inflation problem has become prototypical in the sense that it often has a very similar mathematical structure to other more complicated elastic localization problems. For instance, through a reformulation of the Jacobian determinant bifurcation condition for the inflation problem, Fu et al. (2018) demonstrated that the bifurcation condition for localized necking in a dielectric membrane under in-plane mechanical stretching and an electric field is that the Hessian of the total free-energy function vanishes. The problem of localized pattern formation in soft cylinders and tubes under axial loading and surface tension can also be very well understood as a result of the inflation problem, and this will be illustrated over a substantial part of this thesis.

1.2.2 Elasto-capillarity and localized pattern formation

In fluid mechanics, surface tension is the architect of many fascinating phenomena from spherical droplet formation to water striding insects (De Gennes et al., 2004; Bush and Hu, 2006). It is also heavily implicated in the famous Rayleigh-Plateau instability (Plateau, 1873; Rayleigh, 1892) where a cylindrical column of fluid breaks up into a sequence of droplets in order to reduce its surface area, and hence its overall surface energy; see Fig. 1.2. It is therefore no surprise that surface tension is one of the most studied areas of fluid mechanics (Levich and Krylov, 1969).

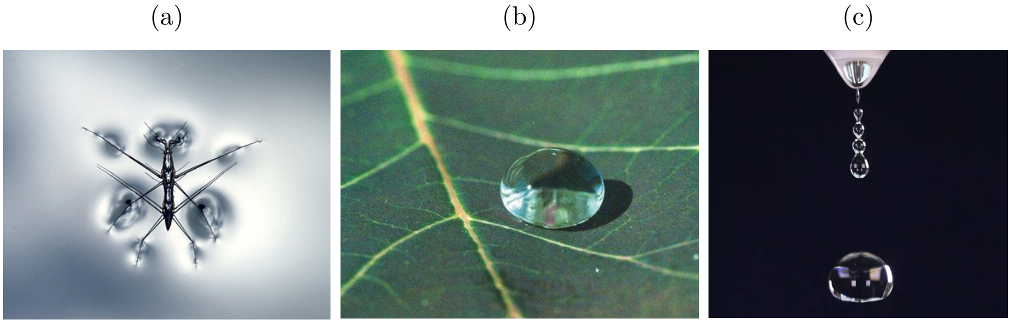

Figure 1.2: Examples of surface-tension-induced phenomena in fluids. Surface tension (a) prevents the submergence of certain insects in water (image by Water Science School) and (b) triggers spherical droplet formation to minimize the overall surface-to-volume ratio and surface energy of the fluid (image from phys.org). (c) An illustration of the Rayleigh-Plateau instability in which a cylindrical stream of water from a tap destabilizes into a chain of spherical droplets (image by N. Sharp).

Whilst the surface tension effect upon fluids is widely appreciated, in solid mechanics it is often overlooked. In fluids, there exists a tensile surface stress, σ_s, which opposes surface stretching, and minimizes the surface-to-volume ratio of the liquid. In simple liquids, σ_s is a spherical, second-order, two-dimensional tensor, and can be represented by $\sigma_s = \bar{\gamma} I$, where the scalar $\bar{\gamma}$ is the surface tension (with constant magnitude) and I is the identity tensor. A key difference with solids is the ability of their surfaces to sustain finite normal and shear stresses. This means that, in general, the surface stress tensor σ_s for a solid is non-spherical (anisotropic), and the surface tension $\bar{\gamma}$ is dependent on the deformation Gurtin and Murdoch (1975).

In elastic materials, surface tension operates at the *elasto-capillary length scale* $\bar{\gamma}/\mu$, where $\bar{\gamma}$ is the surface tension and μ the ground state shear modulus (Style et al., 2017; Bico et al., 2018). For many materials, the shear modulus is large enough to ensure that this length scale is subatomic, and that surface tension can be safely ignored in the continuum setting. However, for extremely soft and compliant materials such as gels, creams and biological tissue, the elasto-capillary length has an order of magnitude ranging from tens of nanometres to millimetres; at such scales, surface tension effects on these materials are non-negligible in comparison to bulk elastic forces. Given the recent surge of interest in the behaviour, functionality and development of micro-to nano-scale soft materials for various technological applications, an understanding of surface tension effects upon elastic materials has never been more important. Examples of such applications are soft robotics (Wang et al., 2018) and the construction of artificial muscles (Qiu et al., 2019) and other biomedical devices (Cooke et al., 2018).

Great headway has been made in developing the field of *elasto-capillarity*, which concerns itself with the large deformations of elastic materials with bulk *and* surface energy. The seminal work in this area can be attributed to Gurtin and Murdoch (1975), who derived a general surface elasticity theory based on the principles of continuum mechanics which accounted explicitly for large deformations; tensorial quantities of surface stress and strain can be non-linearly related to each other using this theory. Steigmann and Ogden (1997) later generalized this framework to include the effects of surface bending stiffness. Two-dimensional and three-dimensional finite element method (FEM) frameworks for non-linear elastic materials under surface tension have been constructed by Javili and Steinmann (2009, 2010), respectively. These frameworks were implemented in the commercial FEM software Abaqus (2013) by Henann and Bertoldi (2014) to investigate various elasto-capillary phenomena. Further studies have considered the effects of surface stresses on plate bending (Liu et al., 2017) and elastic materials (e.g. biological tissue) under volumetric growth (Papastavrou et al., 2013).

1.2.2.1 Soft solid cylinders and hollow tubes

Soft cylinders and tubes are widespread in physiological systems in the form of brain organoids, nerve fibres, arteries, airways and intestines, for instance. The villification of the gastrointestinal tract (Shyer et al., 2013), the closure of pulmonary airways (Seow et al., 2000) and the gyrification of the brain (Balbi et al., 2020) are examples of physiological pattern formations and bifurcation phenomena which, despite the compliance of the materials they occur in, have predominantly not been treated as the result of coupled elastic and capillary effects. However, consideration is given to the surface-tension-induced buckling of liquid-lined tubes as a model for airway closure in

Hazel and Heil (2005), and insights into the elasto-capillary circumferential buckling of tubes under biological growth (Riccobelli and Bevilacqua, 2020) and uniform pressure and geometric everting (Wang et al., 2021) have very recently transpired.

Soft slender cylinders and tubes have been widely observed in experiments to adopt a localized axi-symmetric pattern which bears a striking resemblance to beads on a string; see Fig. 1.3. Consequently, the pattern is often referred to as *beading* in the literature. This phenomenon can occur in nerve fibres (Bar-Ziv and Moses, 1994) and axons under tension from traumatic brain injuries (Kilinc et al., 2009; Lang et al., 2017), and it has also been implicated in neurodegenerative disorders such as Alzheimer's and Parkinson's diseases (Datar et al., 2019). Furthermore, *tunnelling nano-tubes* under tension have been observed between migrating cells; these nano-tubes allow for inter-cellular communications and migration support (Veranič et al., 2008). As shown in Fig. 1.3 (g – i), the formation of localized axi-symmetric patterns has also been observed in these nano-tubes. Bead formation has likewise been observed in hollow tubes which are filled with magnetic fluids (Ménager et al., 2002), submerged in hydrophilic polymer solutions (Tsafrir et al., 2001) and under growth (Hannezo et al., 2012), and has been implicated in the synthesis of soft matter nano-tubes (Ma et al., 2017) which have a variety of physical, biological and chemical applications (Shimizu et al., 2020). It is known from Wilkes (1955) that a cylinder or tube under a purely mechanical axial load cannot form a localized pattern. Instead, it may admit a periodic pattern in the axial direction provided that the load is sufficiently *compressive*. Given the small scale and softness of the cylinders and tubes in the previously discussed experiments, it is plausible that the additional effect of surface tension is what triggers localized pattern formation in this context.

The beading of an *incompressible solid cylinder* under axial loading and surface tension was initially analyzed using non-linear elasticity theory by Taffetani and Ciarletta (2015a,b) and Xuan and Biggins (2016). These studies concluded unanimously that the preferred bifurcation mode is characterized by infinite wavelength, or zero wavenumber, in the axial direction. Despite the previously discussed connections between the zero wavenumber mode and localized inhomogeneous bifurcation solutions from the general dynamical systems theory and the inflation problem, the weakly non-linear analysis conducted in Taffetani and Ciarletta (2015b) was centred around seeking periodic solutions, and they did not yield the quadratic amplitude equation which is typically expected to arise in elastic localization problems. Furthermore, FEM simulations conducted in Abaqus (2013) by Henann and Bertoldi (2014) suggested that beading is a supercritical bifurcation phenomenon, but this conclusion would later be challenged.

Xuan and Biggins (2017) and Giudici and Biggins (2020) highlighted that beading is a *phase-transition-like* phenomenon which culminates in a *two-phase* state characterized by two sections with distinct but uniform axial stretch connected by a smooth transition zone. The weakly non-linear analysis of Fu et al. (2021) demonstrated that a subcritical localized bulging or necking solution is indeed the initial bifurcation behaviour, depending on the loading scenario. The connection between the initial localized pattern and the final "two-phase" deformation observed by Xuan and Biggins (2017) and Giudici and Biggins (2020) was also explained both theoretically and numerically via FEM simulations in Abaqus (2013). The post-bifurcation process was seen to display a similar pattern of initiation, growth and propagation as is observed in the inflation problem, and the bifurcation condition for localized necking or bulging (and equivalently for a zero wavenumber mode to exist) was shown to take an analytical form analogous to the Jacobian determinant condition in the inflation problem. The beading instability in incompressible solid cylinders has since been studied dynamically (Pandey et al., 2021) and through the active strain approach (Riccobelli, 2021).

Theoretical studies of *incompressible hollow tubes* under the effect of axial loading and surface tension are far less prevalent. FEM simulations were conducted by Henann and Bertoldi (2014) for two separate cases of boundary conditions where the inner or outer lateral surface is fixed to prevent displacement in the radial direction. Xuan and Biggins (2016) studied the bifurcation behaviour of a cylindrical cavity in an infinite solid, and showed that the preferred mode is again associated with zero wavenumber. A first attempt at a theoretical investigation of the hollow tube case

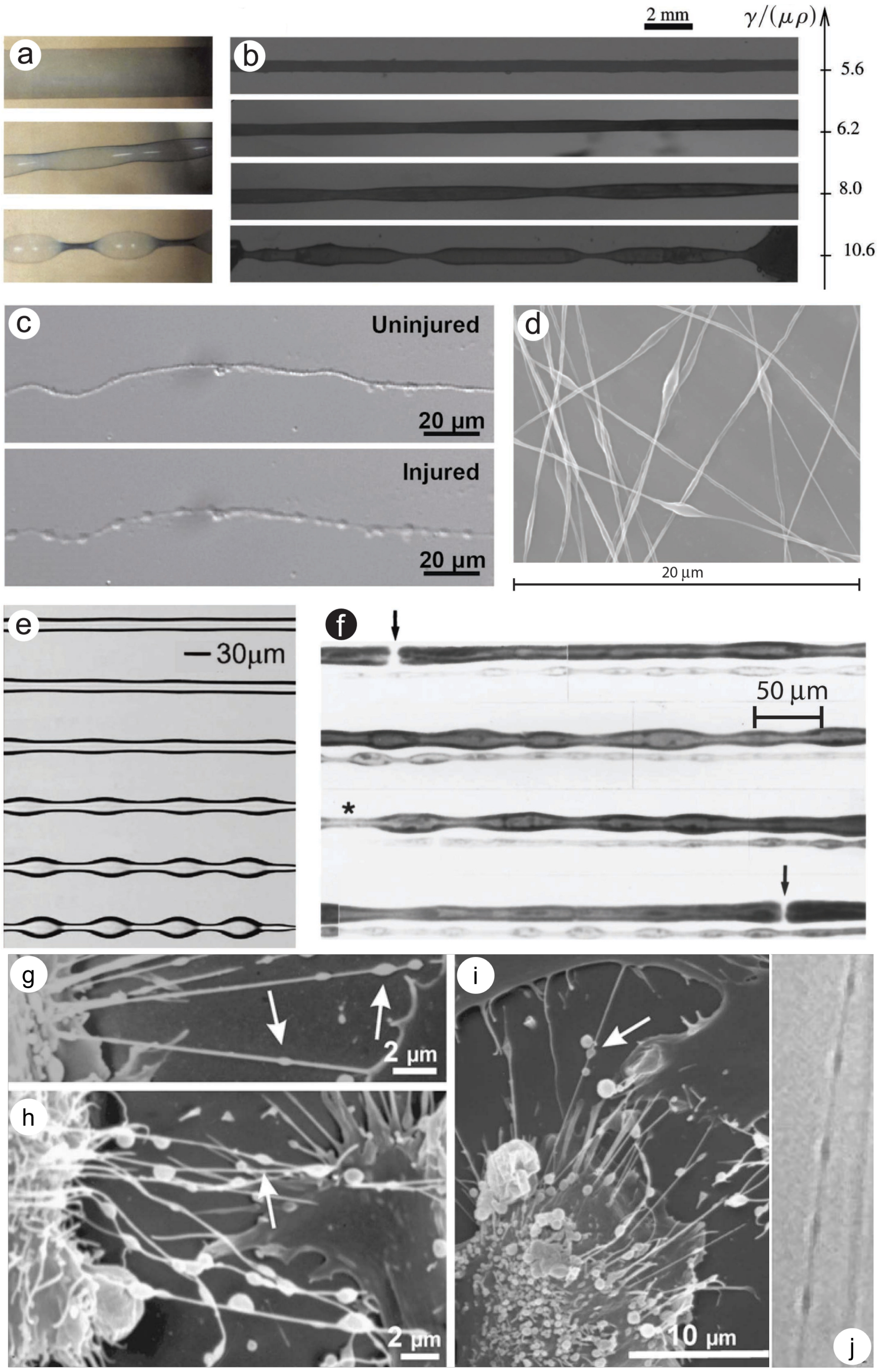

Figure 1.3: Examples of elasto-capillary *beading* in soft slender cylinders/tubes. (a) Beading of a shrinking acrylamide cylindrical gel immersed in an acetone-water mixture (Matsuo and Tanaka, 1992). (b) Beading of soft cylindrical gels immersed in toluene (Mora et al., 2010). (c) Axonal beading due to mechanical trauma (Hemphill et al., 2015). (d) Beading of nanofibers formed during electrospinning (Fong et al., 1999). (e) Beading due to thinning of polymer nanofibers (Sattler et al., 2008). (f) Beading of a single myelinated fiber teased from a rat sciatic nerve stretched with a weight of 4.5 g (Markin et al., 1999). (g – i) Beading of tunnelling nanotubes connecting migrating cells (Veranič et al., 2008). (j) Beading of phospholipid tubes filled with a magnetic fluid (Ménager et al., 2002).

was made by Wang (2020). Surprisingly, an analytical solution to the governing equation was obtained. This was contrary to expectations since, in the investigations of Haughton and Ogden (1979b) into tubes under axial loading and internal pressure, the boundary value problem could only be solved numerically. There is clearly a need to resolve this discrepancy and to determine absolutely whether localized or periodic pattern formation is preferred in the hollow tube case, and how such patterns evolve in the post-bifurcation regime; this will be the first focus of this thesis.

Localized pattern formation in *compressible solid cylinders* has also received very little attention in the literature. This is surprising since, whilst the incompressibility assumption typically makes the bifurcation analysis far easier, soft hydrogels can often possess a large degree of compressibility; see Geissler et al. (1988) and Chippada et al. (2010), for instance. Furthermore, in the case of soft biological tissue, whilst incompressibility is often assumed due to the high water content of the material, there is very little supporting experimental evidence for this assumption. Only Carew et al. (1968) has provided evidence that incompressibility is a suitable assumption when modelling arterial tissue. Very recently, Dortdivanlioglu and Javili (2022) analyzed the effect of material compressibility on solid cylinders under axial loading and surface tension via numerical simulations, extending what is already known for the incompressible case. Numerical simulation predictions for the initial bifurcation points are presented, and an extensive post-bifurcation analysis tracking the axial propagation of the localized pattern is performed. The work offers a different numerical perspective on the existing literature for the incompressible case, but does not present any analytical results to compare with the numerical predictions for the compressible case. The second focus of this thesis is therefore to make use of the similar mathematical structures of the inflation and elasto-capillary problems and extend the established analytical bifurcation conditions and post-bifurcation results of Fu et al. (2021) to the compressible case. A comparison between our theory and the numerical simulation results of Dortdivanlioglu and Javili (2022) can then be made.

1.3 Creasing: a unique localized pattern

When an elastic half-space is subjected to a horizontal compression, the formation of a *crease*, which we define as an isolated region of self-contact at the material's free surface, will occur at some critical load. Whilst creasing is indeed a localized pattern formation, it is mathematically dissimilar to the localized bulging and necking phenomena discussed previously since it is a *non-linear* bifurcation phenomenon which is disassociated from the zero wavenumber bifurcation mode. Crease formation is considered one of the most complex and challenging localized pattern formation problems to tackle theoretically, and it has attracted a wide range of interest in the non-linear elasticity community as a result.

In physiology and nature, creasing is widespread. For instance, it may be observed in the form of sulci patterns across the cerebral cortex of the brain, on the surface of a contorted elephants trunk and in many soft foods and gels under stress; see Fig. 1.4. However, there are many motivations for studying

(a) (b) (c)

Figure 1.4: Evidence of creasing on the surface of (a) the human brain, (b) a twisted elephants trunk and (c) Liangfen, a northern Chinese delicacy, under compression (Hong et al., 2009).

the fundamental mechanics of creasing aside from the general curiosity stemming from natural observations. For instance, creases are widely observed in growing tubular biological tissue (Ciarletta et al., 2014; Razavi et al., 2016), and have also been shown to influence the in vitro behaviour of cells (Chen et al., 2015) and to mitigate biofouling (Shivapooja et al., 2013). Even as far back as 100 years ago, crease formation greatly influenced the quality of photographs produced through Collotype (Sheppard and Elliott, 1918).

In the seminal theoretical work of Biot (1963), a linear bifurcation analysis showed that the surface of a compressed elastic half-space may develop a periodic *wrinkling* pattern with *undefined wavelength* at the critical stretch $\lambda \approx 0.54$. A discrepancy followed some time later when Gent and Cho (1999) experimentally observed the formation of *creases* in bent rubber blocks at the critical stretch $\lambda \approx 0.65$. A theme ensued where creases were widely observed in experimental studies of homogeneous elastic bodies under mechanical loading (Ghatak and Das, 2007; Mora et al., 2011), spatially constrained growth or swelling (Tanaka et al., 1987; Trujillo et al., 2008; Yoon et al., 2010; Dervaux and Ben Amar, 2012) and electric fields (Xu and Hayward, 2013; Park et al., 2013). In contrast, the periodic pattern formation predicted by Biot (1963) remained elusive in reality.

Post-bifurcation analyses of Biot's wrinkling pattern were also formulated (Fu, 1999; Cao and Hutchinson, 2011). In particular, Fu (1999) considered the uni-axial compression of an elastic half space with a sinusoidal surface profile imperfection, and showed that static shocks evolved in the elevated surface profiles at smaller compressions than Biot's threshold. This suggested that a solution characterized by locally large displacement gradients was preferred. Hohlfeld and Mahadevan (2012) showed numerically that creasing is indeed a distinct bifurcation phenomenon to wrinkling, and determined a prediction of $\lambda = 0.6474$ for the onset of the former; see Fig. 1.5. To elaborate, wrinkling is a solution where the displacement field relative to a primary uni-axially compressed state is *small*. In contrast, the displacement field of the region affected by a crease relative to the uni-axially compressed state is *large*. Moreover, whilst wrinkling is a periodic surface displacement which is *non-local* in physical space, creasing is a localized phenomenon which produces a self-contacting region of the free-surface which ends in a sharp singular tip. Hence, crease formation is inherently non-linear and thus undetectable through a conventional linear bifurcation analysis such as the one conducted in Biot (1963).

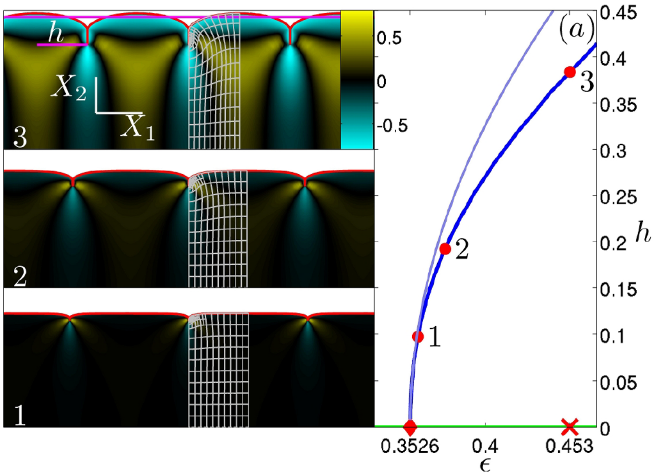

Figure 1.5: A plot of the crease depth h against the compressive strain $\epsilon = 1 - \lambda$ (right) from Hohlfeld and Mahadevan (2012). At $\epsilon = 0.3526$ ($\lambda = 0.6474$), we have the emergence of a non-zero h, which corresponds to the initiation of a crease. The deformation fields labelled $1, 2$ and 3 on the left coincide with the identically labelled points on the solid blue numerically simulated bifurcation curve on the right.

Further numerical studies (Trujillo et al., 2008; Hong et al., 2009; Yoon et al., 2010; Chen et al., 2012; Tallinen et al., 2013) provided bifurcation points for crease formation which were agreeable with the one found in Hohlfeld and Mahadevan (2012). Chen et al. (2012) showed that surface tension effects can delay the onset of creases. Hohlfeld (2013) then attributed crease formation to the coexistence of two scale-invariant deformation fields. Jin and Suo (2015) conducted numerical simulations of strain-stiffening materials in Abaqus (2013) by applying the Gent material model (Gent, 1996), and found that creasing in this class of materials occurs supercritically. Most recently, Yang et al. (2021) proposed, and also verified numerically, a perturbation force-based criterion whereby creasing will occur when the application of a concentrated force to the primary deformed configuration would produce infinite displacement (when fully non-linear governing equations are employed). In conjunction, Pandurangi et al. (2022) conducted a solution branch following numerical simulation procedure guided by group-theoretic considerations to study creasing in a functionally graded layer and a thin-film on a substrate layer.

By extending the work in Ciarletta (2018), Ciarletta and Truskinovsky (2019) produced the first analytical prediction of the critical stretch for crease formation. The central idea is to assume that the effect of crease formation on the material sufficiently far away from the crease tip is equivalent to the action of a concentrated force, and then to use a conservation law associated with the energy-momentum tensor to determine the critical stretch. This idea is undoubtedly ground-breaking, but the paper is notably brief with very limited detail surrounding crucial steps in the analysis. As a consequence, a reproduction of the presented results is particularly difficult to achieve, and this arguably restricts the level of attention that this seminal study should receive. The final focus of this thesis is therefore to present a rephrasing of the original paper with clearer and more precise derivations produced independently using, in part, slightly different albeit well-justified approaches. It will be shown that this in turn leads to slightly different results. It is hoped that this will generate a greater appreciation of the original idea of Ciarletta and Truskinovsky (2019) which may well prove to be the final solution to this fundamentally challenging bifurcation problem.

1.4 Overview of the thesis

The thesis will be organized in the following manner. As a starting point, we will present in chapter 2 the underlying theory of continuum mechanics and several other advanced mathematical techniques which play a pivotal role in our research. Chapters 3 through 5 contain a series of systematic studies into the bifurcation behaviour of soft incompressible hollow tubes under various elasto-capillary-based loading types and boundary conditions. These chapters are based, respectively, on analysis which has been published in Emery and Fu (2021a,b,c). Chapter 3 formulates conjectured analytical bifurcation conditions for localized pattern formation in these tubes based on known results for the prototypical inflation problem previously discussed. A linear bifurcation analysis is also performed to determine if an axi-symmetric pattern formation associated zero wavenumber or strictly positive wavenumber is favoured. An initial connection between the zero wavenumber bifurcation mode and localized pattern formation is made. In chapter 4, we investigate circumferential buckling modes and the competition with the axi-symmetric bifurcation modes studied in chapter 3 to determine the overall preferred bifurcation behaviour. Chapter 5 finally focusses on the scenarios where the axi-symmetric zero wavenumber mode is favoured. A weakly non-linear analysis is conducted to verify explicitly that this bifurcation mode corresponds to a localized pattern formation, and to determine whether the localized pattern arises subcritically or supercritically. Although the corresponding fully non-linear post-bifurcation behaviour is investigated initially through FEM simulations, it will be shown, remarkably, that the entire bifurcation process which the tube undergoes can be understood analytically. In chapter 6, we use the analytical tools established in chapters 3 through 5 to study elasto-capillary-based localized pattern formation in *compressible* solid cylinders. Comparisons between our theory and newly emerged numerical simulation results are made. The paper associated with this chapter (Emery, 2023) is currently under peer review. Chapter 7 presents a theoretical study of crease formation in a compressed elastic material based on the seminal idea of Ciarletta and Truskinovsky (2019). Conclusions and perspectives on the entire body of research are finally offered in chapter 8.

2

Mathematical Preliminaries

Contents

2.1 Introduction

In this chapter, we begin by presenting the classical theory of continuum mechanics which underpins our research. Specifically, we discuss kinematics, balance laws and field equations, constitutive equations, hyperelastic materials and strain-energy functions. For a complete accounting of the fundamental concepts of continuum mechanics, we refer the reader to Ogden (1997) and Chadwick (1999). We then move on to summarizing further advanced mathematical techniques employed over the course of the thesis. To elaborate, we cover: the incremental equations governing infinitesimal perturbations of a finitely deformed elastic body; a mixed coordinate stream function approach to satisfying material incompressibility; variational principles and conservation laws; numerical techniques for solving variable-coefficient linear eigenvalue problems; and a perturbation approach to weakly non-linear analysis in the context of non-linear elasticity.

2.2 Theory of continuum mechanics

2.2.1 Kinematics

Consider an elastic material body with an undeformed *reference* configuration $\mathcal{B}_0$ and a deformed *current* configuration $\mathcal{B}_e$. A representative material particle in $\mathcal{B}_0$ and $\mathcal{B}_e$ has the position vector $\boldsymbol{X}$ and $\boldsymbol{x}$, respectively, and we may define the injective mapping function $\boldsymbol{\chi} : \mathcal{B}_0 \to \mathcal{B}_e$ to describe the deformation of the material body. The vector function $\boldsymbol{\chi}$ and its inverse $\boldsymbol{\chi}^{-1}$ are defined through

$$\boldsymbol{x} = \boldsymbol{\chi}(\boldsymbol{X}, t) \quad \text{and} \quad \boldsymbol{X} = \boldsymbol{\chi}^{-1}(\boldsymbol{x}, t), \tag{2.1}$$

where t denotes time; see Fig. 2.1. For any coordinate system, the differentials of $\boldsymbol{X}$ and $\boldsymbol{x}$, $d\boldsymbol{X}$ and $d\boldsymbol{x}$, may be defined as follows:

$$d\boldsymbol{X} = \frac{\partial \boldsymbol{X}}{\partial S_A} dS_A = \boldsymbol{G}_A dS_A \quad \text{and} \quad d\boldsymbol{x} = \frac{\partial \boldsymbol{x}}{\partial s_i} ds_i = \boldsymbol{g}_i ds_i, \tag{2.2}$$

where S_A and s_i are the coordinates pertaining to $\boldsymbol{X}$ and $\boldsymbol{x}$, respectively, $\boldsymbol{G}_A$ and $\boldsymbol{g}_i$ are the associated *covariant* vectors and Einstein's summation convention over repeated indices is employed. We may also introduce the *contravariant* vectors $\boldsymbol{G}^A$ and $\boldsymbol{g}^i$ through

$$\boldsymbol{G}_A \cdot \boldsymbol{G}^B = \delta_{AB} \quad \text{and} \quad \boldsymbol{g}_i \cdot \boldsymbol{g}^j = \delta_{ij}, \tag{2.3}$$

where
$$\delta_{ij} = \begin{cases} 1, & \text{if} \quad i = j \\ 0, & \text{if} \quad i \neq j \end{cases}, \tag{2.4}$$

is the Kroenecker delta function.

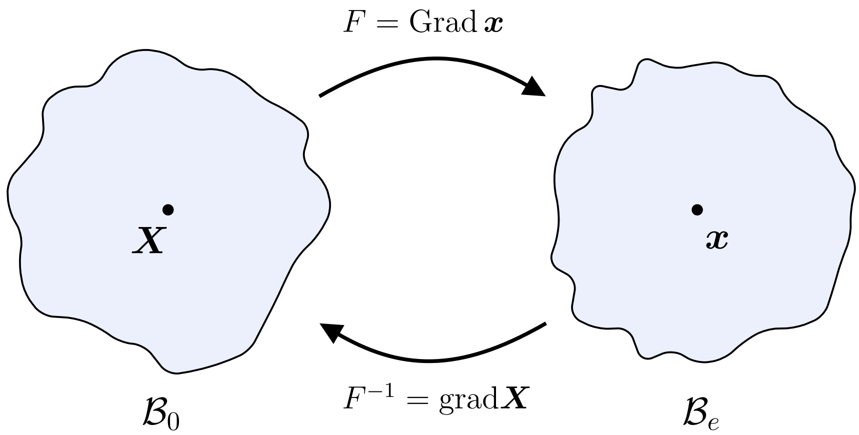

Figure 2.1: A schematic of the reference configuration $\mathcal{B}_0$ and the current configuration $\mathcal{B}_e$.

The *deformation gradient tensor* F underpinning the analysis of local deformation and motion is expressible through

$$d\boldsymbol{x} = F d\boldsymbol{X}, \quad \text{where} \quad F = \text{Grad}\,\boldsymbol{x} = \frac{\partial \boldsymbol{x}}{\partial S_A} \otimes \boldsymbol{G}^A, \tag{2.5}$$

with Grad denoting the gradient operator with respect to the coordinates in $\mathcal{B}_0$ and $\otimes$ the tensor product between two vectors. Note that F is an invertible tensor, and we have that

$$F^{-1} = \text{grad}\boldsymbol{X} = \frac{\partial \boldsymbol{X}}{\partial s_i} \otimes \boldsymbol{g}^i, \tag{2.6}$$

where grad is the gradient operator with respect to the coordinates in $\mathcal{B}_e$. When a three-dimensional Cartesian coordinate system is adopted, the position vectors $\boldsymbol{X}$ and $\boldsymbol{x}$ are expressed generally as follows:

$$\boldsymbol{X} = X_A \boldsymbol{E}_A \quad \text{and} \quad \boldsymbol{x} = x_i \boldsymbol{e}_i, \tag{2.7}$$

where $(\boldsymbol{E}_A)$ and $(\boldsymbol{e}_i)$ are the associated orthonormal bases with $i, A = 1, 2, 3$. The corresponding deformation gradient is given by

$$F = \frac{\partial (x_i \boldsymbol{e}_i)}{\partial X_A} \otimes \boldsymbol{E}_A = \frac{\partial x_i}{\partial X_A} \boldsymbol{e}_i \otimes \boldsymbol{E}_A. \tag{2.8}$$

In cylindrical polar coordinates, the position vectors $\boldsymbol{X}$ and $\boldsymbol{x}$ are expressed as

$$\boldsymbol{X} = R\boldsymbol{E}_R + Z\boldsymbol{E}_Z \quad \text{and} \quad \boldsymbol{x} = r\boldsymbol{e}_r + z\boldsymbol{e}_z. \tag{2.9}$$

In terms of the orthonormal bases $(\boldsymbol{E}_R, \boldsymbol{E}_\Theta, \boldsymbol{E}_Z)$ and $(\boldsymbol{e}_r, \boldsymbol{e}_\theta, \boldsymbol{e}_z)$, the corresponding deformation gradient can be shown to take the following form:

$$\begin{aligned} F = {} & \frac{\partial r}{\partial R} \boldsymbol{e}_r \otimes \boldsymbol{E}_R + \frac{1}{R}\frac{\partial r}{\partial \Theta} \boldsymbol{e}_r \otimes \boldsymbol{E}_\Theta + \frac{\partial r}{\partial Z} \boldsymbol{e}_r \otimes \boldsymbol{E}_Z + r\frac{\partial \theta}{\partial R} \boldsymbol{e}_\theta \otimes \boldsymbol{E}_R + \frac{r}{R}\frac{\partial \theta}{\partial \Theta} \boldsymbol{e}_\theta \otimes \boldsymbol{E}_\Theta \\ & + r\frac{\partial \theta}{\partial Z} \boldsymbol{e}_\theta \otimes \boldsymbol{E}_Z + \frac{\partial z}{\partial R} \boldsymbol{e}_z \otimes \boldsymbol{E}_R + \frac{1}{R}\frac{\partial z}{\partial \Theta} \boldsymbol{e}_z \otimes \boldsymbol{E}_\Theta + \frac{\partial z}{\partial Z} \boldsymbol{e}_z \otimes \boldsymbol{E}_Z. \end{aligned} \tag{2.10}$$

Let dV and dv denote infinitesimal volume elements in $\mathcal{B}_0$ and $\mathcal{B}_e$, respectively. It can be shown directly from $(2.5)_1$ that the following relation holds:

$$dv = JdV, \quad \text{where} \quad J \equiv \det F \neq 0; \tag{2.11}$$

see Chadwick (1999, pp. 60-62). Thus, the quantity J characterizes the change in volume of an infinitesimal element due to the effected deformation, and it is strictly non-zero under the assumption that material cannot be destroyed. If a material is incompressible, its volume remains unchanged under the deformation $\mathcal{B}_0 \to \mathcal{B}_e$, and hence the following constraint of *isochorism* holds:

$$\det F = 1. \tag{2.12}$$

Suppose also that $d\boldsymbol{X}_1$ and $d\boldsymbol{X}_2$ are two arbitrary line elements at an arbitrary point on a material surface in $\mathcal{B}_0$. Furthermore, let $\boldsymbol{N}$ be the outward unit normal to the surface at this point and let dA be the area of the parallelogram spanned by $d\boldsymbol{X}_1$ and $d\boldsymbol{X}_2$. Then, we have

$$\boldsymbol{n}da = J(F^{-1})^T \boldsymbol{N} dA, \tag{2.13}$$

where $\boldsymbol{n}$ and da are the *images* of $\boldsymbol{N}$ and dA (respectively) in $\mathcal{B}_e$, and a superscript T denotes transposition. Equation (2.13) is more commonly known as *Nanson's formula* (Chadwick, 1999, pp. 60-61), and measures the change in area of a material surface element in a body under deformation.

Since the deformation gradient F is invertible, it has the following *unique* right and left polar decompositions (Chadwick, 1999, pp. 33-35):

$$F = QU = VQ, \tag{2.14}$$

where U and V are positive-definite symmetric right and left stretch tensors (respectively) and Q is a *proper orthogonal* or *rotation* tensor which possesses the properties

$$Q^T Q = QQ^T = I \quad \text{and} \quad \det Q = 1. \tag{2.15}$$

It is known from matrix theory that any symmetric tensor possesses three real eigenvalues and an associated orthonormal set of eigenvectors; these tensors are uniquely determined by their eigenvalues and eigenvectors. For instance, U and V may have the spectral representations

$$U = \sum_{i=1}^{3} \lambda_i (\boldsymbol{p}_i \otimes \boldsymbol{p}_i) \quad \text{and} \quad V = \sum_{i=1}^{3} \lambda_i (\boldsymbol{q}_i \otimes \boldsymbol{q}_i), \tag{2.16}$$

where λ_i are the eigenvalues (or *principal stretches*) of U and V, and $\boldsymbol{p}_i$ and $\boldsymbol{q}_i = Q\boldsymbol{p}_i$ are associated the eigenvectors. From the polar decomposition $(2.14)_1$ we deduce that the local deformation of a material body about a representative particle is induced by first applying stretches λ_i in the principal directions of U, followed by a rigid rotation given by Q. The same is true for the polar decomposition $(2.14)_2$, except we apply the rigid rotation of the body first followed by stretches in the principal directions of V. The right and left Cauchy-Green strain tensors are then given respectively by

$$C = F^T F = U^2 \quad \text{and} \quad B = FF^T = V^2, \tag{2.17}$$

and it is noted that both C and B are symmetric tensors. It follows immediately from (2.16) that

$$C = \sum_{i=1}^{3} \lambda_i^2 (\boldsymbol{p}_i \otimes \boldsymbol{p}_i) \quad \text{and} \quad B = \sum_{i=1}^{3} \lambda_i^2 (\boldsymbol{q}_i \otimes \boldsymbol{q}_i). \tag{2.18}$$

We may also define the following three principal invariants of B (or C):

$$\begin{aligned} I_1 &= \operatorname{tr} B = \lambda_1^2 + \lambda_2^2 + \lambda_3^2, \\ I_2 &= \frac{1}{2}(I_1^2 - \operatorname{tr} B^2) = \lambda_1^2\lambda_2^2 + \lambda_2^2\lambda_3^2 + \lambda_1^2\lambda_3^2, \\ I_3 &= \det B = J^2 = \lambda_1^2\lambda_2^2\lambda_3^2. \end{aligned} \tag{2.19}$$

The *velocity gradient* L of a material point $\boldsymbol{x}$ is given by

$$L = \operatorname{grad} \boldsymbol{v}, \quad \text{where} \quad \boldsymbol{v} = \dot{\boldsymbol{x}}, \tag{2.20}$$

and a superimposed dot denotes the material time derivative. Using (2.20) and the identity $\operatorname{Grad} \boldsymbol{v} = (\operatorname{grad} \boldsymbol{v})\, F$, it is straightforward to show that

$$\dot{F} = \frac{\partial}{\partial t} F = \frac{\partial}{\partial t} \operatorname{Grad} \boldsymbol{x} = \operatorname{Grad} \boldsymbol{v} \quad \text{and} \quad LF = (\operatorname{grad} \boldsymbol{v}) F = \operatorname{Grad} \boldsymbol{v}, \tag{2.21}$$

and hence

$$\dot{F} = LF. \tag{2.22}$$

Alternatively, we can consider the decomposition $L = D + W$, where D is a symmetric *rate of strain tensor* and W is a skew-symmetric *spin tensor*. As their names suggest, D and W measure the rate of change of stretch and rotation (respectively) as the material body passes through its current configuration.

2.2.2 Balance laws and field equations

2.2.2.1 Conservation of mass

Let $\rho_0(\boldsymbol{X})$ and $\rho(\boldsymbol{x}, t)$ denote the *mass densities* of the material body in the reference configuration $\mathcal{B}_0$ and the current configuration $\mathcal{B}_e$, respectively. Conservation of mass requires that mass in a material body must not be created or destroyed under deformation. Mathematically, we have that

$$\rho_0 \, dV = \rho \, dv. \tag{2.23}$$

On making use of (2.11), the relation (2.23) becomes

$$\rho_0 = J\rho. \tag{2.24}$$

Then, on differentiating (2.24) with respect to t and using the identity $\dot{J} = J\mathrm{div}\boldsymbol{v}$ (with div being the *divergence operator* in $\mathcal{B}_e$), we obtain the *spatial equation of continuity*

$$\dot{\rho} + \rho \, \mathrm{div}\boldsymbol{v} = 0. \tag{2.25}$$

For incompressible materials, $J = 1$ and hence the density $\rho = \rho_0$ is constant. In this case, (2.25) reduces to

$$\mathrm{div} \, \boldsymbol{v} = 0. \tag{2.26}$$

2.2.2.2 Principle of linear momentum

The principle of linear momentum states that the rate of change of the total linear momentum is equal to the resultant force acting on the body. Thus, if the body is under no external forces, the total linear momentum of the body should remain constant. Let $\mathcal{R}_0$ and $\mathcal{R}$ be *arbitrary material regions* in the reference and current configurations, respectively. Also, let $\boldsymbol{b}$ denote the body force acting on $\mathcal{R}$ and let $\boldsymbol{t} = \boldsymbol{t}(\boldsymbol{x}, \boldsymbol{n})$ be the vector field representing the *force per unit area* acting on an arbitrary material surface $\partial\mathcal{R}$ with outward unit normal $\boldsymbol{n}$ in the region $\mathcal{R}$. Indeed, $\boldsymbol{t}$ is commonly referred to as the *traction vector*, and is assumed to be a continuous vector function of $\boldsymbol{x}$ and $\boldsymbol{n}$. Then, the principle of linear momentum states that

$$\frac{d}{dt}\int_{\mathcal{R}} \rho \boldsymbol{v} \, dv = \int_{\mathcal{R}} \rho \boldsymbol{b} \, dv + \int_{\partial\mathcal{R}} \boldsymbol{t} da. \tag{2.27}$$

With use of (2.11) and (2.24), the integral on the left-hand side of (2.27) can be reformulated as such:

$$\frac{d}{dt}\int_{\mathcal{R}} \rho \boldsymbol{v} \, dv = \frac{d}{dt}\int_{\mathcal{R}_0} \rho \boldsymbol{v} J dV = \int_{\mathcal{R}_0} \frac{d}{dt}(\rho_0 \boldsymbol{v}) dV = \int_{\mathcal{R}} \rho \dot{\boldsymbol{v}} dv. \tag{2.28}$$

Then, on substituting the identity (2.28) back into (2.27), we obtain

$$\int_{\mathcal{R}} \rho \dot{\boldsymbol{v}}\, dv = \int_{\mathcal{R}} \rho \boldsymbol{b}\, dv + \int_{\partial\mathcal{R}} \boldsymbol{t} da. \tag{2.29}$$

2.2.2.3 Equations of motion and stress boundary conditions

Cauchy's Theorem (Ogden, 1997) states that the tractions $\boldsymbol{t}$ acting on a material surface $\partial\mathcal{R}$ with outward unit normal $\boldsymbol{n}$ in the current configuration can be related to the aforementioned normal through the second-order tensor field $\sigma = \sigma(\boldsymbol{x}, t)$ as follows:

$$\boldsymbol{t} = \sigma^T \boldsymbol{n}. \tag{2.30}$$

The tensor σ is known as the *Cauchy stress tensor*, and it is independent of $\boldsymbol{n}$. Upon substitution of (2.30), (2.29) becomes

$$\int_{\mathcal{R}} \rho \dot{\boldsymbol{v}}\, dv = \int_{\mathcal{R}} \rho \boldsymbol{b}\, dv + \int_{\partial\mathcal{R}} \sigma^T \boldsymbol{n} da. \tag{2.31}$$

With use of the *Divergence Theorem*, the surface integral on the right-hand side of (2.31) can be converted to a volume integral as such:

$$\int_{\partial\mathcal{R}} \sigma^T \boldsymbol{n} da = \int_{\mathcal{R}} \operatorname{div} \sigma dv, \qquad \text{where} \qquad \operatorname{div} \sigma = \boldsymbol{g}^i \cdot \frac{\partial \sigma}{\partial s_i}. \tag{2.32}$$

Since the region $\mathcal{R}$ is arbitrarily chosen, we obtain the following equations of motion on substituting (2.32) into (2.31):

$$\operatorname{div} \sigma + \rho \boldsymbol{b} = \rho \dot{\boldsymbol{v}}. \tag{2.33}$$

Moreover, we may deduce from the principle of angular momentum (Chadwick, 1999, pp. 90-101) that σ is a symmetric tensor. That is, the following relation holds:

$$\sigma = \sigma^T. \tag{2.34}$$

If the material body is in *mechanical equilibrium*, then $\boldsymbol{b} = \boldsymbol{0}$ and $\dot{\boldsymbol{v}} = \boldsymbol{0}$, and the equations of motion (2.33) reduce to the equilibrium equations

$$\operatorname{div} \sigma = \boldsymbol{0}. \tag{2.35}$$

With use of (2.13), we can write

$$\sigma^T \boldsymbol{n} da = \sigma^T J (F^{-1})^T \boldsymbol{N} dA = S^T \boldsymbol{N} dA, \tag{2.36}$$

where S, defined by

$$S = J F^{-1} \sigma, \tag{2.37}$$

is the *nominal stress tensor*. The nominal stress gives the contact force in the current configuration per unit area in the *reference configuration*. On transposing S, we obtain a further measure of stress in the first Piola-Kirchhoff stress tensor π, i.e.:

$$\pi = S^T. \tag{2.38}$$

The equations of motion (2.33) and the equilibrium equations (2.35) can be respectively defined in $\mathcal{B}_0$ in terms of S as follows:

$$\operatorname{Div} S + \rho_0 \boldsymbol{b} = \rho_0 \dot{\boldsymbol{v}} \quad \text{and} \quad \operatorname{Div} S = \mathbf{0}. \tag{2.39}$$

Let $\partial\mathcal{B}_0$ be the portion of the boundary in the reference configuration where the traction is prescribed to be $\boldsymbol{t}_0$, say. Then the following boundary condition holds:

$$S^T \boldsymbol{N}|_{\partial\mathcal{B}_0} = \boldsymbol{t}_0. \tag{2.40}$$

We assume that the material body is subject to *dead-loading*, by which we mean that the resultant of the traction $\boldsymbol{t}_0$ is held fixed throughout the deformation $\mathcal{B}_0 \to \mathcal{B}_e$; see Fu and Ogden (2001). With use of (2.36), the associated boundary condition in $\mathcal{B}_e$ is

$$\sigma^T \boldsymbol{n}|_{\partial\mathcal{B}_e} = \boldsymbol{t}_0 \frac{dA}{da}, \tag{2.41}$$

where $\partial\mathcal{B}_e$ is the image of $\partial\mathcal{B}_0$ in $\mathcal{B}_e$.

2.2.3 Constitutive equations

The governing equations (2.33) – (2.34) and boundary conditions (2.41) are valid for any continuum. The constitutive equations allow us to distinguish between the many types of continua, such as inviscid fluids, Newtonian viscous fluids, non-Newtonian fluids, elastic materials and plastic materials. In order to facilitate our later work, we need to specify these equations to an elastic material in mechanical equilibrium. Currently, we have six dependent variables which are specifically the six distinct components of σ. However, there are only three equilibrium equations in (2.35). Thus, in order to close the system, we require three further constitutive equations which relate σ to the deformation. In elasticity, we assume that the Cauchy stress depends solely on the deformation gradient F through the relation

$$\sigma = g(F), \tag{2.42}$$

where g is a symmetric tensor-valued function. However, when the aim is to find unique solutions to well-posed problems in elasticity, (2.42) is too general to make headway. To overcome this, we may impose various principles onto the constitutive relation (2.42) which restrict the multitude of mathematical forms it may take.

2.2.3.1 Principle of objectivity

The principle of objectivity (or *material frame-indifference*) states that the response of a material (and hence the constitutive equation (2.42)) is invariant with respect to any equivalent pair of observers. In the case of an elastic material, the principle of objectivity requires that the symmetric tensor-valued function g defined in (2.42) satisfies the condition

$$g(QF) = Qg(F)Q^T, \tag{2.43}$$

$\forall$ proper orthogonal rotation tensors Q.

2.2.3.2 Isotropic materials

An elastic material is said to possess a *symmetry* if its constitutive response is invariant to changes in the reference configuration $\mathcal{B}_0$ (e.g. through a rotation or an in-plane reflection). A transformation of the reference configuration from $\mathcal{B}_0$ to $\mathcal{B}_0^\star$, say, is equivalent to multiplying F from the right by P, where P is the deformation gradient corresponding to $\mathcal{B}_0 \to \mathcal{B}_0^\star$. Thus, if the constitutive response of a material is invariant with respect to the transformation $\mathcal{B}_0 \to \mathcal{B}_0^\star$, then

$$g(FP) = g(F) \quad \forall \text{ arbitrarily invertible } F. \tag{2.44}$$

The set of all P satisfying (2.44) forms a group called the *symmetry group* of the material.

A material is said to be *isotropic* if its symmetry group is the set of all orthogonal tensors Q. Therefore, isotropy requires that

$$g(FQ) = g(F) \quad \forall \text{ orthogonal } Q. \tag{2.45}$$

Physically, isotropy means that the material's properties and constitutive behaviour are independent of direction. On replacing F in the left-hand side of (2.45) with the left polar decomposition VR and setting $Q = R^T$, we obtain

$$g(V) = g(F). \tag{2.46}$$

Given (2.17), we deduce from (2.46) that

$$g(F) = g(B^{1/2}) = h(B), \tag{2.47}$$

where h is a symmetric tensor-valued function. With further use of the objectivity condition (2.43) and the isotropy condition (2.45), we determine that

$$g(RFQ) = g(RF) = Rg(F)R^T = Rh(B)R^T. \tag{2.48}$$

Then, on setting $Q = R^T$ and making use of the identity (2.47), (2.48) becomes

$$h(RBR^T) = Rh(B)R^T, \tag{2.49}$$

and (2.49) demonstrates that h is an isotropic tensor function of B. It then follows that the function h, and hence the Cauchy stress σ, admits the representation

$$\sigma = h(B) = \eta_0 I + \eta_1 B + \eta_2 B^2, \tag{2.50}$$

where η_0, η_1 and η_2 are scalar functions of the principal invariants (2.19) of B, and I is the identity tensor; see Truesdell and Noll (2004).

2.2.4 Hyperelastic materials

A material is said to be *hyperelastic* if there exists a *strain-energy function* $W(F)$ measured per unit volume in the reference configuration which satisfies the constitutive relation

$$\dot{W} = J\,\mathrm{tr}\,\{\sigma L\}. \tag{2.51}$$

With use of the identity (2.22), we may deduce

$$\dot{W} = \frac{\partial W}{\partial F_{iA}}\frac{\partial F_{iA}}{\partial t} = \mathrm{tr}\left\{\frac{\partial W}{\partial F}\dot{F}\right\} = \mathrm{tr}\left\{\frac{\partial W}{\partial F}LF\right\} = \mathrm{tr}\left\{F\frac{\partial W}{\partial F}L\right\}. \tag{2.52}$$

Then, on comparing (2.51) and (2.52), and using the fact that L is arbitrary for any given F, we obtain the following relationship between the Cauchy stress and the strain-energy function:

$$\sigma = J^{-1}F\frac{\partial W}{\partial F}, \quad \text{where} \quad \sigma_{ij} = J^{-1}F_{iA}\frac{\partial W}{\partial F_{jA}}. \tag{2.53}$$

Also, by applying (2.37), we may determine the following relationship between the nominal stress S and W:

$$S = \frac{\partial W}{\partial F}, \quad \text{where} \quad S_{Ai} = \frac{\partial W}{\partial F_{iA}}. \tag{2.54}$$

When specifying to an incompressible material, the relations (2.53) and (2.54) must be modified as such:

$$\sigma = F\frac{\partial W}{\partial F} - pI \quad \text{and} \quad S = \frac{\partial W}{\partial F} - pF^{-1}, \tag{2.55}$$

where p is the *Lagrangian multiplier* enforcing the incompressibility constraint (2.12) which may be interpreted as kinematic pressure. To elaborate, we may define the scalar field $\mathrm{tr}(\sigma D)$ as the *stress power* per unit volume in the current configuration, and this constitutes the rate of work done by the stress due to the stretching of material volume elements. Loosely speaking, the term involving p in the above expression for σ is a *workless constraint stress* in the sense that $\mathrm{tr}(-pID) = 0$, and this result emerges directly from (2.12); see Chadwick (1999, pp. 145-147).

Isotropy requires that W depends on F through B. Given the spectral representations (2.18) and the expressions (2.19), it follows that W may be expressed as a function of the three principal invariants of B in this case. It then follows from (2.53) that the Cauchy stress for a general isotropic hyperelastic material takes the form

$$\sigma = 2I_3^{1/2}W_3 I + 2I_3^{-1/2}\left\{W_1 + I_1 W_2\right\}B - 2I_3^{-1/2}W_2 B^2, \tag{2.56}$$

where $W_i = \partial W/\partial I_i$ for $i = 1, 2, 3$. When the material is incompressible also, the third invariant $I_3 = 1$ and W depends only on I_1 and I_2. In this instance, the constitutive equation $(2.55)_1$ becomes

$$\sigma = 2W_1 B - 2W_2 B^{-1} - pI. \tag{2.57}$$

2.2.5 Strain-energy functions

In the previous section, we stated that the constitutive behaviour of isotropic, hyperelastic materials may be underpinned by a strain-energy function of the form $W = W(I_1, I_2, I_3)$. When the material is also incompressible, the most general strain-energy function is of the form $W = W(I_1, I_2)$. In the following, we present some examples of strain-energy functions of these forms which are widely used in the literature.

2.2.5.1 Neo-Hookean material model

The *incompressible* neo-Hookean strain-energy function depends only on the first invariant I_1 and is defined through

$$W(I_1) = \frac{1}{2}\mu(I_1 - 3), \tag{2.58}$$

where μ is the *ground state shear modulus* of the material. Although the model gives reasonable agreement with experimental results at small strains, it provides less accuracy when deformations are large (Ogden, 1972). In spite of this, it is highly popular in the non-linear elasticity community due to its simplicity.

For a *compressible* neo-Hookean material, two widely used models in the literature are the so-called *quadratic* and *logarithmic* strain-energy functions. These are defined, respectively, through

$$W(I_1, I_3) = \frac{1}{2}\mu(I_1 - 3 - 2\log J) + \frac{1}{2}\hat{\lambda}\left\{\frac{1}{2}(J^2 - 1) - \log J\right\}, \tag{2.59}$$

and

$$W(I_1, I_3) = \frac{1}{2}\mu(I_1 - 3 - 2\log J) + \frac{1}{2}\hat{\lambda}(\log J)^2, \tag{2.60}$$

where

$$\hat{\lambda} = \frac{2\nu}{1 - 2\nu}, \tag{2.61}$$

is the first Lamé constant and $\nu \in [0, 1/2]$ is Poisson's ratio. Both models (2.59) and (2.60) have been shown to give good agreement with experimental data; see Horgan and Saccomandi (2004) and the references therein. It is noted that the material becomes incompressible in the limit $\nu \to 1/2$ and fully compressible in the limit $\nu \to 0$.

2.2.5.2 Mooney-Rivlin material model

The Mooney-Rivlin material model generalizes the neo-Hookean model (2.58) by incorporating the second invariant I_2. It takes the form

$$W(I_1, I_2) = \frac{1}{2}\mu_1(I_1 - 3 + \frac{1}{2}\mu_2(I_2 - 3), \tag{2.62}$$

where μ_1 and μ_2 are constants. The model was first proposed by Mooney (1940) and developed further by Rivlin (1948). Unlike the neo-Hookean model, the Mooney-Rivlin model is fairly accurate at moderate strains and provides physically adequate results provided that $\mu_1 > 0$ and $\mu_2 < 0$.

2.2.5.3 Gent material model

Gent (1996) proposed the following strain-energy function for incompressible hyperelastic materials which depends only on the first invariant I_1:

$$W(I_1) = -\frac{1}{2}\mu J_{\mathrm{m}}\ln\left(1 - \frac{I_1 - 3}{J_{\mathrm{m}}}\right), \tag{2.63}$$

where J_{m} is a positive constant representing the maximum extensibility of the material. To elaborate, in the limit $J_{\mathrm{m}} \to I_1 - 3$ the material becomes completely rigid, and in the limit $J_{\mathrm{m}} \to \infty$ the Gent model reduces to the neo-Hookean model (2.58). The theoretical predictions provided by the Gent model have been shown to be accurate at larger strains, and the additional benefit of its simplistic form means it is a highly popular model in the literature. A compressible version of the Gent model may be written as

$$W(I_1, I_3) = -\frac{\mu}{2}\left\{J_\mathrm{m}\ln\left(1-\frac{I_1-3}{J_\mathrm{m}}\right)+2\ln J\right\}+\frac{1}{2}\hat{\lambda}\left\{\frac{1}{2}(J^2-1)-\log J\right\}. \quad (2.64)$$

2.2.5.4 Gent-Gent material model

One downside to the Gent model was highlighted by Pucci and Saccomandi (2002) who, on comparing with the classical experimental stress-strain data in Treloar (1944) for rubber under extension, showed that it loses accuracy in the small-to-moderate strain regime. To overcome this, they modified (2.63) by adding an extra term which involves the second principal invariant I_2 and a new material constant Λ. The resulting *Gent-Gent material model* takes the following form:

$$W(I_1, I_2) = -\frac{1}{2}\mu J_\mathrm{m}\ln\left(1-\frac{I_1-3}{J_\mathrm{m}}\right)+\Lambda\ln\left(\frac{I_2}{3}\right), \quad (2.65)$$

and its fitting with experimental data in the small stretch regime has been shown to have a much smaller relative error than the Gent model counterpart (Zhou et al., 2018).

2.3 The incremental equations

The method of superposing incremental deformation fields onto large deformation fields (otherwise know as the *small-on-large theory*) is widely used to analyze the linear bifurcation behaviour and stability of elastic solids under finite strain. The approach was originally developed by Green et al. (1952) and Pipkin and Rivlin (1961). For a complete overview of the method of incremental deformations, we refer the reader to Fu and Ogden (2001) and Ogden (2007). In the following, we give a summary of the stress-based linearized incremental equations governing infinitesimal perturbations of a finitely deformed elastic material.

To begin, consider an incompressible, isotropic, hyperelastic body and assume it possesses an unstressed reference configuration $\mathcal{B}_0$ and a finitely deformed configuration $\mathcal{B}_e$. It is the stability and bifurcation behaviour of the latter configuration which we are interested in studying. To this end, suppose that we further subject $\mathcal{B}_e$ to a small-amplitude perturbation which produces a *resulting configuration* $\mathcal{B}_t$; see Fig. 2.2. The question we then ask is: what are the equations governing such incremental perturbations?

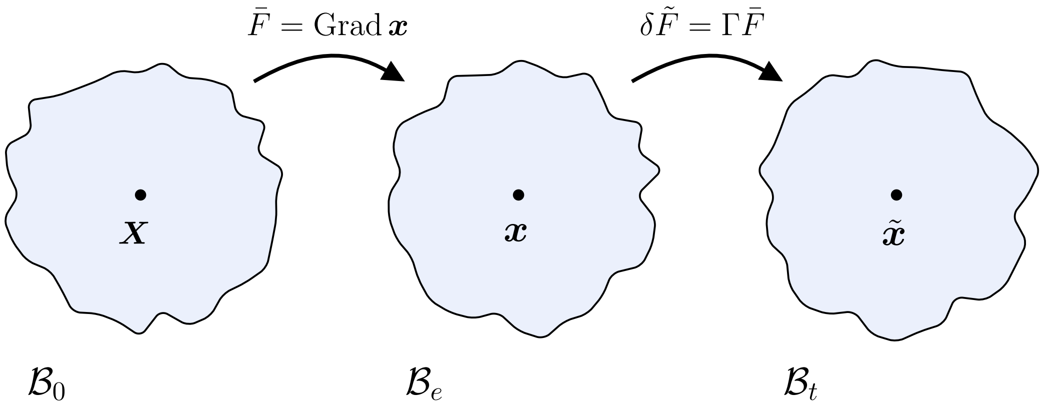

Figure 2.2: A schematic of the reference configuration $\mathcal{B}_0$, the finitely deformed configuration $\mathcal{B}_e$ and the resulting configuration $\mathcal{B}_t$.

The position vector of a representative material particle in $\mathcal{B}_0$, $\mathcal{B}_e$ and $\mathcal{B}_t$ is denoted by $\boldsymbol{X}$, $\boldsymbol{x}(\boldsymbol{X})$ and $\tilde{\boldsymbol{x}}(\boldsymbol{X}, t)$, respectively. We may then write

$$\tilde{\boldsymbol{x}} = \boldsymbol{x}(\boldsymbol{X}) + \boldsymbol{u}(\boldsymbol{x}, t), \tag{2.66}$$

where $\boldsymbol{u}$ is the incremental displacement vector field associated with the deformation $\mathcal{B}_e \to \mathcal{B}_t$. Denote by $\bar{F}$ and $\tilde{F}$ the deformation gradients corresponding to $\mathcal{B}_0 \to \mathcal{B}_e$ and $\mathcal{B}_0 \to \mathcal{B}_t$, respectively. For the remainder of this section, a bar and a tilde signifies association with the deformations $\mathcal{B}_0 \to \mathcal{B}_e$ and $\mathcal{B}_0 \to \mathcal{B}_t$, respectively. On making use of (2.66) and the identity $\mathrm{Grad}\,\boldsymbol{u} = (\mathrm{grad}\boldsymbol{u})F$, we have that

$$\bar{F} = \mathrm{Grad}\,\boldsymbol{x} \quad \text{and} \quad \tilde{F} = \mathrm{Grad}\,\tilde{\boldsymbol{x}} = (I + \Gamma)\bar{F}, \tag{2.67}$$

where $\Gamma = \operatorname{grad}\boldsymbol{u}$ is the *displacement gradient tensor.* Given (2.67), the incompressibility constraints associated with $\mathcal{B}_0 \to \mathcal{B}_e$ and $\mathcal{B}_e \to \mathcal{B}_t$ take the respective forms

$$\bar{J} \equiv \det \bar{F} = 1 \quad \text{and} \quad \operatorname{tr}\Gamma = 0, \tag{2.68}$$

with the latter presented in its linearized form. Then, with use of (2.38) and $(2.55)_2$, the nominal stress tensors $\bar{S}$ and $\tilde{S}$ associated with the deformations $\mathcal{B}_0 \to \mathcal{B}_e$ and $\mathcal{B}_0 \to \mathcal{B}_t$ (respectively) are found to take the form

$$\bar{S} = \left.\frac{\partial W}{\partial F}\right|_{F=\bar{F}} - \bar{p}\bar{F}^{-1} \quad \text{and} \quad \tilde{S} = \left.\frac{\partial W}{\partial F}\right|_{F=\tilde{F}} - \tilde{p}\tilde{F}^{-1}, \tag{2.69}$$

where $\bar{p}$ and $\tilde{p} = \bar{p} + \delta p$ are the Lagrangian multipliers in $\mathcal{B}_e$ and $\mathcal{B}_t$, respectively, and δp is the incremental pressure. Under the assumption that the superposed incremental displacement is static, the equilibrium equations in $\mathcal{B}_0$ and $\mathcal{B}_e$ then become

$$\operatorname{Div}\bar{S} = 0 \quad \text{and} \quad \operatorname{Div}\tilde{S} = 0, \tag{2.70}$$

respectively. Through simple subtraction of $(2.70)_1$ from $(2.70)_2$, the *incremental* equilibrium equations in $\mathcal{B}_e$ can be written in the following form

$$\operatorname{Div}\left\{\tilde{S} - \bar{S}\right\} = \operatorname{div}\left\{\bar{J}^{-1}\bar{F}\left(\tilde{S} - \bar{S}\right)\right\} = 0. \tag{2.71}$$

Through inspection of (2.71), it is convenient to introduce an *incremental stress tensor* χ through

$$\chi = \bar{J}^{-1}\left(\tilde{S} - \bar{S}\right)^T \bar{F}^T, \tag{2.72}$$

so that (2.71) becomes

$$\operatorname{div}\chi^T = 0. \tag{2.73}$$

On expanding $(2.69)_2$ to leading order around $F = \bar{F}$, the expansions for the components χ_{ij} of χ are found to take the form

$$\chi_{ij} = \mathcal{A}_{jilk}\Gamma_{kl} + \bar{p}\,\Gamma_{ji} - \delta p\,\delta_{ji}, \tag{2.74}$$

where the *first-order instantaneous elastic moduli* $\mathcal{A}_{jilk}$ are defined through

$$\mathcal{A}_{jilk} = \bar{F}_{jA}\bar{F}_{lB}\frac{\partial^2 W}{\partial F_{iA}\partial F_{kB}}\bigg|_{F=\bar{F}}. \tag{2.75}$$

For the special case where the strain-energy function W depends only on the first invariant I_1, the above moduli are given by

$$\mathcal{A}_{jilk} = 2\left\{2W''(\bar{I}_1)\bar{B}_{ij}\bar{B}_{kl} + W'(\bar{I}_1)\,\delta_{ik}\bar{B}_{jl}\right\}, \tag{2.76}$$

where $\bar{B} = \bar{F}\bar{F}^T$ and $\bar{I}_1 = \mathrm{tr}\bar{B}$.

2.4 Mixed coordinate stream functions for isochoric transformations

Previously, we introduced the concept of incorporating a *Lagrangian multiplier* p, interpreted as pressure, into the expression for the Cauchy stress σ in order to enforce the constraint of incompressibility (2.12). An alternate approach was proposed initially by Rooney and Carroll (1984) who, in the context of two-dimensional deformations in Cartesian coordinate space, realized that incompressibility can be satisfied *exactly* by re-expressing the displacement components in terms of a *stream function*. The use of the term *stream function* in this context originates from an analogous formulation applied to the two-dimensional Stokes flow (Batchelor, 1967, pp. 75-79). The distinction is that the stream function we seek is defined in terms of *mixed coordinates*. That is, it depends on coordinates both in the reference *and* current configurations.

The work of Rooney and Carroll (1984) was later extended by Carroll (2004) to the three-dimensional case, and the solutions of the incompressibility constraint were expressed implicitly in terms of *two* stream functions restricted by two admissible conditions. However, Ciarletta (2011) was able to define a generic transformation of *n-dimensional* coordinates using a *single* mixed coordinate stream function. Many recent studies of important problems in non-linear elasticity have adopted this stream function formulation. Notable examples are the analysis of periodic surface pattern formation in soft materials (Ciarletta and Ben Amar, 2012a,b; Ciarletta, 2013; Ciarletta and Fu, 2015; Ben Amar and Bordner, 2017) and the elasto-capillary localized beading of soft solid cylinders and tubes (Taffetani and Ciarletta, 2015a; Wang, 2020; Fu et al., 2021; Emery and Fu, 2021a,c). In the following, we summarize the main ideas of the stream function approach given in Ciarletta (2011) for both Cartesian and cylindrical polar coordinate systems.

2.4.1 Three-dimensional Cartesian coordinates

We begin by considering a transformation of three functions $x_i = x_i(X_1, X_2, X_3)$ of three variables X_1, X_2 and X_3, where $i = 1, 2$ and 3. Assuming that this transformation describes a large deformation from a reference configuration $\mathcal{B}_0$ to a current configuration $\mathcal{B}_e$, the constraint of incompressibility takes the form

$$J \equiv \det \left\{ \frac{\partial x_i}{\partial X_A} \right\} = 1. \tag{2.77}$$

The main idea is to simplify (2.77) by introducing an intermediate configuration $\mathcal{B}_m$ defined through the basis vectors $(\boldsymbol{E}_1, \boldsymbol{E}_2, \boldsymbol{e}_3)$, say. To this end, we define the following transformations:

$$x_1 = f_1(X_1, X_2, x_3), \qquad x_2 = f_2(X_1, X_2, x_3), \qquad X_3 = f_3(X_1, X_2, x_3), \tag{2.78}$$

and a multiplicative decomposition of the deformation gradient $F = F_1 F_2$ can then be imposed; see Fig. 2.3. It can be shown that the deformation gradients F_1 and F_2 mapping $\mathcal{B}_m \to \mathcal{B}_e$ and $\mathcal{B}_0 \to \mathcal{B}_m$, respectively, take the following forms:

$$\begin{aligned} F_1 = \frac{\partial x_1}{\partial X_1}\boldsymbol{e}_1 \otimes \boldsymbol{E}_1 + \frac{\partial x_1}{\partial X_2}\boldsymbol{e}_1 \otimes \boldsymbol{E}_2 + \frac{\partial x_1}{\partial x_3}\boldsymbol{e}_1 \otimes \boldsymbol{e}_3 + \frac{\partial x_2}{\partial X_1}\boldsymbol{e}_2 \otimes \boldsymbol{E}_1 + \frac{\partial x_2}{\partial X_2}\boldsymbol{e}_2 \otimes \boldsymbol{E}_2 \\ + \frac{\partial x_2}{\partial x_3}\boldsymbol{e}_2 \otimes \boldsymbol{e}_3 + \boldsymbol{e}_3 \otimes \boldsymbol{e}_3, \end{aligned} \tag{2.79}$$

$$F_2 = \boldsymbol{E}_1 \otimes \boldsymbol{E}_1 + \boldsymbol{E}_2 \otimes \boldsymbol{E}_2 + \frac{\partial x_3}{\partial X_1}\boldsymbol{e}_3 \otimes \boldsymbol{E}_1 + \frac{\partial x_3}{\partial X_2}\boldsymbol{e}_3 \otimes \boldsymbol{E}_2 + \frac{\partial x_3}{\partial X_3}\boldsymbol{e}_3 \otimes \boldsymbol{E}_3. \tag{2.80}$$

We then assume that there exists a stream function $\varphi = \varphi(X_1, X_2, x_3)$ such that

$$f_1 = \frac{\partial^2 \varphi}{\partial X_2 \partial x_3}, \qquad f_2 = \frac{\partial^2 \varphi}{\partial X_1 \partial x_3}. \tag{2.81}$$

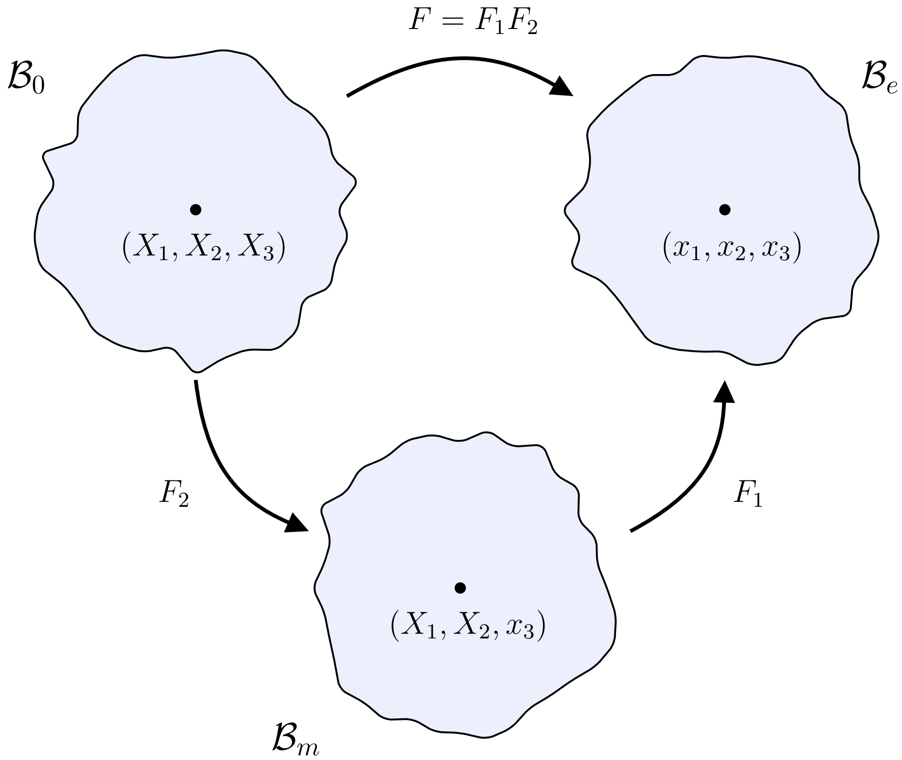

Figure 2.3: A schematic of the reference configuration $\mathcal{B}_0$, the mixed coordinate configuration $\mathcal{B}_m$ and the current configuration $\mathcal{B}_e$.

Given (2.78) – (2.81), the incompressibility constraint $\det F = \det F_1 \det F_2 = 1$ reduces to

$$\frac{\partial f_3}{\partial x_3} = \left(\frac{\partial^3 \varphi}{\partial X_1 \partial X_2 \partial x_3}\right)^2 - \frac{\partial^3 \varphi}{\partial X_2^2 \partial x_3}\frac{\partial^3 \varphi}{\partial X_1^2 \partial x_3}. \tag{2.82}$$

Finally, on integrating (2.82) with respect to x_3, we obtain

$$f_3 = \int \left\{ \left(\frac{\partial^3 \varphi}{\partial X_1 \partial X_2 \partial x_3}\right)^2 - \frac{\partial^3 \varphi}{\partial X_2^2 \partial x_3}\frac{\partial^3 \varphi}{\partial X_1^2 \partial x_3} \right\} dx_3 + \hat{f}_3(X_1, X_2). \tag{2.83}$$

2.4.2 Cylindrical polar coordinates

We now consider a reference configuration $\mathcal{B}_0$ and a current configuration $\mathcal{B}_e$ defined by the cylindrical polar coordinates (R, Θ, Z) and (r, θ, z), respectively.

2.4.2.1 A general axi-symmetric transformation

Suppose that the mapping $\mathcal{B}_0 \to \mathcal{B}_e$ is enforced through the variable transformations

$$r = r(R, Z), \qquad \theta = \Theta, \qquad z = z(R, Z). \tag{2.84}$$

We then let

$$r = g_1(R, z), \qquad Z = g_2(R, z), \tag{2.85}$$

and suppose also that there exists an intermediate configuration $\mathcal{B}_m$ defined through the basis vectors $(\boldsymbol{E}_R, \boldsymbol{E}_\Theta, \boldsymbol{e}_z)$. Then, we can decompose the deformation gradient corresponding to (2.84) multiplicatively through $F = F_1 F_2$ such that $F_1 : \mathcal{B}_m \to \mathcal{B}_e$ and $F_2 : \mathcal{B}_0 \to \mathcal{B}_m$. Specifically, we have

$$F_1 = \frac{\partial r}{\partial R}\boldsymbol{e}_r \otimes \boldsymbol{E}_R + \frac{\partial r}{\partial z}\boldsymbol{e}_r \otimes \boldsymbol{e}_z + \frac{r}{R}\boldsymbol{e}_\theta \otimes \boldsymbol{E}_\Theta + \frac{\partial z}{\partial R}\boldsymbol{e}_z \otimes \boldsymbol{E}_R + \boldsymbol{e}_z \otimes \boldsymbol{e}_z, \tag{2.86}$$

$$F_2 = \boldsymbol{E}_R \otimes \boldsymbol{E}_R + \boldsymbol{E}_\Theta \otimes \boldsymbol{E}_\Theta + \frac{\partial z}{\partial R}\boldsymbol{e}_z \otimes \boldsymbol{E}_R + \frac{\partial z}{\partial Z}\boldsymbol{e}_z \otimes \boldsymbol{E}_Z. \tag{2.87}$$

It follows from (2.86) – (2.87) that the incompressibility constraint $\det F = 1$ takes the simplified form:

$$\frac{r}{R}\frac{\partial z}{\partial Z}\left\{\frac{\partial r}{\partial R} - \frac{\partial r}{\partial Z}\frac{\partial z}{\partial R}\right\} = 1. \tag{2.88}$$

Now, with use of (2.84) and (2.85), we deduce that (2.88) is equivalently

$$\frac{g_1}{R}\left(\frac{\partial g_2}{\partial z}\right)^{-1}\frac{\partial g_1}{\partial R} = \frac{1}{R}\left(\frac{\partial g_2}{\partial z}\right)^{-1}\frac{\partial}{\partial R}\left(\frac{1}{2}g_1^2\right) = 1. \tag{2.89}$$

We may then introduce a *mixed coordinate stream function* $\phi = \phi(R, z)$ through

$$g_1^2 = 2\frac{\partial \phi}{\partial z} = 2\,\phi_{,z}, \qquad g_2 = \frac{1}{R}\frac{\partial \phi}{\partial R} = \frac{1}{R}\phi_{,R}, \tag{2.90}$$

such that the condition (2.89) is automatically satisfied. Here and hereafter, a comma in the subscript is used to denote partial differentiation with respect to the implied coordinate.

2.4.2.2 A class of non-axi-symmetric transformations

Alternatively, suppose that the mapping $\mathcal{B}_0 \to \mathcal{B}_e$ is enforced through the variable transformations

$$r = r(R, \Theta), \qquad \theta = \theta(R, \Theta), \qquad z = cZ, \tag{2.91}$$

where c is a positive constant. Then, let

$$r = h_1(R, \theta), \qquad \Theta = h_2(R, \theta), \tag{2.92}$$

and suppose that there exists an intermediate configuration $\mathcal{B}_m$ defined by the basic vectors $(\boldsymbol{E}_R, \boldsymbol{e}_\theta, \boldsymbol{E}_Z)$. Then, we can decompose the deformation gradient corresponding to (2.84) multiplicatively through $F = F_1 F_2$ such that $F_1 : \mathcal{B}_m \to \mathcal{B}_e$ and $F_2 : \mathcal{B}_0 \to \mathcal{B}_m$. Specifically, we have

$$F_1 = \frac{\partial r}{\partial R}\boldsymbol{e}_r \otimes \boldsymbol{E}_R + \frac{1}{R}\frac{\partial r}{\partial \theta}\boldsymbol{e}_r \otimes \boldsymbol{e}_\theta + \frac{r}{R}\boldsymbol{e}_\theta \otimes \boldsymbol{e}_\theta + r\frac{\partial \theta}{\partial R}\boldsymbol{e}_\theta \otimes \boldsymbol{E}_R + c\,\boldsymbol{e}_z \otimes \boldsymbol{E}_Z, \quad (2.93)$$

$$F_2 = \boldsymbol{E}_R \otimes \boldsymbol{E}_R + R\frac{\partial \theta}{\partial R}\boldsymbol{e}_\theta \otimes \boldsymbol{E}_R + \frac{\partial \theta}{\partial \Theta}\boldsymbol{e}_\theta \otimes \boldsymbol{E}_\Theta + \boldsymbol{E}_Z \otimes \boldsymbol{E}_Z. \quad (2.94)$$

It follows from (2.93) – (2.94) that the incompressibility constraint $\det F = 1$ takes the simplified form:

$$c\,\frac{r}{R}\frac{\partial \theta}{\partial \Theta}\left\{\frac{\partial r}{\partial R} - \frac{\partial r}{\partial \theta}\frac{\partial \theta}{\partial R}\right\} = 1. \quad (2.95)$$

With use of (2.91) and (2.92), the condition (2.95) reduces to

$$c\frac{h_1}{R}\frac{\partial h_1}{\partial R} = \frac{c}{R}\frac{\partial}{\partial R}\left(\frac{1}{2}h_1^2\right) = \frac{\partial h_2}{\partial \theta}. \quad (2.96)$$

Then, we may introduce an alternate *mixed coordinate stream function* $\psi = \psi(R, \theta)$ through

$$h_1^2 = 2\frac{\partial \psi}{\partial \theta} = 2\psi_{,\theta}, \qquad h_2 = \frac{c}{R}\frac{\partial \psi}{\partial R} = \frac{c}{R}\psi_{,R}, \quad (2.97)$$

so that (2.96) is is automatically satisfied.

2.5 Variational principles and conservation laws

2.5.1 The principle of stationary potential energy

In the pioneering work of Noether (1918), it was proven that for a system of equations arising from a *variational principle*, any symmetry of this variational principle gives rise to a conservation law. An elastic material in a state of mechanical equilibrium conforms to the *principle of stationary potential energy.*

To illustrate, consider a general three-dimensional hyperelastic material with reference and finitely deformed configurations $\mathcal{B}_0$ and $\mathcal{B}_e$, respectively. Let $\boldsymbol{X}$ and $\boldsymbol{x}$

be the position vectors of a representative material particle in these respective configurations. Then, the bulk energy $\mathcal{E}$ of the system is given generally by the *functional*

$$\mathcal{E} = \int_{\mathcal{B}_0} W(X_A, x_i, x_{i,A}) dV, \tag{2.98}$$

where dV is an infinitesimal volume element in $\mathcal{B}_0$ and X_A, x_i and $x_{i,A} = \partial x_i/\partial X_A$ $(i, A = 1, 2, 3)$ are the Cartesian components of $\boldsymbol{X}$, $\boldsymbol{x}$ and $F = \text{Grad}\,\boldsymbol{x}$, respectively. For cylindrical or spherical polar coordinates, say, the partial derivatives $x_{i,A}$ are replaced by the covariant derivatives $x_{i;A}$. The *principle of stationary potential energy* states that a deformation $\boldsymbol{\chi} : \mathcal{B}_0 \to \mathcal{B}_e$ is a solution to the equilibrium equations of the system if and only if the first variation $\delta\mathcal{E}$ of $\mathcal{E}$ vanishes for all variations $\delta\boldsymbol{x}$ of $\boldsymbol{x}$, where $\boldsymbol{x} = \boldsymbol{\chi}(\boldsymbol{X})$. Thus, by Noether's Theorem, the equilibrium equations $(2.39)_2$ must arise naturally from the condition that the functional (2.98) is invariant with respect to *infinitesimal* variations in $\boldsymbol{x}$. On taking the first variation of (2.98), we obtain

$$\begin{aligned} \delta\mathcal{E} &= \int_{\mathcal{B}_0} \left[\frac{\partial W}{\partial x_i} \delta x_i + \frac{\partial W}{\partial x_{i,A}} \delta x_{i,A} \right] dV \\ &= \int_{\mathcal{B}_0} \left[\frac{\partial W}{\partial x_i} \delta x_i + \frac{\partial}{\partial X_A} \left(\frac{\partial W}{\partial x_{i,A}} \delta x_i \right) - \frac{\partial}{\partial X_A} \left(\frac{\partial W}{\partial x_{i,A}} \right) \delta x_i \right] dV \\ &= \int_{\mathcal{B}_0} \left[\mathfrak{E}_i(W) \delta x_i + \text{Div}\, \hat{\boldsymbol{t}} \right] dV, \end{aligned} \tag{2.99}$$

where

$$\mathfrak{E}_i(W) = \frac{\partial W}{\partial x_i} - \frac{\partial}{\partial X_A} \left(\frac{\partial W}{\partial x_{i,A}} \right) \quad \text{and} \quad \hat{\boldsymbol{t}} = \left(\hat{t}_A \right) = \left(\frac{\partial W}{\partial F_{iA}} \delta x_i \right). \tag{2.100}$$

Thus, for $\delta\mathcal{E}$ to vanish for arbitrary variations in δx_i, we must satisfy the *Euler-Lagrange* equations

$$\mathfrak{E}_i(W) = 0. \tag{2.101}$$

The equivalence of (2.101) to the equilibrium equations $(2.39)_2$ will be verified explicitly in the following sections.

2.5.2 Conservation laws in non-linear elasticity

A variational integral of the form (2.98) is invariant with respect to the *general* transformations

$$X'_A = X_A + \varepsilon\, \zeta_A(X_B, x_j) + \mathcal{O}(\varepsilon^2),$$

$$x'_i = x_i + \varepsilon\, \phi_i(X_B, x_j) + \mathcal{O}(\varepsilon^2), \tag{2.102}$$

if $\forall\ \mathcal{B} \subset \mathcal{B}_0$ we have

$$\int_{\mathcal{B}'} W(X'_A, x'_i, x'_{i,A})dV' = \int_{\mathcal{B}} W(X_A, x_i, F_{iA})dV, \tag{2.103}$$

where $\mathcal{B}'$ is the image of $\mathcal{B}$ under the transformations (2.102), ε is a small parameter and $x'_{i,A} = \partial x'_i/\partial X'_A$. From (2.102), we can deduce that

$$\frac{\partial X'_B}{\partial X_A} = \delta_{BA} + \varepsilon \mathcal{D}_A\zeta_B + \mathcal{O}(\varepsilon^2), \qquad \frac{\partial X_B}{\partial X'_A} = \delta_{BA} - \varepsilon \mathcal{D}_A\zeta_B + \mathcal{O}(\varepsilon^2),$$

$$\frac{\partial x'_i}{\partial X'_A} = \frac{\partial x'_i}{\partial X_A} - \varepsilon \frac{\partial x_i}{\partial X_B}\mathcal{D}_A\zeta_B + \mathcal{O}(\varepsilon^2), \tag{2.104}$$

where the total derivative operator $\mathcal{D}_A$ is given by

$$\mathcal{D}_A = \frac{\partial}{\partial X_A} + \frac{\partial x_i}{\partial X_A}\frac{\partial}{\partial x_i}. \tag{2.105}$$

We also have from (2.104) that

$$\begin{aligned} dV' &= \det\left\{\frac{\partial X'_A}{\partial X_B}\right\} dV, \\ &= \det\left\{\delta_{AB} + \varepsilon\mathcal{D}_B\zeta_A + \mathcal{O}(\varepsilon^2)\right\} dV, \\ &= \left\{1 + \mathrm{tr}(\varepsilon\mathcal{D}_B\zeta_A) + \mathcal{O}(\varepsilon^2)\right\} dV, \\ &= \left\{1 + \varepsilon\mathcal{D}_A\zeta_A + \mathcal{O}(\varepsilon^2)\right\} dV. \end{aligned} \tag{2.106}$$

On substituting (2.102), (2.104) and (2.106) into (2.103) and neglecting terms of $\mathcal{O}(\varepsilon^2)$ and above, we obtain

$$\delta \int_{\mathcal{B}} W(X_A, x_i, x_{i,A})dV + \varepsilon \int_{\mathcal{B}} \left\{ W\mathcal{D}_A\zeta_A + \frac{\partial W}{\partial X_A}\zeta_A - \frac{\partial W}{\partial x_{i,A}} x_{i,B}\mathcal{D}_A\zeta_B \right\} dV = 0. \tag{2.107}$$

With use of the relation $(2.102)_2$, the first term in (2.107) is expressible as follows:

$$\delta \int_{\mathcal{B}} W(X_A, x_i, x_{i,A}) dV = \varepsilon \int_{\mathcal{B}} \left[\mathcal{E}_i(W)\phi_i + \text{Div}\left(\phi_i \frac{\partial W}{\partial x_{i,A}} \right) \right] dV + \mathcal{O}(\varepsilon^2), \quad (2.108)$$

On examination of the second integrand in (2.107), we find

$$\begin{aligned}
& W\mathcal{D}_A\zeta_A + \frac{\partial W}{\partial X_A}\zeta_A - \frac{\partial W}{\partial x_{i,A}} x_{i,B}\mathcal{D}_A\zeta_B \\
&= W\mathcal{D}_A\zeta_A + \frac{\partial W}{\partial X_A}\zeta_A - \mathcal{D}_A(\frac{\partial W}{\partial x_{i,A}} x_{i,B}\zeta_B) + \mathcal{D}_A(\frac{\partial W}{\partial x_{i,A}}) x_{i,B}\zeta_B + \frac{\partial W}{\partial x_{i,A}} x_{i,AB}\zeta_B \\
&= W\mathcal{D}_A\zeta_A + \frac{\partial W}{\partial X_A}\zeta_A - \mathcal{D}_A(\frac{\partial W}{\partial x_{i,A}} x_{i,B}\zeta_B) + x_{i,B}\zeta_B[\frac{\partial W}{\partial x_i} - \mathcal{E}_i(W)] + \frac{\partial W}{\partial x_{i,A}} x_{i,AB}\zeta_B \\
&= W\mathcal{D}_A\zeta_A + \zeta_A\mathcal{D}_A W - \mathcal{D}_A(\frac{\partial W}{\partial x_{i,A}} x_{i,B}\zeta_B) - x_{i,B}\zeta_B\mathcal{E}_i(W) \\
&= \mathcal{D}_A \left(\zeta_A W - \frac{\partial W}{\partial x_{i,A}} x_{i,B}\zeta_B \right) - x_{i,B}\zeta_B\mathcal{E}_i(W), \qquad (2.109)
\end{aligned}$$

where $x_{i,AB} = \partial^2 x_i / \partial X_A \partial X_B$, say. Finally, on substituting (2.108) - (2.109) into (2.107), we obtain the conservation law

$$\text{Div}P = \mathcal{D}_A P_A = -(\phi_i - x_{i,A}\zeta_A)\mathcal{E}_i(W) = 0, \qquad (2.110)$$

where
$$P_A = \zeta_A W - (\phi_i - x_{i,B}\zeta_B) \frac{\partial W}{\partial x_{i,A}}. \qquad (2.111)$$

2.5.2.1 Translational invariance in $\boldsymbol{x}$

Consider the transformation

$$X'_A = X_A, \qquad x'_i = x_i + \varepsilon\delta_{ij}, \qquad (2.112)$$

which constitutes a translation in x_i. Through comparison with (2.102), we have that

$$\zeta_A = 0 \quad \text{and} \quad \phi_i = \delta_{ij}. \qquad (2.113)$$

Then, equation (2.111) reduces to

$$P_A = -\delta_{ij} \frac{\partial W}{\partial x_{i,A}} = -\frac{\partial W}{\partial x_{j,A}}. \qquad (2.114)$$

Thus, the conservation law arising from the translational invariance of $\mathcal{E}$ with respect to x_i is

$$\mathcal{D}_A P_A = -\mathcal{D}_A \left(\frac{\partial W}{\partial x_{j,A}} \right) = -\mathrm{Div} S = \mathbf{0}, \tag{2.115}$$

and this is simply the equilibrium equation in the reference configuration which we defined in $(2.39)_2$.

2.5.2.2 Translational invariance in $\boldsymbol{X}$

Alternatively, consider the transformation

$$X'_A = X_A + \varepsilon \delta_{AB}, \qquad x'_i = x_i, \tag{2.116}$$

which constitutes a translation in X_A. Then, we have that

$$\zeta_A = \delta_{AB} \quad \text{and} \quad \phi_i = 0, \tag{2.117}$$

and equation (2.111) reduces to

$$P_A = \delta_{AB} W + \delta_{BC} \frac{\partial W}{\partial F_{iA}} F_{iC} = \delta_{AB} W + (SF)_{AB}. \tag{2.118}$$

Thus, the associated conservation law takes the form

$$\mathcal{D}_A P_A = \mathrm{Div}\, \Sigma = \mathbf{0}, \quad \text{where} \quad \Sigma = W\, I - SF, \tag{2.119}$$

is the *elastic energy-momentum tensor*. This tensor plays an important role in phase transformation problems and in the theory of materials with defects; it has the physical interpretation of force (or energy release rate) due to the translation of a defect. For instance, by integrating Σ around the tip of a crack, we may obtain the energy released due to an infinitesimal propagation of said crack. For more information on the elastic energy-momentum tensor, we refer the reader to Chadwick (1975) and Eshelby (1975), and the references therein.

2.6 Variable-coefficient linear eigenvalue problems

In a sizeable part of the work presented in this thesis, we study the bifurcation behaviour of hollow cylindrical tubes. It is well established in the non-linear elasticity literature that the incremental equilibrium equations associated with hollow tubes often possess variable coefficients (Haughton and Ogden, 1979b; Haughton and Orr, 1995), and such equations rarely admit analytical solutions. To this end, we outline in this section two numerical approaches, the *determinant method* and the *compound matrix method*, which enable us to solve for the eigenvalues of a certain class of boundary value problems with variable coefficients.

To begin, consider the following two-point boundary value problem:

$$\frac{d\boldsymbol{y}}{dx} = A(x,\xi)\boldsymbol{y}, \qquad a \leq x \leq b, \tag{2.120}$$

$$B_1(x,\xi)\boldsymbol{y} = \mathbf{0}, \qquad x = a, \tag{2.121}$$

$$B_2(x,\xi)\boldsymbol{y} = \mathbf{0}, \qquad x = b, \tag{2.122}$$

where A is a $2n \times 2n$ matrix, and B_1 and B_2 are $n \times 2n$ matrices. All three of these matrices are known functions of the independent variable x and the parameter ξ. Furthermore, $\boldsymbol{y}$ is an unknown $2n$-dimensional vector function of x. The aim is to determine values of the parameter ξ (i.e. the *eigenvalues*) for which there exists non-trivial solutions to the system (2.120) $-$ (2.122).

2.6.1 Determinant method

Assuming that the matrix B_1 has rank n, we can always find n *linearly independent* vectors $\boldsymbol{y}_a^{(1)}, \boldsymbol{y}_a^{(2)}, \ldots, \boldsymbol{y}_a^{(n)}$ such that

$$B_1(a,\xi)\boldsymbol{y}_a^{(i)} = \mathbf{0}, \qquad \text{where} \qquad i = 1, 2, \ldots, n. \tag{2.123}$$

By using each of these vectors as initial data for $\boldsymbol{y}$ at $x = a$, we may integrate (2.120) forward from $x = a$ to obtain n linearly independent solutions, say $\boldsymbol{y}^{(1)}(x)$, $\boldsymbol{y}^{(2)}(x)$, $\ldots$, $\boldsymbol{y}^{(n)}(x)$, for $\boldsymbol{y}$. Thus, a general solution of (2.120) which also satisfies the boundary condition (2.121) is given by

$$\boldsymbol{y} = \sum_{i=1}^{n} c_i\, \boldsymbol{y}^{(i)}(x), \tag{2.124}$$

where c_1, c_2, $\ldots$, c_n are arbitrary constants. Then, define $M(x,\xi)$ to be a $2n \times n$ matrix which takes the form

$$M(x,\xi) = \left[\boldsymbol{y}^{(1)},\, \boldsymbol{y}^{(2)},\, \ldots,\, \boldsymbol{y}^{(n)}\right]. \tag{2.125}$$

Given (2.125), equation (2.124) can be rewritten as

$$\boldsymbol{y} = M(x,\xi)\,\boldsymbol{c}, \qquad \text{where} \qquad \boldsymbol{c} = \left[c_1,\, c_2,\, \ldots,\, c_n\right]^T. \tag{2.126}$$

It remains to ensure that the general solution (2.126) satisfies the boundary condition (2.122) at $x = b$. To this end, we substitute (2.126) into (2.122) and obtain

$$B_2(b,\xi)M(b,\xi)\,\boldsymbol{c} = \boldsymbol{0}. \tag{2.127}$$

Then, since $\boldsymbol{c}$ is arbitrarily defined, we deduce from (2.127) the determinantal equation

$$\det\left\{B_2(b,\xi)M(b,\xi)\right\} = 0. \tag{2.128}$$

We finally iterate on ξ until (2.128) is satisfied; the values of ξ satisfying (2.128) are the eigenvalues of the original system.

An alternate approach is to obtain two sets of n linearly independent solutions, say $\boldsymbol{y}^{(1)}(x)$, $\boldsymbol{y}^{(2)}(x), \ldots,$ $\boldsymbol{y}^{(n)}(x)$ and $\boldsymbol{y}^{(n+1)}(x)$, $\boldsymbol{y}^{(n+2)}(x), \ldots,$ $\boldsymbol{y}^{(2n)}(x)$, by integrating (2.120) forward from $x = a$ and backwards from $x = b$, respectively. We may then define the following two general solutions to (2.120) which satisfy the boundary condition (2.121) on $x = a$ and (2.122) on $x = b$ respectively:

$$\boldsymbol{y} = \sum_{i=1}^{n} c_i\, \boldsymbol{y}^{(i)}(x) \quad \text{and} \quad \boldsymbol{y} = \sum_{i=n+1}^{2n} c_i\, \boldsymbol{y}^{(i)}(x). \tag{2.129}$$

The idea then is to match the solutions (2.129) at an intermediate point $x = d$, where $a < d < b$. That is, we set

$$\sum_{i=1}^{n} c_i\, \boldsymbol{y}^{(i)}(x) = \sum_{i=n+1}^{2n} c_i\, \boldsymbol{y}^{(i)}(x), \qquad \text{where} \qquad x = d. \tag{2.130}$$

Equivalently, we have

$$N(d, \xi)\boldsymbol{c} = \mathbf{0}, \tag{2.131}$$

where
$$N(x, \xi) = [\boldsymbol{y}^{(1)},\ \boldsymbol{y}^{(2)},\ \ldots,\ \boldsymbol{y}^{(n)},\ \boldsymbol{y}^{(n+1)},\ \boldsymbol{y}^{(n+2)},\ \ldots,\ \boldsymbol{y}^{(2n)}], \tag{2.132}$$

and $\boldsymbol{c} = [c_1, c_2, \ldots, c_n, -c_{n+1}, -c_{n+2}, \ldots, -c_{2n}]^T$, with $c_{n+1}, c_{n+2}, \ldots, c_{2n}$ being additional arbitrary constants. It then remains to iterate on ξ until the determinantal equation

$$\det N(d, \xi) = 0, \tag{2.133}$$

is satisfied. Clearly, the matching condition (2.133) is dependent on the matching point d as well as ξ. However, the following condition:

$$D(\xi) = e^{-\int_a^d \operatorname{tr} A(t,\xi)dt} \det N(d, \xi) = 0, \tag{2.134}$$

is independent of the matching point $x = d$, and this can be shown with the aid of *Jacobi's formula*

$$\frac{d}{dx}(\det A) = (\det A)\operatorname{tr}\left(\frac{dA}{dx}A^{-1}\right), \tag{2.135}$$

which holds for any invertible tensor A dependant on x; see Chadwick (1999, pp. 16-20). The function $D(\xi)$ is called the *Evan's function* and is an invariant of (2.120).

2.6.2 Compound matrix method

Whilst conceptually simple, the previously outlined determinant method is ill-equipped to solve systems of the form (2.120) – (2.122) when the parameter ξ takes particularly large values. In such a case, the eigenvalue problem becomes *numerically stiff* in the sense that, as x is increased from a, the solutions $\boldsymbol{y}^{(1)}$, $\boldsymbol{y}^{(2)}$, $\ldots$, $\boldsymbol{y}^{(n)}$ quickly become linearly dependent due to the dominance of exponentially growing solutions; see Conte (1966) and Davey (1983). To address these issues, the *compound matrix method* was introduced by Ng and Reid (1979a,b, 1985); see also Lindsay and Rooney (1992) and Bridges (1999). In the following, we give an outline of this approach.

Let $\boldsymbol{y}^{(1)}$, $\boldsymbol{y}^{(2)}$, ..., $\boldsymbol{y}^{(n)}$ and $\boldsymbol{y}^{(n+1)}$, $\boldsymbol{y}^{(n+2)}$, ..., $\boldsymbol{y}^{(2n)}$ be the two sets of linearly independent solutions to (2.120) as defined in the previous section. Then, the key idea is to compute the minors of the associated solution matrices M^- and M^+ given by

$$M^- = \left[\boldsymbol{y}^{(1)},\, \boldsymbol{y}^{(2)},\, \ldots,\, \boldsymbol{y}^{(n)}\right] \quad \text{and} \quad M^+ = \left[\boldsymbol{y}^{(n+1)},\, \boldsymbol{y}^{(n+2)},\, \ldots,\, \boldsymbol{y}^{(2n)}\right]. \tag{2.136}$$

The matrices $M^\mp$ each have ${}^{2n}C_n$ minors denoted by $\varphi_1^\mp$, $\varphi_2^\mp$, etc. To illustrate, if $n = 2$, we have

$$\begin{aligned}
\varphi_1^- &= y_1^{(1)}y_2^{(2)} - y_1^{(2)}y_2^{(1)}, \qquad & \varphi_2^- &= y_1^{(1)}y_3^{(2)} - y_1^{(2)}y_3^{(1)},\\
\varphi_3^- &= y_1^{(1)}y_4^{(2)} - y_1^{(2)}y_4^{(1)}, \qquad & \varphi_4^- &= y_2^{(1)}y_3^{(2)} - y_2^{(2)}y_3^{(1)},\\
\varphi_5^- &= y_2^{(1)}y_4^{(2)} - y_2^{(2)}y_4^{(1)}, \qquad & \varphi_6^- &= y_3^{(1)}y_4^{(2)} - y_3^{(2)}y_4^{(1)},
\end{aligned} \tag{2.137}$$

where $y_j^{(i)}$ is the j^{th} component of $\boldsymbol{y}^{(i)}$. Then, with the aid of the property

$$\frac{d\boldsymbol{y}^{(i)}}{dx} = A(x,\xi)\boldsymbol{y}^{(i)}, \tag{2.138}$$

we may compute the associated expressions for the first derivatives of $\varphi_1^\mp$, $\varphi_2^\mp$, etc. For instance, for $n = 2$, we may deduce

$$\begin{aligned}
\frac{d\varphi_1^-}{dx} &= \frac{dy_1^{(1)}}{dx}y_2^{(2)} + y_1^{(1)}\frac{dy_2^{(2)}}{dx} - \frac{dy_1^{(2)}}{dx}y_2^{(1)} - y_1^{(2)}\frac{dy_2^{(1)}}{dx},\\
&= \sum_{j=1}^{4} A_{1j}y_j^{(1)}y_2^{(2)} + y_1^{(1)}\sum_{j=1}^{4} A_{2j}y_j^{(2)} - \sum_{j=1}^{4} A_{1j}y_j^{(2)}y_2^{(1)} - y_1^{(2)}\sum_{j=1}^{4} A_{2j}y_j^{(1)},\\
&= A_{11}\varphi_1^- - A_{13}\varphi_4^- - A_{14}\varphi_5^- + A_{22}\varphi_1^- + A_{23}\varphi_2^- + A_{24}\varphi_3^-.
\end{aligned} \tag{2.139}$$

On repeating this process for the other five minors, we arrive at the following compound matrix equation:

$$\frac{d\boldsymbol{\varphi}^-}{dx} = \hat{A}(x,\xi)\boldsymbol{\varphi}^-, \qquad a \le x \le b, \tag{2.140}$$

where $\boldsymbol{\varphi}^- = [\varphi_1^-, \varphi_2^-, \ldots, \varphi_6^-]^T$ and

$$\hat{A} = \begin{bmatrix}
A_{11}+A_{22} & A_{23} & A_{24} & -A_{13} & -A_{14} & 0\\
A_{32} & A_{11}+A_{33} & A_{34} & A_{12} & 0 & -A_{14}\\
A_{42} & A_{43} & A_{11}+A_{44} & 0 & A_{12} & A_{13}\\
-A_{31} & A_{21} & 0 & A_{22}+A_{33} & A_{34} & -A_{24}\\
-A_{41} & 0 & A_{21} & A_{43} & A_{22}+A_{44} & A_{23}\\
0 & -A_{41} & A_{31} & -A_{42} & A_{32} & A_{33}+A_{44}
\end{bmatrix}.$$

The boundary conditions for $\boldsymbol{\varphi}^-$ at $x = a$ can then be obtained from the $\boldsymbol{y}_a^{(i)}$, $i = 1, 2, \ldots, n$, which satisfy (2.123). For example, we have

$$\varphi_1^-(a) = y_{a1}^{(1)} y_{a2}^{(2)} - y_{a1}^{(2)} y_{a2}^{(1)}, \tag{2.141}$$

where $y_{aj}^{(i)}$ is the j^{th} component of $\boldsymbol{y}_a^{(i)}$. We may then integrate forward (2.140) from $x = a$ in order to obtain a general solution for $\boldsymbol{\varphi}^-$. The corresponding general solution for $\boldsymbol{\varphi}^+$ can be obtained in a similar manner.

The matching condition (2.133) may be expressed solely in terms of $\varphi_1^{\mp}, \varphi_2^{\mp}$ etc. through a *Laplacian expansion*. For example, when $n = 2$, we may write

$$\det N(x,\xi) = \det\left\{[\boldsymbol{y}^{(1)},\, \boldsymbol{y}^{(2)},\, \boldsymbol{y}^{(3)},\, \boldsymbol{y}^{(4)}]\right\} = \begin{vmatrix} y_1^{(1)} & y_1^{(2)} & y_1^{(3)} & y_1^{(4)} \\ y_2^{(1)} & y_2^{(2)} & y_2^{(3)} & y_2^{(4)} \\ y_3^{(1)} & y_3^{(2)} & y_3^{(3)} & y_3^{(4)} \\ y_4^{(1)} & y_4^{(2)} & y_4^{(3)} & y_4^{(4)} \end{vmatrix}$$

$$= \begin{vmatrix} y_1^{(1)} & y_1^{(2)} \\ y_2^{(1)} & y_2^{(2)} \end{vmatrix} \cdot (-1)^{1+2+1+2} \begin{vmatrix} y_3^{(3)} & y_3^{(4)} \\ y_4^{(3)} & y_4^{(4)} \end{vmatrix} + \begin{vmatrix} y_1^{(1)} & y_1^{(2)} \\ y_3^{(1)} & y_3^{(2)} \end{vmatrix} \cdot (-1)^{1+2+1+3} \begin{vmatrix} y_2^{(3)} & y_2^{(4)} \\ y_4^{(3)} & y_4^{(4)} \end{vmatrix}$$

$$+ \begin{vmatrix} y_1^{(1)} & y_1^{(2)} \\ y_4^{(1)} & y_4^{(2)} \end{vmatrix} \cdot (-1)^{1+2+1+4} \begin{vmatrix} y_2^{(3)} & y_2^{(4)} \\ y_3^{(3)} & y_3^{(4)} \end{vmatrix} + \begin{vmatrix} y_2^{(1)} & y_2^{(2)} \\ y_3^{(1)} & y_3^{(2)} \end{vmatrix} \cdot (-1)^{1+2+2+3} \begin{vmatrix} y_1^{(3)} & y_1^{(4)} \\ y_4^{(3)} & y_4^{(4)} \end{vmatrix}$$

$$+ \begin{vmatrix} y_2^{(1)} & y_2^{(2)} \\ y_4^{(1)} & y_4^{(2)} \end{vmatrix} \cdot (-1)^{1+2+2+4} \begin{vmatrix} y_1^{(3)} & y_1^{(4)} \\ y_3^{(3)} & y_3^{(4)} \end{vmatrix} + \begin{vmatrix} y_3^{(1)} & y_3^{(2)} \\ y_4^{(1)} & y_4^{(2)} \end{vmatrix} \cdot (-1)^{1+2+3+4} \begin{vmatrix} y_1^{(3)} & y_1^{(4)} \\ y_2^{(3)} & y_2^{(4)} \end{vmatrix}.$$

Thus, we have that

$$\det N(x,\xi) = \varphi_1^-\varphi_6^+ - \varphi_2^-\varphi_5^+ + \varphi_3^-\varphi_4^+ + \varphi_4^-\varphi_3^+ - \varphi_5^-\varphi_2^+ + \varphi_6^-\varphi_1^+. \tag{2.142}$$

It then remains to iterate on ξ until the condition $\det N(d,\xi) = 0$ is satisfied, and a re-expression of this condition in terms of the *Evan's function* as shown previously in the determinantal approach is still valid.

2.7 Weakly non-linear analysis

In the past, apart from in a select few cases (Sawyers and Rivlin, 1982; Fu, 1993; Fu and Rogerson, 1994; Fu and Ogden, 1999), problems of algebraic complexity confined researchers to the linear regime when studying the bifurcation behaviour of elastic materials under large deformations. However, the emergence of powerful symbolic manipulation software packages such as *Mathematica* (Wolfram Research Inc., 2021) has allowed us to overcome such obstacles. This is fortunate since it has long been understood that linearization techniques are insufficient in capturing the post-bifurcation behaviour of a material. Many past experimental studies of compressed plates and thin shell structures found that the experimentally determined critical load may often be far higher or lower than the theoretical prediction obtained from a linear analysis, and the critical load may also be drastically altered due to material or loading imperfections; see Von Karman and Tsien (1939), Cox (1940) and the references therein. In essence, a linear analysis gives only a *necessary condition* for which bifurcation can occur, and it fails to yield the amplitude of the first-order solution. To determine whether the bifurcation solution exists in reality, what the explicit nature of the solution is and whether it arises supercritically or subcritically, we must perform a *weakly non-linear analysis*. This fact was first realized by Koiter (1945), and a framework for a perturbation approach to non-linear bifurcation analysis in the context of non-linear elasticity was later given by Fu (2001). Given the focus of this thesis, we illustrate this perturbation approach by applying it to a simple model problem for which the preferred bifurcation mode is associated with zero wavenumber.

Consider the model problem

$$\frac{\partial^2 u}{\partial x^2} + \frac{\partial^2 u}{\partial y^2} + P\,u - u^2 = 0, \qquad |y| < 1/2, \quad |x| < \infty,$$

$$u(x, \pm 1/2) = 0, \tag{2.143}$$

where u is a function of x and y, and P is the *bifurcation* or *control* parameter. We can clearly see that $u = 0$ is a trivial solution to (2.143) for any value of P. Our aim is to determine for which values of P there exists non-trivial solutions for u.

The starting point is to consider the linearized form of (2.143) and to assume a solution for u of the form

$$u = H(y)e^{ikx} + c.c., \tag{2.144}$$

where k is the wavenumber in the x direction, $H(y)$ is a function to be determined and *c.c.* denotes the complex conjugate of the preceding term. On substitution of (2.144) into the linearized form of (2.143), we find that the function H must satisfy the following linear eigenvalue problem:

$$H''(y) + (P - k^2)H(y) = 0, \qquad H(\pm 1/2) = 0. \tag{2.145}$$

There exists two sets of solutions to (2.145) which take the form

$$H(y) = \cos{(2n-1)\pi y}, \quad P = k^2 + (2n-1)^2\pi^2,$$

and

$$H(y) = \sin{2n\pi y}, \quad P = k^2 + 4n^2\pi^2, \tag{2.146}$$

where $n \in \mathbb{Z}^+$. Then, the critical value of P, denoted P_{cr}, is determined from the lowest branch of $(2.146)_1$ (i.e. that corresponding to $n = 1$):

$$P = k^2 + \pi^2, \tag{2.147}$$

and is obtained at $k = k_{\text{cr}} = 0$, i.e. $P_{\text{cr}} = \pi^2$.

In a weakly non-linear analysis, we are interested in the behaviour of non-trivial solutions to the system (2.143) near the critical point $P = P_{\text{cr}}$. To this end, we consider the following expansion of P:

$$P = \pi^2 + \varepsilon P_1, \tag{2.148}$$

where ε is a small parameter and P_1 is a constant of $\mathcal{O}(1)$. On comparing (2.147) and (2.148), we observe that $k = \mathcal{O}(\varepsilon^{1/2})$. Then, given the presence of the product kx in the exponent of the ansatz (2.144), it makes sense to introduce a far distance variable X through

$$X = \varepsilon^{1/2} x. \tag{2.149}$$

We also consider an asymptotic expansion for u of the form

$$u(x, y) = \varepsilon u_1(X, y) + \varepsilon^2 u_2(X, y) + \varepsilon^3 u_3(X, y) + \mathcal{O}(\varepsilon^4). \tag{2.150}$$

The idea then is to substitute the expansion (2.150) into (2.143). By equating coefficients of like powers of ε, we obtain a hierarchy of boundary value problems to solve. Specifically, by equating coefficients of ε and ε^2, we obtain, respectively:

$$\mathcal{L}[u_1] = 0, \qquad u_1(X, \pm 1/2) = 0, \tag{2.151}$$

and

$$\mathcal{L}[u_2] = -\frac{\partial^2 u_1}{\partial X^2} - P_1 u_1 + u_1^2, \qquad u_2(X, \pm 1/2) = 0, \tag{2.152}$$

where $\mathcal{L}[u] = \partial^2 u/\partial y^2 + \pi^2 u$.

The leading order problem (2.151) has the particular solution

$$u_1(X, y) = \mathcal{C}_1(X) \cos(\pi y), \tag{2.153}$$

where $\mathcal{C}_1(X)$ is the amplitude of the first-order solution to be determined. Then, on substituting (2.153) into $(2.152)_1$, a general solution to the resulting inhomogeneous equation is found to take the form

$$u_2(X, y) = \mathcal{D}_1(X) \sin(\pi y) + \mathcal{D}_2(X) \cos(\pi y) + \mathcal{I}(X, y), \tag{2.154}$$

where the coefficients $\mathcal{D}_1$ and $\mathcal{D}_2$ are arbitrary functions of X and $\mathcal{I}$ is a particular integral given by

$$\mathcal{I}(X, y) = -\frac{1}{2\pi}\{\mathcal{C}_1'' + P_1 \mathcal{C}_1\} y \sin(\pi y) + \frac{1}{2\pi^2}\mathcal{C}_1^2\{1 - \frac{1}{3}\cos(2\pi y)\}. \tag{2.155}$$

Then, on substituting (2.154) – (2.155) into the boundary conditions $(2.152)_2$, we find that $\mathcal{I}(X, 1/2) = -\mathcal{I}(X, -1/2)$. From this condition, we obtain the *amplitude equation*

$$\mathcal{C}_1'' + P_1 \mathcal{C}_1 - \frac{8}{3\pi}\mathcal{C}_1^2 = 0. \tag{2.156}$$

This equation admits the following *standing solitary wave solution*:

$$\mathcal{C}_1(X) = \frac{9\pi}{16} P_1 \operatorname{sech}^2\left(\frac{1}{2}\sqrt{-P_1}X\right). \tag{2.157}$$

We observe that the solution (2.157) is valid only for $P_1 < 0$, i.e. for values of P less than the critical value P_{cr}. Bifurcation solutions with this property are called *sub-critical*, and are generally understood to be sensitive to imperfections. We then note that $|\mathcal{C}_1| = -\mathcal{C}_1$, and hence the solution is a *dark solitary wave*. If the solution instead satisfied the condition $|\mathcal{C}_1| = \mathcal{C}_1$, then we would refer to it as a *bright solitary wave*.

We note that the solution (2.157) is a essentially a solitary wave with zero wave speed. Solitary waves were first observed in the context of water waves by Russell (1845), and the associated model equation was first derived by Korteweg and De Vries (1895) and is nowadays known as the KdV equation. The other simplest model equation that admits a solitary wave solution is the non-linear Schrödinger equation (NLSE) which was first derived in Chiao et al. (1965) for propagation of light in non-linear optical fibers (mathematically the amplitude evolution of wave trains). The static counterpart of NLSE has been derived to describe the amplitude variation of periodic buckling modes (Lange and Newell, 1971; Potier-Ferry, 1987). In recent decades, buckling of an Euler beam on a non-linear foundation has been much studied in relation to localized solutions (Hunt et al., 2000). Such localized solutions again correspond to amplitude localization of periodic buckling modes. A huge variety of other model equations have also been derived for a range of physical processes to incorporate additional effects and/or to describe degenerate cases. Some of these equations involve higher order spatial derivatives and multi spatial dimensions, e.g. the Swift-Hohenberg equation for thermal convection (Swift and Hohenberg, 1977). We refer to the monograph by Peletier and Troy (2001) for a discussion of some of these equations. Physically speaking, solitary waves arise from a balance of non-linearity and dispersion, and this balance underpins all the amplitude equations that admit solitary wave solutions.

3

Axi-symmetric pattern formation in soft tubes under elasto-capillary effects

Contents

3.1 Introduction

In this chapter, we initiate our investigations into the axi-symmetric bifurcation behaviour of an incompressible hyperelastic tube under the combined action of surface tension $\bar{\gamma}$ and a resultant axial force $\mathcal{N}$. We begin by formulating the problem and deriving the equilibrium equations and three distinct sets of boundary conditions pertaining to a general axi-symmetric deformation. We then present the primary axial tension deformation and derive corresponding analytical expressions for both the dimensionless form of $\bar{\gamma}$ and $\mathcal{N}$. By drawing upon the well studied problem of localized bulging in a tube under axial loading and internal inflation, conjectured bifurcation conditions for localized pattern formation are presented in terms of these analytical expressions.

After elaborating on the need for further analysis of the problem beyond the study of Wang (2020), we conduct a comprehensive linear bifurcation analysis for the three sets of boundary conditions alluded to previously, as well as for several types of loading. From this analysis, we produce a numerical relationship between the bifurcation parameter and the axial wavenumber, and determine whether the preferred bifurcation mode is associated with zero wavenumber or a strictly positive wavenumber. Recall that the former case has been previously been associated with the emergence of a localized inhomogeneous bifurcation solution. Given this, we compare our numerical bifurcation condition in the limit of vanishing wave number with our conjectured bifurcation condition for localized pattern formation in order to see if they are in agreement. We conclude by presenting a spectral interpretation of the linear bifurcation analysis and by summarizing the main results of the chapter.

3.2 Problem formulation

Consider an incompressible, isotropic, hyperelastic cylindrical tube with a referential inner radius R_{i}, outer radius R_{o} and axial half-length $L \gg R_{\mathrm{o}}$. The reference configuration $\mathcal{B}_0$ and finitely deformed configuration $\mathcal{B}_e$ are defined in terms of the cylindrical polar coordinates (R, Θ, Z) and (r, θ, z), respectively. Under a general deformation $\mathcal{B}_0 \to \mathcal{B}_e$, the referential values R_{i}, R_{o} and L become $r_{\mathrm{i}} = r_{\mathrm{i}}(\theta, z)$, $r_{\mathrm{o}} =$

$r_o(\theta, z)$ and $\ell \gg r_o$, respectively. The position vectors $\boldsymbol{X}$ and $\boldsymbol{x}$ of a representative material particle in $\mathcal{B}_0$ and $\mathcal{B}_e$ (respectively) are given by

$$\boldsymbol{X} = R\boldsymbol{E}_R + Z\boldsymbol{E}_Z, \qquad \boldsymbol{x} = r\boldsymbol{e}_r + z\boldsymbol{e}_z, \tag{3.1}$$

where $(\boldsymbol{E}_R, \boldsymbol{E}_\Theta, \boldsymbol{E}_Z)$ and $(\boldsymbol{e}_r, \boldsymbol{e}_\theta, \boldsymbol{e}_z)$ are the orthonormal bases corresponding to the two previously defined sets of coordinates. More specifically, we assume that the tube undergoes a general *axi-symmetric* deformation of the form

$$r = r\,(R, Z)\,, \qquad \theta = \Theta, \qquad z = z\,(R, Z)\,. \tag{3.2}$$

The deformation gradient F is then defined through $d\boldsymbol{x} = F d\boldsymbol{X}$ and is expressed as

$$F = \frac{\partial r}{\partial R}\boldsymbol{e}_r \otimes \boldsymbol{E}_R + \frac{\partial r}{\partial Z}\boldsymbol{e}_r \otimes \boldsymbol{E}_Z + \frac{r}{R}\boldsymbol{e}_\theta \otimes \boldsymbol{E}_\Theta + \frac{\partial z}{\partial R}\boldsymbol{e}_z \otimes \boldsymbol{E}_R + \frac{\partial z}{\partial Z}\boldsymbol{e}_z \otimes \boldsymbol{E}_Z. \tag{3.3}$$

The constitutive behaviour of the tube is assumed to be governed by a general strain-energy function W of the form

$$W = W\,(I_1)\,, \tag{3.4}$$

where I_1 is the first principal invariant of the left Cauchy-Green strain tensor $B = FF^T$, i.e. $I_1 = \operatorname{tr} B$. This class of strain-energy functions has been shown to be suitable for many different materials under tension (Wineman, 2005), and in the illustration of our results we will adopt both the neo-Hookean material model (2.58) and the Gent material model (2.63).

For this general static axi-symmetric solution, the *bulk elastic energy* $\mathcal{E}_b$ and the *surface energies* $\mathcal{E}_s^{\mathrm{i}}$ and $\mathcal{E}_s^{\mathrm{o}}$ on the inner and outer lateral surfaces (respectively) take the following forms:

$$\mathcal{E}_b = 2\pi \int_{-L}^{L} \int_{R_\mathrm{i}}^{R_\mathrm{o}} W(I_1) R dR dZ, \qquad \mathcal{E}_s^\beta = 2\pi\bar{\gamma} \int_{-\ell}^{\ell} r_\beta(z)\sqrt{1 + r'_\beta(z)^2} dz, \tag{3.5}$$

where $\beta = \mathrm{i}$ or o. Then, when both lateral surfaces of the tube are under the effect of surface tension, the *total energy* $\mathcal{E}$ is defined through

$$\mathcal{E} = \mathcal{E}_b + \mathcal{E}_s^{\mathrm{i}} + \mathcal{E}_s^{\mathrm{o}}. \tag{3.6}$$

Hereafter, unless stated otherwise, we scale all lengths by R_o and all stresses by the ground state shear modulus μ. Thus, we may set $R_o = 1$ and $\mu = 1$ without loss of generality, and we use the same symbols to denote these scaled quantities. We also introduce the non-dimensionalized surface tension $\gamma = \bar{\gamma}/(\mu R_o)$.

3.2.1 Stream function formulation

As was explained in the previous chapter, the problem can be elegantly re-formulated in terms of a single mixed coordinate stream function $\phi = \phi\,(R,\, z)$ so that the incompressibility constraint (2.12) is satisfied exactly (Ciarletta, 2011). This stream function is defined through the relations

$$r^2 = 2\frac{\partial \phi}{\partial z} = 2\,\phi_{,z}, \qquad Z = \frac{1}{R}\frac{\partial \phi}{\partial R} = \frac{1}{R}\phi_{,R}, \tag{3.7}$$

and, accordingly, F can be re-written in the form

$$\begin{aligned} F = {} & \frac{1}{\sqrt{2\,\phi_{,z}}}\left[\phi_{,Rz} - R\,\frac{\phi_{,zz}}{\phi_{,Rz}}\frac{\partial}{\partial R}\left(\frac{\phi_{,R}}{R}\right)\right]\boldsymbol{e}_r \otimes \boldsymbol{E}_R + \frac{R\,\phi_{,zz}}{\sqrt{2\,\phi_{,z}\,\phi_{,Rz}}}\,\boldsymbol{e}_r \otimes \boldsymbol{E}_Z \\ & + \frac{\sqrt{2\,\phi_{,z}}}{R}\,\boldsymbol{e}_\theta \otimes \boldsymbol{E}_\Theta - \frac{R}{\phi_{,Rz}}\frac{\partial}{\partial R}\left(\frac{\phi_{,R}}{R}\right)\boldsymbol{e}_z \otimes \boldsymbol{E}_R + \frac{R}{\phi_{,Rz}}\,\boldsymbol{e}_z \otimes \boldsymbol{E}_Z. \end{aligned} \tag{3.8}$$

The invariant I_1 may then be computed from (3.8), and is expressed as follows:

$$\begin{aligned} I_1 = {} & \frac{1}{2}\left[\frac{\phi_{,Rz}}{\phi_{,z}} - \frac{R\,\phi_{,zz}}{\phi_{,z}\phi_{,Rz}}\frac{\partial}{\partial R}\left(\frac{\phi_{,R}}{R}\right)\right]^2 + \frac{1}{2}\frac{R^2\,\phi_{,zz}^2}{\phi_{,z}\,\phi_{Rz}^2} \\ & + \frac{2\,\phi_{,z}}{R^2} + \frac{R^2}{\phi_{,Rz}^2} - \frac{R^2}{\phi_{,Rz}^2}\left[\frac{\partial}{\partial R}\left(\frac{\phi_{,R}}{R}\right)\right]^2. \end{aligned} \tag{3.9}$$

The total energy $\mathcal{E}$ as defined in (3.5) and (3.6) can be reformulated in terms of the stream function as such:

$$\mathcal{E} = 2\pi\int_{-\ell}^{\ell}\int_{R_i}^{R_o} \mathcal{L}_b\, dR\, dz \;+\; 2\pi\int_{-\ell}^{\ell}\left(\mathcal{L}_s^{i} + \mathcal{L}_s^{o}\right) dz, \tag{3.10}$$

where the bulk Lagrangian $\mathcal{L}_b$ and the inner and outer surface Lagrangians $\mathcal{L}_s^{i}$ and $\mathcal{L}_s^{o}$ are defined through

$$\mathcal{L}_b = \phi_{,Rz}\, W(I_1), \qquad \mathcal{L}_s^{\beta} = \gamma\,\sqrt{2\,\phi_{,z} + \phi_{,zz}^2}\,\Big|_{R=R_\beta}, \tag{3.11}$$

with $\beta = \mathrm{i}$ or o as before. Thus, $\mathcal{E}$ as presented in (3.10) is a functional in its arguments $\phi_{,R}$, $\phi_{,z}$, $\phi_{,RR}$, $\phi_{,Rz}$ and $\phi_{,zz}$. On taking the first variation of (3.10) with respect to these arguments and then integrating by parts repeatedly, the resulting expression for $\delta\mathcal{E}$ can be shown to contain a single volume integral. Equilibrium of bulk elastic forces requires we set the corresponding integrand to zero, and we arrive at the *Euler-Lagrange equation* given by

$$\left(\frac{\partial \mathcal{L}_b}{\partial \phi_{,RR}}\right)_{,RR} + \left(\frac{\partial \mathcal{L}_b}{\partial \phi_{,Rz}}\right)_{,Rz} + \left(\frac{\partial \mathcal{L}_b}{\partial \phi_{,zz}}\right)_{,zz} - \left(\frac{\partial \mathcal{L}_b}{\partial \phi_{,R}}\right)_{,R} - \left(\frac{\partial \mathcal{L}_b}{\partial \phi_{,z}}\right)_{,z} = 0. \qquad (3.12)$$

Experimentally, it has been shown that localization phenomena such as bulging or necking in inflated tubes are fairly insensitive to the boundary conditions at $z = \pm\ell$ provided that the length to diameter ratio exceeds a certain value (Wang et al., 2019). As in the approach of center-manifold reduction, it has been commonplace to treat these localization phenomena as a bifurcation problem with zero wavenumber (infinite wavelength), and to conduct the analysis without considering end effects, which are lumped together and treated as imperfections (Ye et al., 2020; Fu et al., 2021; Emery and Fu, 2021c). The alternate approach has been to treat localization phenomena as a bifurcation from the primary deformation with non-zero wavenumber, but this is only valid for certain types of end conditions (Wang and Fu, 2021). The validity of the zero wavenumber approach has been examined in Wang and Fu (2021), and it was found that it was valid for cylinders with a length to diameter ratio as low as two in the reference configuration. We adopt this approach of ignoring end effects here, and consider three separate cases of boundary conditions on the lateral surfaces of the tube which are summarized as follows:

Case 1:

In case 1, both lateral surfaces of the tube in $\mathcal{B}_e$ are under surface tension, but are free of any other types of external forces. The simplest approach is to assume that the effect of surface tension on the lateral surfaces is equivalent to a normal traction of magnitude $|\gamma\mathcal{K}|$, where $\mathcal{K}$ is the trace of the curvature tensor. Mathematically, this boundary condition may be defined through the Cauchy stress tensor σ as such:

$$\sigma\boldsymbol{n}\cdot\boldsymbol{n} = \gamma\mathcal{K}, \qquad r = r_{\mathrm{i}},\, r_{\mathrm{o}}, \qquad (3.13)$$

where $\boldsymbol{n}$ *is the outward unit normal to the lateral surface in question. However, more sophisticated models which take into account area stretch (Gurtin and Murdoch, 1975; Huang and Wang, 2006) or even surface stiffness (Steigmann and Ogden, 1997) may be considered. It can be shown that, on the inner and outer lateral surfaces* $r = r_i$ *and* r_o*, the value of* $\mathcal{K}$ *is* $1/r_i$ *and* $-1/r_o$*, respectively, and the boundary conditions* (3.13) *arise naturally from the variational principle of energy stationarity; see Appendix 3.A. Here, there is a net difference in the force per unit deformed area between the inner and outer lateral surface. This is in contrast to when the tube is subjected to an internal and external pressure* P*, in which case there is no net difference in the force per unit deformed area between the inner and outer lateral surface. Also, we have zero shear stress on these lateral surfaces. Mathematically, this boundary condition takes the form*

$$\sigma \boldsymbol{n} \cdot \boldsymbol{e}_z = 0, \qquad r = r_{\mathrm{i}},\, r_{\mathrm{o}}. \tag{3.14}$$

Case 2:

In case 2, the outer lateral surface is under surface tension, whilst the inner lateral surface is assumed to be constrained so that radial displacement is prohibited (i.e. the inner radius is fixed at its referential value R_i*), but displacement in the axial direction is not restricted. As a result, there is still zero shear traction on both lateral surfaces. This boundary condition can be realized if the inner lateral surface is in smooth contact with a rigid cylinder or roller-supported. It is noted that, in the limit* $R_i \to 0$*, we recover the case of a solid cylinder which has been analyzed in Fu et al. (2021).*

Case 3**:**

In case 3, the inner lateral surface is under surface tension, whilst the outer lateral surface is fixed in the radial direction but unconstrained in the axial direction. In reality, the outer lateral surface could be in smooth contact with a rigid exterior annulus or under roller-support. On both lateral surfaces, there is still zero shear *traction.*

Cases 2 and 3 have previously been investigated through FEM simulations (Henann and Bertoldi, 2014), with motivation stemming from the fact that the two types of boundary conditions seem to appear in many biological systems. Indeed, consideration of these different boundary conditions allows us to analyze how different constraints influence the emergence of potential localized or periodic patterns. Each of the three sets of boundary conditions listed previously can be visualized in Fig. 3.1.

The aforementioned expression for $\delta\mathcal{E}$ also contains integrals over each lateral surface, and the boundary conditions for each case listed previously can be obtained from the condition that the associated integrands must vanish. These integrands contain terms proportional to $\delta\phi$ and $\delta\phi_{,R}$ evaluated at both $R = R_{\mathrm{i}}$ and R_{o}. In *case 1*, there are no initial constraints imposed upon $\delta\phi$ since

$$\delta\phi = \int_{-\ell}^{\ell} r\delta r dz, \tag{3.15}$$

by (3.7), and both r and δr at $R = R_{\mathrm{i}}$ and R_{o} are unrestricted. Therefore, we must instead set the coefficients of $\delta\phi$ evaluated at $R = R_{\mathrm{i}}$ and R_{o} to zero. In doing so, we obtain the surface tension boundary conditions

$$\frac{\partial\mathcal{L}_b}{\partial\phi_{,R}} - \left(\frac{\partial\mathcal{L}_b}{\partial\phi_{,RR}}\right)_{,R} - \left(\frac{\partial\mathcal{L}_b}{\partial\phi_{,Rz}}\right)_{,z} = \left(\frac{\partial\mathcal{L}_s^{\mathrm{i}}}{\partial\phi_{,zz}}\right)_{,zz} - \left(\frac{\partial\mathcal{L}_s^{\mathrm{i}}}{\partial\phi_{,z}}\right)_{,z}, \qquad R = R_{\mathrm{i}}, \tag{3.16}$$

$$\frac{\partial\mathcal{L}_b}{\partial\phi_{,R}} - \left(\frac{\partial\mathcal{L}_b}{\partial\phi_{,RR}}\right)_{,R} - \left(\frac{\partial\mathcal{L}_b}{\partial\phi_{,Rz}}\right)_{,z} = \left(\frac{\partial\mathcal{L}_s^{\mathrm{o}}}{\partial\phi_{,z}}\right)_{,z} - \left(\frac{\partial\mathcal{L}_s^{\mathrm{o}}}{\partial\phi_{,zz}}\right)_{,zz}, \qquad R = R_{\mathrm{o}}. \tag{3.17}$$

It is noted that (3.16) and (3.17) are the variational equivalents of (3.13) with $\mathcal{K} = 1/r_{\mathrm{i}}$ and $-1/r_{\mathrm{o}}$, respectively. In contrast, when a lateral surface is fixed in the radial direction (*case 2 or 3*), we have that $\delta r = 0$ on $R = R_{\mathrm{i}}$ or R_{o}, and so it is $\delta\phi$ on $R = R_{\mathrm{i}}$ or R_{o} which must vanish by (3.15) as opposed to its coefficient. Lastly, we have zero shear traction on both lateral surfaces in all three cases under

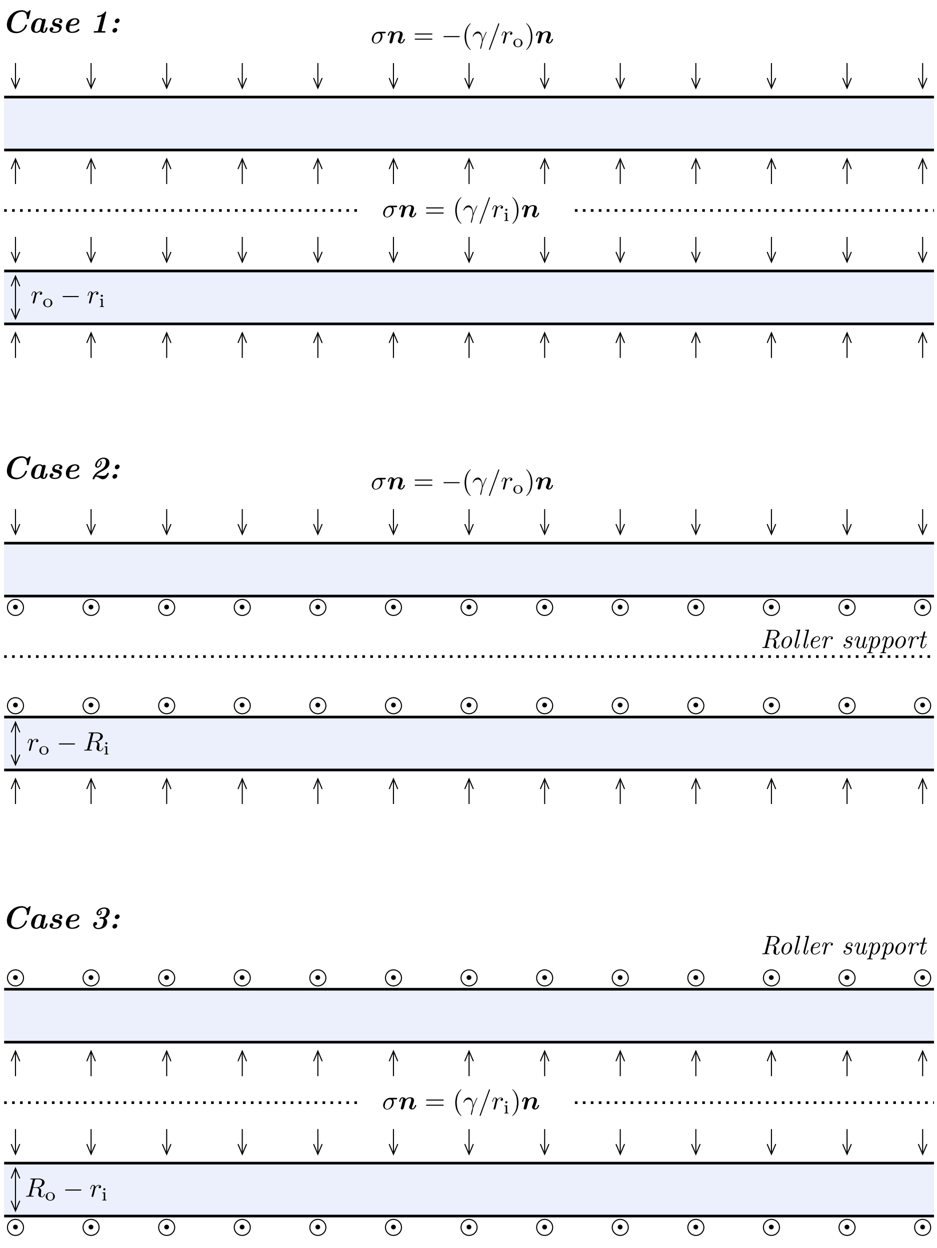

Figure 3.1: A schematic of the three different types of boundary conditions under consideration.

consideration. This boundary condition can be obtained by setting the coefficient of $\delta\phi_{,R}$ evaluated at $R = R_\mathrm{i}$ and R_o to zero. We obtain

$$\frac{\partial \mathcal{L}_b}{\partial \phi_{,RR}} = 0, \qquad R = R_\mathrm{i},\, R_\mathrm{o}, \tag{3.18}$$

and note that (3.18) is the variational equivalent of (3.14).

To summarize, in *case 1* we would impose (3.16), (3.17) and (3.18). In *case 2* we must satisfy (3.17), $\delta r = 0$ on $R = R_\mathrm{i}$ and (3.18), whilst in *case 3* we require that (3.16), $\delta r = 0$ on $R = R_\mathrm{o}$ and (3.18) hold.

3.3 Primary deformation and conditions for localized pattern formation

We now narrow our focus towards the following primary axial tension deformation, a sub-class of (3.2), which is theoretically possible for all strain-energy functions:

$$r = r(R), \qquad \theta = \Theta, \qquad z = \lambda Z. \tag{3.19}$$

The parameter λ is defined as the *principal axial stretch*, and the deformation gradient corresponding to (3.19) is

$$F = \frac{\partial r}{\partial R}\boldsymbol{e}_r \otimes \boldsymbol{E}_R + \frac{r}{R}\boldsymbol{e}_\theta \otimes \boldsymbol{E}_\Theta + \lambda\, \boldsymbol{e}_z \otimes \boldsymbol{E}_Z. \tag{3.20}$$

Upon substitution of (3.20) into (2.12), the primary radial displacement r_0 which satisfies incompressibility exactly is found to take the form

$$r_0(R) = \sqrt{\lambda^{-1}\left(R^2 - R_\mathrm{i}^2\right) + r_\mathrm{i}^2}, \tag{3.21}$$

and the outer deformed radius is hence $r_\mathrm{o} = r_0(R_\mathrm{o})$. In *case 1*, there are no radial displacement constraints on the inner and outer surfaces. Thus, r_i (and hence r_o) is unknown and the primary deformation given by (3.19) and (3.21) is governed entirely by the two deformation parameters λ and r_i. The situation is different in *cases 2* and *3*. In the former, the radial fixing of the inner surface means we must set $r_{\rm i} = R_{\rm i}$, whilst in the latter the radial fixing of the outer surface requires $r_0(R_{\rm o}) = R_{\rm o}$, from which we deduce that

$$r_{\rm i} = \sqrt{\lambda^{-1}(R_{\rm i}^2 - R_{\rm o}^2) + R_{\rm o}^2}. \tag{3.22}$$

Thus, in case 2 and 3, the primary deformation is determined entirely via the single deformation parameter λ.

In *case 3*, we see from (3.22) that $r_{\rm i} \to 0$ as $\lambda \to (1 - R_{\rm i}^2/R_{\rm o}^2)$. Therefore, incompressibility prohibits axial stretches less than $1 - R_{\rm i}^2/R_{\rm o}^2$ since a self-contacting of the inner surface will occur when this lower bound is attained. Also, when taking the limit $R_{\rm i}/R_{\rm o} \to 0$ in *case 3*, we recover the case of a cylindrical cavity in an infinite solid. From (3.22), we see that this limit can only be taken when $\lambda = 1$, otherwise $r_{\rm i}$ will be undefined. In this scenario, the primary deformation governed by (3.19), (3.21) and (3.22) becomes homogeneous since $\partial r_0/\partial R$ and r_0/R are constant. This special case was first analyzed in Xuan and Biggins (2016).

By substituting (3.21) into (3.7) and integrating the resulting equations, the primary solution for ϕ, denoted by ϕ_0, can be shown to take the form

$$\phi_0 = \frac{R^2 z}{2\,\lambda} + \frac{1}{2}\left(r_{\rm i}^2 - \frac{R_{\rm i}^2}{\lambda}\right) z. \tag{3.23}$$

Then, on substituting (3.23) into (3.9), the associated expression for I_1, denoted by I_0, is

$$I_0 = I_1|_{\phi=\phi_0} = \frac{(r_{\rm i}^2\lambda - R_{\rm i}^2)^2}{r_0^2\, R^2\, \lambda^2} + \frac{2 + \lambda^3}{\lambda}. \tag{3.24}$$

Now, in its current configuration $\mathcal{B}_e$, the tube is considered to be under the combined action of a surface tension γ on $r = r_{\rm i}$, $r = r_{\rm o}$ or both (depending on which of the three boundary condition cases we are focussing on), and a resultant axial force $\mathcal{N}$. That is, in the reference configuration $\mathcal{B}_0$, there is no surface tension effect or resultant axial force, and the tube is completely unstressed. In *case 1*, for instance, the total energy $\mathcal{E}_0$ corresponding to the primary deformation is

$$\mathcal{E}_0 = 2\pi\left[\int_{-\lambda L}^{\lambda L}\int_{R_{\rm i}}^{R_{\rm o}} \mathcal{L}_b\, dR\, dz + \int_{-\lambda L}^{\lambda L}\left(\mathcal{L}_s^{\rm i} + \mathcal{L}_s^{\rm o}\right)\, dz\right]_{\phi=\phi_0} - (\lambda - 1)\,\mathcal{N}, \tag{3.25}$$

where the third term on the right hand side is the potential energy due to the resultant force $\mathcal{N}$ acting perpendicular to any cross section of the tube. In *cases 2* and *3*, we must remove $\mathcal{L}_s^{\mathrm{i}}$ and $\mathcal{L}_s^{\mathrm{o}}$ (respectively) from (3.25) since the radial displacement constraint on the relevant lateral surface negates the associated surface energy.

Recall in *case 1* that we have two deformation parameters in λ and r_{i}. Given this, equilibrium of the primary deformation configuration requires that we satisfy $\partial\mathcal{E}_0/\partial\lambda = 0$ and $\partial\mathcal{E}_0/\partial r_{\mathrm{i}} = 0$, and from these equations the following expressions for $\mathcal{N} = \mathcal{N}(\lambda, r_{\mathrm{i}})$ and $\gamma = \gamma(\lambda, r_{\mathrm{i}})$ are respectively obtained:

$$\mathcal{N} = \pi\left[\frac{\gamma}{r_{\mathrm{o}}}(r_{\mathrm{i}} + r_{\mathrm{o}})^2 + 2\int_{R_{\mathrm{i}}}^{R_{\mathrm{o}}} W_d\, I_{0\lambda} R\, dR\right], \tag{3.26}$$

$$\gamma = -\frac{r_{\mathrm{o}}}{\lambda(r_{\mathrm{i}} + r_{\mathrm{o}})}\int_{R_{\mathrm{i}}}^{R_{\mathrm{o}}} W_d\, I_{0\mathrm{i}} R\, dR, \tag{3.27}$$

where $W_d = W'(I_0)$, $W_{dd} = W''(I_0)$ etc., $I_{0\lambda} = \partial I_0/\partial\lambda$ and $I_{0\mathrm{i}} = \partial I_0/\partial r_{\mathrm{i}}$. We note that the γ in (3.26) is eliminated through substitution of (3.27). Alternatively, (3.27) can be derived with the aid of the Cauchy stress tensor σ, defined through the constitutive equation $\sigma = 2\,W_d\,B - pI$, together with the boundary conditions (3.13). Recall that p is the Lagrangian multiplier associated with the constraint of incompressibility and I is the identity tensor. The axial force $\mathcal{N}$ is then equal to the resultant of σ_{zz} plus $2\pi\gamma\,(r_{\mathrm{i}} + r_{\mathrm{o}})$. Thus, in *case 1*, γ and $\mathcal{N}$ represent two force parameters which are solely dependant on the deformation parameters λ and r_{i}.

In the absence of any other loads, surface tension will have a compressive effect on the tube by inducing an axial stretch $\lambda < 1$. As an illustrative example, consider a tube composed of neo-Hookean material with initial inner and outer (scaled) radii $R_{\mathrm{i}} = 0.4$ and $R_{\mathrm{o}} = 1$, and say that we apply no mechanical loading such that $\mathcal{N} = 0$, and a surface tension $\gamma = 8$. Setting the left hand side of (3.26) to 0, we can express r_{i} implicitly as a function of λ. Then, on setting the left hand side of (3.27) to 8, we can solve the resulting equation for λ, and we find that the surface tension induces a compressive axial stretch $\lambda = 0.26$. From (3.26), we find that the inner radius reduces from $R_{\mathrm{i}} = 0.4$ to $r_{\mathrm{i}} = 0.15$. The outer radius increases from $R_{\mathrm{o}} = 1$ to $r_{\mathrm{o}} = 1.8$.

The situation in *cases 2* and *3* is somewhat different since we have only one deformation parameter in λ. We need only satisfy the single equilibrium equation $\partial\mathcal{E}_0/\partial\lambda = 0$, and this can be solved for $\mathcal{N} = \mathcal{N}(\lambda)$ with γ fixed or $\gamma = \gamma(\lambda)$ with $\mathcal{N}$ fixed. For instance, in *case 2* equilibrium requires that

$$\mathcal{N} = \pi\left[\frac{\gamma}{r_{\rm o}}(R_{\rm i}^2 + r_{\rm o}^2) + 2\int_{R_{\rm i}}^{R_{\rm o}} W_d\, I_{0\lambda} R\, dR\right], \quad \text{with } \gamma \text{ fixed,} \tag{3.28}$$

or
$$\gamma = \frac{r_{\rm o}}{\pi(R_{\rm i}^2 + r_{\rm o}^2)}\left[\mathcal{N} - 2\pi\int_{R_{\rm i}}^{R_{\rm o}} W_d\, I_{0\lambda} R\, dR\right], \quad \text{with } \mathcal{N} \text{ fixed,} \tag{3.29}$$

where $r_{\rm i} \to R_{\rm i}$. Also, in *case 3* we have

$$\mathcal{N} = \pi\left[\frac{\gamma}{r_{\rm i}}(R_{\rm o}^2 + r_{\rm i}^2) + 2\int_{R_{\rm i}}^{R_{\rm o}} W_d\, I_{0\lambda} R\, dR\right], \quad \text{with } \gamma \text{ fixed,} \tag{3.30}$$

or
$$\gamma = \frac{r_{\rm i}}{\pi(R_{\rm o}^2 + r_{\rm i}^2)}\left[\mathcal{N} - 2\pi\int_{R_{\rm i}}^{R_{\rm o}} W_d\, I_{0\lambda} R\, dR\right], \quad \text{with } \mathcal{N} \text{ fixed,} \tag{3.31}$$

where $r_{\rm i}$ is given by the expression in (3.22).

3.3.1 Localized bulging in inflated rubber tubes

Recall our earlier statement that the problem of localized bulging in a tube under internal pressure and axial loading has become prototypical in the sense that it often has a very similar mathematical structure to other more complicated localized pattern formation problems in elasticity. To elaborate, recall that in *case 1* of the elasto-capillary problem at hand, there are two force parameters in the resultant axial force $\mathcal{N}$ and the surface tension γ, and both of these are functions of the deformation parameters λ and $r_{\rm i}$. The situation in the inflation problem is mathematically quite similar, except the force parameters are $\mathcal{N}$ and the *internal pressure* P, and they depend on the deformation parameters λ and *circumferential stretch* $\lambda_{\rm i} = r_{\rm i}/R_{\rm i}$ on the inner surface. Note that the choice of $r_{\rm i}$ as a deformation parameter in the our case (rather than $\lambda_{\rm i}$) is due to mathematical convenience.

Now, in Fu et al. (2016), it was demonstrated numerically that, for a tube of *arbitrary thickness* under any form of loading, the vanishing of the Jacobian determinant of the vector function $(P, \mathcal{N})$ coincides with the emergence of an axi-symmetric bifurcation solution with zero wavenumber. Recall that the general theory of dynamical systems suggests that the latter criterion also signals a bifurcation into a localized inhomogeneous solution (Kirchgässner, 1982; Haragus and Iooss, 2010). Thus, the bifurcation condition for localized bulging in tubes under inflation is given by

$$\frac{\partial P}{\partial \lambda}\frac{\partial \mathcal{N}}{\partial \lambda_{\mathrm{i}}} - \frac{\partial \mathcal{N}}{\partial \lambda}\frac{\partial P}{\partial \lambda_{\mathrm{i}}} = 0, \tag{3.32}$$

and can be derived in the following manner. We note first that the condition (3.32) has the interpretation that the force parameters cannot be inverted to express the deformation parameters λ and λ_{i} in terms of $\mathcal{N}$ and P. Now, the internal volume ratio is defined by $v = \lambda_{\mathrm{i}}^2\lambda$, and we consider for the meantime the loading scenario where the axial force $\mathcal{N}$ is held fixed and the inflation pressure is gradually increased from zero. From the equation $\mathcal{N}(\lambda, \lambda_{\mathrm{i}}) = \mathcal{N}_0$, where $\mathcal{N}_0$ is a constant, we may express λ implicitly in terms of λ_{i}. As a consequence, v is merely a function of λ_{i}. Then, the existence of a pressure maximum requires that

$$\frac{dP}{dv} = \frac{dP}{d\lambda_{\mathrm{i}}}\left(\frac{dv}{d\lambda_{\mathrm{i}}}\right)^{-1} = 0 \implies \frac{dP}{d\lambda_{\mathrm{i}}} = \frac{\partial P}{\partial \lambda_{\mathrm{i}}} + \frac{\partial P}{\partial \lambda}\frac{d\lambda}{d\lambda_{\mathrm{i}}} = 0. \tag{3.33}$$

Elimination of the ordinary derivative in (3.33) can be achieved by differentiating the equation $\mathcal{N} = \mathcal{N}_0$ with respect to λ_{i}, i.e.:

$$\frac{\partial \mathcal{N}}{\partial \lambda_{\mathrm{i}}} + \frac{\partial \mathcal{N}}{\partial \lambda}\frac{d\lambda}{d\lambda_{\mathrm{i}}} = 0 \implies \frac{d\lambda}{d\lambda_{\mathrm{i}}} = -\left(\frac{\partial \mathcal{N}}{\partial \lambda_{\mathrm{i}}}\right)\left(\frac{\partial \mathcal{N}}{\partial \lambda}\right)^{-1}, \tag{3.34}$$

where $\partial\mathcal{N}/\partial\lambda \neq 0$. On substitution of (3.34) into (3.33), it is straightforward to show that the condition (3.32) follows. In the loading scenario where the tube length (i.e. λ) is held fixed and the pressure is gradually increased from zero, the same condition (3.32) can be reached through a similar argument to the one just presented.

In the next section, we will draw upon the results presented here for the inflation problem in order to formulate *conjectured* bifurcation conditions for elasto-capillary localized pattern formation.

3.3.2 Bifurcation conditions for localized pattern formation

3.3.2.1 Case 1

In *case 1*, the force parameters $\mathcal{N} = \mathcal{N}(\lambda, r_{\rm i})$ and $\gamma = \gamma(\lambda, r_{\rm i})$ cannot be inverted to express the deformation parameters λ and $r_{\rm i}$ uniquely in terms of $\mathcal{N}$ and γ when

$$\mathcal{J}(\gamma, \mathcal{N}) \equiv \frac{\partial \gamma}{\partial \lambda}\frac{\partial \mathcal{N}}{\partial r_{\rm i}} - \frac{\partial \mathcal{N}}{\partial \lambda}\frac{\partial \gamma}{\partial r_{\rm i}} = 0, \tag{3.35}$$

where $\mathcal{J}(\gamma, \mathcal{N})$ is the Jacobian of the vector function $(\gamma, \mathcal{N})$. Based on the analysis of Fu et al. (2016) summarized in the previous section, we may conjecture that (3.35) is the bifurcation condition for elasto-capillary localized pattern formation in hollow tubes. It will later be shown that this is equivalently the condition for a bifurcation mode characterized by zero wavenumber to exist *and* for zero to become a triple eigenvalue of the spectral problem governing incremental perturbations of the primary solution (3.23). When $r_{\rm i}$ or $r_{\rm o}$ are fixed at their referential values (i.e. cases 2 or 3 to be discussed shortly), the condition (3.35) reduces to $d\mathcal{N}/d\lambda = 0$ when the surface tension is fixed or $d\gamma/d\lambda = 0$ when the axial force is fixed.

Now, there are several different loading scenarios we can consider, though in any case the simplest way to analyze the bifurcation condition (3.35) would seem to be plotting its contours in the $(\lambda, r_{\rm i})$ plane. Say we initially fix the surface tension and then vary the axial force monotonically from some starting value, then we may plot $\mathcal{J}(\gamma, \mathcal{N}) = 0$ and $\gamma(\lambda, r_{\rm i}) = \gamma_0$ together in the $(\lambda, r_{\rm i})$ plane, where $\gamma(\lambda, r_{\rm i})$ is given by (3.27) and $\gamma_0 \geq 0$ is a constant. If the two contours have intersection points, then the bifurcation condition (3.35) is satisfied at these points under the outlined loading conditions. As a simple illustrative example, we adopt the neo-Hookean material model (2.58) with $R_{\rm i} = 0.4$. We plot in Fig. 3.2 (a) the contour $\mathcal{J}(\gamma, \mathcal{N}) = 0$ in the $(\lambda, r_{\rm i})$ plane, along with $\gamma(\lambda, r_{\rm i}) = 3$ and 8. We see that $\mathcal{J}(\gamma, \mathcal{N}) = 0$ and $\gamma(\lambda, r_{\rm i}) = 3$ have no intersections, yet $\mathcal{J}(\gamma, \mathcal{N}) = 0$ and $\gamma(\lambda, r_{\rm i}) = 8$ have intersections at $\lambda \approx 0.85$ and 2.25. We also find that intersection points cease to exist for any fixed $\gamma < 6.35$. At $\gamma \approx 6.35$, a single intersection point emerges, and for larger fixed γ above this value the two intersection points move

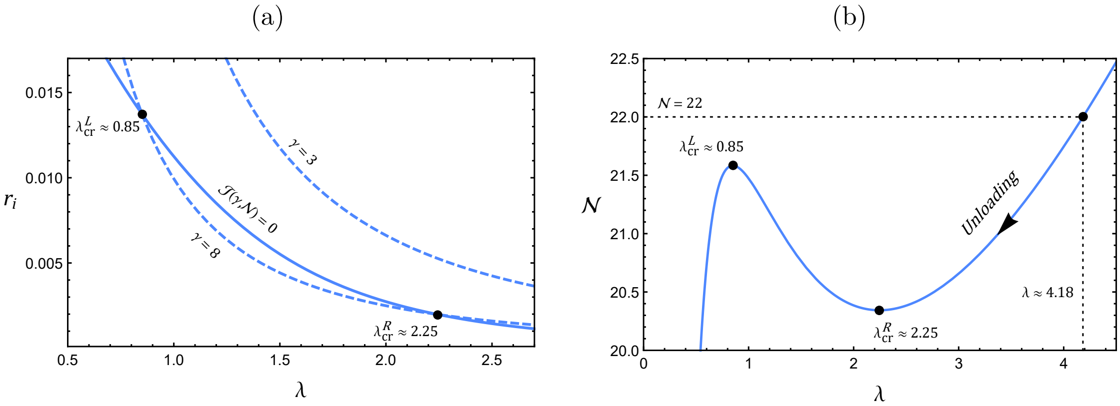

Figure 3.2: Analysis of the bifurcation condition (3.35) with fixed γ for the neo-Hookean model (2.58) with $R_\mathrm{i} = 0.4$ (a) Plots of $\mathcal{J}(\gamma, \mathcal{N}) = 0$ and $\gamma(\lambda, r_\mathrm{i}) = 3, 8$ in the (λ, r_i) plane. (b) A plot of $\mathcal{N}$ against λ with $\gamma(\lambda, r_\mathrm{i}) = 8$ fixed. On fixing $\mathcal{N} = 22$ initially, an axial stretch $\lambda \approx 4.18$ is produced and we unload until reaching the bifurcation point $\lambda_\mathrm{cr}^R \approx 2.25$.

progressively further apart. Also, from $\gamma(\lambda, r_\mathrm{i}) = \gamma_0$ we can relate r_i implicitly to λ, and we may then plot $\mathcal{N} = \mathcal{N}(\lambda, r_\mathrm{i}(\lambda))$ in the $(\lambda, \mathcal{N})$ plane; see Fig. 3.2 (b). We observe that the left and right intersection points in (a) correspond to a local maximum and minimum of $\mathcal{N}$, respectively. The question then is when, if at all, are the left and right bifurcation points $\lambda_\mathrm{cr}^{L,R}$ of interest in case 1? Intuitively, one loading path could be to fix γ with $\mathcal{N} = 0$ initially, inducing an initial axial stretch $\lambda < 1$; see Fig. 3.2 (b). We could then in theory increase $\mathcal{N}$ (i.e. apply a “loading”) from this initial value until we reach $\lambda = \lambda_\mathrm{cr}^L$. However, it is known that compressed unconstrained slender structures are instead highly sensitive to the Euler buckling instability (Goriely et al., 2008). Given that we are interested in localized pattern formation here, we neglect this “loading” path in case 1. We may instead choose to apply a sufficiently large dead load $\mathcal{N} > 0$ to an end of the tube initially along with the fixed surface tension in order to produce an initial axial stretch $\lambda > 1$. We could then gradually decrease $\mathcal{N}$ (i.e. apply an “unloading”) from this point until we hit $\lambda = \lambda_\mathrm{cr}^R$. As an illustrative example, for a tube with initial inner radius $R_\mathrm{i} = 0.4$, say we fix $\gamma = 8$ and $\mathcal{N} = 22$ initially. Then, an axial stretch $\lambda \approx 4.18$ is produced; see Fig. 3.2 (b). From this point, we “unload” by decreasing $\mathcal{N}$, and the first bifurcation point encountered is hence $\lambda_\mathrm{cr}^R \approx 2.25$.

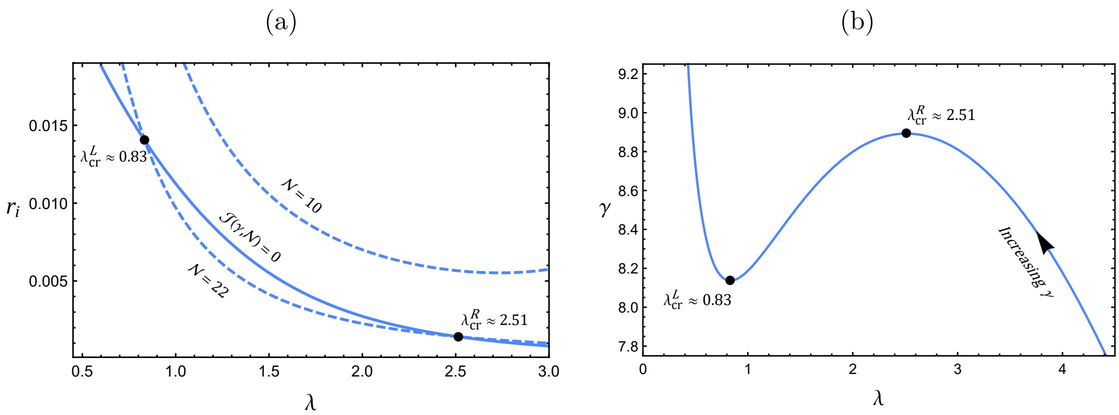

Figure 3.3: Analysis of the bifurcation condition (3.35) with fixed $\mathcal{N}$ for the neo-Hookean model (2.58) with $R_{\rm i} = 0.4$. (a) Plots of $\mathcal{J}(\gamma, \mathcal{N}) = 0$ and $\mathcal{N}(\lambda, r_{\rm i}) = 10$, 22 in the $(\lambda, r_{\rm i})$ plane. (b) A plot of γ against λ with $\mathcal{N}(\lambda, r_{\rm i}) = 22$ fixed.

A second loading scenario could be to fix $\mathcal{N} \geq 0$ initially, and then to increase the surface tension gradually from zero. We note that varying the surface tension is not easy to achieve experimentally. It can be done, to a certain extent, by varying the temperature of the chemical composition of the material, and this would mean navigating a complex path in the $(\gamma, \mathcal{N})$. In this work, when taking γ as the control parameter, we are primarily interested in the mathematical structure of the problem, as we expect it will be similar to more realistic loading scenarios in the current, and alternate, elastic localization problems.

Similarly to before, we may plot $\mathcal{J}(\gamma, \mathcal{N}) = 0$ and $\mathcal{N}(\lambda, r_{\rm i}) = \mathcal{N}_0 \geq 0$ in the $(\lambda, r_{\rm i})$ plane, where $\mathcal{N}_0$ is a constant, and investigate for which values of $\mathcal{N}_0$ the two contours have intersection points. To illustrate, we again take $R_{\rm i} = 0.4$ and plot $\mathcal{J}(\gamma, \mathcal{N}) = 0$ and $\mathcal{N}(\lambda, r_{\rm i}) = 10$ and 22 in the $(\lambda, r_{\rm i})$ plane; see Fig. 3.3 (a). We observe that $\mathcal{J}(\gamma, \mathcal{N}) = 0$ and $\mathcal{N}(\lambda, r_{\rm i}) = 22$ have two intersection points at $\lambda_{\rm cr}^{L} \approx 0.83$ and $\lambda_{\rm cr}^{R} \approx 2.51$, whilst $\mathcal{J}(\gamma, \mathcal{N}) = 0$ and $\mathcal{N}(\lambda, r_{\rm i}) = 10$ do not intersect. We find that intersections do not occur for $\mathcal{N} < 16.9$. Using $\mathcal{N}(\lambda, r_{\rm i}) = \mathcal{N}_0$, we can relate $r_{\rm i}$ implicitly to λ, and plot $\gamma(\lambda, r_{\rm i}(\lambda))$ against λ. We indeed do this in Fig. 3.3 (b) for $\mathcal{N}_0 = 22$, and find that the left and right intersection points $\lambda_{\rm cr}^{L,R}$ in (a) correspond to the local minimum and maximum of $\gamma = \gamma(\lambda, r_{\rm i}(\lambda))$, respectively. However, as in the previous scenario, it is only the right point $\lambda_{\rm cr}^{R}$ which is of practical interest, and this can be explained as follows. When fixing $\mathcal{N} > 0$ with

$\gamma = 0$ initially, an axial stretch $\lambda > 1$ is produced. Then, as we increase γ gradually from zero, we must in turn decrease λ from this starting value to maintain the constant value of $\mathcal{N}$. In other words, we must traverse in the direction of the arrow along the curve in (b), and we therefore reach λ_{cr}^R first. Thus, we observe graphically in Fig. 3.2 and 3.3 that, for fixed γ and fixed $\mathcal{N}$, the bifurcation condition (3.35) reduces to $d\mathcal{N}/d\lambda = 0$ and $d\gamma/d\lambda = 0$, respectively.

Thirdly, we could apply a fixed axial stretch $\lambda \geq 1$ and increase the surface tension from zero. Clearly, from the bifurcation condition (3.35), we can relate the bifurcation value of the inner deformed radius, say r_{icr}, implicitly to the fixed λ. We can then plot $\gamma_{\text{cr}} \equiv \gamma(\lambda, r_{\text{icr}}(\lambda))$ against λ; see Fig. 3.4.

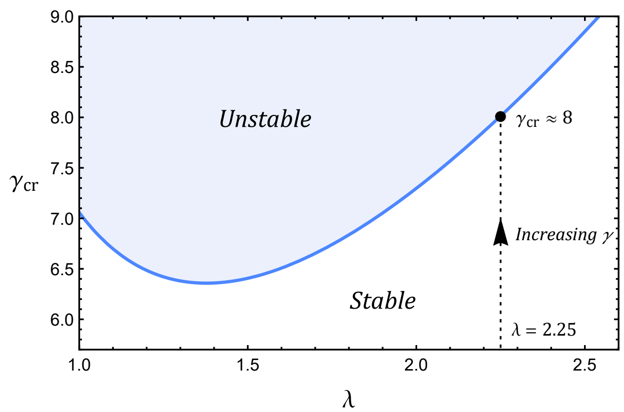

Figure 3.4: Analysis of the bifurcation condition (3.35) with fixed $\lambda > 1$ for the neo-Hookean model (2.58) with $R_{\text{i}} = 0.4$. For fixed $\lambda = 2.25$, we observe that the bifurcation value of γ is approximately 8.

3.3.2.2 Case 2

We note firstly that, in case 2, the internal support the inner surface will prevent the occurrence of *Euler buckling*. Hence, we can be less restrictive in our choice of loading paths here. In case 2 and case 3 to follow, we will adopt the Gent material model (2.63) unless stated otherwise.

Recall that, when γ is fixed in case 2, we are able to determine from the equilibrium equation an explicit expression for $\mathcal{N} = \mathcal{N}(\lambda)$ as given in (3.28). Guided by the results for case 1 in Fig. 3.2, we may conjecture that the bifurcation condition for localized pattern formation in this case is simply $d\mathcal{N}/d\lambda = 0$. This condition may be expressed as the following implicit relationship between the fixed surface tension γ and the critical axial stretch $\lambda_{\rm cr}$:

$$\gamma = \frac{4r_{\rm o}^3\lambda^3}{(R_{\rm o}^2 - R_{\rm i}^2)^2}\int_{R_{\rm i}}^{R_{\rm o}} \frac{\partial}{\partial\lambda}\left(W_d I_{0\lambda}\right) R\,dR\bigg|_{\lambda=\lambda_{\rm cr}}. \tag{3.36}$$

An important feature of (3.36) (and indeed (3.35) in case 1) is that the associated bifurcation curves in the $(\lambda_{\rm cr}, \gamma)$ plane have a minimum at $(\lambda_{\rm min}, \gamma_{\rm min})$, say. For each fixed $\gamma > \gamma_{\rm min}$, there exists a single bifurcation value for λ either side of $\lambda = \lambda_{\rm min}$, say $\lambda_{\rm cr}^L < \lambda_{\rm min}$ and $\lambda_{\rm cr}^R > \lambda_{\rm min}$, which corresponds to the local maximum and minimum of $\mathcal{N} = \mathcal{N}(\lambda)$, respectively; see Fig. 3.5. In the limit $\gamma \to \gamma_{\rm min}$, these two extrema of $\mathcal{N}$ coalesce to form an inflection point, and for any $\gamma < \gamma_{\rm min}$, $\mathcal{N}$ is a monotonic increasing function of λ and the bifurcation condition (3.36) cannot be satisfied. Unlike in case 1, we may consider in case 2 both the "loading" and "unloading" scenarios described previously. As illustrated in Fig. 3.5 (b) for a representative case, for any fixed $\gamma > \gamma_{\rm min}$, the axial force $\mathcal{N}$ is a monotonic function of λ up to the first bifurcation point encountered. Therefore, when either "loading" or "unloading", we may equivalently take λ or $\mathcal{N}$ as the control parameter. We refer to taking λ as the control parameter in this scenario as *displacement controlled loading*, and to taking $\mathcal{N}$ as the control parameter as *force controlled loading*.

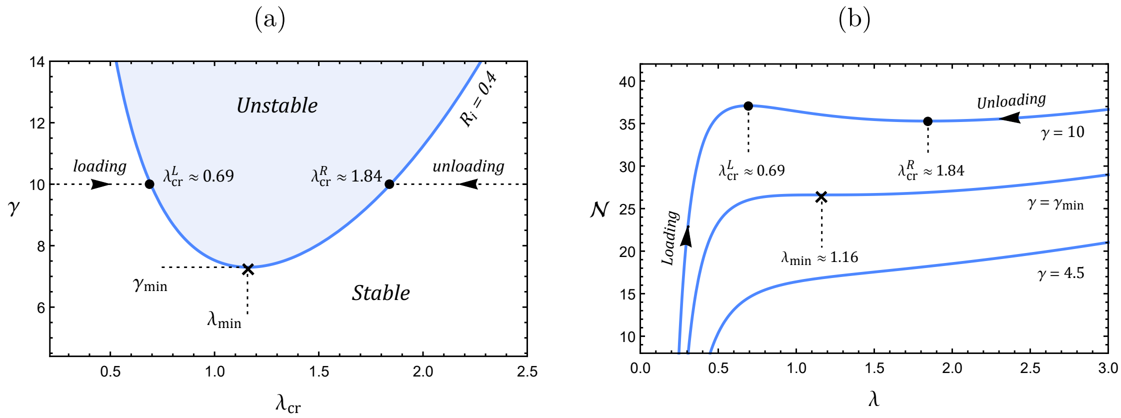

Figure 3.5: (a) The bifurcation condition (3.36) plotted in the $(\lambda_{\rm cr}, \gamma)$ plane for the Gent material model (2.63) with $J_{\rm m} = 100$ and $R_{\rm i} = 0.4$. The bifurcation curve has a minimum at $(\lambda_{\rm min}, \gamma_{\rm min}) \approx (1.16, 7.3)$. Then, for each fixed $\gamma > \gamma_{\rm min}$, there exists a bifurcation point either side of $\lambda = \lambda_{\rm min}$. For example, where $\gamma = 10$, the tube can bifurcate into a localised solution at $\lambda_{\rm cr}^L \approx 0.69 < \lambda_{\rm min}$ and $\lambda_{\rm cr}^R \approx 1.84 > \lambda_{\rm min}$ as shown by the black dots. (b) The variation of $\mathcal{N}$ with respect to λ for $\gamma = 10, \gamma_{\rm min}$ and 4.5.

Alternatively, we may fix $\mathcal{N} \geq 0$ and increase γ gradually from zero. In this scenario, we have previously shown that the equilibrium equation $\partial\mathcal{E}/\partial\lambda = 0$ yields a relation $\gamma = \gamma(\lambda)$ as given in (3.29). We then conjecture that the associated bifurcation condition for localized pattern formation is $d\gamma/d\lambda = 0$, and the following implicit relation between the fixed $\mathcal{N}$ and λ_{cr} is obtained:

$$\frac{\mathcal{N}}{2\pi} = \left[\int_{R_\text{i}}^{R_\text{o}} W_d I_{0\lambda} R\, dR + \frac{2\,(r_\text{o}\lambda)^2(r_\text{o}+R_\text{i})}{(R_\text{i}-r_\text{o})(R_\text{i}^2-1)} \int_{R_\text{i}}^{R_\text{o}} \frac{\partial}{\partial\lambda}\,(W_d I_{0\lambda})\, R\, dR\right]\Bigg|_{\lambda=\lambda_{\text{cr}}}. \tag{3.37}$$

Similar to the fixed γ and varying $\mathcal{N}$ scenario, the bifurcation curves in the $(\lambda_{\text{cr}}, \mathcal{N})$ plane from (3.37) have a minimum value at $(\lambda_{\text{min}}, \mathcal{N}_{\text{min}})$, say; see Fig. 3.6 (a). However, as explained previously, for each $\mathcal{N} > \mathcal{N}_{\text{min}}$ it is only the right bifurcation point λ_{cr}^R which is of practical interest here. In Fig. 3.6 (b) we plot (3.29) in the (λ, γ) plane for three distinct fixed values of $\mathcal{N}$.

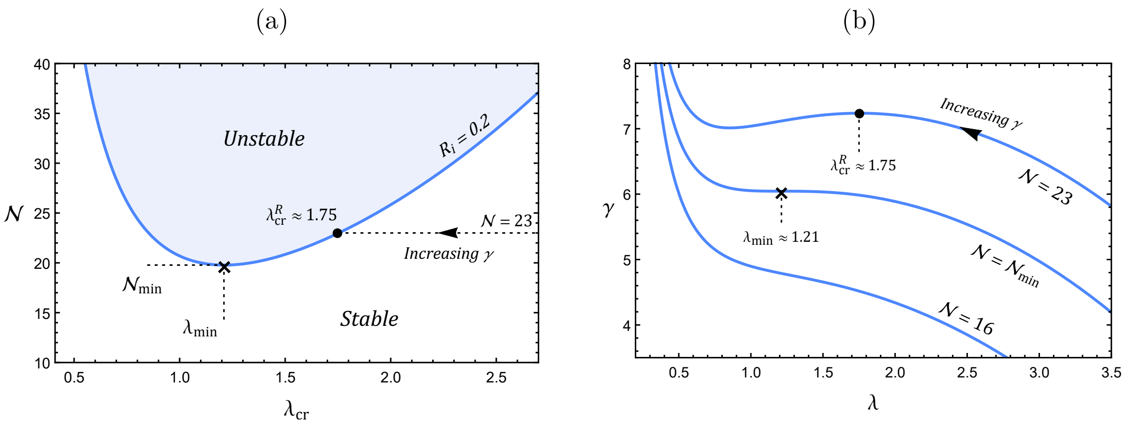

Figure 3.6: (a) The bifurcation condition (3.37) plotted in the $(\lambda_{\text{cr}}, \mathcal{N})$ plane for the Gent material model (2.63) with $J_\text{m} = 100$ and $R_\text{i} = 0.2$. The bifurcation curve has a minimum at $(\lambda_{\text{min}}, \mathcal{N}_{\text{min}}) \approx (1.21, 19.78)$ as marked by the black cross. Then, for each fixed $\mathcal{N} > \mathcal{N}_{\text{min}}$, the bifurcation point of interest is $\lambda_{\text{cr}}^R > \lambda_{\text{min}}$ since we increase γ from zero. (b) The variation of γ with respect to λ for $\mathcal{N} = 23, \mathcal{N}_{\text{min}}, 16$. We see that each bifurcation point λ_{cr}^R occurs at the local maximum of $\gamma = \gamma(\lambda)$.

We could also choose to apply a fixed axial stretch to the tube and then gradually increase the surface tension from zero. In this case, the bifurcation condition would remain as (3.36), except the λ_{cr} on the right-hand side is replaced by the fixed λ and the γ becomes γ_{cr}. As a consistency check, we may take the limit $R_\text{i} \to 0$ in the resulting bifurcation condition and compare with the corresponding condition for a *solid cylinder* given in Fu et al. (2021). In this limiting case, our bifurcation condition reduces to

$$\gamma_{\mathrm{cr}} = \frac{4}{\lambda^{5/2}} \left\{ 2(\lambda^3 - 1)^2 W_{dd} + \lambda(2 + \lambda^3) W_d \right\}, \tag{3.38}$$

and this is indeed the bifurcation condition for a solid cylinder given in equation (3.11) of Fu et al. (2021). Henann and Bertoldi (2014) also investigated localized pattern formation in this loading scenario when $\lambda = 1$ through FEM simulations, and this facilitates a further verification of our analytical results. It is noted that, for fixed $\lambda = 1$, our conjectured bifurcation condition is independent of J_{m} and reduces to

$$\gamma_{\mathrm{cr}} = \frac{2\,(3 + R_{\mathrm{i}}^2)}{1 - R_{\mathrm{i}}^2}. \tag{3.39}$$

In Fig. 3.7, we plot in the $(R_{\mathrm{i}}, \gamma_{\mathrm{cr}})$ plane our conjectured bifurcation condition (3.39) (solid blue curve) and the corresponding FEM simulation results in Fig. 4 (b) of Henann and Bertoldi (2014) (black squares). We observe that there is excellent agreement between the two sets of results.

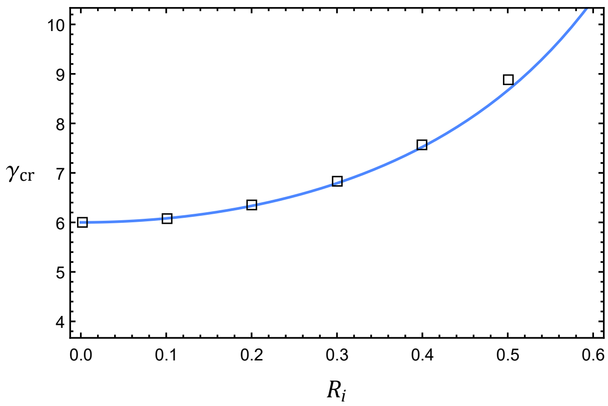

Figure 3.7: A comparison of our conjectured bifurcation condition (3.39) (blue curve) and the FEM simulations of Henann and Bertoldi (2014) (black squares) in the $(R_{\mathrm{i}}, \gamma_{\mathrm{cr}})$ plane when $\lambda = 1$ is fixed.

3.3.2.3 Case 3

In case 3, our conjectured bifurcation condition for localized pattern formation $d\mathcal{N}/d\lambda = 0$ when γ is fixed may be expressed as the following implicit relationship between λ_{cr} and γ:

$$\gamma = \frac{4 r_{\mathrm{i}}^3 \lambda^3}{(R_{\mathrm{o}}^2 - R_{\mathrm{i}}^2)^2} \int_{R_{\mathrm{i}}}^{R_{\mathrm{o}}} \frac{\partial}{\partial \lambda} \left(W_d I_{0\lambda}\right) R\, dR \bigg|_{\lambda = \lambda_{\mathrm{cr}}}, \tag{3.40}$$

where r_i is given by (3.22). For a wide range of parameter values, the bifurcation curve in the $(\lambda_\mathrm{cr}, \gamma)$ plane has a single minimum point as in case 2; see Fig. 3.8. However, when reducing to the neo-Hookean model (i.e. when taking the limit

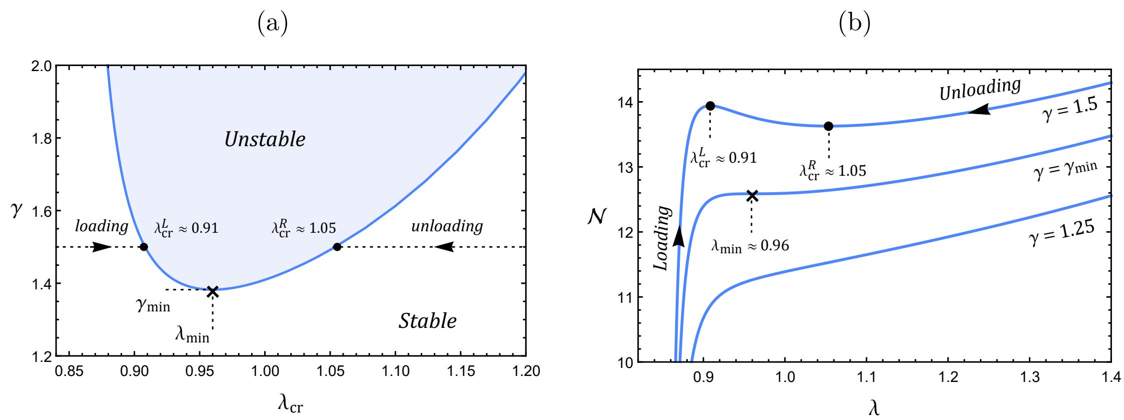

Figure 3.8: (a) The bifurcation condition (3.40) plotted in the $(\lambda_\mathrm{cr}, \gamma)$ plane for the Gent material model (2.63) with $J_\mathrm{m} = 100$ and $R_\mathrm{i} = 0.4$. The bifurcation curve has a minimum at $(\lambda_\mathrm{min}, \gamma_\mathrm{min}) \approx (0.96, 1.38)$ as marked by the black cross. Then, for each fixed $\gamma > \gamma_\mathrm{min}$, there exists a bifurcation point either side of $\lambda = \lambda_\mathrm{min}$. (b) The variation of $\mathcal{N}$ with respect to λ for $\gamma = 1.5, \gamma_\mathrm{min}, 1.25$.

$J_\mathrm{m} \to \infty$), there exists a threshold value $R_\mathrm{i} \approx 0.08567$ below which two *additional* local extrema (i.e. a maximum and a minimum) of γ with respect to λ_cr emerge. In the limit $R_\mathrm{i} \to 0.08567$, these two additional extrema of γ coalesce to form an inflection point; see Fig. 3.9.

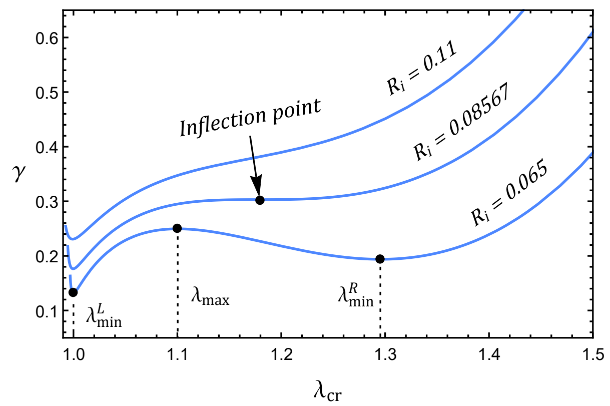

Figure 3.9: Plots of γ against λ_cr when the neo-Hookean model (2.58) is employed with $R_\mathrm{i} = 0.065, 0.08567, 0.11$. On the curve corresponding to $R_\mathrm{i} = 0.065$, the black dots mark the two additional local extrema of γ with respect to λ which emerge in the large thickness regime. In the limit $R_\mathrm{i} \to 0.08567^-$, these two extrema coalesce to form an inflection point (as shown by the arrow), and above this threshold, γ has a single minimum value.

When $\mathcal{N} \geq 0$ is fixed and γ is increased gradually from zero, the conjectured bifurcation condition for localized pattern formation $d\gamma/d\lambda = 0$ takes the form:

$$\frac{\mathcal{N}}{2\pi} = \left[\int_{R_\mathrm{i}}^{R_\mathrm{o}} W_d I_{0\lambda} R\, dR + \frac{2\,(r_\mathrm{o}\lambda)^2 (r_\mathrm{o} + R_\mathrm{i})}{(R_\mathrm{i} - r_\mathrm{o})(R_\mathrm{i}^2 - 1)} \int_{R_\mathrm{i}}^{R_\mathrm{o}} \frac{\partial}{\partial \lambda} \left(W_d I_{0\lambda}\right) R\, dR \right] \Bigg|_{\lambda=\lambda_\mathrm{cr}}. \tag{3.41}$$

As in case 2, the bifurcation condition for fixed λ and increasing γ can be obtained from (3.40) by replacing γ with γ_cr and λ_cr with the fixed λ. This boundary condition case has also been investigated through FEM simulations by Henann and Bertoldi (2014) for $\lambda = 1$. In this special case, our conjectured bifurcation condition is independent of J_m when specifying to the Gent material model and takes the form

$$\frac{\gamma_\mathrm{cr}}{R_\mathrm{i}} = \frac{2(1 - R_\mathrm{i}^2)(3R_\mathrm{i}^2 + R_\mathrm{o}^4)}{(R_\mathrm{i} - R_\mathrm{o})^2 (R_\mathrm{i} + R_\mathrm{o})^2}. \tag{3.42}$$

In order to validate this analytical result, we plot (3.42) in Fig. 3.10 along with the FEM simulation results presented in Fig. 4 (c) of Henann and Bertoldi (2014). We observe that there is exceptional agreement between the two sets of results. We note also that, in the limit $R_\mathrm{i} \to 0$, we recover the bifurcation condition $\gamma_\mathrm{cr}/R_\mathrm{i} = 2$ for a cylindrical cavity in an infinite solid first reported by Xuan and Biggins (2016).

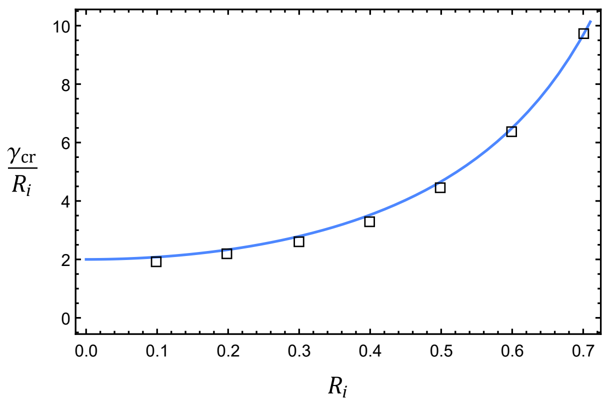

Figure 3.10: A comparison of our conjectured bifurcation condition for localized pattern formation (3.42) (blue curve) and the FEM simulations of Henann and Bertoldi (2014) (black squares) in the $(R_\mathrm{i}, \gamma_\mathrm{cr}/R_\mathrm{i})$ plane when $\lambda = 1$ is fixed.

3.4 Linear bifurcation analysis

A common starting point in the bifurcation analysis of elastic materials undergoing large deformations is to consider a solution to the linearized equilibrium equations and boundary conditions of the *normal mode* type. In the present context, the term *normal mode solution* refers to a perturbation of the primary deformation solution which is proportional to $e^{\mathrm{i}kz}$, where k is the *axial wavenumber.* The resulting linear eigenvalue problem can then be solved to obtain the bifurcation condition. This condition may be analytical or numerical depending on the complexity of the linearized system, and it relates the control parameter to the axial wavenumber. The way in which we interpret this relationship will be discussed shortly after we formulate the linear analysis.

To begin, consider a pertubation $\phi_1 = \phi_1(R, z)$ of the primary solution given by (3.23). On substituting the perturbed solution $\phi = \phi_0 + \phi_1$ into the equilibrium equation (3.12) and linearizing in terms of ϕ_1, we obtain

$$\begin{aligned}&\frac{\partial^4\phi_1}{\partial R^4} + a_1(R)\frac{\partial^3\phi_1}{\partial R^3} + a_2(R)\frac{\partial^2\phi_1}{\partial R^2} + a_3(R)\frac{\partial\phi_1}{\partial R} + a_4(R)\frac{\partial^4\phi_1}{\partial z^4} + a_5(R)\frac{\partial^2\phi_1}{\partial z^2}\\ &+ a_6(R)\frac{\partial^3\phi_1}{\partial R\partial z^2} + a_7(R)\frac{\partial^4\phi_1}{\partial R^2\partial z^2} = 0, \end{aligned} \tag{3.43}$$

with the variable coefficients $a_i = a_i(R)$ $(i = 1, 2, \ldots, 7)$ given in Appendix 3.B. When specifying to the neo-Hookean model (2.58), the expressions for the coefficients in (3.43) differ from those in equation (26) of Wang (2020). Agreement can only be achieved if we make the generally invalid substitution $r_i \to R_\mathrm{i}/\sqrt{\lambda}$. The only scenario where this substitution is valid is when the primary deformation is homogeneous. This may only be achieved when the outer radius tends to infinity or when $\lambda = 1$ in cases 2 and 3, and as a consequence incompressibility forces $r_0 = R/\sqrt{\lambda}$.

To further validate our governing equation (3.43), we make the substitution $\phi_1 = rf(r)e^{\mathrm{i}kz}$ and obtain a fourth-order differential equation for $f(r)$. We have verified that this equation is identical to equation (53) of Haughton and Ogden (1979b).

We look for a *normal mode solution* of the form

$$\phi_1 = \varepsilon g(R)e^{\mathrm{i}kz}, \tag{3.44}$$

where $k \geq 0$ is the axial wavenumber, ε is a small parameter and i is the imaginary unit. On substituting (3.44) into (3.43), we obtain a fourth-order ordinary differential equation (ODE) for g, which may be re-written as the following system of first order ODEs;

$$\frac{d\boldsymbol{g}}{dR} = A(R, \lambda, k)\,\boldsymbol{g}, \qquad A = \begin{bmatrix} 0 & 1 & 0 & 0 \\ 0 & 0 & 1 & 0 \\ 0 & 0 & 0 & 1 \\ A_{41} & A_{42} & A_{43} & A_{44} \end{bmatrix}, \tag{3.45}$$

where $\boldsymbol{g} = [\,g,\, g',\, g'',\, g'''\,]^T$ and the variable components of A are given as follows:

$$A_{41} = k^2(a_5 - k^2 a_4), \qquad A_{42} = k^2 a_6 - a_3,$$
$$A_{43} = k^2 a_7 - a_2, \qquad A_{44} = -a_1. \tag{3.46}$$

On substituting $\phi = \phi_0 + \phi_1$ and (3.44) into (3.16), (3.17) and (3.18) and then linearizing in terms of g, we find that the surface tension and zero shear traction boundary conditions on $R = R_\mathrm{i}$ and $R = R_\mathrm{o}$ in *case 1* may be expressed as the following matrix equations:

$$\begin{aligned} B_\mathrm{i}(R_\mathrm{i}, \lambda, \gamma, k)\,\boldsymbol{g} = \boldsymbol{0}, \\ B_\mathrm{o}(R_\mathrm{o}, \lambda, \gamma, k)\,\boldsymbol{g} = \boldsymbol{0}, \end{aligned} \quad \text{where} \quad \begin{cases} B_\mathrm{i} = \begin{bmatrix} b_{11} & -1/R & 1 & 0 \\ b_{21}^{+} & b_{22} & b_{23} & 1 \end{bmatrix}, \\ \\ B_\mathrm{o} = \begin{bmatrix} b_{11} & -1/R & 1 & 0 \\ b_{21}^{-} & b_{22} & b_{23} & 1 \end{bmatrix}, \end{cases} \tag{3.47}$$

and the expressions for the components of B_i and B_o are likewise given in Appendix 3.B. For *cases 2* and *3*, both (3.7) and (4.16) imply that we must impose the respective zero radial displacement constraints $g(R_\mathrm{i}) = 0$ and $g(R_\mathrm{o}) = 0$ in place of the corresponding surface tension boundary condition. In these cases, the boundary conditions may still be expressed in the form $(3.47)_1$, but the matrices B_i or B_o must be modified accordingly. For instance, in *case 2*, B_o remains unchanged from (3.47) but B_i must take the form

$$B_\mathrm{i} = \begin{bmatrix} b_{11} & -1/R & 1 & 0 \\ 1 & 0 & 0 & 0 \end{bmatrix}. \tag{3.48}$$

In *case 3*, B_i remains unchanged from (3.47), but B_o must take the form

$$B_\mathrm{o} = \begin{bmatrix} b_{11} & -1/R & 1 & 0 \\ 1 & 0 & 0 & 0 \end{bmatrix}. \tag{3.49}$$

To analyze the two-point boundary value problem (3.45) – (3.47), we employ the *determinant method* described in section 2.6.1. For the sake of brevity, we outline the solution procedure for *case 1*, but note that the approach is identical in cases 2 and 3 when the previously mentioned modifications are enforced. We begin by noting that the linear system $B_\mathrm{i}(R_\mathrm{i}, \lambda, \gamma, k)\boldsymbol{g} = \boldsymbol{0}$ has two independent solutions, say $\boldsymbol{g}_\mathrm{i}^{(1)}$ and $\boldsymbol{g}_\mathrm{i}^{(2)}$. For instance, in case 1 we have

$$\boldsymbol{g}_\mathrm{i}^{(1)} = \Big[\,1,\,0,\,-b_{11},\,b_{11}b_{23} - b_{21}^{+}\,\Big]^T_{R\,=\,R_\mathrm{i}},$$

and
$$\boldsymbol{g}_\mathrm{i}^{(2)} = \Big[\,0,\,1,\,1/R,\,-b_{23}/R - b_{22}\,\Big]^T_{R\,=\,R_\mathrm{i}}. \tag{3.50}$$

We may then integrate (3.45) from $R = R_\mathrm{i}$ towards $R = R_\mathrm{o}$, using (3.50) or equivalent as initial data for $\boldsymbol{g}$ at $R = R_\mathrm{i}$. Two linearly independent solutions for $\boldsymbol{g}$, say $\boldsymbol{g}^{(1)}$ and $\boldsymbol{g}^{(2)}$, are consequently obtained, and a general solution for $\boldsymbol{g}$ therefore takes the form

$$\boldsymbol{g} = c_1\,\boldsymbol{g}^{(1)} + c_2\,\boldsymbol{g}^{(2)} = M(R, \lambda, \gamma, k)\,\boldsymbol{c}, \tag{3.51}$$

where $\boldsymbol{c} = [\,c_1,\,c_2\,]^T$ is an arbitrary constant vector and $M = [\boldsymbol{g}^{(1)},\,\boldsymbol{g}^{(2)}]$. By its construction, (3.51) satisfies the boundary conditions on $R = R_\mathrm{i}$, and it remains only to satisfy the corresponding conditions on $R = R_\mathrm{o}$. On substituting (3.51) into $B_\mathrm{o}(R_\mathrm{o}, \lambda, \gamma, k)\boldsymbol{g} = \boldsymbol{0}$, we obtain $B_\mathrm{o}\,M(R_\mathrm{o}, \lambda, \gamma, k)\,\boldsymbol{c} = \boldsymbol{0}$. Then, since $\boldsymbol{c}$ is arbitrary, the existence of a non-trivial solution to the eigenvalue problem is conditional on satisfying

$$\det\, B_\mathrm{o}\,M(R_\mathrm{o}, \lambda, \gamma, k) = 0. \tag{3.52}$$

Equation (3.52) represents a numerical bifurcation condition which must be satisfied by the control parameter (which we may take as either the resultant axial force $\mathcal{N}$ or the surface tension γ) and k. For any fixed $k \geq 0$, the bifurcation points can be obtained by iterating on the control parameter until (3.52) is satisfied.

As previously stated, the primary aim is to determine the relationship between the control parameter and k numerically through (3.52). Then, as we vary the control parameter in the desired manner, we seek the values of both the control parameter and k first encountered on the corresponding bifurcation curve. For instance, say we apply a fixed axial stretch λ and monotonically increase γ from zero. Then, on plotting the bifurcation condition (3.52) in the (k, γ) plane, we would encounter the minimum of the associated bifurcation curve first, and so this is the bifurcation point of interest. The values of γ and k at this minimum are defined as the critical surface tension γ_{cr} and axial wave number k_{cr}. Say that k_{cr} is strictly positive. Then, we expect that beyond the critical load the tube may in theory develop a periodic axi-symmetric pattern with wavelength $1/k_{\mathrm{cr}}$ in the axial direction. This result is, however, invalid if $k_{\mathrm{cr}} = 0$ since the wavelength of the emerging pattern would be infinite. The question then is what non-trivial solution, if any, emerges when $k_{\mathrm{cr}} = 0$? Whilst there is strong evidence to suggest that it is a localized inhomogeneous bifurcation solution that emerges in this scenario, we shall refer to the solution associated with $k_{\mathrm{cr}} = 0$ as the *zero wavenumber bifurcation solution* until this has been explicitly established.

3.4.1 Case 1 results

For the sake of simplicity, we adopt the neo-Hookean material model (2.58) for case 1. From the bifurcation condition (3.52), we analyse in Fig. 3.11 the variation of the control parameter with respect to k for three separate loading scenarios, with $R_{\mathrm{i}} = 0.4$ taken as a representative example. In (a), we apply a fixed axial stretch $\lambda = 2.25$ and gradually increase γ from zero. In (b), we fix $\gamma = 8$ and $\mathcal{N} = 20.5$ initially, and then gradually decrease the axial force from this point. In (c), we fix $\mathcal{N} = 22$ and then gradually increase γ from zero. In all three scenarios, we observe that the critical axial wave number is $k_{\mathrm{cr}} = 0$, and we have verified that this is true generally outside of the representative examples considered. Therefore, a zero wavenumber bifurcation solution is determined to be widely favoured over periodic axi-symmetric modes in case 1.

Given the results in Fig. 3.11, we then analyze the bifurcation condition (3.52) in the limit $k \to 0$ for the same three loading scenarios. In doing so, we can determine the dependence of the critical value of the control parameter on various parameters.

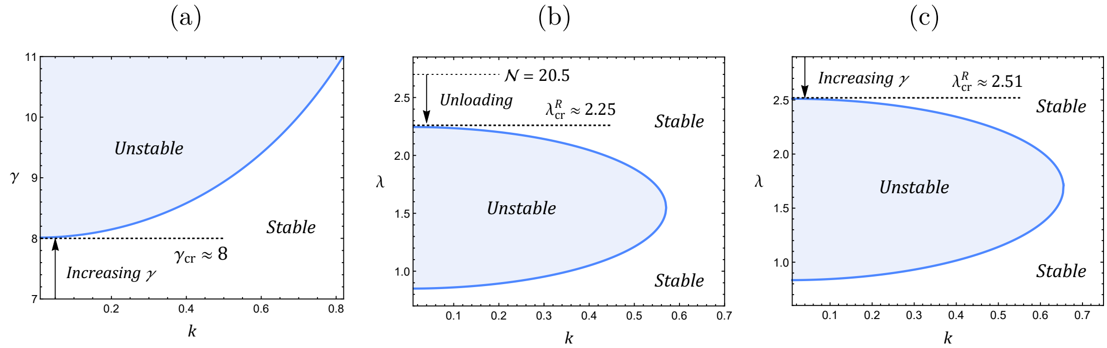

Figure 3.11: Analysis of the bifurcation condition (3.52) with the neo-Hookean model (2.58) employed and $R_\mathrm{i} = 0.4$. The plots show the condition (3.52) in (a) the (k, γ) plane with $\lambda = 2.25$ fixed, (b) the (k, λ) plane with $\gamma = 8$ fixed and (c) the (k, λ) plane with $\mathcal{N} = 22$ fixed.

We begin with the fixed λ and increasing γ approach. In Fig. 3.12 (a) and (b), we plot γ_cr against λ for several values of R_i, and γ_cr against R_i for several fixed $\lambda \geq 1$, respectively. We observe in (a) that, below the threshold value $\lambda \approx 2.25$, a larger inner radius R_i will delay the zero wavenumber bifurcation solution. Above this threshold value for λ, the relationship between γ_cr and R_i is seen in (b) to become non-monotonic. To provide further insights, consider the case where $\lambda = 2.4$ is fixed. We see in (b) that the associated bifurcation curve has a minimum value at $(R_\mathrm{i}, \gamma_\mathrm{cr}) \approx (0.863, 8.03)$. Thus, the tube with inner radius $R_\mathrm{i} \approx 0.863$ will be the most susceptible to the zero wavenumber bifurcation solution in this scenario. In (a), we also plot our conjectured bifurcation condition for localized pattern formation in the $(\lambda, \gamma_\mathrm{cr})$ plane for $R_\mathrm{i} = 0.2$ (black squares), and we observe that there is perfect agreement with the numerical results from the linear analysis.

We next apply a fixed surface tension γ with $\mathcal{N} > 0$ initially, and then perform a force controlled unloading by decreasing $\mathcal{N}$ monotonically from the resulting starting point. In Fig. 3.13, we plot the critical axial force $\mathcal{N}_\mathrm{cr}$ against R_i for several fixed values of γ. We observe that a smaller fixed γ delays the onset of the zero wavenumber bifurcation solution. Also, $\mathcal{N}_\mathrm{cr}$ is a decreasing function of R_i for all fixed γ considered. Thus, a larger initial inner radius will delay the zero wavenumber solution.

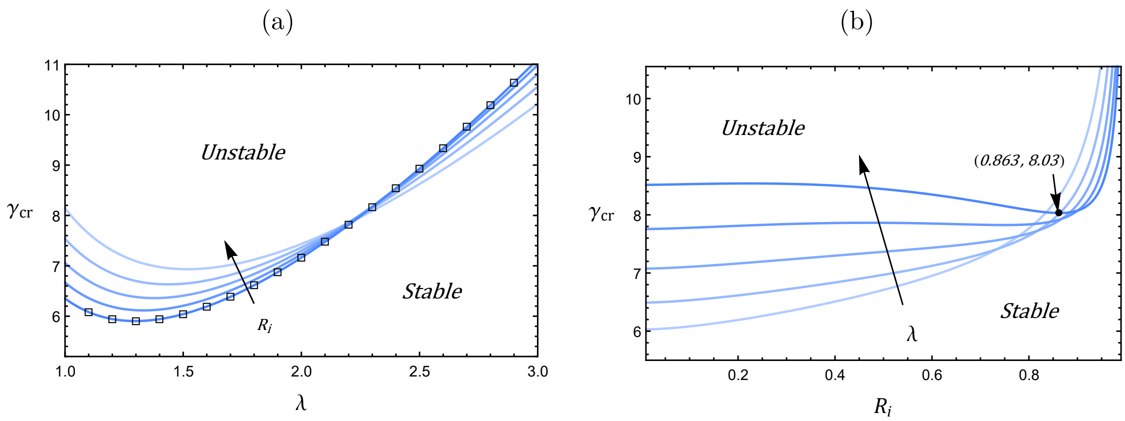

Figure 3.12: Plots of the bifurcation condition (3.52) in the limit $k \to 0$ for the neo-Hookean material model (2.58) when $\lambda \geq 1$ is fixed and γ is increased gradually from zero. (a) The variation of γ_{cr} with respect to λ with R_{i} increasing from 0.2 to 0.6 in increments of 0.1. The black squares are from our conjectured condition (3.35) corresponding to $R_{\mathrm{i}} = 0.2$. (b) The variation of γ_{cr} with respect to R_{i} with λ increasing from 1.6 to 2.4 in increments of 0.2. The arrows indicate the direction of parameter growth.

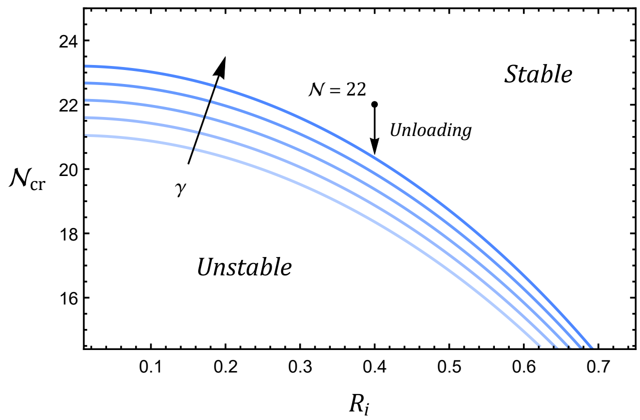

Figure 3.13: A plot of the bifurcation condition (3.52) in the limit $k \to 0$ for the neo-Hookean material model (2.58) when γ is fixed with $\mathcal{N} > 0$ initially, and a *force controlled unloading* is applied. We show the variation of $\mathcal{N}_{\mathrm{cr}}$ with respect to R_{i} with γ increasing from 7 to 8 in increments of 0.25. The arrow indicate the direction of parameter growth. In (a), the black squares represent our conjectured condition for localized pattern formation when $R_{\mathrm{i}} = 0.2$.

Thirdly, we choose to apply a fixed axial force $\mathcal{N} > 0$ initially after which we increase the surface tension monotonically from zero. In Fig. 3.14 (a) and (b), we plot the critical surface tension γ_{cr} against R_{i} and $\mathcal{N}$, respectively. We observe generally that tubes subjected to a smaller fixed axial force, or tubes with a smaller initial inner radius, will be more susceptible to the zero wavenumber solution.

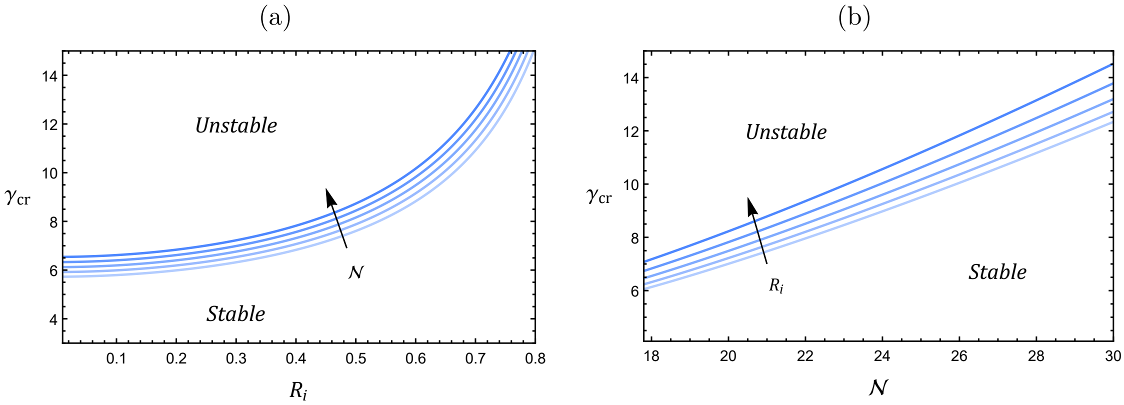

Figure 3.14: Plots of the bifurcation condition (3.52) in the limit $k \to 0$ for the neo-Hookean material model (2.58) when $\mathcal{N} \geq 0$ is fixed and γ is increased gradually from zero. (a) The variation of $\gamma_{\rm cr}$ with respect to $R_{\rm i}$ with $\mathcal{N}$ increasing from 18 to 20 in increments of 0.5 and (b) the variation of $\gamma_{\rm cr}$ with respect to $\mathcal{N}$ with $R_{\rm i}$ increasing from 0.25 to 0.45 in increments of 0.05. The arrows indicate the direction of parameter growth.

3.4.2 Case 2 results

In case 2 we adopt the Gent material model (2.63). As in the case 1, we begin by plotting in Fig. 3.15 the relationship between the control parameter and the axial wavenumber k obtained from the bifurcation condition (3.52). We do this for the three loading scenarios that we have already established, but note that when γ is fixed we may also now consider the case where $\mathcal{N} = 0$ initially and a "loading" is applied. For the representative example of $R_{\rm i} = 0.4$ and $J_{\rm m} = 100$ in Fig. 3.15, we see that $k_{\rm cr} = 0$ in all three loading scenarios, and we have verified that this is generally the case.

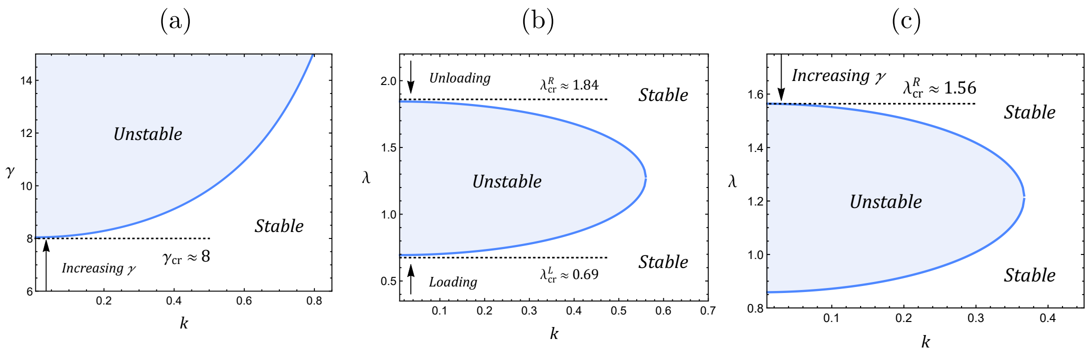

Figure 3.15: Analysis of the bifurcation condition (3.52) with the Gent material model (2.63) employed, and $R_{\rm i} = 0.4$ and $J_{\rm m} = 100$. The plots show the condition (3.52) in (a) the (k, γ) plane with $\lambda = 1.5$ fixed, (b) the (k, λ) plane with $\gamma = 10$ fixed and (c) the (k, λ) plane with $\mathcal{N} = 30$ fixed.

Given this, we then analyze the variation of the critical control parameter values corresponding to $k_{\mathrm{cr}} = 0$ with respect to several different parameters. Where λ is fixed and γ is increased from zero, we observe in Fig. 3.16 that a larger extensibility limit J_{m} or a smaller inner radius R_{i} will see the zero wavenumber bifurcation solution emerge earlier in the loading process. Also, curves in the $(\lambda, \gamma_{\mathrm{cr}})$ plane have a minimum value; see (a). Thus, a larger fixed stretch above the minimum value of λ (or a smaller fixed stretch below the minimum value of λ) will result in the onset of the zero wavenumber solution being delayed. In each plot we also present a set of points from our conjectured bifurcation condition for localized pattern formation in the form of black squares. We observe that our conjectured condition for localized pattern formation clearly coincides with the condition that a bifurcation solution with zero wavenumber emerges.

In Fig. 3.18 we fix γ and vary $\mathcal{N}$, and plot the bifurcation points corresponding to $k_{\mathrm{cr}} = 0$ and $J_{\mathrm{m}} = 50$ on the curve $\mathcal{N} = \mathcal{N}(\lambda)$ given by (3.28) for different values of R_{i} and γ. We observe that the bifurcation points are always situated at the local maxima and minima of $\mathcal{N}$, demonstrating that our conjectured condition $d\mathcal{N}/d\lambda = 0$ for localized pattern formation in this loading scenario corresponds to the condition that a zero wavenumber bifurcation solution initiates. In (b), we see that for larger values of R_{i}, the pairs of bifurcation points are closer together. At $R_{\mathrm{i}} = 0.463$, the two points meet at an inflection point on the loading curve, and above this value bifurcation points cease to exist. Thus, for a given fixed value of γ, the zero wavenumber solution becomes impossible in tubes below a certain level of thickness. When applying a force controlled "loading" from $\mathcal{N} = 0$, *larger* values of R_{i} and γ will delay the onset of the zero wavenumber solution since they produce larger bifurcation values of $\mathcal{N}$. In contrast, when applying a force controlled "unloading", *smaller* values of R_{i} and γ will delay the onset of the zero wavenumber solution.

Finally, for the fixed $\mathcal{N}$ and increasing γ scenario, we plot in Fig. 3.18 bifurcation points corresponding to $k_{\mathrm{cr}} = 0$ on the curve $\gamma = \gamma(\lambda)$ given by (3.29) for different values of R_{i} and $\mathcal{N}$. Again, we observe that the bifurcation points are always situated at the local maxima of $\gamma = \gamma(\lambda)$, demonstrating a correspondence between

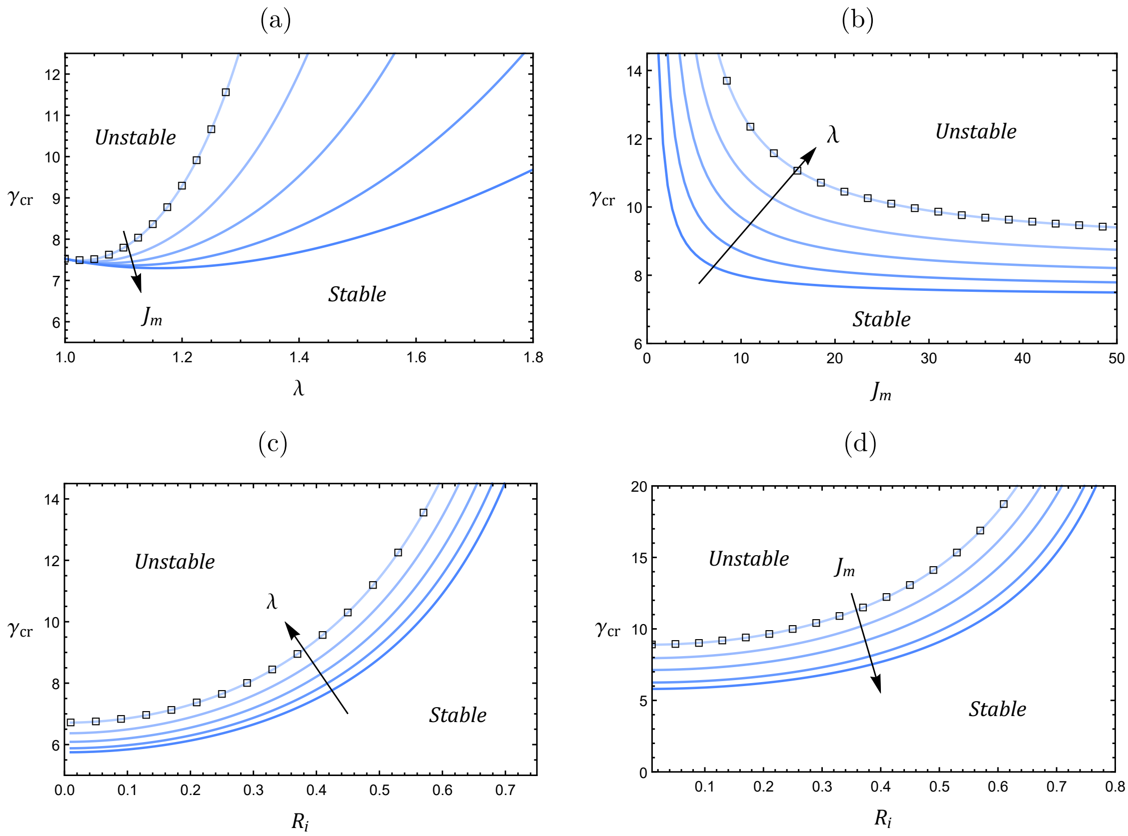

Figure 3.16: Plots of the bifurcation condition (3.52) in the limit $k \to 0$ for the Gent material model (2.63) where λ is fixed and γ is gradually increased from zero. We have γ_{cr} against (a) λ with $R_{\mathrm{i}} = 0.4$ and $J_{\mathrm{m}} = 1.5, 3, 6, 15, 100$, (b) J_{m} with $R_{\mathrm{i}} = 0.4$ and $\lambda = 1.3, 1.4, 1.5, 1.6, 1.7$, (c) R_{i} with J_{m} and $\lambda = 1.3, 1.4, 1.5, 1.6, 1.7$, and (d) R_{i} with $\lambda = 1.4$ and $J_{\mathrm{m}} = 3, 4, 6, 15, 100$. Arrows indicate the direction of parameter growth, and the black squares give the associated bifurcation points from our conjectured condition.

the bifurcation condition corresponding to $k_{\mathrm{cr}} = 0$ and our conjectured condition $d\gamma/d\lambda = 0$ for localized pattern formation. We observe also that for smaller values of R_{i} or larger values of fixed $\mathcal{N}$, a greater amount of surface tension is required to trigger the zero wavenumber bifurcation solution.

3.4.3 Case 3 results

In case 3, the critical wave number is predominantly $k_{\mathrm{cr}} = 0$; see Fig. 3.19. However, there are certain circumstances where the value of k_{cr} is strictly positive. To elaborate, it was shown in Liu (2018) that a tube under a sufficient axial *compression* in case 3 can admit periodic wrinkling modes in the axial direction. This can also be the case when surface tension effects are taken into account.

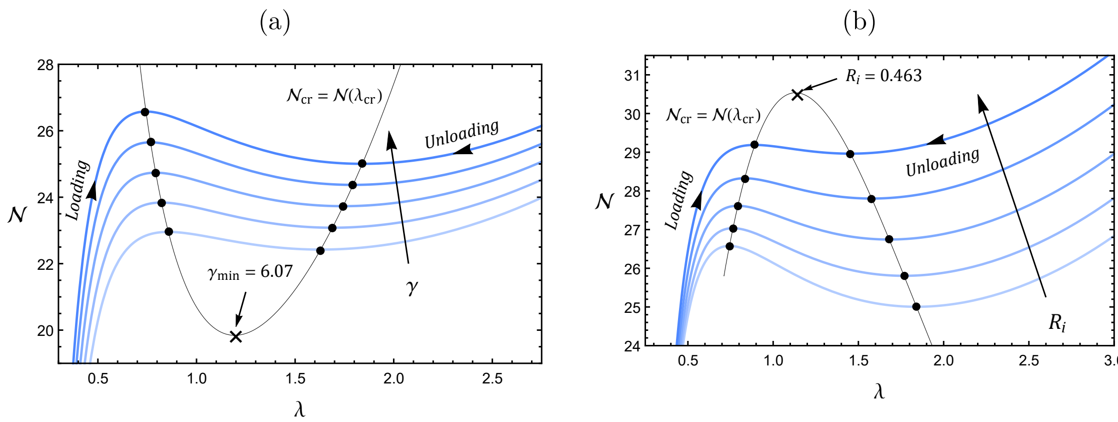

Figure 3.17: Plots of bifurcation points $(\lambda_{cr}, \mathcal{N}_{cr})$ corresponding to $k_{cr} = 0$ (black curves), and the load curves $\mathcal{N} = \mathcal{N}(\lambda)$ given by (3.28) (blue curves). We set $J_m = 50$ with (a) $\gamma = 8$ and various values of R_i, and (b) $R_i = 0.2$ and various fixed values of γ. The blue load curves in (a) and (b) correspond to $R_i = 0.2, 0.25, 0.3, 0.35, 0.4$ and $\gamma = 7, 7.25, 7.5, 7.75, 8$, respectively, and the black dots mark their intersections with the black bifurcation curve. Arrows indicate the direction of parameter growth.

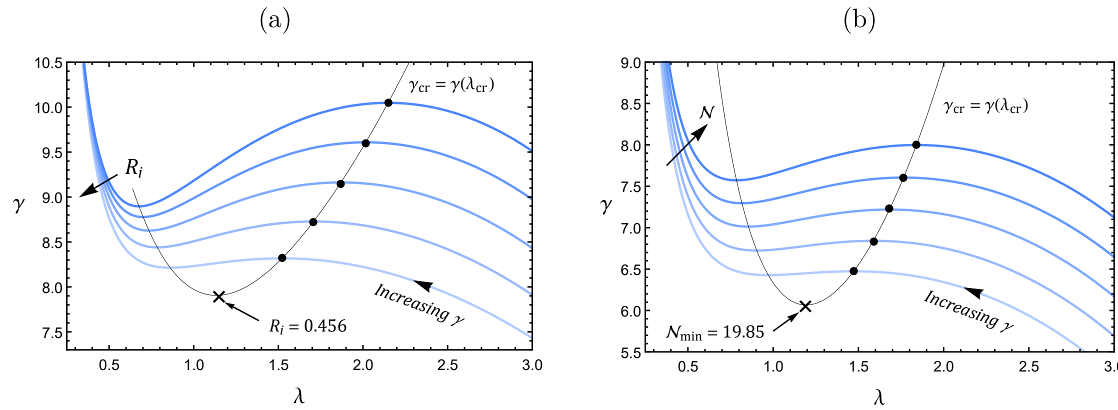

Figure 3.18: Plots of bifurcation points $(\lambda_{cr}, \gamma_{cr})$ corresponding to $k_{cr} = 0$ (black curves), and the load curves $\gamma = \gamma(\lambda)$ given by (3.28) (blue curves). We set $J_m = 50$ with (a) $\mathcal{N} = 30$ and various values of R_i, and (b) $R_i = 0.2$ and various fixed values of $\mathcal{N}$. The blue load curves in (a) and (b) correspond to $R_i = 0.2, 0.25, 0.3, 0.35, 0.4$ and $\mathcal{N} = 21, 22, 23, 24, 25$, respectively, and the black dots mark their intersections with the black bifurcation curve. Arrows indicate the direction of parameter growth.

For instance, if the axial stretch λ is fixed sufficiently below 1, then it will be a periodic wrinkling solution which is preferred over a zero wavenumber solution when increasing γ gradually. As an illustrative example, say we apply a fixed stretch $\lambda = 0.865$ to a tube with $R_i = 0.4$ and $J_m = 50$. Then, the linear analysis predicts that a bifurcation into a periodic wrinkling solution with $k_{cr} = 2.45$ will occur once the surface tension is increased to $\gamma_{cr} = 1.52$; see Fig. 3.20 (a). In contrast, a zero wavenumber solution only becomes possible beyond $\gamma = 1.7$. Alternatively, we have established that when fixing γ with $\mathcal{N} = 0$ initially, and axial stretch $\lambda < 1$ will be produced. We find that, provided the fixed value of γ is large enough, the critical wave number k_{cr} will be strictly positive when increasing $\mathcal{N}$ from zero (i.e. when "loading"). For instance say we apply a fixed surface tension $\gamma = 1.49$ to a tube with $R_{\mathrm{i}} = 0.4$ and $J_{\mathrm{m}} = 50$, and that $\mathcal{N}$ is initially zero. Then, an axial stretch $\lambda \approx 0.85$ is induced, and the linear analysis predicts that a periodic wrinkling solution with $k_{\mathrm{cr}} = 0.97$ emerges once λ is increased to approximately 0.8856; see Fig. 3.20 (b). A zero wavenumber solution, however, does not become possible until λ reaches approximately 0.8865.

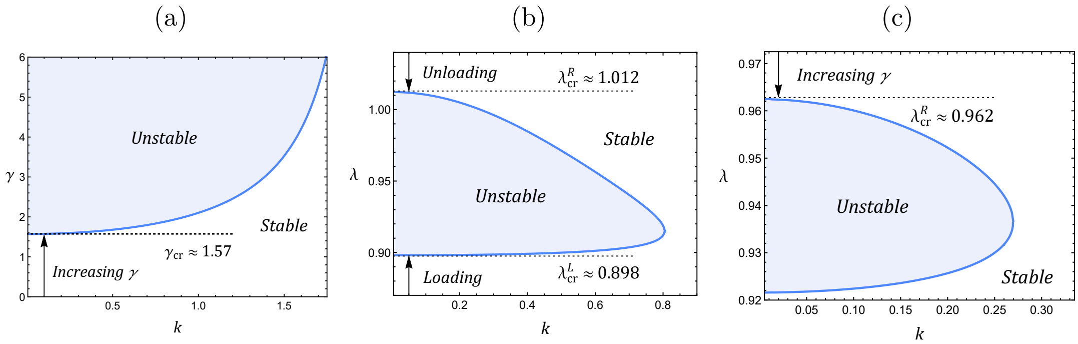

Figure 3.19: Analysis of the bifurcation condition (3.52) with the Gent material model (2.63) employed, and $R_{\mathrm{i}} = 0.4$ and $J_{\mathrm{m}} = 50$. The plots show the condition (3.52) in (a) the (k, γ) plane with $\lambda = 1.1$ fixed, (b) the (k, λ) plane with $\gamma = 1.425$ fixed and (c) the (k, λ) plane with $\mathcal{N} = 12.5$ fixed.

In Fig. 3.21, we plot the bifurcation condition (3.52) in the limit $k \to 0$ for the fixed λ and increasing γ loading scenario. We observe that, as in case 2, a larger extensibility limit J_{m} will reduce the amount of surface tension required to trigger the zero wavenumber bifurcation solution. However, unlike in case 2, γ_{cr} is a non monotonic function of R_{i}. For each value of λ and J_{m}, γ_{cr} as a function of R_{i} has a minimum value, and for a tube of very high thickness, the zero wavenumber becomes unattainable.

In Fig. 3.22, for the fixed γ and varying $\mathcal{N}$ scenario, we plot the bifurcation points predicted by the linear analysis on the curve $\mathcal{N} = \mathcal{N}(\lambda)$ given by (3.30) for several fixed values of R_{i} and γ. We see that the bifurcation points predicted by

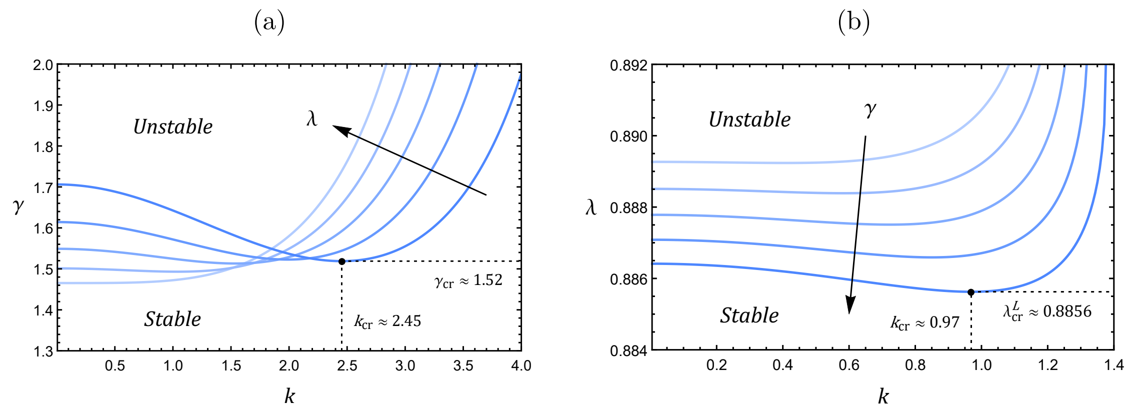

Figure 3.20: The bifurcation condition (3.52) for $R_\mathrm{i} = 0.4$ and $J_\mathrm{m} = 100$ in (a) the (k, γ) plane with the fixed λ ranging from 0.865 to 0.89 in intervals of 0.005, and (b) the (k, λ) plane with the fixed γ ranging from 1.47 to 1.49 in increments of 0.005. Arrows indicate the direction of parameter growth.

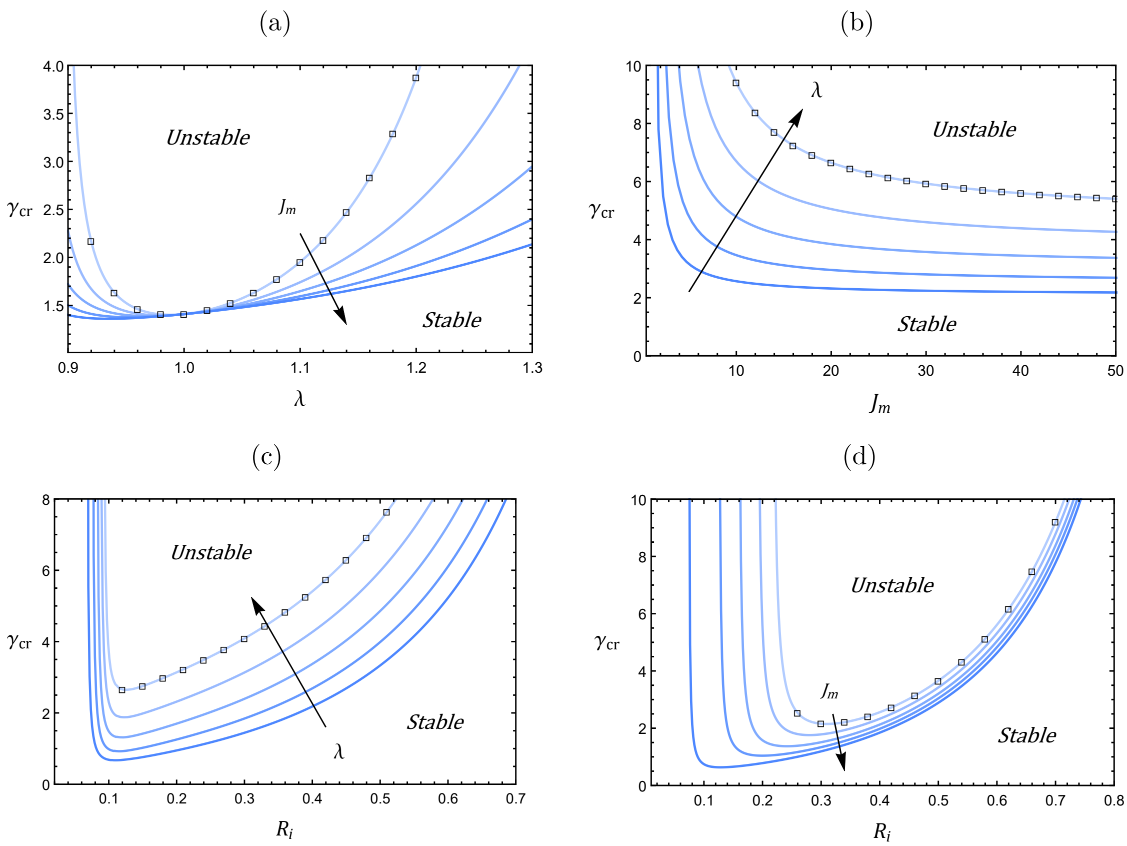

Figure 3.21: Plots of the bifurcation condition (3.52) in the limit $k \to 0$ for the Gent material model (2.63) where $\lambda > 1 - R_\mathrm{i}^2$ is fixed and γ is gradually increased from zero. We have γ_{cr} against (a) λ with $R_\mathrm{i} = 0.4$ and $J_\mathrm{m} = 1.5, 3, 6, 15, 100$, (b) J_m with $R_\mathrm{i} = 0.4$ and $\lambda = 1.3, 1.4, 1.5, 1.6, 1.7$, (c) R_i with J_m and $\lambda = 1.3, 1.4, 1.5, 1.6, 1.7$, and (d) R_i with $\lambda = 1.4$ and $J_\mathrm{m} = 3, 4, 6, 15, 100$. Arrows indicate the direction of parameter growth, and the black squares give the associated bifurcation points from our conjectured condition.

the linear analysis (black dots) are generally situated at the local extrema of the $\mathcal{N} = \mathcal{N}(\lambda)$ curves. When "loading" ("unloading"), we show in (a) that a smaller $R_{\rm i}$ will delay (encourage) the onset of the zero wavenumber bifurcation solution. This is in contrast to the corresponding results in case 2, and so the effect of the tube's radial thickness on the bifurcation point in this loading scenario is greatly influenced by the choice of boundary conditions.

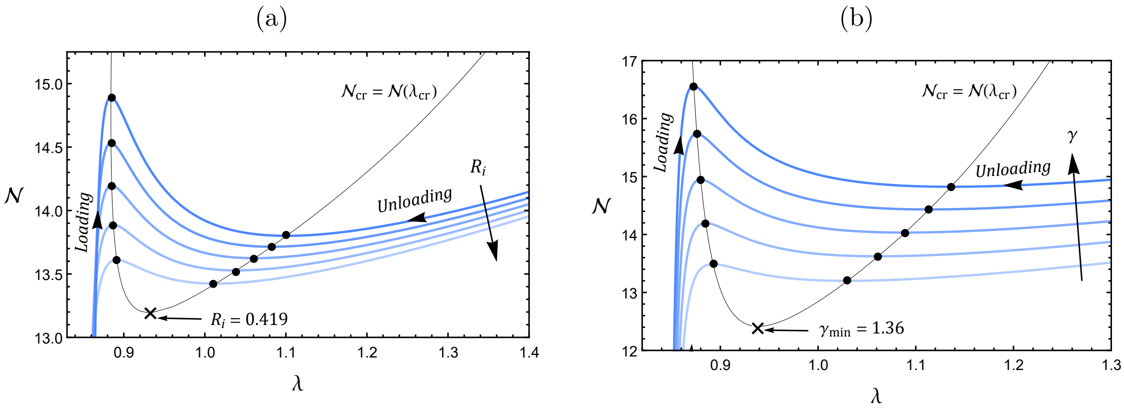

Figure 3.22: Plots of bifurcation points $(\lambda_{\rm cr}, \mathcal{N}_{\rm cr})$ corresponding to $k_{\rm cr} = 0$ (black curves) and the loading curves $\mathcal{N} = \mathcal{N}(\lambda)$ (blue) given by (3.30). We set $J_{\rm m} = 50$ with (a) $\gamma = 1.5$ and (b) $R_{\rm i} = 0.4$. The loading curves in (a) and (b) correspond to $R_{\rm i} = 0.39, 0.395, 0.4, 0.405, 0.41$ and $\gamma = 1.45, 1.5, 1.55, 1.6, 1.65$, respectively. Arrows indicate the direction of parameter growth.

In Fig. 3.23 we fix $\mathcal{N}$ and increase gradually from zero. We plot the bifurcation points corresponding to $k_{\rm cr} = 0$ on the curves $\gamma = \gamma(\lambda)$ given by (3.31) for several fixed $R_{\rm i}$ and $\mathcal{N}$. In (a) we see that smaller values of $R_{\rm i}$ will reduce the amount of surface tension required to trigger the zero wavenumber solution. This is also in contrast to the corresponding results presented in Fig. 3.18 (a) for case 2. Like in case 2, we see in (b) that a larger fixed value of $\mathcal{N}$ will delay the zero wavenumber solution.

3.4.4 A spectral interpretation

The results presented so far in this chapter can be further interpreted through a spectral approach. For the sake of brevity, we will restrict the presentation of this interpretation here to *case 2*, but note that similar interpretations can also be formulated for *cases 1* and *3*.

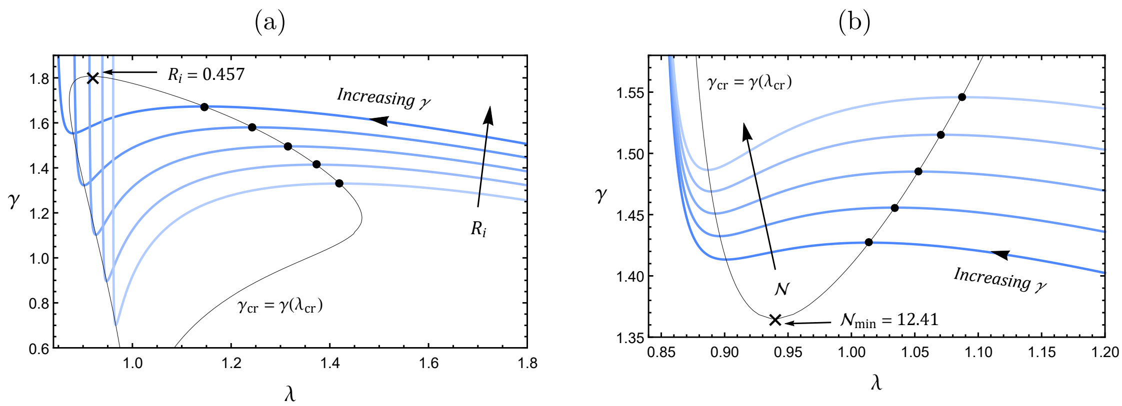

Figure 3.23: Plots of bifurcation points corresponding to $k_{\rm cr} = 0$ (black curves) on loading curves $\gamma = \gamma(\lambda)$ (blue) given by (3.31). We set $J_{\rm m} = 50$ with (a) $\mathcal{N} = 15$ and (b) $R_{\rm i} = 0.4$. The blue loading curves in (a) and (b) correspond to $R_{\rm i} = 0.2, 0.25, 0.3, 0.35, 0.4$ and $\mathcal{N} = 13, 13.25, 13.5, 13.75, 14$, respectively. Arrows indicate the direction of parameter growth.

To begin, we consider a solution for ϕ of the form

$$\phi(R, z) = \phi_0 + \varepsilon g(R) e^{\alpha z}, \tag{3.53}$$

where α is the *spectral parameter* to be determined. On substituting (3.53) into the Euler-Lagrange equations (2.101) and the boundary conditions associated with case 2, and then linearizing in terms of g, we obtain a system of the form (3.45) – $(3.47)_1$. The sole difference is that, in the expressions for the components of the matrices A, $B_{\rm i}$ and $B_{\rm o}$, the axial wavenumber k is replaced by $-\mathrm{i}\alpha$. The aim then is to determine the values of α such that the system has a non-trivial solution, and we achieve this by implementing the previously established determinant method. Since α appears through α^2 in all of the components of the matrices A, $B_{\rm i}$ and $B_{\rm o}$, and since these components are also all real, we expect that the distribution of the eigenvalues of α is symmetric with respect to both axes in the complex α-plane.

As an illustrative example, we set $R_{\rm i} = 0.4$ and $J_{\rm m} = 100$, and we fix $\lambda = 1.5$. We then assess the movement of the eigenvalues in the complex α-plane as we increase γ gradually. In Fig. 3.24 we present the distribution of the eigenvalues of λ for (a) $\gamma < \gamma_{\rm cr}$, (b) $\gamma = \gamma_{\rm cr}$ and (c) $\gamma > \gamma_{\rm cr}$. In all three instances, we see that zero is an eigenvalue of α. Where $\gamma < \gamma_{\rm cr}$, there exists infinitely many *real* eigenvalues $\alpha = 0, \pm\alpha_1, \pm\alpha_2, \pm\alpha_3, \ldots$, where $|\alpha_1| < |\alpha_2| < |\alpha_3| < \cdots$; see (a). In the limit

$\gamma \to \gamma_{\rm cr}^{-}$, we see in (b) that the eigenvalues $\pm\alpha_1$ translate along the Re(α) axis and coalesce at the origin. Thus, our conjectured bifurcation condition for localized pattern formation is equivalently the condition for which zero becomes a *triple eigenvalue* of the spectral eigenvalue problem governing incremental perturbations of the primary solution ϕ_0. As γ is increased beyond its critical value $\gamma_{\rm cr}$, the eigenvalues $\pm\alpha_1$ move onto the Im(α) axis and the solution (3.53) therefore becomes *periodic*; see (c). This movement of the eigenvalues further reinforces the main result

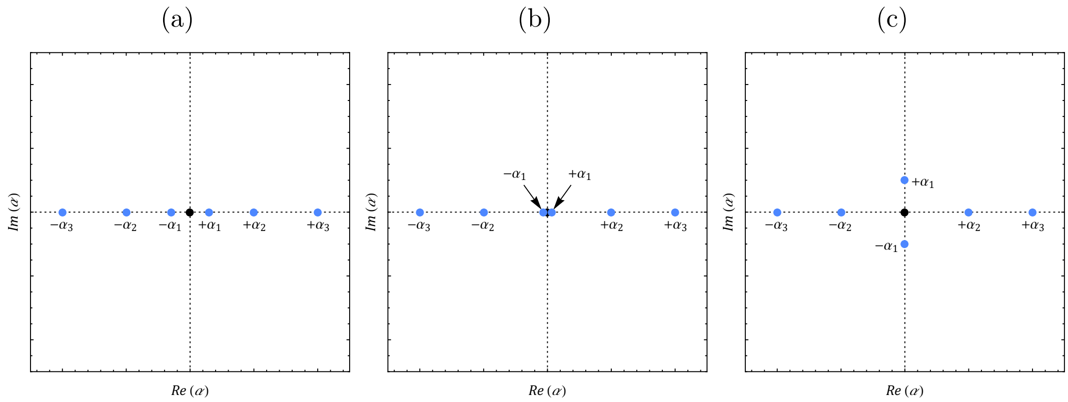

Figure 3.24: The distribution of the eigenvalues $0, \pm\alpha_1, \pm\alpha_2, \pm\alpha_3, \ldots$ of α in the complex α plane for $R_{\rm i} = 0.4$, $J_{\rm m} = 100$, $\lambda = 1.5$ and (a) $\gamma < \gamma_{\rm cr}$, (b) $\gamma = \gamma_{\rm cr}$ and (c) $\gamma > \gamma_{\rm cr}$.

of the linear bifurcation analysis that a zero wavenumber bifurcation solution will necessarily emerge before any periodic bifurcation solution. This is also illustrated in Fig. 3.25 where we plot γ against α_1^2 with λ fixed, and λ against α_1^2 with γ fixed. In the former case, for instance, we observe that $\alpha_1^2 \to 0$ as γ is increased towards $\gamma_{\rm cr} = 8$. Above this critical value, α_1^2 becomes negative, and hence $\pm\alpha_1$ become purely imaginary as expected.

3.5 Discussion

The objective of the work presented in this chapter was twofold. Firstly, we aimed to conjecture analytical bifurcation conditions for axi-symmetric localized pattern formation in a hollow hyperelastic tube under various elasto-capillary-based boundary conditions and loading scenarios. Secondly, we endeavoured to perform

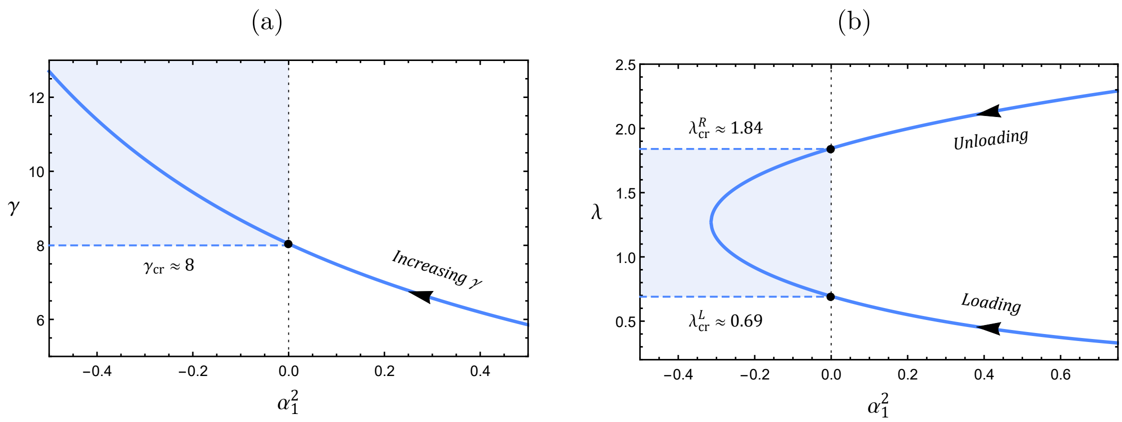

Figure 3.25: Plots of (a) γ against α_1^2 with $\lambda = 1.5$ fixed and (b) λ against α_1^2 with $\gamma = 10$ fixed. In both cases we have taken $R_{\rm i} = 0.4$ and $J_{\rm m} = 100$. In the loading process, once we reach the black dot, zero becomes a triple eigenvalue and an infinite wavelength bifurcation solution may necessarily emerge. It is only in the blue region beyond this dot that $\pm\alpha_1$ become purely imaginary and that periodic bifurcation solutions become possible.

a comprehensive linear bifurcation analysis in order to ascertain the preferred axi-symmetric bifurcation behaviour of the tube.

Three distinct sets of boundary conditions were considered. In *case 1*, both lateral surfaces are under zero shear traction and a normal traction with magnitude equal to the absolute value of the surface tension γ multiplied by the mean curvature $\mathcal{K}$ of the surface. In *case 2* (*case 3*), the inner (outer) lateral surface is fixed in the radial direction, whilst the outer (inner) lateral surface is under the surface tension boundary condition. Both lateral surfaces remain under zero shear traction. We firstly considered a primary deformation where the tube is under the combined effect of surface tension γ and a resultant axial force $\mathcal{N}$, and analytical expressions for both γ and $\mathcal{N}$ were derived from the corresponding equilibrium equations. In *case 1*, we then conjectured that the tube may in general admit a localized bifurcation solution when the Jacobian of the vector function $(\gamma, \mathcal{N})$ vanishes. In *cases 2* and *3*, this bifurcation condition reduces to $d\mathcal{N}/d\lambda = 0$ when γ is fixed or $d\gamma/d\lambda = 0$ when $\mathcal{N}$ is fixed.

A detailed linear bifurcation analysis was then conducted for the three cases previously mentioned. We also considered three separates types of loading: fixed axial stretch with increasing surface tension, fixed surface tension with monotonically varying axial force, and fixed axial force with increasing surface tension. By considering the numerical relationship between the control parameter and the axial wave number k, we determined the preferred axi-symmetric bifurcation mode in each scenario. The key results of the linear analysis are summarized in Table 3.1.

Given the established links between the zero wavenumber bifurcation mode and localized inhomogeneous bifurcation solutions from the dynamical systems theory and the inflation problem, we compared our conjectured conditions for localized pattern formation with the numerical bifurcation conditions obtained from the linear analysis in the limit $k \to 0$. It was shown that the two sets of conditions were in complete agreement. Despite this, we still need to explicitly show the equivalence of the zero wavenumber bifurcation solution and localized pattern formation, and whether this bifurcation is subcritical or supercritical. Since a linear analysis can offer no new information in any of these respects, it is required that we conduct a weakly non-linear near-critical analysis. Before we do this, however, we must recognise that circumferential buckling modes may also be possible. In the next chapter, we analyze both the existence of such modes as well as their competition with the axi-symmetric modes studied in the current chapter in order to determine the overall preferred bifurcation behaviour of the tube.

Table 3.1: A summary of the results of the linear bifurcation analysis in section 3.4.

	Fixed λ *and increasing* γ	*Fixed* $\gamma > 0$ *and varying* $\mathcal{N}$	*Fixed* $\mathcal{N} \geq 0$ *and increasing* γ
Case 1	• $k_{\mathrm{cr}} = 0$ (when $\lambda \geq 1$) • γ_{cr} as a function of λ has a minimum • Bifurcation is delayed in thinner (thicker) tubes below (above) a threshold value of λ	• $k_{\mathrm{cr}} = 0$ (when unloading) • Bifurcation delayed in thinner tubes when unloading • A smaller $\gamma > \gamma_{\mathrm{min}}$ delays bifurcation when unloading	• $k_{\mathrm{cr}} = 0$ • Bifurcation is delayed in thinner tubes • A larger $\mathcal{N} \geq \mathcal{N}_{\mathrm{min}}$ delays bifurcation
Case 2	• $k_{\mathrm{cr}} = 0$ • γ_{cr} as a function of λ has a minimum • Bifurcation is delayed in thinner tubes or in tubes with reduced extensibility	• $k_{\mathrm{cr}} = 0$ • A larger (smaller) $\gamma > \gamma_{\mathrm{min}}$ delays bifurcation when loading (unloading) • Bifurcation is impossible in sufficiently thin tubes	• $k_{\mathrm{cr}} = 0$ • A larger $\mathcal{N} > \mathcal{N}_{\mathrm{min}}$ delays bifurcation • Bifurcation is impossible in sufficiently thin tubes
Case 3	• $k_{\mathrm{cr}} = 0$ (unless λ is sufficiently less than 1) • γ_{cr} as a function of $\lambda > 1 - R_{\mathrm{i}}^2$ and $R_{\mathrm{i}} > (1-\lambda)^{1/2}$ has a minimum • Bifurcation is delayed in tubes with reduced extensibility	• $k_{\mathrm{cr}} = 0$ (unless γ is sufficiently large) • A larger (smaller) $\gamma > \gamma_{\mathrm{min}}$ delays bifurcation when loading (unloading) • Bifurcation is delayed in thicker (thinner) tubes when loading (unloading)	• $k_{\mathrm{cr}} = 0$ • A larger $\mathcal{N} > \mathcal{N}_{\mathrm{min}}$ delays bifurcation • Bifurcation is delayed in thinner tubes

3.A Appendix – Hollow tube surface tension boundary conditions

Consider the following energy functional

$$\mathcal{E} = \int_{\mathcal{B}_0} W(F)dV + \int_{\partial\mathcal{B}_e} \gamma da = \int_{\mathcal{B}_e} J^{-1}W(F)dv + \int_{\partial\mathcal{B}_e} \gamma da, \tag{3.54}$$

where $\mathcal{B}_0$ and $\mathcal{B}_e$ are the reference and current configurations, repspectively. Our aim is to derive the equilibrium equations and boundary conditions by setting the first variation of $\mathcal{E}$ to zero. For the first term, we have

$$\delta \int_{\mathcal{B}_0} W(F)dV = \int_{\mathcal{B}_0} \frac{\partial W}{\partial F_{iA}} \delta F_{iA} dV = \int_{\mathcal{B}_0} \pi_{iA}\delta x_{i,A} dV$$

$$= \int_{\mathcal{B}_0} \left\{ (\pi_{iA}\delta x_i)_{,A} - \pi_{iA,A}\delta x_i \right\} dV = \int_{\partial\mathcal{B}_0} \pi_{iA} N_A \delta x_i dA - \int_{\mathcal{B}_0} \pi_{iA,A}\delta x_i dV$$

$$= \int_{\partial\mathcal{B}_0} \pi \boldsymbol{N} \cdot \delta\boldsymbol{x} dA - \int_{\mathcal{B}_0} \mathrm{Div} S \cdot \delta\boldsymbol{x} dV$$

$$= \int_{\partial\mathcal{B}_e} \sigma\boldsymbol{n} \cdot \delta\boldsymbol{x} da - \int_{\mathcal{B}_e} \mathrm{div}\sigma \cdot \delta\boldsymbol{x} dv. \tag{3.55}$$

For the second term, we begin by considering a smooth part P of $\partial\mathcal{B}_0$ which is locally parametrized by the coordinates θ^α, where $\alpha \in \{1, 2\}$. Then, the position function $\boldsymbol{Y}$ on the surface is identified with the restriction of $\boldsymbol{X}$ to P, i.e.

$$\boldsymbol{Y}(\theta^1, \theta^2) = \boldsymbol{X}|_P. \tag{3.56}$$

The surface is then assumed to be convected by a deformation $\boldsymbol{x} = \boldsymbol{\chi}(\boldsymbol{X})$ such that its image in the current configuration admits the local parametrization

$$\boldsymbol{y}(\theta^1, \theta^2) = \boldsymbol{\chi}(\boldsymbol{Y}(\theta^1, \theta^2)). \tag{3.57}$$

We may then introduce the covariant vectors

$$\boldsymbol{G}_\alpha = \boldsymbol{Y}_{,\alpha}, \qquad \boldsymbol{g}_\alpha = \boldsymbol{y}_{,\alpha}, \tag{3.58}$$

and the corresponding contravariant vectors $\boldsymbol{G}^\alpha$ and $\boldsymbol{g}^\alpha$ are defined as in (2.3). In general, we should represent the covariant vector derivatives $\boldsymbol{g}_{\alpha,\beta}$ as a linear combination of the basis vectors $\boldsymbol{g}_1$, $\boldsymbol{g}_2$ and $\boldsymbol{n}$, where $\boldsymbol{n}$ denotes the outward unit normal to the surface. That is, we may write

$$\boldsymbol{g}_{\alpha,\beta} = \Gamma^{\gamma}_{\alpha\beta}\boldsymbol{g}_{\gamma} + b_{\alpha\beta}\boldsymbol{n}, \tag{3.59}$$

where

$$\Gamma^{\gamma}_{\alpha\beta} = \boldsymbol{g}^{\gamma} \cdot \boldsymbol{g}_{\alpha,\beta} \quad \text{and} \quad b_{\alpha\beta} = \boldsymbol{n} \cdot \boldsymbol{g}_{\alpha,\beta}, \tag{3.60}$$

are the *Christoffel symbols* and the *normal curvatures* (respectively) on the deformed surface; see Steigmann and Ogden (1999). It is also necessary to define the following quantities:

$$g_{\alpha\beta} = \boldsymbol{g}_{\alpha} \cdot \boldsymbol{g}_{\beta}, \quad g^{\alpha\beta} = \boldsymbol{g}^{\alpha} \cdot \boldsymbol{g}^{\beta}, \quad G_{\alpha\beta} = \boldsymbol{G}_{\alpha} \cdot \boldsymbol{G}_{\beta}, \quad G^{\alpha\beta} = \boldsymbol{G}^{\alpha} \cdot \boldsymbol{G}^{\beta},$$

$$g = \det(g_{\alpha\beta}), \quad G = \det(G_{\alpha\beta}), \quad g^{-1} = \det(g^{\alpha\beta}), \quad G^{-1} = \det(G^{\alpha\beta}), \tag{3.61}$$

where $(g_{\alpha\beta})$ denotes the matrix with components $g_{\alpha\beta}$, say. Then, on combining the expressions

$$\boldsymbol{g}_1 \wedge \boldsymbol{g}_2 d\theta_1 d\theta_2 = \boldsymbol{n} da \quad \text{and} \quad \boldsymbol{G}_1 \wedge \boldsymbol{G}_2 d\theta_1 d\theta_2 = \boldsymbol{N} dA, \tag{3.62}$$

it can be shown that

$$\frac{da}{dA} = \frac{\sqrt{g}}{\sqrt{G}} \equiv J_2. \tag{3.63}$$

Moreover, by Jacobi's Formula (2.77), we have the identity

$$\frac{\partial g}{\partial g_{\alpha\beta}} = g g^{\alpha\beta}. \tag{3.64}$$

We may then calculate the first variation of da, or equivalently, J_2. We have

$$\delta J_2 = \frac{1}{2}\frac{1}{\sqrt{gG}}\delta g = \frac{1}{2}\frac{1}{\sqrt{gG}}\frac{\partial g}{\partial g_{\alpha\beta}}\delta g_{\alpha\beta} = \frac{1}{2}\frac{\sqrt{g}}{\sqrt{G}}g^{\alpha\beta}\delta g_{\alpha\beta}$$

$$= \frac{1}{2}\frac{\sqrt{g}}{\sqrt{G}}g^{\alpha\beta}\left\{\boldsymbol{g}_{\beta}\delta\boldsymbol{g}_{\alpha} + \boldsymbol{g}_{\alpha}\delta\boldsymbol{g}_{\beta}\right\} = \frac{1}{2}\frac{\sqrt{g}}{\sqrt{G}}\left\{\boldsymbol{g}^{\alpha} \cdot \delta\boldsymbol{g}_{\alpha} + \boldsymbol{g}^{\beta} \cdot \delta\boldsymbol{g}_{\beta}\right\} = J_2\boldsymbol{g}^{\alpha} \cdot \delta\boldsymbol{y}_{,\alpha}$$

$$= J_2 g^{-1/2}\left\{(g^{1/2}\boldsymbol{g}^{\alpha} \cdot \delta\boldsymbol{y})_{,\alpha} - (g^{1/2}\boldsymbol{g}^{\alpha})_{,\alpha} \cdot \delta\boldsymbol{y}\right\}. \tag{3.65}$$

Thus, we have that

$$\delta \int_{\partial \mathcal{B}_e} \gamma da = \delta \int_{\partial \mathcal{B}_e} \gamma J_2 dA = \gamma \int_{\partial \mathcal{B}_e} g^{-1/2} \left\{ (g^{1/2} \boldsymbol{g}^{\alpha} \cdot \delta \boldsymbol{y})_{,\alpha} - (g^{1/2} \boldsymbol{g}^{\alpha})_{,\alpha} \cdot \delta \boldsymbol{x} \right\} da. \tag{3.66}$$

On applying *Green-Stokes' theorem*, the first term in (3.66) becomes

$$\gamma \int_{\partial \mathcal{B}_e} g^{-1/2} (g^{1/2} \boldsymbol{g}^{\alpha} \cdot \delta \boldsymbol{y})_{,\alpha} da = \gamma \oint_{\partial P} (\boldsymbol{g}^{\alpha} \cdot \delta \boldsymbol{y}) \nu_{\alpha} ds, \tag{3.67}$$

where ∂P is the contour along the boundary of the surface $\partial \mathcal{B}_e$, (ν_α) is the unit vector along this contour and ds is an infinitesimal line element on ∂P. The contour integral in (3.67) does not contribute to our boundary conditions, however, and it remains to manipulate the second term in (3.66). Firstly, with the use of (3.60), (3.61) and (3.64), it can be shown that

$$g_{,\alpha} = \frac{\partial g}{\partial g_{\gamma\beta}} g_{\gamma\beta,\alpha} = 2g \left(\boldsymbol{g}^{\beta} \cdot \boldsymbol{g}_{\beta,\alpha} \right) = 2g \Gamma^{\beta}_{\beta\alpha}. \tag{3.68}$$

Then, from (3.68), we determine that

$$\left(g^{1/2} \boldsymbol{g}^{\alpha} \right)_{,\alpha} = g^{1/2} \Gamma^{\beta}_{\beta\alpha} \boldsymbol{g}^{\alpha} + g^{1/2} \boldsymbol{g}^{\alpha}_{,\alpha}. \tag{3.69}$$

Now, we can evaluate $\boldsymbol{g}^{\alpha}_{,\alpha}$ in two separate ways:

$$\boldsymbol{g}^{\alpha}_{,\alpha} = \left(\boldsymbol{g}_{\gamma} \cdot \boldsymbol{g}^{\alpha}_{,\alpha} \right) \boldsymbol{g}^{\gamma} + \left(\boldsymbol{n} \cdot \boldsymbol{g}^{\alpha}_{,\alpha} \right) \boldsymbol{n}, \tag{3.70}$$

or

$$\boldsymbol{g}^{\alpha}_{,\alpha} = \left(g^{\alpha\beta} \boldsymbol{g}_{\beta} \right)_{,\alpha} = g^{\alpha\beta}_{,\alpha} \boldsymbol{g}_{\beta} + g^{\alpha\beta} \boldsymbol{g}_{\beta,\alpha} = g^{\alpha\beta}_{,\alpha} \boldsymbol{g}_{\beta} + g^{\alpha\beta} \left(\Gamma^{\gamma}_{\alpha\beta} \boldsymbol{g}_{\gamma} + b_{\alpha\beta} \boldsymbol{n} \right). \tag{3.71}$$

On comparing the coefficients of $\boldsymbol{n}$ in (3.70) and (3.71), we find that

$$\boldsymbol{n} \cdot \boldsymbol{g}^{\alpha}_{,\alpha} = g^{\alpha\beta} b_{\alpha\beta} = \mathcal{K}, \tag{3.72}$$

where $\mathcal{K}$ is the trace of the curvature tensor. Also, on differentiating the equation $\boldsymbol{g}_{\gamma} \cdot \boldsymbol{g}^{\alpha} = \delta_{\gamma\alpha}$ with respect to α, we deduce

$$\boldsymbol{g}_{\gamma} \cdot \boldsymbol{g}^{\alpha}_{,\alpha} = -\boldsymbol{g}_{\gamma,\alpha} \cdot \boldsymbol{g}^{\alpha} = -\Gamma^{\alpha}_{\gamma\alpha}. \tag{3.73}$$

It then follows that the expression (3.70) may be rewritten as

$$\boldsymbol{g}^{\alpha}_{,\alpha} = -\Gamma^{\alpha}_{\alpha\gamma}\boldsymbol{g}^{\gamma} + \mathcal{K}\boldsymbol{n}. \tag{3.74}$$

Finally, on substituting (3.74) into (3.69), we obtain

$$\left(g^{\frac{1}{2}}\boldsymbol{g}^{\alpha}\right)_{,\alpha} = g^{\frac{1}{2}}\mathcal{K}\boldsymbol{n}, \tag{3.75}$$

and hence (3.66) reduces to

$$\delta\int_{\partial\mathcal{B}_e}\gamma da = \gamma\oint_{\partial P}\left(\boldsymbol{g}^{\alpha}\cdot\delta\boldsymbol{y}\right)\nu_{\alpha}ds - \gamma\int_{\partial\mathcal{B}_e}\mathcal{K}\boldsymbol{n}\cdot\delta\boldsymbol{x}da. \tag{3.76}$$

Thus, given (3.55), (3.67) and (3.76), we have that

$$\delta\mathcal{E} = \int_{\partial\mathcal{B}_e}(\sigma\boldsymbol{n} - \gamma\mathcal{K}\boldsymbol{n})\cdot\delta\boldsymbol{x}\,da - \int_{\mathcal{B}_e}\mathrm{div}\sigma\cdot\delta\boldsymbol{x}\,dv + \gamma\oint_{\partial P}(\boldsymbol{g}^{\alpha}\cdot\delta\boldsymbol{y})\nu_{\alpha}ds. \tag{3.77}$$

If this variation is zero for arbitrary variations $\delta\boldsymbol{x}$ of $\boldsymbol{x}$ in the interior and on the boundaries where surface tension exists, then we must have the usual equilibrium equation $\mathrm{div}\sigma = 0$ and the boundary conditions

$$\sigma\boldsymbol{n} = \gamma\mathcal{K}\boldsymbol{n}. \tag{3.78}$$

Specialization to a hollow cylindrical tube: A representative material particle on the outer lateral surface of the tube has the position vector

$$\boldsymbol{x} = r_{\mathrm{o}}\boldsymbol{e}_r + z\boldsymbol{e}_z. \tag{3.79}$$

The outward unit normal to this surface is $\boldsymbol{n} = \boldsymbol{e}_r$, and we may take $\theta_1 = \theta$ and $\theta_2 = z$. We therefore have

$$\begin{gathered}\boldsymbol{g}_1 = \frac{\partial\boldsymbol{x}}{\partial\theta} = r_{\mathrm{o}}\boldsymbol{e}_{\theta}, \qquad \boldsymbol{g}_2 = \frac{\partial\boldsymbol{x}}{\partial z} = \boldsymbol{e}_z,\\ \boldsymbol{g}_{1,1} = -r_{\mathrm{o}}\boldsymbol{e}_r, \qquad \boldsymbol{g}_{1,2} = 0, \qquad \boldsymbol{g}_{2,1} = 0, \qquad \boldsymbol{g}_{2,2} = 0.\end{gathered} \tag{3.80}$$

It then follows that

$$\begin{gathered}b_{11} = -r_{\mathrm{o}}, \qquad b_{12} = 0, \qquad b_{21} = 0, \qquad b_{22} = 0,\\ g_{11} = r_{\mathrm{o}}^2, \qquad g_{12} = 0, \qquad g_{21} = 0, \qquad g_{22} = 1,\\ g^{11} = r_{\mathrm{o}}^{-2}, \qquad g^{12} = 0, \qquad g^{21} = 0, \qquad g^{22} = 0,\end{gathered} \tag{3.81}$$

and hence

$$\mathcal{K} = g^{\alpha\beta} b_{\alpha\beta} = -\frac{1}{r_{\mathrm{o}}}. \tag{3.82}$$

For the inner lateral surface, the calculation is identical except that $\boldsymbol{n} = -\boldsymbol{e}_r$. As a result, $b_{11} = r_{\mathrm{i}}$ and hence

$$\mathcal{K} = g^{\alpha\beta} b_{\alpha\beta} = \frac{1}{r_{\mathrm{i}}}. \tag{3.83}$$

Thus, the surface tension boundary conditions for a hollow cylindrical tube must be

$$\sigma\boldsymbol{n} = -\frac{\gamma}{r_{\mathrm{o}}}\boldsymbol{n} \quad \text{on} \quad r = r_{\mathrm{o}}, \quad \text{and} \quad \sigma\boldsymbol{n} = \frac{\gamma}{r_{\mathrm{i}}}\boldsymbol{n} \quad \text{on} \quad r = r_{\mathrm{i}}. \tag{3.84}$$

3.B Appendix – Coefficients in the linear eigenvalue problem

The expressions for the variable coefficients $a_i = a_i(R)$ $(i = 1, 2, \ldots, 7)$ in (3.43) may be given as follows:

$$
\begin{aligned}
a_1 &= -\frac{2}{R} + 2\,\omega_1\, I_{0R}, \qquad a_2 = \frac{3}{R^2} + \omega_2 I_{0R}^2 + 2\omega_1 I_{0RR} - \frac{8\omega_1}{\eta_1^3\lambda}\eta_2^2,\\
a_3 &= -\frac{3}{R^3} - \frac{\omega_2}{R} I_{0R}^2 - \frac{2\omega_1}{R} I_{0RR} + \frac{8\omega_1}{\eta_1^3 R\lambda}\eta_2^2, \qquad a_4 = \frac{R^2\lambda}{\eta_1},\\
a_5 &= \frac{R^2\omega_2}{\eta_2\lambda}(1-\lambda^3) - \frac{R}{\eta_2} I_{0R} + \frac{2\omega_1\eta_2}{\lambda^2\eta_1^3}\left\{2(1-\lambda^3)(3\eta_1 + R^2) - \frac{\eta_2^3}{R^4} - \frac{2\eta_2^2}{R^2}(\lambda^3 - 2)\right\},\\
a_6 &= \frac{R(\eta_1 - 2R^2)}{\lambda\eta_1^2} - \frac{\lambda^2}{R} + 2\omega_2\eta_3^2 I_{0R} - \frac{2R\omega_1\eta_2^2}{\lambda^2\eta_1^3}(2 + 4\lambda^3 + 3\lambda^6) - \frac{6R^3\omega_1\eta_2}{\lambda^2\eta_1^2}(1-\lambda^6)\\
&\quad + \frac{2\omega_1\eta_2^3}{\eta_1^3\lambda^2}(1 + 3\lambda^3 + \lambda^6) - \frac{2\omega_1}{R^3\lambda^2\eta_1^3}\left\{\lambda^3\eta_2^2 + R^8(\lambda^3 - 1)^2\right\},\\
a_7 &= \lambda^2 + \frac{R^2}{\lambda\eta_1} + 2\omega_1\eta_3^2,
\end{aligned}
\tag{3.85}
$$

where

$$
\omega_1 = \frac{W_{dd}}{W_d}, \qquad \omega_2 = \frac{W_{ddd}}{W_d}, \qquad \eta_1 = r_0^2\lambda, \qquad \eta_2 = R^2 - \eta_1, \qquad \eta_3 = \lambda^2 - \frac{R^2}{\eta_1\lambda}. \tag{3.86}
$$

From (3.47), we have that $b_{11} = (k^2R^2)/(\lambda\eta_1)$ and

$$
\begin{aligned}
b_{21}^{\pm} &= k^2\left\{\frac{R}{\lambda\eta_1^2}(1 - 2\eta_1) - \frac{1}{R\lambda} + \frac{R^2\omega_1(\lambda^3 - 1)}{\lambda\eta_2} I_{0,R} \pm \frac{\gamma\, r_0 R}{2w_d\eta_1^2}(k^2\eta_1 - \lambda)\right\},\\
b_{22} &= \frac{1}{R^2} - k^2\left(\lambda^2 + \frac{2R^2}{\eta_1\lambda}\right) - \frac{\omega_1}{R} I_{0R} - 2\omega_1 k^2\eta_3^2, \qquad b_{23} = -\frac{1}{R} + \omega_1 I_{0R}.
\end{aligned}
\tag{3.87}
$$

4

Circumferential buckling vs. axi-symmetric pattern formation in soft tubes under elasto-capillary effects

Contents

4.1 Introduction

In this chapter, we move on to studying the *circumferential buckling* of an incompressible hyperelastic tube under the combined action of surface tension $\bar{\gamma}$ and a resultant axial force $\mathcal{N}$. After formulating the problem and reintroducing the primary axial tension deformation, we perform an extensive linear bifurcation analysis for the same three sets of boundary conditions considered in the previous chapter. We also consider the three types of loading which were analyzed in the previous chapter.

In all of the aforementioned scenarios, we produce a numerical relationship between the control parameter and the *circumferential mode number* m. From this relationship, we determine the preferred (or critical) values of the control parameter and m. We then compare these critical values with the corresponding values for the *axi-symmetric* zero wavenumber mode from the previous chapter. In doing so, we can rigorously assess the competition between axi-symmetric and circumferential modes in order to determine the preferred overall bifurcation behaviour. The chapter is concluded with a summary of our main findings.

4.2 Problem formulation

Contrary to in the previous chapter, we now assume that the tube undergoes a deformation of the form

$$r = r(R, \Theta), \qquad \theta = \theta(R, \Theta), \qquad z = \lambda Z, \tag{4.1}$$

where λ is still defined as the principal axial stretch. The notation for the radial and axial coordinates at the extremities of the tube is unchanged from the previous chapter. Then, given that the positions vectors $\boldsymbol{X}$ and $\boldsymbol{x}$ of a representative material particle in $\mathcal{B}_0$ and $\mathcal{B}_e$ (respectively) are of the form given in (3.1), the deformation gradient F is defined through $d\boldsymbol{x} = Fd\boldsymbol{X}$ and is expressible as

$$F = \frac{\partial r}{\partial R}\boldsymbol{e}_r \otimes \boldsymbol{E}_R + \frac{1}{R}\frac{\partial r}{\partial \Theta}\boldsymbol{e}_r \otimes \boldsymbol{E}_\Theta + \frac{r}{R}\frac{\partial \theta}{\partial \Theta}\boldsymbol{e}_\theta \otimes \boldsymbol{E}_\Theta + r\frac{\partial \theta}{\partial R}\boldsymbol{e}_\theta \otimes \boldsymbol{E}_R + \lambda \boldsymbol{e}_z \otimes \boldsymbol{E}_Z. \tag{4.2}$$

We continue to operate under the assumption given in (3.4) that the strain-energy function W is solely dependant on the first invariant, I_1, of $B = FF^T$. In the calculation of our results further into the chapter, we will adopt the Gent material model (2.63).

For the static solution (4.1), the *bulk elastic energy* $\mathcal{E}_b$ and the *surface energies* $\mathcal{E}_s^{\mathrm{i}}$ and $\mathcal{E}_s^{\mathrm{o}}$ on the inner and outer lateral surfaces (respectively) take the following forms:

$$\mathcal{E}_b = 2L\int_0^{2\pi}\int_{R_\mathrm{i}}^{R_\mathrm{o}} W(I_1) R dR d\Theta, \qquad \mathcal{E}_s^\beta = 2L\bar{\gamma}\int_0^{2\pi} r_\beta(\theta)\sqrt{1+r_\beta'(\theta)^2} d\Theta, \tag{4.3}$$

where $\beta = \mathrm{i}$ or o.

Again, unless stated otherwise, we scale all lengths by R_o and all stresses by the ground state shear modulus μ. Thus, we may set $R_\mathrm{o} = 1$ and $\mu = 1$ without loss of generality. As before, we use the same symbols to denote scaled quantities, and we also introduce the non-dimensionalized surface tension $\gamma = \bar{\gamma}/(\mu R_\mathrm{o})$.

4.2.1 Stream function formulation

We may introduce a mixed co-ordinate stream function $\psi = \psi(R, \theta)$ so that the incompressibility constraint (2.12) is satisfied exactly (Ciarletta, 2011). This stream function is defined through the relations

$$r^2 = 2\frac{\partial\psi}{\partial\theta} = 2\psi_{,\theta}, \qquad \Theta = \frac{\lambda}{R}\frac{\partial\psi}{\partial R} = \frac{\lambda}{R}\psi_{,R}. \tag{4.4}$$

Then, F can be re-written in the form

$$\begin{aligned} F = {} & \frac{1}{\sqrt{2\,\psi_{,\theta}}}\left[\psi_{,R\theta} - R\frac{\psi_{,\theta\theta}}{\psi_{,R\theta}}\frac{\partial}{\partial R}\left(\frac{\psi_{,R}}{R}\right)\right]\boldsymbol{e}_r\otimes\boldsymbol{E}_R + \frac{\psi_{,\theta\theta}}{\lambda\sqrt{2\,\psi_{,\theta}}\,\psi_{,R\theta}}\boldsymbol{e}_r\otimes\boldsymbol{E}_\Theta \\ & + \frac{\sqrt{2\,\psi_{,\theta}}}{\lambda\psi_{,R\theta}}\boldsymbol{e}_\theta\otimes\boldsymbol{E}_\Theta - \frac{R\sqrt{2\psi_{,\theta}}}{\psi_{,R\theta}}\frac{\partial}{\partial R}\left(\frac{\psi_{,R}}{R}\right)\boldsymbol{e}_\theta\otimes\boldsymbol{E}_R + \lambda\,\boldsymbol{e}_z\otimes\boldsymbol{E}_Z, \end{aligned} \tag{4.5}$$

and it follows that the invariant I_1 is expressible as

$$\begin{aligned} I_1 = {} & \frac{1}{2\,\psi_{,\theta}}\left[\psi_{,R\theta} - \frac{R\,\psi_{,\theta\theta}}{\psi_{,R\theta}}\frac{\partial}{\partial R}\left(\frac{\psi_{,R}}{R}\right)\right]^2 + \frac{1}{2}\frac{\phi_{,\theta\theta}^2}{\lambda^2\phi_{,\theta}\,\phi_{R\theta}^2} \\ & + \frac{2\,\phi_{,\theta}}{\lambda^2\psi_{,R\theta}^2} - \frac{2R^2\psi_{,\theta}}{\phi_{,R\theta}^2}\left[\frac{\partial}{\partial R}\left(\frac{\psi_{,R}}{R}\right)\right]^2 + \lambda^2. \end{aligned} \tag{4.6}$$

The total energy $\mathcal{E}$ may also be rewritten in terms of the stream function as such:

$$\mathcal{E} = 2\lambda L\int_0^{2\pi}\int_{R_\mathrm{i}}^{R_\mathrm{o}} \mathcal{L}_b\, dR\, d\theta \,+\, 2\lambda L\int_0^{2\pi}\left(\mathcal{L}_s^\mathrm{i} + \mathcal{L}_s^\mathrm{o}\right) d\theta, \tag{4.7}$$

where the bulk Lagrangian $\mathcal{L}_b$ and the inner and outer surface Lagrangians $\mathcal{L}_s^{\mathrm{i}}$ and $\mathcal{L}_s^{\mathrm{o}}$ take the form

$$\mathcal{L}_b = \psi_{,R\theta}\, W(I_1), \qquad \mathcal{L}_s^{\beta} = \gamma\, \sqrt{2\,\psi_{,\theta} + \psi_{,\theta\theta}^2}\Big|_{R=R_\beta}, \tag{4.8}$$

with $\beta = \mathrm{i}$ or o. Thus, $\mathcal{E}$ as presented in (4.7) is a functional in its arguments $\psi_{,R}$, $\psi_{,\theta}$, $\psi_{,RR}$, $\psi_{,R\theta}$ and $\psi_{,\theta\theta}$. On taking the first variation of (4.7) with respect to these arguments and then integrating by parts repeatedly, we arrive at the *Euler-Lagrange equation* given by

$$\left(\frac{\partial \mathcal{L}_b}{\partial \psi_{,RR}}\right)_{,RR} + \left(\frac{\partial \mathcal{L}_b}{\partial \psi_{,R\theta}}\right)_{,R\theta} + \left(\frac{\partial \mathcal{L}_b}{\partial \psi_{,\theta\theta}}\right)_{,\theta\theta} - \left(\frac{\partial \mathcal{L}_b}{\partial \psi_{,R}}\right)_{,R} - \left(\frac{\partial \mathcal{L}_b}{\partial \psi_{,\theta}}\right)_{,\theta} = 0. \tag{4.9}$$

We consider the same three cases of boundary conditions which were analyzed in the previous chapter; see Fig. 3.1. The surface tension boundary conditions on $R = R_{\mathrm{i}}$ and R_{o} are expressible as

$$\frac{\partial \mathcal{L}_b}{\partial \psi_{,R}} - \left(\frac{\partial \mathcal{L}_b}{\partial \psi_{,RR}}\right)_{,R} - \left(\frac{\partial \mathcal{L}_b}{\partial \psi_{,R\theta}}\right)_{,\theta} = \left(\frac{\partial \mathcal{L}_s^{\mathrm{i}}}{\partial \psi_{,\theta\theta}}\right)_{,\theta\theta} - \left(\frac{\partial \mathcal{L}_s^{\mathrm{i}}}{\partial \psi_{,\theta}}\right)_{,\theta}, \qquad R = R_{\mathrm{i}}, \tag{4.10}$$

$$\frac{\partial \mathcal{L}_b}{\partial \psi_{,R}} - \left(\frac{\partial \mathcal{L}_b}{\partial \psi_{,RR}}\right)_{,R} - \left(\frac{\partial \mathcal{L}_b}{\partial \psi_{,R\theta}}\right)_{,\theta} = \left(\frac{\partial \mathcal{L}_s^{\mathrm{o}}}{\partial \psi_{,\theta}}\right)_{,\theta} - \left(\frac{\partial \mathcal{L}_s^{\mathrm{o}}}{\partial \psi_{,\theta\theta}}\right)_{,\theta\theta}, \qquad R = R_{\mathrm{o}}. \tag{4.11}$$

In the event that a lateral surface is in smooth contact with a rigid boundary (i.e. cases 2 and 3 defined previously), we require that $\delta r = 0$ on $R = R_{\mathrm{i}}$ or R_{o}, and this replaces the surface tension boundary condition (4.10) or (4.11), respectively. Lastly, the zero shear traction condition on the lateral surfaces which applies in all three cases takes the form

$$\frac{\partial \mathcal{L}_b}{\partial \psi_{,RR}} = 0, \qquad R = R_{\mathrm{i}},\, R_{\mathrm{o}}. \tag{4.12}$$

4.2.2 The primary deformation

As in the previous chapter, we consider the primary axial tension deformation given by

$$r = r_0 = \sqrt{\lambda^{-1}\left(R^2 - R_{\mathrm{i}}^2\right) + r_{\mathrm{i}}^2}, \qquad \theta = \Theta, \qquad z = \lambda Z, \tag{4.13}$$

noting that it is also a subclass of (4.1). On substituting (4.13) into (4.4) and integrating the resulting equations, we determine that the corresponding primary solution for ψ, denoted by ψ_0, takes the form

$$\psi_0 = \frac{R^2\theta}{2\lambda} + \frac{1}{2}\left(r_{\mathrm{i}}^2 - \frac{R_{\mathrm{i}}^2}{\lambda}\right)\theta. \tag{4.14}$$

On solving the associated equilibrium equations, it can be shown that the expressions derived for γ and $\mathcal{N}$ in the previous chapter remain true here.

4.3 Linear bifurcation analysis

We consider a perturbation $\psi_1 = \psi_1(R,\theta)$ of the primary solution governed by (4.14). On substituting the perturbed solution $\psi = \psi_0 + \psi_1$ into the equilibrium equation (4.9) and linearizing in terms of ψ_1, we obtain

$$\frac{\partial^4\psi_1}{\partial R^4} + \hat{a}_1(R)\frac{\partial^3\psi_1}{\partial R^3} + \hat{a}_2(R)\frac{\partial^2\psi_1}{\partial R^2} + \hat{a}_3(R)\frac{\partial\psi_1}{\partial R} + \hat{a}_4(R)\frac{\partial^4\psi_1}{\partial\theta^4} + \hat{a}_5(R)\frac{\partial^2\psi_1}{\partial\theta^2}$$
$$+ \hat{a}_6(R)\frac{\partial^3\psi_1}{\partial R\partial\theta^2} + \hat{a}_7(R)\frac{\partial^4\psi_1}{\partial R^2\partial\theta^2} = 0, \tag{4.15}$$

with the variable coefficients $\hat{a}_i = \hat{a}_i(R)$ $(i = 1, 2, \ldots, 7)$ given in Appendix 4.A.

More specifically, we look for a solution of the form

$$\psi_1 = \varepsilon\hat{g}(R)e^{\mathrm{i}m\theta}, \tag{4.16}$$

where $m \in \mathbb{Z}^+\backslash\{1\}$ is the circumferential mode number, ε is a small parameter and i is the imaginary unit. On substituting (4.16) into (4.15), the resulting fourth-order ODE for $\hat{g}$ can be reformulated into the following system of first-order linear ODEs;

$$\frac{d\hat{\boldsymbol{g}}}{dR} = \hat{A}(R,\lambda,m)\,\hat{\boldsymbol{g}}, \qquad \hat{A} = \begin{bmatrix} 0 & 1 & 0 & 0 \\ 0 & 0 & 1 & 0 \\ 0 & 0 & 0 & 1 \\ \hat{A}_{41} & \hat{A}_{42} & \hat{A}_{43} & \hat{A}_{44} \end{bmatrix}, \tag{4.17}$$

where $\hat{\boldsymbol{g}} = [\,\hat{g},\, \hat{g}',\, \hat{g}'',\, \hat{g}'''\,]^T$ and the variable components of $\hat{A}$ are given as follows:

$$\hat{A}_{41} = m^2(\hat{a}_5 - m^2\hat{a}_4), \qquad \hat{A}_{42} = m^2\hat{a}_6 - \hat{a}_3$$
$$\hat{A}_{43} = m^2\hat{a}_7 - \hat{a}_2, \qquad \hat{A}_{44} = -\hat{a}_1. \tag{4.18}$$

On substituting $\psi = \psi_0 + \psi_1$ and (4.16) into (4.10), (4.11) and (4.12) and then linearizing in terms of $\hat{g}$, we find that the surface tension and zero shear traction boundary conditions on $R = R_\text{i}$ and $R = R_\text{o}$ in *case 1* may be expressed as the following matrix equations:

$$\begin{aligned} &\hat{B}_\text{i}(R_\text{i}, \lambda, \gamma, m)\,\hat{\boldsymbol{g}} = \mathbf{0}, \\ &\hat{B}_\text{o}(R_\text{o}, \lambda, \gamma, m)\,\hat{\boldsymbol{g}} = \mathbf{0}, \end{aligned} \qquad \text{where} \qquad \begin{cases} \hat{B}_\text{i} = \begin{bmatrix} \hat{b}_{11} & -1/R & 1 & 0 \\ \hat{b}_{21}^{+} & \hat{b}_{22} & \hat{b}_{23} & 1 \end{bmatrix}, \\[2ex] \hat{B}_\text{o} = \begin{bmatrix} \hat{b}_{11} & -1/R & 1 & 0 \\ \hat{b}_{21}^{-} & \hat{b}_{22} & \hat{b}_{23} & 1 \end{bmatrix}, \end{cases} \tag{4.19}$$

and the expressions for the components of $\hat{B}_\text{i}$ and $\hat{B}_\text{o}$ are likewise given in Appendix 4.A. For cases 2 and 3, appropriate modifications to the matrices $\hat{B}_\text{i}$ and $\hat{B}_\text{o}$ should be made as demonstrated in the previous chapter.

In order to account large values of m and prevent numerical stiffness, we analyze the two-point boundary value problem (4.17) – (4.19) through the *compound matrix method* described in section 2.6.2 of chapter 2. For the sake of brevity, we again outline the solution procedure for *case 1*, but note that the approach is identical in cases 2 and 3 when the previously mentioned modifications are enforced. To begin, note that the linear systems $\hat{B}_\text{i}\,\hat{\boldsymbol{g}} = \mathbf{0}$ and $\hat{B}_\text{o}\,\hat{\boldsymbol{g}} = \mathbf{0}$ each have two independent solutions which we denote, respectively, by $\hat{\boldsymbol{g}}_\text{i}^{(j)}$ and $\hat{\boldsymbol{g}}_\text{o}^{(j)}$, with $j = 1, 2$. In case 1, for instance, we have

$$\left.\begin{aligned} \hat{\boldsymbol{g}}_\beta^{(1)} &= \left[1,\, 0,\, -\hat{b}_{11},\, \hat{b}_{23}\,\hat{b}_{11} - \hat{b}_{21}^{+}\right]^T \\ \hat{\boldsymbol{g}}_\beta^{(2)} &= \left[0,\, 1,\, -1/R,\, \hat{b}_{23}/R - \hat{b}_{22}\right]^T \end{aligned}\right\}, \qquad \text{where} \qquad R = R_\beta, \tag{4.20}$$

and $\beta =$ i or o. We can then integrate (4.17) forwards from $R = R_\text{i}$ (using (4.20) as initial data for $\hat{\boldsymbol{g}}$ at $R = R_\text{i}$) and backwards from $R = R_\text{o}$ (using (4.20) as initial data for $\hat{\boldsymbol{g}}$ at $R = R_\text{o}$) towards some interior point $R = R_\text{m} \in (R_\text{i}, R_\text{o})$. In doing so, we obtain two sets of two linearly independent solutions $\{\hat{\boldsymbol{g}}^{(1)}, \hat{\boldsymbol{g}}^{(2)}\}$ and $\{\hat{\boldsymbol{g}}^{(3)}, \hat{\boldsymbol{g}}^{(4)}\}$ which can be presented through the following respective solution matrices:

$$M^- = [\hat{\boldsymbol{g}}^{(1)}, \hat{\boldsymbol{g}}^{(2)}] \quad \text{and} \quad M^+ = [\hat{\boldsymbol{g}}^{(3)}, \hat{\boldsymbol{g}}^{(4)}]. \tag{4.21}$$

The matrices $M^{\mp}$ each have six minors denoted by $\varphi_1^{\mp}, \varphi_2^{\mp}, \dots, \varphi_6^{\mp}$. For instance, the six minors of M^- are

$$\varphi_1^- = \hat{g}_1\hat{g}_2' - \hat{g}_2\hat{g}_1', \qquad \varphi_2^- = \hat{g}_1\hat{g}_2'' - \hat{g}_2\hat{g}_1'', \qquad \varphi_3^- = \hat{g}_1\hat{g}_2''' - \hat{g}_2\hat{g}_1''',$$
$$\varphi_4^- = \hat{g}_1'\hat{g}_2'' - \hat{g}_2'\hat{g}_1'', \qquad \varphi_5^- = \hat{g}_1'\hat{g}_2''' - \hat{g}_2'\hat{g}_1''', \qquad \varphi_6^- = \hat{g}_1''\hat{g}_2''' - \hat{g}_2''\hat{g}_1'''. \tag{4.22}$$

Then, as was shown from equation (2.138) to (2.140), these minors satisfy the following compound matrix equation

$$\frac{d\boldsymbol{\varphi}^-}{dR} = \tilde{A}(R,\lambda,m)\boldsymbol{\varphi}^-, \qquad R_{\rm i} \le R \le R_{\rm m}, \tag{4.23}$$

where $\boldsymbol{\varphi}^- = [\varphi_1^-, \varphi_2^-, \dots, \varphi_6^-]^T$ and

$$\tilde{A} = \begin{bmatrix} 0 & 1 & 0 & 0 & 0 & 0 \\ 0 & 0 & 1 & 1 & 0 & 0 \\ \hat{A}_{42} & \hat{A}_{43} & \hat{A}_{44} & 0 & 1 & 0 \\ 0 & 0 & 0 & 0 & 1 & 0 \\ -\hat{A}_{41} & 0 & 0 & \hat{A}_{43} & \hat{A}_{44} & 1 \\ 0 & -\hat{A}_{41} & 0 & -\hat{A}_{42} & 0 & \hat{A}_{44} \end{bmatrix}. \tag{4.24}$$

The boundary conditions for $\boldsymbol{\varphi}^-$ at $R = R_{\rm i}$ can be constructed from the independent solutions $\hat{\boldsymbol{g}}_{\rm i}^{(1)}$ and $\hat{\boldsymbol{g}}_{\rm i}^{(2)}$ of $B_{\rm i}\,\hat{\boldsymbol{g}} = \mathbf{0}$. For instance, we have

$$\varphi_1^-(R_{\rm i},\lambda,\gamma,m) = \hat{g}_{\rm i1}^{(1)}\hat{g}_{\rm i2}^{(2)} - \hat{g}_{\rm i1}^{(2)}\hat{g}_{\rm i2}^{(1)}, \tag{4.25}$$

where $\hat{g}_{{\rm i}j}^{(i)}$ is the $j^{\rm th}$ component of $\hat{\boldsymbol{g}}_{\rm i}^{(i)}$. We can then integrate forward (4.23) from $R = R_{\rm i}$ towards $R = R_{\rm m}$ in order to obtain a general solution for $\boldsymbol{\varphi}^-$. The corresponding solution for $\boldsymbol{\varphi}^+$ can be obtained in a similar manner. It then remains to match the solutions $\boldsymbol{\varphi}^-$ and $\boldsymbol{\varphi}^+$ at $R = R_{\rm m}$. As was shown in equation (2.142), the matching condition takes the form $\det \hat{N}(R_{\rm m},\lambda,\gamma,m) = 0$, where

$$\det \hat{N}(R,\lambda,\gamma,m) = \varphi_1^-\varphi_6^+ - \varphi_2^-\varphi_5^+ + \varphi_3^-\varphi_4^+ + \varphi_4^-\varphi_3^+ - \varphi_5^-\varphi_2^+ + \varphi_6^-\varphi_1^+. \tag{4.26}$$

However, this condition is dependent on the matching point $R = R_{\rm m}$. As was shown in equation (2.134), we can circumvent this by instead deploying the condition

$$D(\lambda,\gamma,m) = e^{-\int_{R_{\rm i}}^{R_{\rm m}} {\rm tr}\hat{A}(t,\lambda,m)dt} \det \hat{N}(R_{\rm m},\lambda,\gamma,m) = 0, \tag{4.27}$$

which is independent of the matching point.

Equation (4.27) represents a numerical bifurcation condition which must be satisfied by the control parameter (which may again be chosen as $\mathcal{N}$ or γ) and the circumferential mode number m. Similarly to in the previous chapter, for any fixed $m \in \mathbb{Z}^+\backslash\{1\}$, we may iterate on the control parameter until (4.27) is satisfied. We again seek the point on the bifurcation curve relating the control parameter and m which is encountered first during the loading process. The value of m at this point is referred to as the critical circumferential buckling mode, and is denoted by m_{cr}. Beyond the critical value of the control parameter, the tube's cross section may bifurcate into a circumferential buckling pattern with periodicity corresponding to the value of m_{cr}. In Fig. 4.1, we illustrate the circumferential buckling patterns corresponding to $m_{\mathrm{cr}} = 2, 3, 4, 5, 6$ and 7.

4.3.1 Case 1 results

We first consider the case 1 boundary conditions illustrated in Fig. 3.1. We begin by fixing $\lambda \geq 1$ and increasing γ monotonically from zero. In Fig. 4.2 (a) and (b) we plot the bifurcation condition (4.27) in the (λ, γ) and (R_{i}, γ) planes (respectively) for several circumferential mode numbers $m \in \mathbb{Z}^+\backslash\{1\}$ and $J_{\mathrm{m}} = 100$. We observe that, for any fixed value of $\lambda \geq 1$ or R_{i}, the curve corresponding to $m = 2$ is the lowest branch of the bifurcation condition. Thus, the critical mode number is invariably $m_{\mathrm{cr}} = 2$. Physically, this mode number is manifested through the tube's cross section bifurcating from a circular shape into an elliptic shape; see Fig. 4.1. Hereafter, we shall refer to this as the *elliptic mode*. We observe also that the critical surface tension values γ_{cr} for the elliptic mode are generally smaller than the corresponding values for the preferred axi-symmetric mode $k_{\mathrm{cr}} = 0$ (i.e. the *zero wavenumber solution*) from the previous chapter. As an illustrative example, in Fig. 4.2 (a) we notice that, for fixed $\lambda = 1.5$ with $R_{\mathrm{i}} = 0.4$ and $J_{\mathrm{m}} = 100$, bifurcation into the elliptic mode must necessarily occur at $\gamma_{\mathrm{cr}} \approx 0.073$. In contrast, the zero wavenumber solution cannot necessarily emerge until $\gamma_{\mathrm{cr}} \approx 6.4$. Thus,

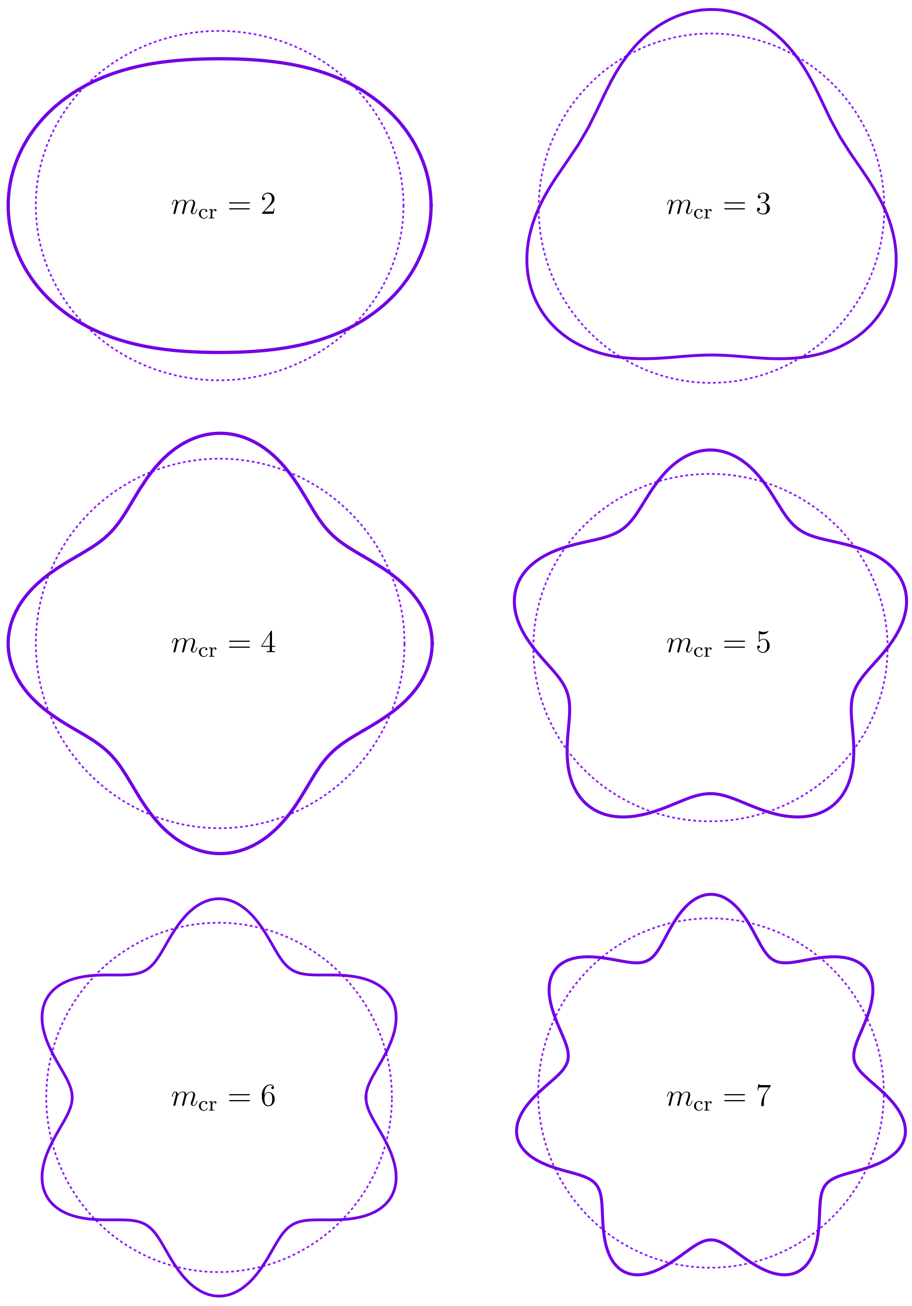

Figure 4.1: A schematic of the bifurcated cross-sectional shapes of the tube (solid curves) corresponding to the critical circumferential buckling modes $m_{\rm cr} = 2, 3, 4, 5, 6$ and 7.

the elliptic mode is preferred over the zero wavenumber solution, and hence any type of axi-symmetric pattern formation, in theory.

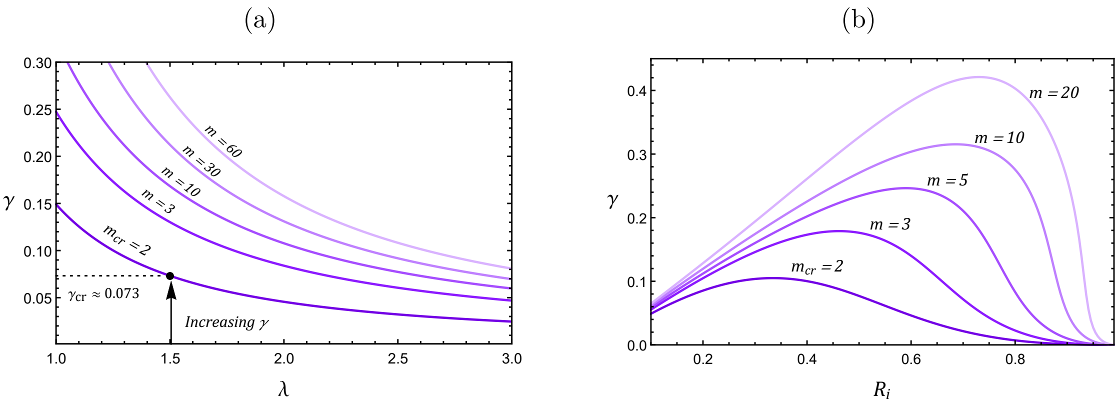

Figure 4.2: Plots of the bifurcation condition (4.27) with $J_{\rm m} = 100$ in (a) the (λ, γ) plane with $R_{\rm i} = 0.4$ and $m = 2, 3, 10, 30, 60$, and (b) the $(R_{\rm i}, \gamma)$ plane with $\lambda = 1.25$ fixed and $m = 2, 3, 5, 10, 20$.

We then plot in Fig. 4.3 the critical surface tension values $\gamma_{\rm cr}$ corresponding to $m_{\rm cr} = 2$ against (a) $R_{\rm i}$ for several fixed $\lambda \geq 1$ and (b) λ for several fixed $J_{\rm m}$. The relationship between $\gamma_{\rm cr}$ and $R_{\rm i}$ is seen in (a) to be non-monotonic for all fixed λ considered and $J_{\rm m} = 100$. Each curve has a maximum at moderate values of $R_{\rm i}$. Thus, tubes with a moderate radial thickness are less prone to the elliptic mode, whereas very thick or thin tubes are highly susceptible to it. For the range of fixed stretches considered, we see in (b) that, for a small enough $J_{\rm m}$, $\gamma_{\rm cr}$ varies non-monotonically with λ. In contrast, for a large enough $J_{\rm m}$, $\gamma_{\rm cr}$ is a decreasing function of λ in the range of fixed stretches considered. Thus, provided the extensibility limit is high enough, a greater axial stretch $\lambda \in [1, 3]$ will encourage elliptic circumferential buckling of the tube. Moreover, a larger extensibility limit will itself cause the elliptic mode the become possible earlier into the loading process.

If we instead fix $\gamma > 0$, we know that an axial stretch $\lambda < 1$ will be produced initially. It is also known that slender structures in axial compression are highly susceptible to the Euler buckling instability (Goriely et al., 2008). Since we are focussed here on circumferential buckling solutions, we choose to also apply an axial force $\mathcal{N} > 0$ so that $\lambda = 1$ initially, and then increase λ monotonically from this point. The required initial axial force $\mathcal{N}$ can be determined by substituting: $\lambda = 1$,

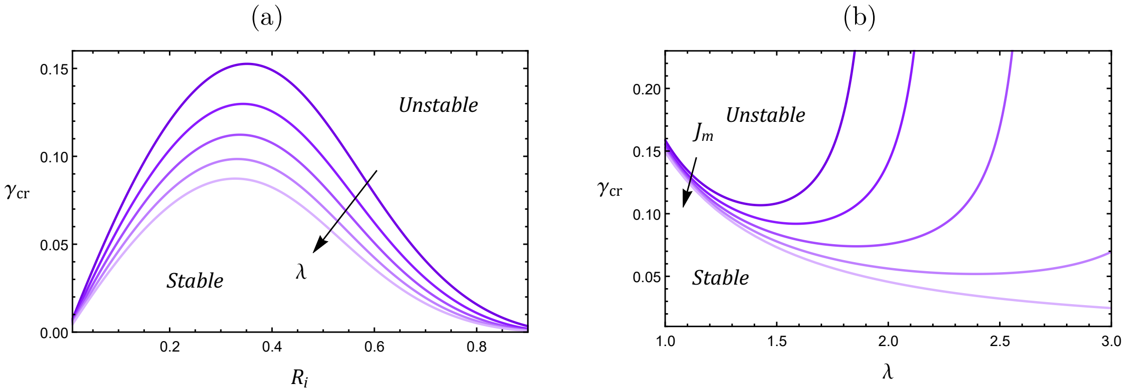

Figure 4.3: Plots of the bifurcation condition (4.27) with $m = m_{\text{cr}} = 2$ in (a) the $(R_{\text{i}}, \gamma_{\text{cr}})$ plane with $J_{\text{m}} = 100$ and $\lambda = 1, 1.1, 1.2, 1.3, 1.4$ fixed, and (b) the $(\lambda, \gamma_{\text{cr}})$ plane with $R_{\text{i}} = 0.4$ fixed and $J_{\text{m}} = 2, 3, 5, 10, 100$. Arrows indicate the direction of parameter growth.

the relevant values for γ, R_{i} and J_{m}, and the value of r_{o} determined implicitly from (3.27), into (3.26). We then plot in Fig. 4.4 (a) and (b) the bifurcation condition (4.27) in the (γ, λ) and (R_{i}, λ) plane (respectively) for several circumferential mode numbers. As in the previous loading scenario, we see that $m = 2$ is always the first mode encountered when increasing λ from unity. We also observe that, above a certain fixed surface tension value, the elliptic mode may be triggered without any increase in λ. For any value of R_{i}, this threshold value of γ is less than the minimum fixed surface tension γ_{min} required to trigger the zero wavenumber solution. As an illustrative example, we see in Fig. 4.4 (a) that for fixed $\gamma \approx 0.15$ with $R_{\text{i}} = 0.4$ and $J_{\text{m}} = 100$, bifurcation into the elliptic mode must necessarily occur at $\lambda_{\text{cr}} = 1$. In contrast, for these same values of R_{i} and J_{m}, the zero wavenumber solution cannot occur unless $\gamma \geq 6.36$. Thus, the tube is already highly unstable towards the elliptic mode in the regime of fixed γ where the zero wavenumber solution must necessarily exist, and so it is the former which is preferred. In Fig. 4.5 (a) and (b) we plot the critical stretch λ_{cr} corresponding to the preferred mode $m_{\text{cr}} = 2$ against R_{i} and J_{m} (respectively) for several fixed γ. We observe that, for larger fixed γ, the value of λ_{cr} decreases and thus the tube is more susceptible to the elliptic mode. Also, λ_{cr} is seen to vary non-monotonically with R_{i}, and λ_{cr} decreases with increasing J_{m} generally.

Finally, we apply a fixed $\mathcal{N} \geq 0$ and increase γ monotonically from zero. We observe once more in Fig. 4.6 that $m = 2$ is always the preferred mode of bifurcation.

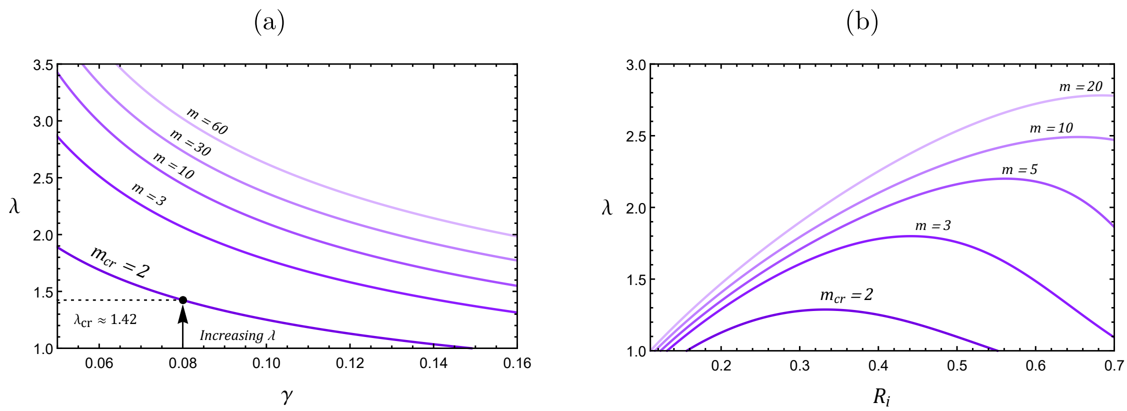

Figure 4.4: Plots of the bifurcation condition (4.27) with $J_{\mathrm{m}} = 100$ in (a) the (γ, λ) plane with $R_{\mathrm{i}} = 0.4$ and $m = 2, 3, 10, 30, 60$, and (b) the $(R_{\mathrm{i}}, \lambda)$ plane with $\gamma = 0.1$ fixed and $m = 2, 3, 5, 10, 20$.

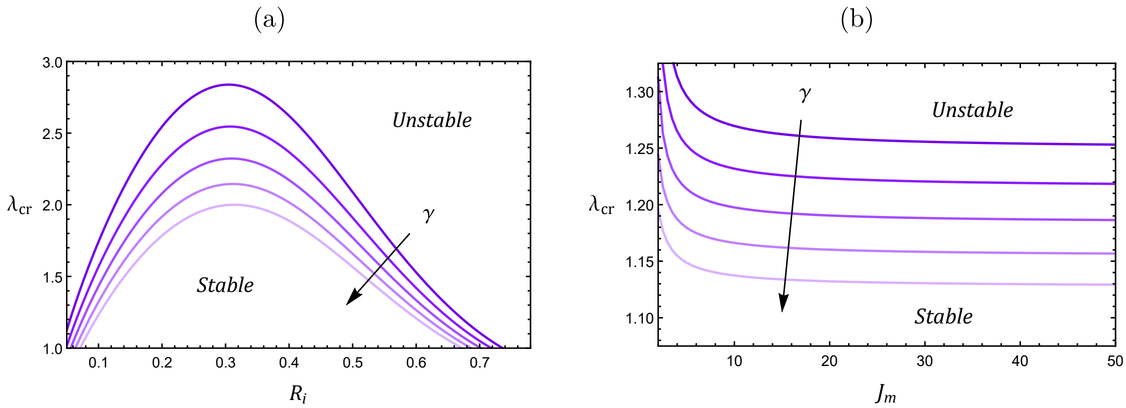

Figure 4.5: Plots of the bifurcation condition (4.27) with $m = m_{\mathrm{cr}} = 2$ in (a) the $(R_{\mathrm{i}}, \lambda_{\mathrm{cr}})$ plane with $J_{\mathrm{m}} = 100$ and the fixed γ increased from 0.03 to 0.05 in increments of 0.005, and (b) the $(J_{\mathrm{m}}, \lambda_{\mathrm{cr}})$ plane with $R_{\mathrm{i}} = 0.4$ and γ increased from 0.1 to 0.3 in increments of 0.05. Arrows indicate the direction of increase in γ.

In Fig. 4.7 (a), we see again that the corresponding γ_{cr} varies non-monotonically with R_{i}. In Fig. 4.7 (b) we observe that, as J_{m} increases above a certain value, γ_{cr} goes from being a non-monotonic function of $\mathcal{N}$ to a decreasing function of $\mathcal{N}$. In other words, for a large enough extensibility limit, a greater initial axial load destabilises the tube towards the elliptic mode. The values of γ_{cr} are found to be generally less than the corresponding values for the zero wavenumber solution, and so elliptic circumferential buckling is again the preferred bifurcation behaviour.

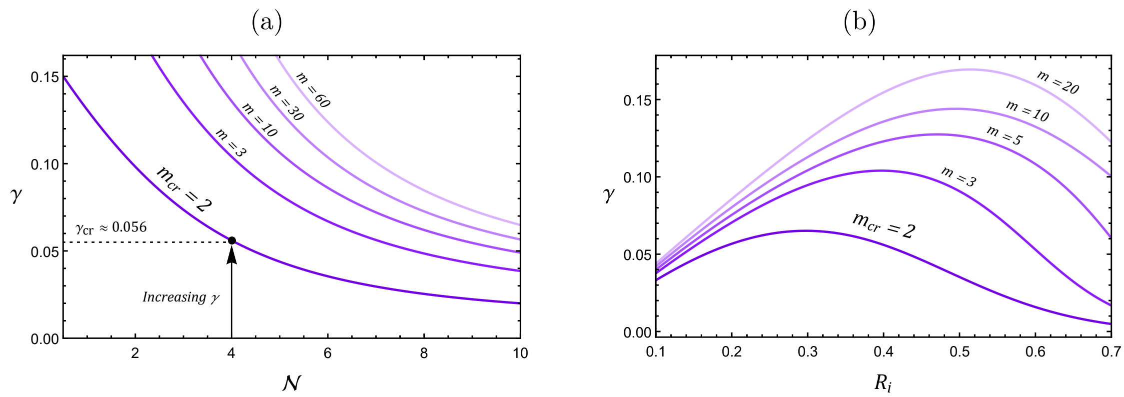

Figure 4.6: Plots of the bifurcation condition (4.27) with $J_{\text{m}} = 100$ in (a) the $(\mathcal{N}, \gamma)$ plane with $R_{\text{i}} = 0.4$ and $m = 2, 3, 10, 30, 60$, and (b) the (R_{i}, γ) plane with $\mathcal{N} = 4$ fixed and $m = 2, 3, 5, 10, 20$.

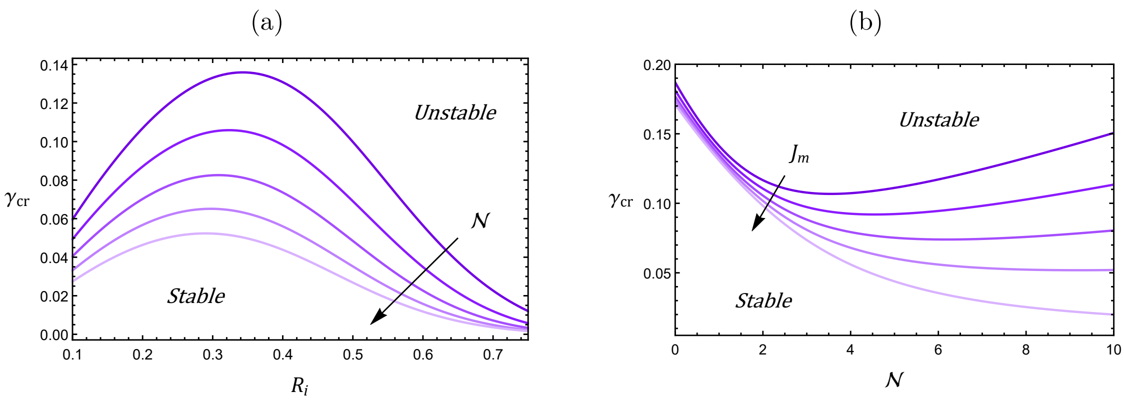

Figure 4.7: Plots of the bifurcation condition (4.27) with $m = m_{\text{cr}} = 2$ in (a) the $(R_{\text{i}}, \gamma_{\text{cr}})$ plane with $J_{\text{m}} = 100$ and $\mathcal{N}$ increased from 1 to 5 in increments of 1, and (b) the $(\mathcal{N}, \gamma_{\text{cr}})$ plane with $R_{\text{i}} = 0.4$ and $J_{\text{m}} = 2, 3, 5, 10, 100$.

4.3.2 Case 2 results

The situation in case 2 is quite different to that in case 1. For example, when fixing λ and increasing γ from zero, we see in Fig. 4.8 that no circumferential buckling bifurcation solutions can exist. The only solutions which exist correspond to negative values of surface tension, which is physically implausible. This is also found to be the case when fixing γ and varying $\mathcal{N}$, and when fixing $\mathcal{N}$ and increasing γ. Thus, circumferential buckling is not possible in case 2, and so the zero solution is generally preferred.

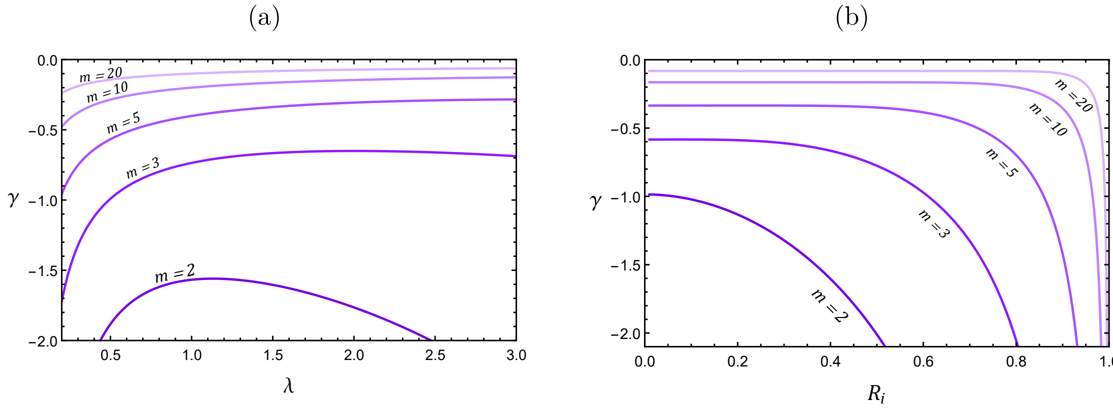

Figure 4.8: Plots of the bifurcation condition (4.27) with $m = m_{\mathrm{cr}} = 2$ in (a) the $(R_{\mathrm{i}}, \lambda_{\mathrm{cr}})$ plane with $J_{\mathrm{m}} = 100$ and the fixed γ increased from 0.03 to 0.05 in increments of 0.005, and (b) the $(J_{\mathrm{m}}, \lambda_{\mathrm{cr}})$ plane with $R_{\mathrm{i}} = 0.4$ and γ increased from 0.1 to 0.3 in increments of 0.05. Arrows indicate the direction of increase in γ.

4.3.3 Case 3 results

We begin by fixing $\gamma \geq 0$ and varying the axial force $\mathcal{N}$ monotonically from some initial value. In Fig. 4.9 (a) we plot the critical axial force $\mathcal{N}_{\mathrm{cr}}$ for circumferential buckling against γ for several extensibility limits J_{m}. When taking $\mathcal{N} = 0$ initially, circumferential buckling can occur before any axial load is applied provided that the surface tension meets a certain fixed value. For instance, for $R_{\mathrm{i}} = 0.4$ and $J_{\mathrm{m}} = 100$, we have that $\mathcal{N}_{\mathrm{cr}} = 0$ for fixed $\gamma \approx 0.45$. For fixed surface tension values below this threshold, circumferential buckling can only be triggered by reducing $\mathcal{N}$ below zero (i.e. by applying an axial *compression* to the tube). For fixed surface tension values above this threshold, the tube is highly unstable to circumferential buckling if $\mathcal{N} = 0$ initially. However, we may instead choose to apply a dead load $\mathcal{N} > 0$ to the tube initially in conjunction with the fixed surface tension, and then unload the tube from the resulting starting point. For instance, for $R_{\mathrm{i}} = 0.4$ and $J_{\mathrm{m}} = 100$ with $\gamma = 0.5$ fixed, we may also apply a dead load $\mathcal{N} = 4$ initially. We can then unload (i.e. decrease $\mathcal{N}$ from 4) until we reach the corresponding bifurcation value $\mathcal{N}_{\mathrm{cr}} \approx 0.58$; see Fig. 4.9 (a).

We observe generally in (a) that larger values of γ and J_{m} destabilize the tube towards circumferential buckling. In Fig. 4.9 (b) we plot the values of m_{cr} corresponding to the values of $\mathcal{N}_{\mathrm{cr}}$ in (a) for $J_{\mathrm{m}} = 1.1$, 5 and 100. We see that, for larger fixed γ, m_{cr} tends to 2. In Fig. 4.9 (c) and (d), we plot $\mathcal{N}_{\mathrm{cr}}$ and m_{cr} (respectively) against R_{i} for several fixed γ. In (c), we observe that for a wide range of values of R_{i}, larger values of fixed surface tension destabilize the tube towards circumferential buckling. However, above some large value of R_{i} (i.e. $R_{\mathrm{i}} \gtrsim 0.73$ in (c)), larger fixed surface tension values stabilise the tube against circumferential buckling. We see also that, for all fixed γ considered, $\mathcal{N}_{\mathrm{cr}}$ is a decreasing function of R_{i}. In other words, a greater radial thickness destabilizes the tube towards circumferential buckling. It is noted from (d) that the associated values of m_{cr} will increase with the value of R_{i} (i.e. as the tube's thickness decreases).

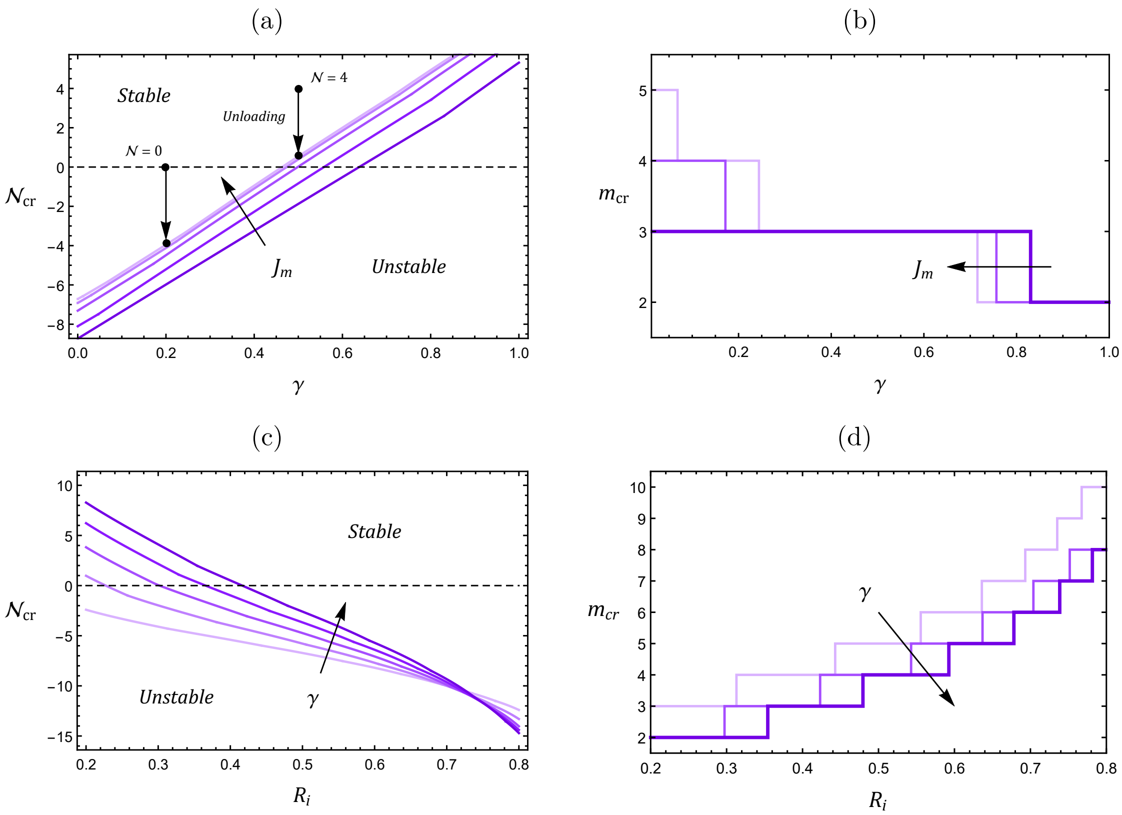

Figure 4.9: A plot of (a) $\mathcal{N}_{\mathrm{cr}}$ against γ with $R_{\mathrm{i}} = 0.4$ and $J_{\mathrm{m}} = 1.1, 2, 5, 15, 100$, (b) m_{cr} against γ with $R_{\mathrm{i}} = 0.4$ and $J_{\mathrm{m}} = 1.1, 5, 100$, (c) $\mathcal{N}_{\mathrm{cr}}$ against R_{i} with $J_{\mathrm{m}} = 50$ and $\gamma = 0.1, 0.2, 0.3, 0.4, 0.5$, and (d) m_{cr} against R_{i} with $J_{\mathrm{m}} = 50$ and $\gamma = 0.1, 0.3, 0.5$.

We now want to assess the competition between circumferential buckling and the axi-symmetric zero wavenumber bifurcation solution in this loading scenario. In Fig. 4.10 (a) we plot the critical stretches λ_{cr} for the zero wavenumber solution (blue) and circumferential buckling (purple) against $\gamma > \gamma_{\mathrm{min}}$ for several J_{m}, where

γ_{min} is the minimum surface tension for which the axi-symmetric solution can occur. We observe that, when fixing $\mathcal{N} > 0$ initially and unloading, the zero wavenumber solution will precede circumferential buckling for all values of J_{m} considered. As an illustrative example, say we fix $\gamma = 1.6$ and $\mathcal{N} \approx 14.6$ initially with $R_{\mathrm{i}} = 0.4$ and $J_{\mathrm{m}} = 100$. This produces an initial stretch $\lambda = 1.3$ to unload from; see (a). When unloading, the zero wavenumber solution must necessarily occur once λ reduces to approximately 1.12. In contrast, circumferential buckling cannot occur until λ has reduced to approximately 0.922. In Fig. 4.11 we compare the critical stretches for

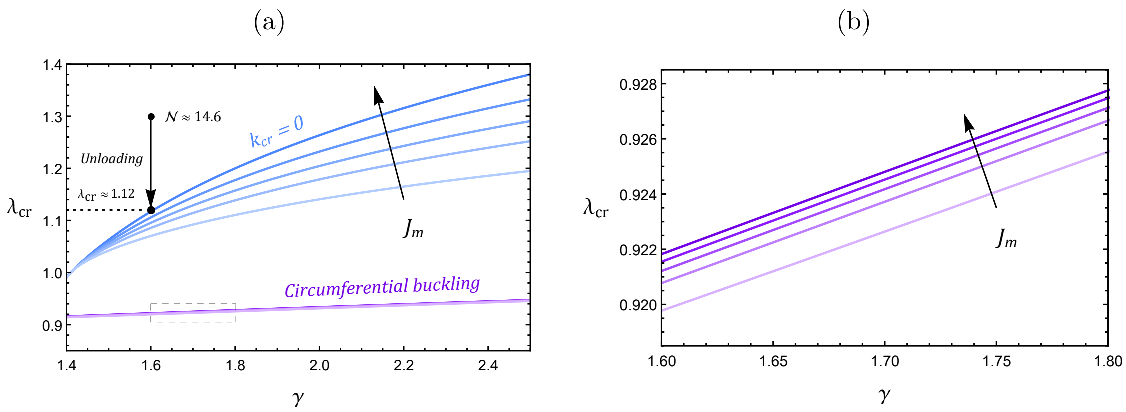

Figure 4.10: (a) A comparison of the critical stretches λ_{cr} for the zero wavenumber solution (blue) and circumferential buckling (purple) against γ with $R_{\mathrm{i}} = 0.4$ and $J_{\mathrm{m}} = 3, 6, 10, 20, 100$. (b) A blow up of the region in (a) enclosed by the dashed box.

the zero wavenumber solution and circumferential buckling for two separate values of R_{i}, and we see again that it is the former that is preferred.

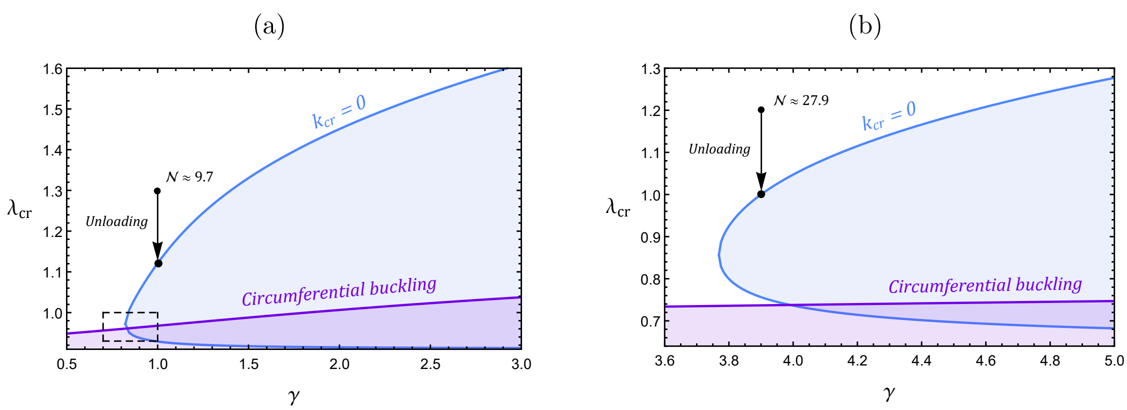

Figure 4.11: A comparison of the critical stretches λ_{cr} for the zero wavenumber solution (blue) and circumferential buckling (purple) against γ with $J_{\mathrm{m}} = 100$ and with (a) $R_{\mathrm{i}} = 0.3$ and (b) $R_{\mathrm{i}} = 0.6$.

Next, we choose to apply a fixed axial force $\mathcal{N} > 0$ initially, and then increase γ monotonically from zero. We see in Fig. 4.12 (a) and (c) that the critical surface tension $\gamma_{\rm cr}$ for circumferential buckling increases with increasing $\mathcal{N}$ and $R_{\rm i}$ and decreasing $J_{\rm m}$. Thus, a larger initial dead load or a smaller radial tube thickness or extensibility limit will stabilize the tube against circumferential buckling. In (b), we see that, for smaller (larger) values of $R_{\rm i}$, $m_{\rm cr}$ increases (decreases) with $\mathcal{N}$. From (d) we note that $m_{\rm cr}$ is minimally affected by the value of $J_{\rm m}$. In Fig. 4.13 and 4.14 we show that, as in the previous loading scenario, the zero wavenumber solution is preferred over circumferential buckling for all fixed $R_{\rm i}$, $J_{\rm m}$ and $\mathcal{N} > \mathcal{N}_{\rm min}$ considered (where $\mathcal{N}_{\rm min}$ is the minimum axial force for which the zero wavenumber solution can necessarily occur).

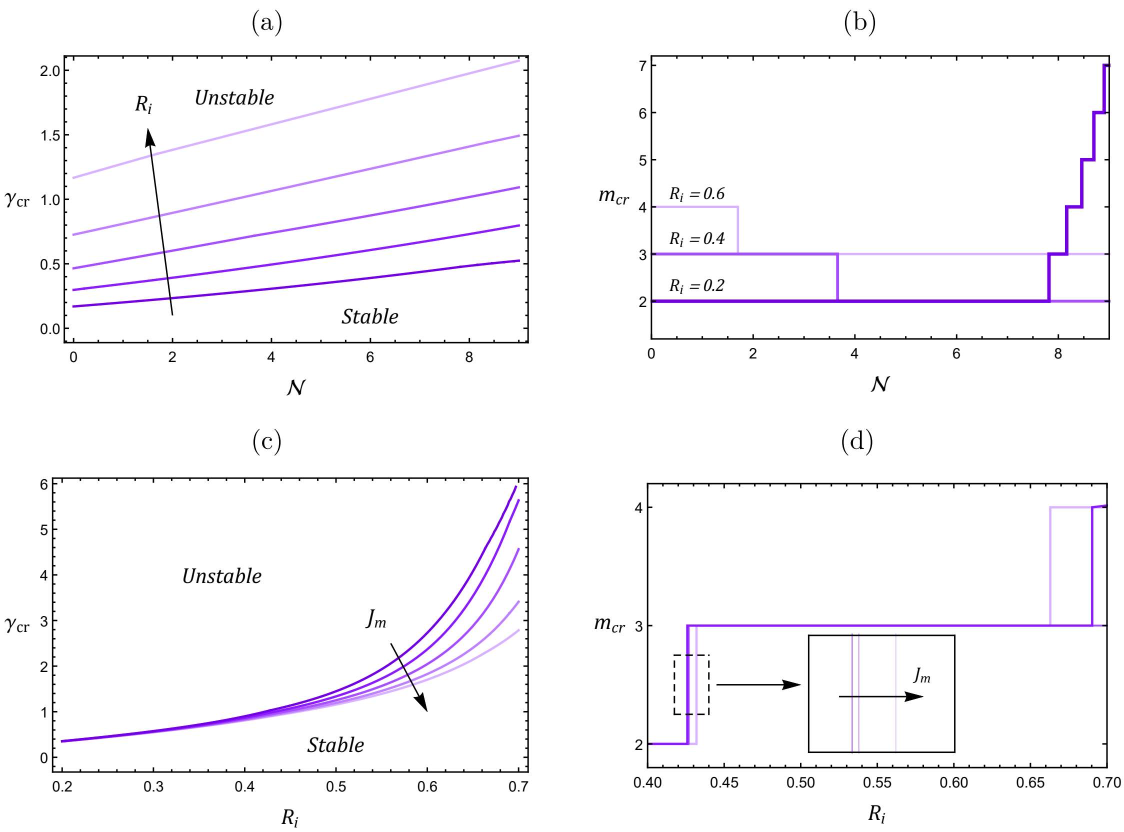

Figure 4.12: A plot of (a) $\gamma_{\rm cr}$ against $\mathcal{N}$ with $J_{\rm m} = 50$ and $R_{\rm i} = 0.2, 0.3, 0.4, 0.5, 0.6$, (b) $m_{\rm cr}$ against $\mathcal{N}$ with $J_{\rm m} = 50$ and $R_{\rm i} = 0.2, 0.6$, (c) $\gamma_{\rm cr}$ against $R_{\rm i}$ with $\mathcal{N} = 5$ and $J_{\rm m} = 2, 3, 5, 10, 30$, and (d) $m_{\rm cr}$ against A with $\mathcal{N} = 5$ and $J_{\rm m} = 2, 5, 30$.

Finally, say we fix the axial stretch λ initially and then increase γ monotonically from zero. In Fig. 4.15 (a) we present a blow up of the region inside the dashed box

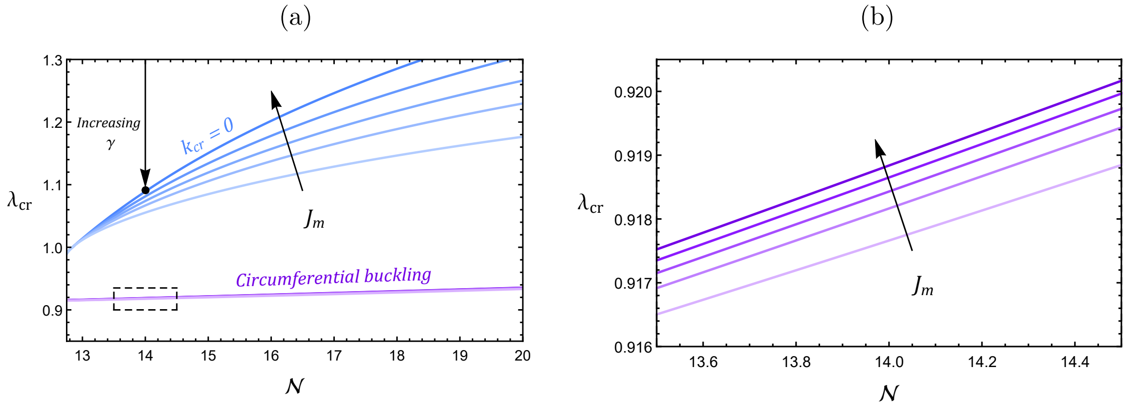

Figure 4.13: (a) A comparison of the critical stretches λ_{cr} for the zero wavenumber solution (blue) and circumferential buckling (purple) against $\mathcal{N}$ with $R_{\mathrm{i}} = 0.4$ and $J_{\mathrm{m}} = 3, 6, 10, 20, 100$. (b) A blow up of the region in (a) enclosed by the dashed box.

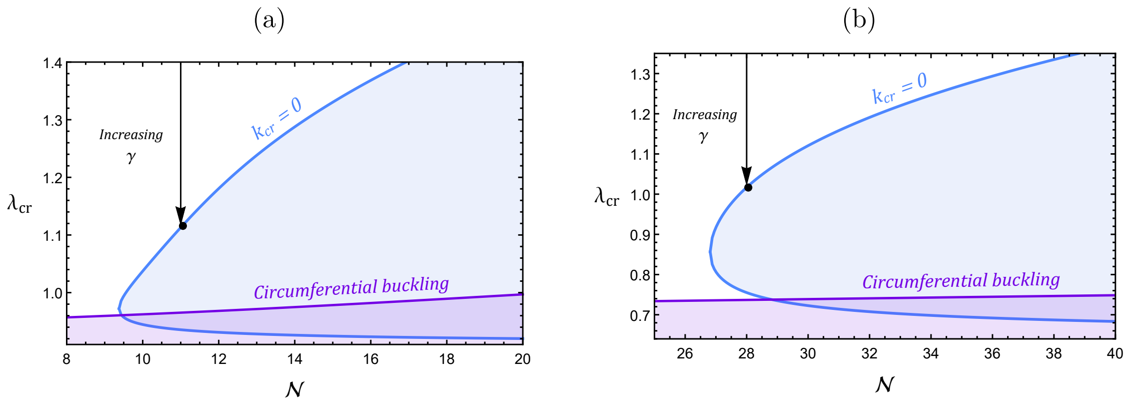

Figure 4.14: A comparison of the critical stretches λ_{cr} for the zero wavenumber solution (blue) and circumferential buckling (purple) against $\mathcal{N}$ with $J_{\mathrm{m}} = 100$ and with (a) $R_{\mathrm{i}} = 0.3$ and (b) $R_{\mathrm{i}} = 0.6$.

in Fig. 4.11 (a). We observe that there is a threshold value for the fixed λ, $\lambda_{\mathrm{th}} \approx 0.961$, above which the zero wavenumber solution is preferred over circumferential buckling, and below which circumferential buckling is preferred over the zero wavenumber solution. In Fig. 4.15 (b), we plot the dependence of λ_{th} on R_{i} for $J_{\mathrm{m}} = 100$. We observe that, for tubes with a lower radial thickness, there exists a wider range of fixed stretches for which the zero wavenumber solution is preferred when increasing γ from zero.

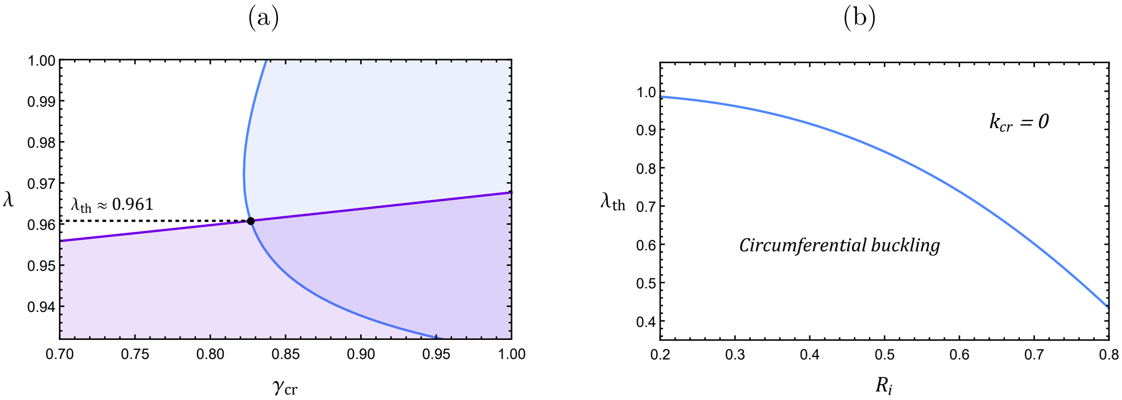

Figure 4.15: (a) A blow up of the region inside the dashed box in Fig. 4.11 (a). For $R_\mathrm{i} = 0.3$, there exists a fixed stretch threshold $\lambda_\mathrm{th} \approx 0.961$ above which the zero wavenumber solution is preferred over circumferential buckling. (b) The variation of the stretch threshold λ_th against R_i for $J_\mathrm{m} = 100$.

4.4 Discussion

The aim of the analysis in this chapter was again twofold. Firstly, we proceeded to investigate the circumferential buckling of hollow hyperelastic tubes under the effects of surface tension and a resultant axial force. Secondly, we aimed to compare the critical control parameter values associated with the axi-symmetric and circumferential buckling modes studied in order to determine the overall preferred bifurcation behaviour of the tube. We studied the same three cases of boundary conditions and types of loading as in the previous chapter. The key results in each of these scenarios are summarized in Table 4.1.

Our analysis has allowed us to determine comprehensively the conditions under which the axi-symmetric zero wavenumber solution is the preferred mode of bifurcation. Thus, we may now conduct further investigations within the confines of these conditions to determine explicitly whether this solution is associated with a localized pattern formation, and how the solution evolves through the near-critical and fully non-linear post-bifurcation regimes. This will be the focus of the next chapter.

Table 4.1: A summary of the results of the linear bifurcation analysis in section 4.3.

	Fixed λ and increasing γ	*Fixed $\gamma > 0$ and varying $\mathcal{N}$*	*Fixed $\mathcal{N} \geq 0$ and increasing γ*
Case 1	• $m_{\mathrm{cr}} = 2$ (elliptic mode) • The elliptic mode is favoured over the axi-symmetric zero wavenumber mode • Bifurcation is delayed in moderately thick tubes or in tubes with reduced extensibility	• $m_{\mathrm{cr}} = 2$ (elliptic mode) • The elliptic mode is favoured over the axi-symmetric zero wavenumber mode • Above a certain threshold value of γ, the tube is unstable to the elliptic mode without an increase in λ above 1	• $m_{\mathrm{cr}} = 2$ (elliptic mode) • The elliptic mode is favoured over the axi-symmetric zero wavenumber mode • Bifurcation is delayed in tubes with moderate-to-high thickness or in tubes with reduced extensibility
Case 2	• Circumferential buckling is physically implausible • The zero wavenumber axi-symmetric bifurcation mode is therefore preferred	• Circumferential buckling is physically implausible • The zero wavenumber axi-symmetric bifurcation mode is therefore preferred	• Circumferential buckling is physically implausible • The zero wavenumber axi-symmetric bifurcation mode is therefore preferred
Case 3	• There exists a threshold value for λ, λ_{th}, below which circumferential buckling is preferred and above which the axi-symmetric zero wavenumber mode is preferred • λ_{th} is typically below 1 and is lower for thinner tubes	• The value of m_{cr} increases with decreasing γ and decreasing tube thickness • For $\gamma > \gamma_{\mathrm{min}}$, the axi-symmetric zero wavenumber mode is favoured over circumferential buckling when unloading, but circumferential buckling is favoured when loading	• The value of m_{cr} increases with $\mathcal{N}$ for highly thick tubes, but decreases with increasing $\mathcal{N}$ in tubes with moderate-to-low thickness • For any $\mathcal{N} > \mathcal{N}_{\mathrm{min}}$, the axi-symmetric zero wavenumber mode is favoured over circumferential buckling

4.A Appendix – Coefficients in the linear eigenvalue problem

The variable coefficients $\hat{a}_i = \hat{a}_i(R)$ in (4.15) take the following form:

$$\hat{a}_1 = -\frac{2}{R} + \frac{4\,R}{\eta_1} + 2\,\omega_1 I_{0R}, \qquad \hat{a}_2 = \frac{3}{R^2} - \frac{4}{\eta_1} + \omega_2 I_{0R}^2 + \frac{4\,\omega_1\eta_2^2(R^3+3\eta)}{R^4\lambda\,\eta_1^2} = -R\hat{a}_3,$$

$$\hat{a}_4 = \frac{1}{\eta_1^2}, \qquad \hat{a}_5 = 2\left(\frac{R^2}{\eta_1^3} + \frac{1}{R^2\eta_1^3}\right) + \frac{\omega_2}{\eta_1} I_{0R}^2 + \frac{2\omega_1\eta_2^2}{R^4\eta_1^4\lambda}\left(5\eta_2^2 + 16\,R^2\eta_1\right),$$

$$\hat{a}_6 = -\omega_2\left(\frac{R}{\eta_1} + \frac{1}{R}\right) I_{0R}^2 - \frac{2\omega_1\eta_2^2(R^2+\eta_1)}{R^5\eta_1^4\lambda}\left\{6\eta_2^2 + R^2(13\eta_1 - R^2)\right\}$$

$$-\frac{3}{R^3} + \frac{2}{R\,\eta_1} + \frac{R}{\eta_1^2} - \frac{2\,R^3}{\eta_1^3}, \qquad a_7 = \frac{1}{R^2} + \frac{R^2}{\eta_1^2} - \omega_1\left(\frac{R}{\eta_1} + \frac{1}{R}\right) I_{0R}, \tag{4.28}$$

where ω_1, ω_2, η_1, η_2 and η_3 are as defined in (3.86).

The expressions for $\hat{b}_{11}$, $\hat{b}_{21}^{\pm}$, $\hat{b}_{22}$ and $\hat{b}_{23}$ in (4.19) are

$$\hat{b}_{11} = \frac{m^2R^2}{\eta_1^2}, \qquad \hat{b}_{21}^{\pm} = \frac{m^2(\eta_1+R^2)^2}{R\,\eta_1^3} - \frac{m^2\omega_1}{\eta_1} I_{0R} \pm \frac{m^2\gamma\,R\,(m^2\eta_1 - \lambda)}{2\,w_d\,r\,\eta_1^2},$$

$$\hat{b}_{22} = \frac{1}{R^2} - \frac{2}{\eta_1} - \frac{m^2}{R^2} - \frac{2\,m^2R^2}{\eta_1^2} - \frac{\omega_1}{R} I_{0,R} - \frac{m^2\omega_1}{R\,\eta_1}\left(\frac{R}{\eta_1} + \frac{1}{R}\right) I_{0R},$$

$$\hat{b}_{23} = \frac{2\,R}{\eta_1} - \frac{1}{R} + \omega_1 I_{0R}. \tag{4.29}$$

5

Localized pattern formation in soft tubes: near-critical and post-bifurcation behaviour

Contents

5.1 Introduction

In the previous two chapters, we have demonstrated that, for an incompressible hollow tube under certain types of boundary conditions and elasto-capillary-based loading, it is a non-trivial axi-symmetric solution characterized by zero wavenumber which may bifurcate from the primary state of axial tension at a critical value of the load. Specifically, this bifurcation behaviour may occur for *any* type of loading when the inner surface of the tube is fixed in the radial direction (case 2), and for *certain* types of loading when the outer surface is fixed in the radial direction (case 3). However, when both lateral surfaces are free of displacement constraints (case 1), circumferential buckling modes are preferred over this zero wavenumber solution.

The aims of this chapter are: to determine whether this zero wavenumber mode is in-fact associated with a localized pattern formation (as is suggested by the dynamical systems theory and the inflation problem); to determine whether the initial bifurcation solution arises *supercritically* or *subcritically*; and to investigate the complete evolution of the solution in the post-bifurcation regime. We naturally focus these investigations on the scenarios where the zero wavenumber solution is the preferred bifurcation behaviour. Since the analysis for case 2 and 3 is found to be near-identical, we fix our attention here solely on case 2 for the sake of brevity.

We first perform a weakly non-linear near-critical analysis. In such an analysis, we are interested in determining the relationship between the small increment of the control parameter from its bifurcation value and the amplitude of the associated first-order bifurcation solution. Fully non-linear numerical simulations conducted in Abaqus (2013) are then shown to support our linear and weakly non-linear theory. However, it will be demonstrated that our analytical expressions for the primary axial tension deformation can in-fact be applied to predict the entire bifurcation process. This offers a further source of comparison between our theory and numerical simulations.

5.2 Weakly non-linear near-critical analysis

In this section, we construct an exhaustive weakly non-linear analysis in terms of a general strain-energy function and consider the three established loading scenarios separately. To recap, we fix γ and take λ as the control parameter, we fix λ and take γ as the control parameter, or we fix $\mathcal{N}$ and take γ as the control parameter.

5.2.1 Fixed γ and monotonically varying λ

We first consider a small deviation of the axial stretch from its critical value $\lambda_{\text{cr}} \equiv \lambda_{\text{cr}}^{L}$ or λ_{cr}^{R} corresponding to the preferred axi-symmetric mode $k_{\text{cr}} = 0$. That is, we set

$$\lambda = \lambda_{\text{cr}} + \varepsilon\lambda_1, \tag{5.1}$$

where ε is a small parameter and λ_1 is a constant of $\mathcal{O}(1)$. In this near-critical regime, the bifurcation curve in the (k, λ) plane extracted from (3.52) is parabolic, and we therefore have that $\lambda - \lambda_{\text{cr}} = \mathcal{O}(k^2)$. On comparing this order relation with (5.1), we deduce that $k = \mathcal{O}(\varepsilon^{1/2})$. Then, the presence of the product kz in the exponent of the normal mode solution (3.44) motivates the introduction of a *far distance variable* s which is defined through

$$s = \varepsilon^{1/2} z. \tag{5.2}$$

Guided by Fu (2001), we now look for an asymptotic solution for the stream function ϕ, defined through (3.7), of the form

$$\phi = \phi_0 + \varepsilon^{1/2}\left\{\phi_1^{(1)}(R,s) + \varepsilon\phi_1^{(2)}(R,s) + \varepsilon^2\phi_1^{(3)}(R,s) + \mathcal{O}(\varepsilon^3)\right\}. \tag{5.3}$$

On substituting (5.3) into $(3.44)_1$, the corresponding expansions for the mixed coordinates r and Z are

$$\begin{aligned} r &= r_{0\text{cr}} + \frac{\varepsilon}{r_{0\text{cr}}}\left\{\phi_{1,s}^{(1)} - \frac{\lambda_1}{2\lambda_{\text{cr}}^2}(R^2 - R_{\text{i}}^2)\right\} + \mathcal{O}(\varepsilon^2), \\ Z &= \frac{z}{\lambda_{\text{cr}}} + \frac{\varepsilon^{1/2}}{R}\phi_{1,R}^{(1)} + \mathcal{O}(\varepsilon), \end{aligned} \tag{5.4}$$

where $r_{0\text{cr}}$ is r_0 as defined in (3.21) with $\lambda = \lambda_{\text{cr}}$. The objective is to substitute (5.3) into (3.12) and the boundary conditions associated with case 2, and equate the coefficients of like powers of ε. In doing so, we obtain a hierarchy of boundary value problems to solve, and we aim to determine an explicit solution for the first-order correction $\phi_1^{(1)}$.

At first order, we obtain the governing equation

$$\mathcal{L}\left[\phi_1^{(1)}\right] = 0, \qquad R_{\text{i}} \leq R \leq R_{\text{o}}, \tag{5.5}$$

and the boundary conditions

$$\mathcal{B}_1\left[\phi_1^{(1)}\right] = 0, \qquad R = R_{\rm o}, \tag{5.6}$$

$$\mathcal{B}_2\left[\phi_1^{(1)}\right] = 0, \qquad R = R_{\rm i},\, R_{\rm o}, \tag{5.7}$$

$$\phi_{1,s}^{(1)}(R,s) = 0, \qquad R = R_{\rm i}, \tag{5.8}$$

where the three differential operators $\mathcal{L}$, $\mathcal{B}_1$ and $\mathcal{B}_2$ are given by

$$\mathcal{L} = \frac{\partial}{\partial R}\mathcal{B}_1, \qquad \mathcal{B}_1 = \frac{1}{R}\frac{\partial}{\partial R}R\,\tilde{W}_d\,\mathcal{B}_2 \quad \text{ and } \quad \mathcal{B}_2 = \frac{\partial}{\partial R}\frac{1}{R}\frac{\partial}{\partial R}. \tag{5.9}$$

We also define $\tilde{W}_d$ as $W_d = W'(I_0(R))$ with λ replaced by $\lambda_{\rm cr}$. It is noted that (5.6) and (5.7) are obtained from (3.17) and (3.18), respectively, whilst (5.8) ensures that the first-order increment of r vanishes on $R = R_{\rm i}$; see (5.4). Through repeated integration of (5.5), the following general solution for $\phi_1^{(1)}$ is determined:

$$\phi_1^{(1)} = C_1(s)R^2 + C_2(s)\,\xi_2(R) + C_3(s)\,\xi_3(R) + C_4(s), \tag{5.10}$$

where $\quad \xi_2(R) = \displaystyle\int_{R_{\rm i}}^{R} u\int_{R_{\rm i}}^{u} t\tilde{W}_d^{-1}dtdu \quad$ and $\quad \xi_3(R) = \displaystyle\int_{R_{\rm i}}^{R} u\int_{R_{\rm i}}^{u}(t\tilde{W}_d)^{-1}dtdu. \qquad (5.11)$

In (5.11), the variable R in $\tilde{W}_d$ should be replaced by t, i.e. $\tilde{W}_d = W'(I_0(t))$. On substituting (5.10) and (5.11) into (5.7), we find that C_2 and C_3 must necessarily be zero. Additionally, (5.6) is automatically satisfied, whilst (5.8) requires that $C_4'(s) = -R_{\rm i}^2 C_1'(s)$. We may integrate the latter equation with respect to s and set the additive constant to zero since the coordinates (5.4) depend only on the partial derivatives of $\phi_1^{(1)}$. Thus, the particular first-order solution is

$$\phi_1^{(1)} = C_1(s)(R^2 - R_{\rm i}^2), \tag{5.12}$$

where $C_1(s)$ is to be determined.

At second order, the governing equation is

$$\mathcal{L}\left[\phi_1^{(2)}\right] = C_1''(s)\,p_1(R), \qquad R_{\rm i} \le R \le R_{\rm o}, \tag{5.13}$$

and the boundary conditions take the form

$$\mathcal{B}_1\left[\phi_1^{(2)}\right] = C_1''(s)\,k_1(R), \qquad R = R_{\mathrm{o}}, \tag{5.14}$$

$$\mathcal{B}_2\left[\phi_1^{(2)}\right] = C_1''(s)\,s_1(R), \qquad R = R_{\mathrm{i}},\, R_{\mathrm{o}}, \tag{5.15}$$

$$\phi_{1,s}^{(2)}(R,s) = 0, \qquad R = R_{\mathrm{i}}, \tag{5.16}$$

with the functions $p_1(R)$, $k_1(R)$ and $s_1(R)$ given in Appendix 5.A. The general solution to (5.13) is

$$\phi_1^{(2)} = D_1(s)R^2 + D_2(s)\,\xi_2(R) + D_3(s)\,\xi_3(R) + D_4(s) + C_1''(s)\mathcal{P}(R), \tag{5.17}$$

where $\mathcal{P}(R)$ is a particular integral given by

$$\mathcal{P}(R) = \int_{R_{\mathrm{i}}}^{R} x \int_{R_{\mathrm{i}}}^{x} (v\tilde{W}_d)^{-1} \int_{R_{\mathrm{i}}}^{v} u \int_{R_{\mathrm{i}}}^{u} p_1(t)\,dt\,du\,dv\,dx. \tag{5.18}$$

We note that $\mathcal{P}(R)$ cannot in general be solved analytically; instead, we evaluate it numerically using the procedure detailed in Appendix 5.B. On substituting (5.17) and (5.18) into (5.15) and (5.16), we find that D_2, D_3 and D_4 are linear in terms of D_1 and C_1''. Then, on substituting (5.17) and (5.18) into (5.14), we obtain an equation for λ_{cr} of the form

$$\frac{R_{\mathrm{o}}^2 - R_{\mathrm{i}}^2}{2}\left\{2k_1(R) - \mathcal{F}_1(R)\right\} + \mathcal{F}_2(t)\big|_{t=R_{\mathrm{i}}}^{R} = \frac{2\tilde{W}_d(R_{\mathrm{o}}^2 - R_{\mathrm{i}}^2)}{(r_{0\mathrm{cr}}\lambda_{\mathrm{cr}})^2}, \qquad R = R_{\mathrm{o}}, \tag{5.19}$$

where the functions $\mathcal{F}_1(R)$ and $\mathcal{F}_2(R)$ are given by

$$\mathcal{F}_1(R) = \int_{R_{\mathrm{i}}}^{R} p_1(t)\,dt \quad \text{and} \quad \mathcal{F}_2(R) = \int_{R_{\mathrm{i}}}^{R} u \int_{R_{\mathrm{i}}}^{u} p_1(t)\,dt\,du. \tag{5.20}$$

We find that (5.19) is numerically equivalent to our conjectured condition (3.36) for localized pattern formation when the Gent material model (2.63) is employed; see Fig. 5.1. In contrast, when the neo-Hookean model (2.58) is used, the condition (3.36) can in-fact be recovered in closed form.

The third order governing equation is expressible as

$$\mathcal{L}\left[\phi_1^{(3)}\right] = D_1''(s)p_1(R) + C_1''''(s)p_2(R) + \bar{C}_1(s)p_3(R), \qquad R_{\mathrm{i}} \le R \le R_{\mathrm{o}}, \tag{5.21}$$

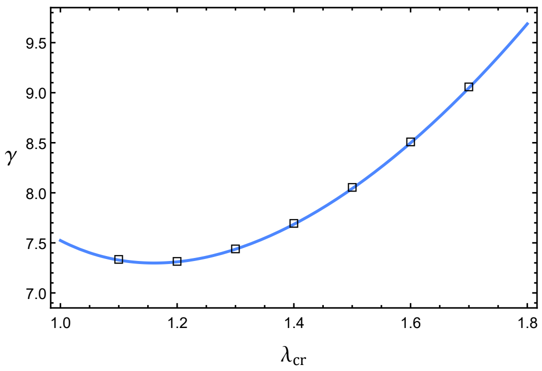

Figure 5.1: A comparison of the conjectured condition (3.36) for localized pattern formation (blue curve) and the explicit bifurcation condition (5.19) corresponding to $k_{\mathrm{cr}} = 0$ (black squares) for the Gent material model (2.63) with $R_{\mathrm{i}} = 0.4$ and $J_{\mathrm{m}} = 100$.

where $\bar{C}_1(s) = C_1''(s)(\lambda_1 - 2\lambda_{\mathrm{cr}}^2 C_1'(s))$. The associated boundary conditions are

$$\mathcal{B}_1\left[\phi_1^{(3)}\right] = D_1''(s)k_1(R) + C_1''''(s)k_2(R) + \bar{C}_1(s)k_3(R), \qquad R = R_{\mathrm{o}}, \tag{5.22}$$

$$\mathcal{B}_2\left[\phi_1^{(3)}\right] = D_1''(s)s_1(R) + C_1''''(s)s_2(R) + \bar{C}_1(s)s_3(R), \qquad R = R_{\mathrm{i}},\ R_{\mathrm{o}}, \tag{5.23}$$

$$\phi_{1,s}^{(3)}(R,s) = 0, \qquad R = R_{\mathrm{i}}. \tag{5.24}$$

The expressions for $p_{\bar{m}}(R)$, $k_{\bar{m}}(R)$ and $s_{\bar{m}}(R)$ ($\bar{m} = 2, 3$) are extremely lengthy, and so obtaining the desired amplitude equation by directly solving the system (5.21) - (5.24) is an arduous task. A simpler approach is to use the fact that, since the homogeneous form of (5.21) - (5.24) has a non-trivial solution, the inhomogeneous terms on the right-hand side of (5.21) - (5.23) must satisfy a solvability condition. In-fact, for sufficiently smooth functions $f(R)$ and $g(R)$, there exists an identity

$$\int_{R_{\mathrm{i}}}^{R_{\mathrm{o}}} \{g\mathcal{L}[f] - f\mathcal{L}[g]\}\, dR = \left[g\mathcal{B}_1[f] - f\mathcal{B}_1[g] + f'\tilde{W}_d\mathcal{B}_2[g] - g'\tilde{W}_d\mathcal{B}_2[f]\right]_{R_{\mathrm{i}}}^{R_{\mathrm{o}}}, \tag{5.25}$$

which is subject to the additional constraints $f(R_{\mathrm{i}}) = 0$ and $g(R_{\mathrm{i}}) = 0$ to prevent terms involving the surface tension boundary condition operator $\mathcal{B}_1$ being evaluated at $R = R_{\mathrm{i}}$. The identity (5.25) implies that the operator $\mathcal{L}$ is self-adjoint, and we prove its existence in Appendix 5.C.

More specifically, we may set g equal to the first-order solution (5.12) and $f = \phi_1^{(\bar{m})}$, with $\bar{m} = 2, 3$, in (5.25). Then, (5.25) reduces to

$$\int_{R_{\mathrm{i}}}^{R_{\mathrm{o}}} (R^2 - R_{\mathrm{i}}^2)\mathcal{L}\left[\phi_1^{(\bar{m})}\right] dR = \left[(R^2 - R_{\mathrm{i}}^2)\mathcal{B}_1\left[\phi_1^{(\bar{m})}\right] - 2R\tilde{W}_d\mathcal{B}_2\left[\phi_1^{(\bar{m})}\right]\right]_{R_{\mathrm{i}}}^{R_{\mathrm{o}}}, \tag{5.26}$$

and we note that $\mathcal{L}[\phi_1^{(\bar{m})}]$, $\mathcal{B}_1[\phi_1^{(\bar{m})}]$ and $\mathcal{B}_2[\phi_1^{(\bar{m})}]$ are each equal to expressions which involve only lower order solutions.

On setting $\bar{m} = 2$ in (5.26) and equating coefficients of C_1'', we obtain an equation which is found to also be numerically equivalent to our conjectured condition (3.36) for localized pattern formation when the Gent material model is deployed. Thus, the case $\bar{m} = 2$ offers a further consistency check on our derivations. On substituting $\bar{m} = 3$ in (5.26), we yield the desired amplitude equation. By integrating once and setting the arbitrary constant to zero for decay solutions, we obtain

$$\mathcal{A}'' = \lambda_1\kappa_1\mathcal{A} + \kappa_2\mathcal{A}^2, \qquad \text{where} \qquad \mathcal{A} \equiv \mathcal{A}(s) = C_1'(s), \tag{5.27}$$

and the coefficients κ_1 and κ_2 are discussed below.

5.2.1.1 Analysis of the amplitude equation

The special relationship $\kappa_2 = -\lambda_{\rm cr}^2\kappa_1$ is found to exist between the coefficients κ_1 and κ_2 in (5.27), and this can be explained as follows. On substituting (5.3) into $F\boldsymbol{E}_Z \cdot \boldsymbol{e}_z$, where F is given by (3.8), the following expansion for the principal axial stretch is determined to $\mathcal{O}(\varepsilon)$:

$$\lambda = \lambda_{\rm cr} + \varepsilon\left\{\lambda_1 - 2\lambda_{\rm cr}^2\mathcal{A}(s)\right\}. \tag{5.28}$$

As is now established, the bifurcation points $\lambda_{\rm cr} = \lambda_{\rm cr}^L$ and $\lambda_{\rm cr} = \lambda_{\rm cr}^R$ occur respectively at the local maximum and minimum of the resultant axial force $\mathcal{N}$ when $\gamma > \gamma_{\rm min}$ is fixed. Thus, the $\mathcal{N} = \mathcal{N}(\lambda)$ curve must be parabolic in a small neighbourhood of $\lambda = \lambda_{\rm cr}$ and, provided the amplitude $\mathcal{A}$ is constant and non-zero, (5.1) and (5.28) are two near-critical solutions which must be equidistant from $\lambda_{\rm cr}$ and yield the same value of $\mathcal{N}$. That is, we must have

$$\lambda_{\rm cr} - \left(\lambda_{\rm cr} + \varepsilon\left\{\lambda_1 - 2\lambda_{\rm cr}^2\mathcal{A}\right\}\right) = (\lambda_{\rm cr} + \varepsilon\lambda_1) - \lambda_{\rm cr}, \tag{5.29}$$

and from this we obtain $\mathcal{A} = \lambda_1/\lambda_{\rm cr}^2$. Then, on substituting this expression back into (5.27), the relation $\kappa_2 = -\lambda_{\rm cr}^2\kappa_1$ follows.

Whilst the determined expression for κ_1 is analytical, it contains several integrals which cannot be evaluated explicitly. Thus, for the chosen material model, these integrals must be evaluated numerically using the same approach as detailed in Appendix 5.B. Nevertheless, by the following interpretation, we expect that κ_1 is negative (positive) for any $\lambda_{\rm cr} = \lambda_{\rm cr}^L < \lambda_{\rm min}$ ($\lambda_{\rm cr} = \lambda_{\rm cr}^R > \lambda_{\rm min}$) such that $\gamma > \gamma_{\rm min}$ is fixed. That is, we expect that κ_1 is negative when "loading" and positive when "unloading". Consider the linearized form of the amplitude equation (5.27). On assuming a solution of the form $\mathcal{A} = e^{\alpha_1 s}$, the spectral parameter α_1 is found to take the non-trivial values $\alpha_1 = \pm\sqrt{\lambda_1\kappa_1}$. We note that these are the same α_1 from the spectral analysis in section 3.4.4 of chapter 3 defined analytically in the near-critical regime. From the spectral analysis, we expect that periodic solutions (i.e. purely imaginary α_1) are possible only *beyond* the bifurcation point when progressing along the chosen loading path. In contrast, we expect that the values α_1 are real *before* we reach the bifurcation point; see Fig. 3.25 (b). Also, on referring back to Fig. 3.5 (a), we note that, when "loading", the region beyond (before) the bifurcation point $\lambda_{\rm cr} = \lambda_{\rm cr}^L$ is defined by $\lambda_1 > 0$ ($\lambda_1 < 0$). However, when "unloading", the region beyond (before) the bifurcation point $\lambda_{\rm cr} = \lambda_{\rm cr}^R$ corresponds to $\lambda_1 < 0$ ($\lambda_1 > 0$). Thus, for α_1 to take its expected form, we must have $\kappa_1 < 0$ when "loading" and $\kappa_1 > 0$ when "unloading". This is fully supported by our numerical calculations of κ_1 which are presented in Fig. 5.2 for a representative case.

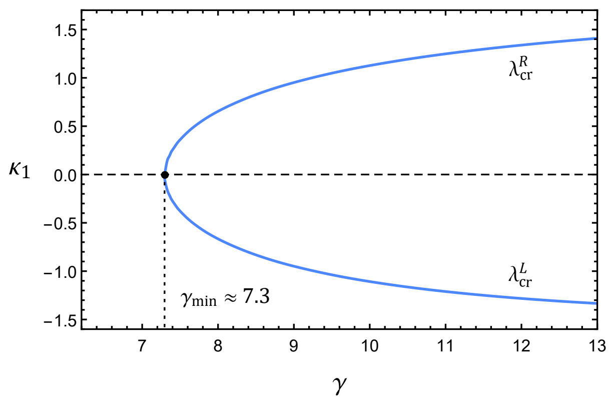

Figure 5.2: A plot of the coefficient κ_1 in (5.27) against γ for the Gent material model (2.63) with $R_{\rm i} = 0.4$ and $J_{\rm m} = 100$. The branch beneath the γ axis gives the values of κ_1 corresponding to $\lambda_{\rm cr} = \lambda_{\rm cr}^L$ (i.e. the bifurcation points encountered when "loading"). The branch above the γ axis gives the values of κ_1 associated with the bifurcation points $\lambda = \lambda_{\rm cr}^R$ encountered when "unloading". In the limit $(\lambda_{\rm cr}, \gamma) \to (\lambda_{\rm min}, \gamma_{\rm min})$, we observe that $\kappa_1 \to 0$.

The amplitude equation (5.27) does indeed admit a *localized* standing solitary wave solution of the form

$$\mathcal{A}(s) = -\frac{3\lambda_1\kappa_1}{2\kappa_2}\operatorname{sech}^2\left(\frac{1}{2}\sqrt{\lambda_1\kappa_1}s\right). \tag{5.30}$$

Given the behaviour of κ_1 illustrated in Fig. 5.2, we deduce by inspection that (5.30) exists only for $\lambda_1 < 0$ when "loading" and $\lambda_1 > 0$ when "unloading". That is, the localized bifurcation solution (5.30) emerges *subcritically* in both scenarios. Explicitly, (5.30) is a dark solitary wave (localized necking) when "loading" and a bright solitary wave (localized bulging) when "unloading". On substituting (5.12) with (5.30) into (5.4), we obtain the corresponding displacement profiles which are plotted in each case in Fig. 5.3.

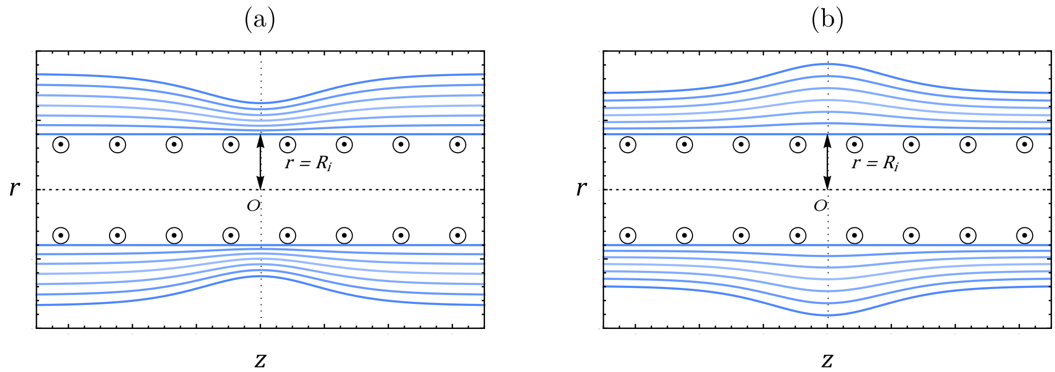

Figure 5.3: Displacement profiles associated with the (a) localized necking and (b) localized bulging solutions which initiate at the critical values λ_{cr}^{L} when "loading" and λ_{cr}^{R} when "unloading", respectively. We fix $R_{\text{i}} = 0.4$ and $J_{\text{m}} = 100$.

As demonstrated numerically in Fig. 5.2, the coefficient $\kappa_1 \to 0$ as $(\lambda_{\text{cr}}, \gamma) \to (\lambda_{\text{min}}, \gamma_{\text{min}})$. The form of (5.30) suggests that a rescaling of the far distance variable s is required in this limit, since $\mathcal{A}$ is a constant under the current scaling. We will analyze this limiting case separately in the next section.

5.2.1.2 The limit $(\lambda_{\text{cr}}, \gamma) \to (\lambda_{\text{min}}, \gamma_{\text{min}})$

In a small neighbourhood of $\lambda_{\text{cr}} = \lambda_{\text{min}}$, the bifurcation curve in the $(\lambda_{\text{cr}}, \gamma)$ plane is parabolic, and so we have that $\lambda - \lambda_{\text{min}} = \mathcal{O}(\sqrt{\gamma - \gamma_{\text{min}}})$. Using this order relation, we may deduce the following expansions for λ and γ in this limiting case:

$$\lambda = \lambda_{\text{min}} + \varepsilon\hat{\lambda}_1 \quad \text{and} \quad \gamma = \gamma_{\text{min}} + \varepsilon^2\hat{\gamma}_1, \tag{5.31}$$

where $\hat{\lambda}_1$ and $\hat{\gamma}_1$ are constants of $\mathcal{O}(1)$. Now, on Taylor expanding the coefficient κ_1 in (5.27) about $\mathcal{Q}\colon(\lambda_{\min},\gamma_{\min})$, we find that

$$\kappa_1 = \kappa_1|_{\mathcal{Q}} + \varepsilon\hat{\lambda}_1\frac{d\kappa_1}{d\lambda}\bigg|_{\mathcal{Q}} + \mathcal{O}(\varepsilon^2). \tag{5.32}$$

Since the first term on the right-hand side of (5.32) is known to be zero, κ_1 is of $\mathcal{O}(\varepsilon)$ in this limit. Then, given the form of (5.30), it is logical to introduce the following re-scaling of the far distance variable s:

$$\hat{s} = \varepsilon^{1/2}s = \varepsilon z. \tag{5.33}$$

Also, on substituting (5.30) with (5.32) into (5.12), we find that $\phi_1^{(1)}$ is of $\mathcal{O}(\varepsilon^{-1/2})$ in this limiting case, and so we implement the following re-scaled asymptotic expansion of ϕ:

$$\phi = \phi_0 + \hat{C}_1(\hat{s})(R^2 - R_{\mathrm{i}}^2) + \varepsilon\hat{\phi}_1^{(1)} + \varepsilon^2\hat{\phi}_1^{(2)} + \varepsilon^3\hat{\phi}_1^{(3)} + \varepsilon^4\hat{\phi}_1^{(4)} + \mathcal{O}(\varepsilon^5). \tag{5.34}$$

We note that, although the expansion is non-uniform in the sense that the first and second terms are both of $\mathcal{O}(1)$, the corresponding expansion for the deformation gradient *is* uniform, making (5.34) valid.

We follow the same procedure as presented previously for the non-limiting case. At $\mathcal{O}(\varepsilon)$, we find that $\hat{\phi}_1^{(1)}$ must necessarily be zero. At $\mathcal{O}(\varepsilon^2)$, an equation is obtained which is found to be equivalent to the bifurcation condition for localized pattern formation (3.36) evaluated at $\mathcal{Q}$ (numerically for the Gent material model, but in closed form for the neo-Hookean model). At $\mathcal{O}(\varepsilon^3)$, we derive an equation which is deduced to be similarly equivalent to $d\gamma/d\lambda = 0$ evaluated at $\lambda = \lambda_{\min}$, and which is automatically satisfied. At $\mathcal{O}(\varepsilon^4)$, by setting $f = \hat{\phi}_1^{(4)}$ and $g = \hat{C}_1(\hat{s})(R^2 - R_{\mathrm{i}}^2)$ in (5.25), we arrive at the following amplitude equation for $\hat{\mathcal{A}} \equiv \hat{\mathcal{A}}(\hat{s})$:

$$\hat{\mathcal{A}}'' = (\hat{\gamma}_1\hat{\kappa}_1 + \hat{\lambda}_1^2\hat{\kappa}_2)\hat{\mathcal{A}} - 2\hat{\lambda}_1\lambda_{\min}^2\hat{\kappa}_2\hat{\mathcal{A}}^2 + \frac{4}{3}\lambda_{\min}^4\hat{\kappa}_2\hat{\mathcal{A}}^3, \tag{5.35}$$

where $\hat{\mathcal{A}}(\hat{s}) = \hat{C}_1'(\hat{s})$, and $\hat{\kappa}_1$ and $\hat{\kappa}_2$ are new constant coefficients.

Whilst we have determined explicit expressions for $\hat{\kappa}_1$ and $\hat{\kappa}_2$ which are in terms of integrals that must be evaluated numerically, simpler connections between these two coefficients can be established as follows. Firstly, on substituting $\hat{\mathcal{A}} = e^{\hat{\alpha}_1 \hat{s}}$ into the linearized form of (5.35), we obtain the expression

$$\hat{\alpha}_1^2 = \hat{\gamma}_1 \hat{\kappa}_1 + \hat{\lambda}_1^2 \hat{\kappa}_2, \tag{5.36}$$

for the spectral parameter $\hat{\alpha}_1$ which will be used repeatedly hereafter. For fixed $\hat{\gamma}_1 > 0$, the local maximum and minimum of $\mathcal{N}$ are near the point of coalescence at an inflection point. On Taylor expanding $\mathcal{N}$ around $\mathcal{Q}$, we obtain

$$\mathcal{N} = \mathcal{N}|_{\mathcal{Q}} + \varepsilon^2 \hat{\gamma}_1 \left.\frac{\partial \mathcal{N}}{\partial \gamma}\right|_{\mathcal{Q}} + \varepsilon^3 \left\{ \hat{\lambda}_1 \hat{\gamma}_1 \left.\frac{\partial^2 \mathcal{N}}{\partial \lambda \partial \gamma}\right|_{\mathcal{Q}} + \frac{1}{6} \hat{\lambda}_1^3 \left.\frac{\partial^3 \mathcal{N}}{\partial \lambda^3}\right|_{\mathcal{Q}} \right\} + \mathcal{O}(\varepsilon^4). \tag{5.37}$$

Then, with use of (5.31) and (5.37), we may solve $d\mathcal{N}/d\lambda = 0$ to obtain the following expressions for the bifurcation points $\lambda = \lambda_{\text{cr}}^L$ and λ_{cr}^R which are valid in the vicinity of $\mathcal{Q}$:

$$\lambda_{\text{cr}}^{L,R} = \lambda_{\min} + \varepsilon \hat{\lambda}_1^{L,R}, \qquad \text{where} \qquad \frac{\hat{\lambda}_1^{L,R}}{\sqrt{2\hat{\gamma}_1}} = \mp \left.\sqrt{-\frac{\partial^2 \mathcal{N}}{\partial \lambda \partial \gamma} \left(\frac{\partial^3 \mathcal{N}}{\partial \lambda^3} \right)^{-1}}\,\right|_{\mathcal{Q}}. \tag{5.38}$$

Note that the L and R correspond to the minus and plus sign, respectively, and when "loading" or "unloading", the bifurcation point of interest is $\lambda_{\text{cr}} = \lambda_{\min} + \varepsilon \hat{\lambda}_1^L$ or $\lambda_{\text{cr}} = \lambda_{\min} + \varepsilon \hat{\lambda}_1^R$, respectively.

By the spectral analysis in section 3.4.4 of chapter 3, $\hat{\alpha}_1$ must vanish in the limit $\lambda \to \lambda_{\text{cr}}$. Thus, with use of (5.36), we have that

$$\lim_{\lambda \to \lambda_{\text{cr}}} \hat{\alpha}_1 = 0 \implies \hat{\kappa}_2 = -\frac{\hat{\gamma}_1 \hat{\kappa}_1}{(\hat{\lambda}_1^L)^2} \quad \text{or} \quad \hat{\kappa}_2 = -\frac{\hat{\gamma}_1 \hat{\kappa}_1}{(\hat{\lambda}_1^R)^2}. \tag{5.39}$$

Alternatively, we may consider the following two term expansion of the bifurcation condition (3.36) around $\lambda = \lambda_{\min}$:

$$\gamma = \gamma_{\min} + \frac{1}{2} (\lambda_{\text{cr}} - \lambda_{\min})^2 \left.\frac{d^2 \gamma}{d\lambda^2}\right|_{\lambda = \lambda_{\min}}. \tag{5.40}$$

On substituting (5.31) and (5.38) into (5.40), the equivalent expressions

$$\hat{\gamma}_1 = \frac{1}{2} (\hat{\lambda}_1^L)^2 \left.\frac{d^2 \gamma}{d\lambda^2}\right|_{\lambda = \lambda_{\min}} \quad \text{or} \quad \hat{\gamma}_1 = \frac{1}{2} (\hat{\lambda}_1^R)^2 \left.\frac{d^2 \gamma}{d\lambda^2}\right|_{\lambda = \lambda_{\min}}, \tag{5.41}$$

are obtained, and since they are derived directly from the bifurcation condition, $\hat{\alpha}_1$ must also vanish in the limit $\lambda \to \lambda_{\text{cr}}$ when they are satisfied. From this condition, a second connection between $\hat{\kappa}_1$ and $\hat{\kappa}_2$ is derived which takes the form

$$\hat{\kappa}_2 = -\frac{1}{2}\hat{\kappa}_1 \frac{d^2\gamma}{d\lambda^2}\bigg|_{\lambda=\lambda_{\min}}. \tag{5.42}$$

The equivalence of (5.39) and (5.42) requires that

$$\frac{\partial^3 \mathcal{N}}{\partial \lambda^3} + \frac{\partial^2 \mathcal{N}}{\partial \gamma \partial \lambda}\frac{d^2\gamma}{d\lambda^2} = 0 \quad \text{at} \quad \mathcal{Q} : (\lambda_{\min}, \gamma_{\min}), \tag{5.43}$$

and we have verified numerically that this result holds.

The two expressions (5.39) and (5.42) can further be used to show that $\hat{\kappa}_1$ must be negative whereas $\hat{\kappa}_2$ must be positive. To illustrate, we focus on the "loading" scenario, and substitute the relevant expression from (5.39) into (5.36) to obtain

$$\hat{\alpha}_1^2 = \hat{\gamma}_1 \hat{\kappa}_1 \left\{1 - \hat{\lambda}_1^2/(\hat{\lambda}_1^L)^2\right\}. \tag{5.44}$$

The regime in the "loading" path prior to the bifurcation point is defined by $\hat{\gamma}_1 > 0$ and $\hat{\lambda}_1 < \hat{\lambda}_1^L < 0$. In this regime, we have established that $\hat{\alpha}_1^2$ must be positive. Through inspection of (5.44), we see that this is only possible if $\hat{\kappa}_1 < 0$. In contrast, the regime in the "loading" path beyond the bifurcation point is defined by $\hat{\gamma}_1 > 0$ and $\hat{\lambda}_1^L < \hat{\lambda}_1 < 0$. In this regime, we require that $\hat{\alpha}_1^2$ is negative, and so $\hat{\kappa}_1$ must remain negative. An analogous interpretation exists when "unloading", and the requirement that $\hat{\kappa}_1$ be negative remains true. The general negativity of $\hat{\kappa}_1$ implied by these interpretations is fully supported by our numerical computations of its explicit expression; see Fig. 5.4. The second connection (5.42) then implies that $\hat{\kappa}_2$ must be positive.

Alternatively, (5.35) can be expressed as the following one-degree-of-freedom Hamiltonian system:

$$\hat{\mathcal{A}}'' = -\frac{d\hat{\mathcal{V}}}{d\hat{\mathcal{A}}}, \qquad \text{where} \qquad \hat{\mathcal{V}} = -\frac{1}{3}\lambda_{\min}^4 \hat{\kappa}_2 \hat{\mathcal{A}}^2(\hat{\mathcal{A}} - \hat{\mathcal{A}}_0^+)(\hat{\mathcal{A}} - \hat{\mathcal{A}}_0^-), \tag{5.45}$$

is the potential energy function whose non-trivial ground states $\hat{\mathcal{A}}_0^{\pm}$ are given by

$$\hat{\mathcal{A}}_0^{\pm} = \frac{1}{\lambda_{\min}^2}\left\{\hat{\lambda}_1 \pm \sqrt{-\frac{1}{2\hat{\kappa}_2}\left(3\hat{\gamma}_1\hat{\kappa}_1 + \hat{\lambda}_1^2\hat{\kappa}_2\right)}\right\}. \tag{5.46}$$

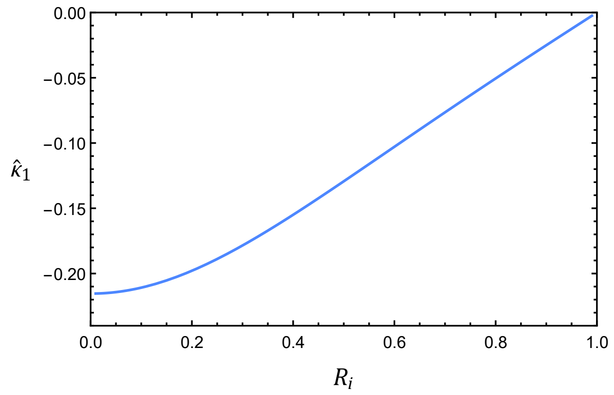

Figure 5.4: A plot of the coefficient $\hat{\kappa}_1$ in (5.35) against $R_{\rm i}$ with the neo-Hookean material model employed.

The non-trivial fixed points $\hat{\mathcal{A}}^{\pm}$ of the system (5.45) are obtained from the equation $d\hat{\mathcal{V}}/d\hat{\mathcal{A}} = 0$, and may be expressed through

$$\lambda_{\min}^2 \hat{\mathcal{A}}^{\pm} = \frac{3}{4}\left\{\hat{\lambda}_1 \pm \sqrt{\hat{\lambda}_1^2 - \frac{4}{3}\left(\hat{\lambda}_1^2 + \frac{\hat{\kappa}_1}{\hat{\kappa}_2}\hat{\gamma}_1\right)}\right\}. \tag{5.47}$$

Equation (5.45) admits a localized solution if and only if the following two conditions are satisfied:

$$\hat{\kappa}_1\hat{\gamma}_1 + \hat{\kappa}_2\hat{\lambda}_1^2 > 0, \qquad 3\hat{\kappa}_1\hat{\gamma}_1 + \hat{\kappa}_2\hat{\lambda}_1^2 \leq 0. \tag{5.48}$$

Firstly, given the form of the linear term on the right-hand side of (5.35), the condition $(5.48)_1$ ensures that the solution to (5.45) is exponentially decaying in the limit $\hat{s} \to \pm\infty$, and hence localized. Secondly, $(5.48)_1$ makes certain that the fixed points $\hat{\mathcal{A}}^{\pm}$ given in (5.47) are real and non-zero. The inequality $(5.48)_2$ must also be satisfied so that the ground states $\hat{\mathcal{A}}_0^{\pm}$ are real. On combining the inequalities in (5.48), we obtain the following range of values of $\hat{\lambda}_1$ for which a localized solution to (5.45) can exist:

$$\sqrt{3}\hat{\lambda}_1^L < \hat{\lambda}_1 < \hat{\lambda}_1^L \quad \text{and} \quad \hat{\lambda}_1^R < \hat{\lambda}_1 < \sqrt{3}\hat{\lambda}_1^R. \tag{5.49}$$

A localized solution to (5.45) is given explicitly by

$$\hat{\mathcal{A}}(\hat{s}) = \frac{\hat{\mathcal{A}}_0^+\hat{\mathcal{A}}_0^-(1-\zeta^2)}{\hat{\mathcal{A}}_0^+ - \hat{\mathcal{A}}_0^-\zeta^2}, \qquad \text{where} \qquad \zeta(\hat{s}) = \tanh\left(-\sqrt{\frac{\hat{\kappa}_2\hat{\mathcal{A}}_0^+\hat{\mathcal{A}}_0^-}{6}}\lambda_{\min}^2\hat{s}\right). \tag{5.50}$$

We first look to analyze how this solution varies across the domain of existence (5.49). In Fig. 5.5 (a) and (b), we plot the magnitude of (5.50) against $\hat{s}$ in the limits $\hat{\lambda}_1 \to \sqrt{3}\hat{\lambda}_1^L$ or $\hat{\lambda}_1 \to \sqrt{3}\hat{\lambda}_1^R$, and $\hat{\lambda}_1 \to \hat{\lambda}_1^L$ or $\hat{\lambda}_1 \to \hat{\lambda}_1^R$, respectively. We see in (a) that, as $\hat{\lambda}_1$ approaches $\sqrt{3}\hat{\lambda}_1^L$ or $\sqrt{3}\hat{\lambda}_1^R$, the localized solution develops a plateau at its peak which grows in the axial direction. In contrast, in the limit $\hat{\lambda}_1 \to \hat{\lambda}_1^L$ or $\hat{\lambda}_1^R$, the localized solution's amplitude decays to zero, whilst spreading out in the axial direction in tandem.

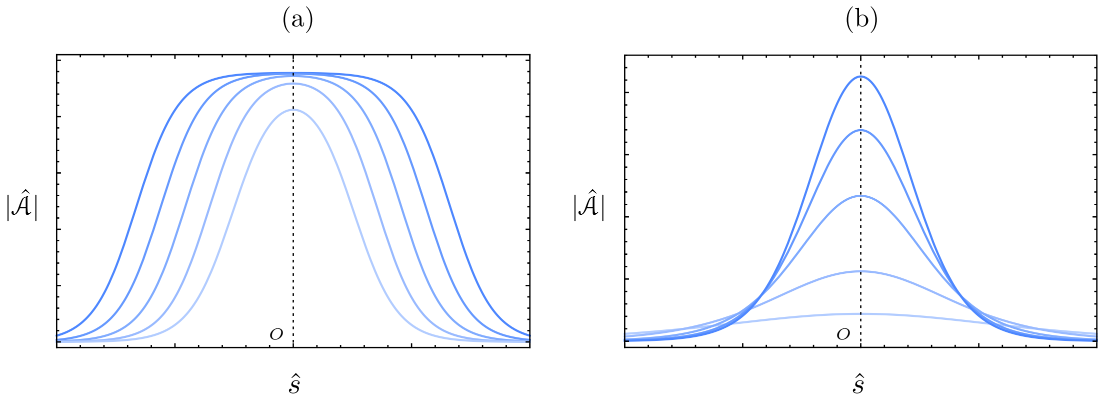

Figure 5.5: Plots of the absolute value of the solution (5.50) against $\hat{s}$ in the limits (a) $\hat{\lambda}_1 \to \sqrt{3}\hat{\lambda}_1^{L,R}$ and (b) $\hat{\lambda}_1 \to \hat{\lambda}_1^{L,R}$. In (a), curves with darker shades of blue correspond to values of $\hat{\lambda}_1$ closer to $\sqrt{3}\hat{\lambda}_1^L$ or $\sqrt{3}\hat{\lambda}_1^R$. In (b), curves with lighter shades of blue correspond to values of $\hat{\lambda}_1$ closer to $\hat{\lambda}_1^L$ or $\hat{\lambda}_1^R$.

To provide further insights, we investigate in Fig. 5.6 the variation of the potential $\hat{\mathcal{V}}$ with respect to $\hat{\mathcal{A}}$, as well as the associated phase plane, both near and away from $\hat{\lambda}_1 = \sqrt{3}\hat{\lambda}_1^L$ or $\hat{\lambda}_1 = \sqrt{3}\hat{\lambda}_1^R$. We first note that there exists a local minimum of $\hat{\mathcal{V}}$ at $\hat{\mathcal{A}} = \hat{\mathcal{A}}^-$ which corresponds to a center in phase space; see Fig. 5.6 (a) and (b). Away from $\hat{\lambda}_1 = \sqrt{3}\hat{\lambda}_1^L$ or $\sqrt{3}\hat{\lambda}_1^R$, this center is enclosed by a homoclinic orbit which connects the ground state $\hat{\mathcal{A}}_0^-$ to the origin. However, as we move beyond the bifurcation point on the desired loading path (i.e. for $\hat{\lambda}_1 > \hat{\lambda}_1^L$ when "loading" or for $\hat{\lambda}_1 < \hat{\lambda}_1^R$ when "unloading"), $\hat{\mathcal{A}}_0^-$ coalesces with the origin and the center $\hat{\mathcal{A}}^-$ ceases to exist. In the limit $\hat{\lambda}_1 \to \sqrt{3}\hat{\lambda}_1^L$ or $\sqrt{3}\hat{\lambda}_1^R$, the local maximum of $\hat{\mathcal{V}}$ at $\hat{\mathcal{A}}^+$, which corresponds to a saddle, moves onto the $\hat{\mathcal{V}} = 0$ axis, and coalesces with the ground states $\hat{\mathcal{A}}_0^\pm$ in tandem; see (c). In phase space, the homoclinic orbit discussed previously degenerates into a heteroclinic orbit connecting $\hat{\mathcal{A}}^+ = \hat{\mathcal{A}}_0^{\pm}$ to the origin; see (d). It is noted that such a heteroclinic orbit can never exist in reality since it may only be defined on an infinite domain. However, the homoclinic solutions close to this heteroclinic orbit can exist in reality, and we refer to these as *kink-wave solutions*. Physically, the *kink-wave solutions* to our problem manifest themselves through the separation of the tube into two regions, or "states", with distinct yet uniform axial stretch

$$\lambda_{L,R} = \lambda_{\min} + \sqrt{3}\varepsilon\hat{\lambda}_1^{L,R}, \tag{5.51}$$

connected by a smooth yet sharp transition zone. Thus, the emergence of a kink-wave configuration is often referred to as a *phase-separation-like phenomenon*.

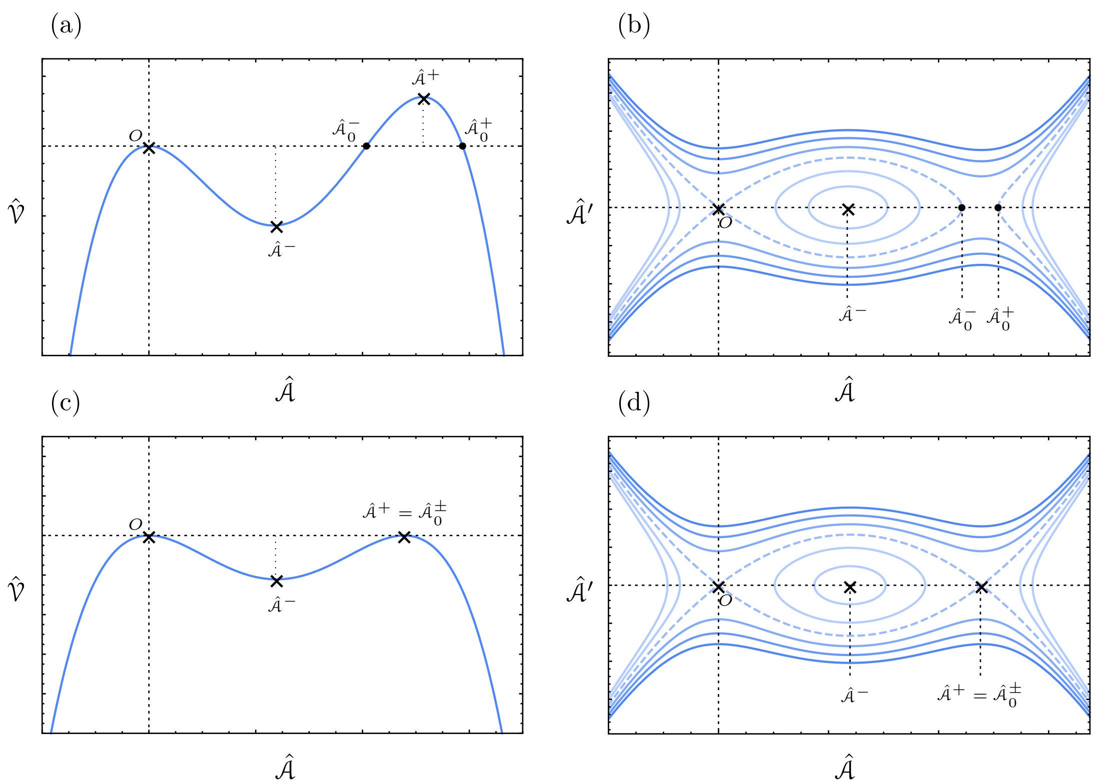

Figure 5.6: Plots of the potential $\hat{\mathcal{V}}$ against $\hat{\mathcal{A}}$ for (a) $\hat{\lambda}_1$ away from $\sqrt{3}\hat{\lambda}_1^L$ or $\sqrt{3}\hat{\lambda}_1^R$, and (c) at $\hat{\lambda}_1 = \sqrt{3}\hat{\lambda}_1^L$ or $\sqrt{3}\hat{\lambda}_1^R$. The plots of $\hat{\mathcal{A}}'$ against $\hat{\mathcal{A}}$ in (b) and (d) give the respective phase planes. In each plot, the fixed points $\hat{\mathcal{A}}^{\pm}$ are marked with black crosses, whereas the ground states $\hat{\mathcal{A}}_0^{\pm}$ are marked with black dots.

The question then is: how do we physically interpret the aforementioned variation in bifurcation behaviour across the domain of existence? Since we first encounter $\hat{\lambda}_1 = \sqrt{3}\hat{\lambda}_1^L$ when "loading" or $\hat{\lambda}_1 = \sqrt{3}\hat{\lambda}_1^R$ when "unloading", we could say intuitively that the initial bifurcation is from the primary state of axial tension to a fully developed kink-wave solution. However, bifurcations of this nature can only be expected to occur if the perturbations applied to the tube are large in amplitude (Ericksen, 1975). Since our axial loading is assumed to be extremely controlled, such a transition is physically infeasible. We may instead conjecture that the bifurcation behaviour follows the same pattern of initiation, growth and propagation that is observed in the mathematically similar inflation problem.

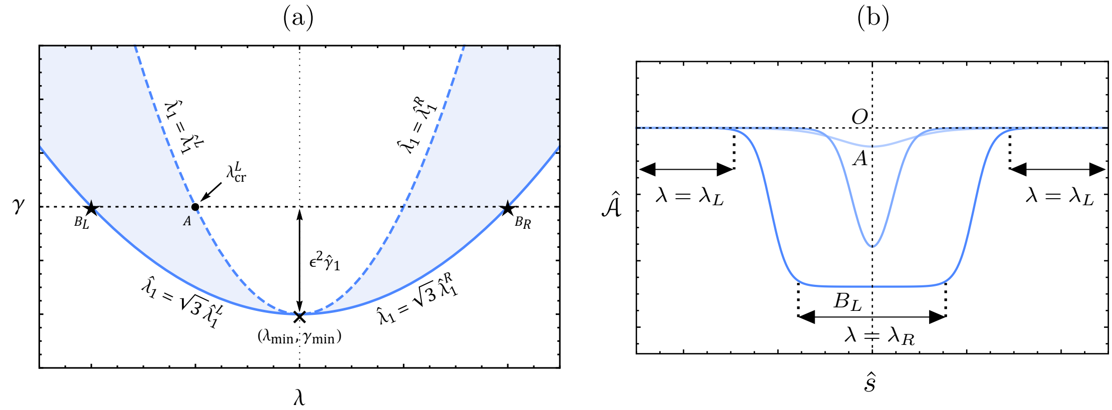

Figure 5.7: (a) A schematic of the interval of existence (5.49) of the localized solution (5.50) (light blue region). Say we fix $\hat{\gamma}_1 > 0$ with $\mathcal{N} = 0$ initially (i.e. we enforce the "loading" scenario). Then, as λ is increased, we move along the horizontal dotted black line from left to right. The initial bifurcation occurs sub-critically as we approach the black dot labelled "A" at $\lambda = \lambda_{\text{cr}}^L$, and takes the form of a localized neck (as shown by the corresponding curve in (b)). On increasing the overall stretch beyond λ_{cr}^L, a transition to a kink-wave solution as shown by the lower curves in (b) is expected, and the stretches λ_L and λ_R associated with the kink-wave configuration are marked by the black stars in (a).

As an illustrative example, say we fix $\hat{\gamma}_1 > 0$ with $\mathcal{N} = 0$ initially, and then apply a "loading" to the tube. We conjecture that the initial bifurcation will occur in the limit $\hat{\lambda}_1 \to \hat{\lambda}_1^L$ (i.e. at the point labelled "A" in Fig. 5.7 (a)), and this will arise subcritically since we must have $\hat{\lambda}_1 < \hat{\lambda}_1^L$ by (5.49). Specifically, the solution will be localized necking, and the corresponding amplitude can be seen through the curve labelled "A" in Fig. 5.7 (b). Then, we expect that any further small positive increment in axial stretch will cause a "snap-back" to the point labelled "B_L" in (a). During this "snap-back", the amplitude of the localized neck will first grow to a near maximum state; see the middle blue curve in (b). This will then be followed by an axial propagation of the necking solution into a “two-phase” state consisting of a “thin” section centred at $z = 0$ with stretch λ_R, in between two “thick” sections with stretch λ_L. Recall that the distinct stretches λ_L and λ_R are given in (5.51), and they are situated respectively at the black stars labelled “B_L” and “B_R” in (a). These thick and thin sections are connected by a sharp, smooth transition region whose length is assumed to be negligible, and the *overall averaged axial stretch* of the tube is $\lambda_{\rm cr}^L$ plus the small positive increment alluded to previously.

Whether the transition from localized necking to kink-wave solution is sudden or gradual depends largely on the stability of the solution (5.50) which we do not study in this thesis. If we were “unloading”, the initial bifurcation would of course be into a localized bulge as $\hat{\lambda}_1 \to \hat{\lambda}_1^R$, and the thicker section of the ensuing “two-phase” solution would be centred at $z = 0$, with the thinner sections situated either side.

5.2.2 Fixed λ and increasing γ

As we have already established, an alternative approach is to apply a fixed axial stretch λ to the tube and then increase the surface tension γ gradually from zero. In this case, we set

$$\gamma = \gamma_{\rm cr} + \varepsilon\tilde{\gamma}_1, \tag{5.52}$$

where $\tilde{\gamma}_1$ is a constant of $\mathcal{O}(1)$ and the bifurcation values $\gamma_{\rm cr}$ satisfy (3.36) with $\lambda_{\rm cr}$ replaced with the fixed λ on the right-hand side. Since the linear analysis predicts that $\gamma - \gamma_{\rm cr} = \mathcal{O}(k^2)$ in the near-critical regime, we continue to operate with the far distance variable s defined in (5.2) by a similar argument to the one explained for the fixed γ and varying λ case. Then, by applying the same solution procedure as before, we obtain the amplitude equation

$$\mathcal{A}'' = \tilde{\gamma}_1\tilde{\kappa}_1\mathcal{A} + \tilde{\kappa}_2\mathcal{A}^2, \tag{5.53}$$

where $\tilde{\kappa}_1$ and $\tilde{\kappa}_2$ are new coefficients which will be discussed shortly.

Equation (5.53) admits the following localized standing solitary wave solution:

$$\mathcal{A}(s) = -\frac{3\tilde{\gamma}_1\tilde{\kappa}_1}{2\tilde{\kappa}_2}\mathrm{sech}^2\left(\frac{1}{2}\sqrt{\tilde{\gamma}_1\tilde{\kappa}_1}s\right). \tag{5.54}$$

Unlike its counterpart κ_1 in (5.27), we expect that the coefficient $\tilde{\kappa}_1$ in (5.53) is generally negative by the following argument. On substituting a solution of the form $\mathcal{A} = e^{\tilde{\alpha}_1 s}$ into the linearized version of (5.53), the spectral parameter $\tilde{\alpha}_1$ is found to take the values $\tilde{\alpha}_1 = \pm\sqrt{\tilde{\gamma}_1\tilde{\kappa}_1}$. We note that, for *any* fixed λ, the constant $\tilde{\gamma}_1$ is negative (positive) in the regime before (beyond) the bifurcation point $\gamma_{\rm cr}$. Moreover, recall from the spectral analysis presented in chapter 3 that we expect $\tilde{\alpha}_1$ to be real (purely imaginary) before (beyond) this bifurcation point. Hence, to satisfy these expectations we must have that $\tilde{\kappa}_1 < 0$ generally, and the form of (5.54) then tells us that the bifurcation solution must arise subcritically. Also, based on the findings from the solid cylinder case (Fu et al., 2021), we conjecture that the following relationship between the two coefficients holds:

$$\tilde{\kappa}_2 = \lambda^2 \tilde{\kappa}_1 \frac{d\gamma_{\rm cr}}{d\lambda}. \tag{5.55}$$

These arguments are fully validated for the Gent material model by numerically evaluating the explicit expressions obtained for $\tilde{\kappa}_1$ and $\tilde{\kappa}_2$ from the asymptotic analysis; see Fig. 5.8 for an illustrative example. From (5.55), we see that $\tilde{\kappa}_2$ will be positive for fixed $\lambda < \lambda_{\rm min}$ and negative for fixed $\lambda > \lambda_{\rm min}$. Given this, we deduce that the solution (5.53) is a dark standing solitary wave (localized necking) for fixed $\lambda < \lambda_{\rm min}$ and a bright standing solitary wave (localized bulging) for fixed $\lambda > \lambda_{\rm min}$.

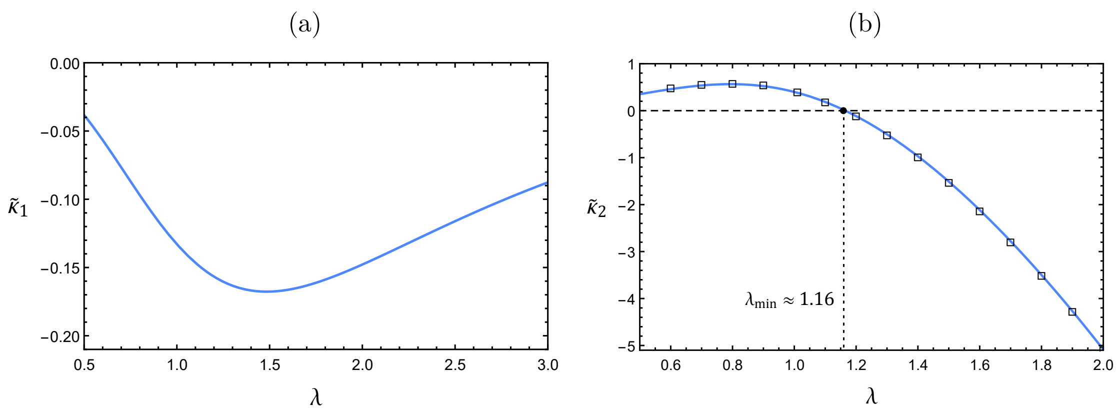

Figure 5.8: Plots of (a) $\tilde{\kappa}_1$ and (b) $\tilde{\kappa}_2$ against λ for $R_{\rm i} = 0.4$ and $J_{\rm m} = 100$. The solid blue curves correspond to the explicit expressions for the coefficients obtained directly from the amplitude equation, whereas the black squares in (b) are computed from (5.55).

In the limit $\lambda \to \lambda_{\min}$, the coefficient $\tilde{\kappa}_2$ vanishes and the solution (5.54) diverges. For this special case, we enforce the expansions

$$\gamma = \gamma_{\min} + \varepsilon\hat{\gamma}_1 \quad \text{and} \quad \lambda = \lambda_{\min} + \varepsilon^{1/2}\hat{\lambda}_1. \tag{5.56}$$

Now, the form of (5.54) suggests that a rescaling of the far distance variable s as in the previous loading scenario is not necessary. However, on Taylor expanding $\tilde{\kappa}_2$ in the amplitude equation (5.53) around $\mathcal{Q}\colon(\lambda_{\min}, \gamma_{\min})$, we obtain

$$\mathcal{A}'' = \mathcal{A}\left\{\tilde{\gamma}_1\tilde{\kappa}_1 + \varepsilon^{1/2}\hat{\lambda}_1\mathcal{A}\left.\frac{d\tilde{\kappa}_2}{d\lambda}\right|_{\mathcal{Q}}\right\}. \tag{5.57}$$

For (5.57) to be valid, $\mathcal{A}$ must be of $\mathcal{O}(\varepsilon^{-1/2})$ in this limiting case. On enforcing this rescaling of $\mathcal{A}$, we find that the amplitude equation (5.35) and the associated solution (5.50) are valid also in this loading scenario, with s substituted in place of $\hat{s}$, and provided that

$$-\frac{\hat{\kappa}_2\hat{\lambda}_1^2}{3\hat{\kappa}_1} < \hat{\gamma}_1 < -\frac{\hat{\kappa}_2\hat{\lambda}_1^2}{\hat{\kappa}_1}, \tag{5.58}$$

where $\hat{\kappa}_1$ and $\hat{\kappa}_2$ are unchanged from section 5.2.1.2. Note that the upper bound of (5.58) is the bifurcation value of $\hat{\gamma}_1$, and so the bifurcation solution in this limiting case is again subcritical.

As an illustrative example, say we fix $\hat{\lambda}_1 > 0$ and then gradually increase γ from zero. We expect that an initial bifurcation into a localized bulging solution (since $\lambda > \lambda_{\min}$) will take place in the limit $\hat{\gamma}_1 \to -\hat{\kappa}_2\hat{\lambda}_1^2/\hat{\kappa}_1$. If we attempt to increase the surface tension beyond this bifurcation value, we conjecture that a *snap-through* to the two axial stretches $\lambda_{L,R} = \lambda_{\min} \mp (3\varepsilon)^{1/2}\hat{\lambda}_1$ will take place as demonstrated in Fig. 5.9. In other words, we conjecture that a *snap-through* from a localized bulging solution to a kink-wave solution will take place. For the latter, the tube configuration comprises of a thicker section with stretch λ_L centred at $s = 0$ in between two thinner sections with stretch λ_R. The overall average stretch remains fixed at $\lambda = \lambda_{\min} + \varepsilon^{1/2}\hat{\lambda}_1$.

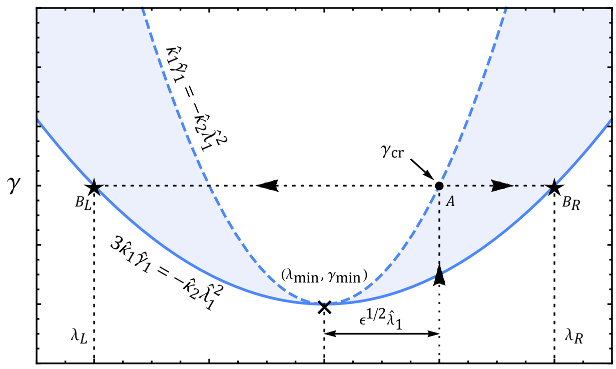

Figure 5.9: A schematic of the domain of existence (5.58) for the localized solution analogous to (5.50) in the fixed λ and increasing γ case. For fixed $\hat{\lambda}_1 > 0$, we move in the direction of the vertical arrow when increasing γ. The initial bifurcation into a localized bulge is expected to occur once we reach $\gamma = \gamma_{\rm cr}$. Beyond this point, we conjecture that a snap-through to the outer two black stars at $\lambda = \lambda_L$ and λ_R will occur, and these stretches characterize the resulting kink-wave configuration.

When $\lambda = \lambda_{\rm min}$ is fixed, the solution (5.50) is in fact invalid since the existence condition (5.58) cannot be satisfied. On taking the limit $\lambda \to \lambda_{\rm min}$ (i.e. $\hat{\lambda}_1 \to 0$) in the rescaled amplitude equation analogous to (5.35) and making the substitution

$$\hat{\mathcal{A}}(s) = \frac{\sqrt{-3\hat{\gamma}_1\hat{\kappa}_1}}{2\sqrt{\hat{\kappa}_2}\lambda_{\rm min}^2}\mathcal{H}(\tilde{s}), \qquad \text{with} \qquad \tilde{s} = \sqrt{-\hat{\gamma}_1\hat{\kappa}_1}\, s, \tag{5.59}$$

we obtain the following reduced equation which has previously been derived by Xuan and Biggins (2016):

$$\mathcal{H}'' = \mathcal{H}(\mathcal{H}^2 - 1). \tag{5.60}$$

Equation (5.60) admits the kink-wave solution

$$\mathcal{H}(\tilde{s}) = \tanh\left(\frac{\tilde{s}}{\sqrt{2}}\right), \tag{5.61}$$

which tends to ± 1 as $\tilde{s} \to \pm\infty$. Given the general negativity of $\hat{\kappa}_1$ and the form of the independent variable $\tilde{s}$, we note that the solution (5.61) is valid only for $\hat{\gamma}_1 > 0$. In other words, the bifurcation solution is *supercritical* when $\lambda = \lambda_{\rm min}$ is fixed, and as we increase γ beyond the associated bifurcation value $\gamma_{\rm min}$, we expect that a continuous transition to the kink-wave solution (5.61) will occur.

5.2.3 Fixed $\mathcal{N}$ and increasing γ

The analysis when $\mathcal{N}$ is fixed and γ is gradually increased is near identical to the analysis presented in section 5.2.1 for the fixed γ and varying λ case. The sole difference here is that γ is eliminated in favour of $\mathcal{N}$ in the successive boundary value problems with the aid of the expression (3.29). We obtain the same amplitude equation (5.27) with the same coefficients κ_1 and κ_2. However, we recall from section 3.3.2 of chapter 3 that $\lambda = \lambda_{\text{cr}}^R$ is the only bifurcation point of interest in this loading scenario. Thus, we deduce that the initial bifurcation solution here is localized bulging, and this arises subcritically.

5.3 Fully non-linear post-bifurcation analysis

The theoretical predictions we have made regarding the near-critical bifurcation behaviour of the tube can be fully supported and extended through FEM simulations conducted in Abaqus (2013). These fully non-linear simulations are conducted for the case of fixed λ (and increasing γ), since this is arguably the least well understood scenario. The simulations are performed by adapting the user subroutines of Henann and Bertoldi (2014), and they confirm that the previously discussed *snap-through* behaviour is prevalent for fixed axial stretches away from λ_{min}.

We take $\mu = 20\,\text{Pa}$, $L = 10\,\text{mm}$, $R_{\text{i}} = 0.10\,\text{mm}$ and $R_{\text{o}} = 0.25\,\text{mm}$, so that the scaled value of R_{i} is 0.4. The simulations are conducted using the Gent material model with $J_{\text{m}} = 100$, and the total length of the tube is assumed to be fixed throughout the entire loading process (that is, for values of γ less than and greater than the bifurcation value γ_{cr}). Consequently, the *averaged axial stretch*, defined as the deformed length of the tube divided by the undeformed length, is fixed. All simulation results have been obtained by adopting the geometrical imperfection recommended by Henann and Bertoldi (2014), namely that the wall thickness is reduced linearly from both ends of the tube towards the middle section ($Z = 0$). The maximum reduction imposed is 0.004%.

In Fig. 5.10 (a) and (b), we present results of the numerical simulations for fixed $\lambda = \lambda_{\text{min}} \approx 1.16$ and $\lambda = 1.5$, respectively. In both plots, the dashed curve represents the theoretical bifurcation condition, whereas the solid curve is the simulation result. We observe that there is exceptional agreement between theory and numerics regarding the bifurcation value γ_{cr}; see the black dots. The results presented in (a) demonstrate that the bifurcation is in-fact supercritical when $\lambda = \lambda_{\text{min}}$ is fixed, as our theoretical results predicted. As γ is increased beyond its bifurcation value γ_{min}, a continuous transition to a static "two-phase" state consisting of a bulged section with stretch λ_L and a depressed section with stretch λ_R is observed. Recall that these stretches have been defined analytically in a small neighbourhood of $\mathcal{Q} : (\lambda_{\text{min}}, \gamma_{\text{min}})$ through (5.51), but they are completely defined in the fully non-linear post-bifurcation regime via the numerical simulations.

In Fig. 5.10 (b), we show firstly that, if λ is fixed at a value away from λ_{min} (we have used $\lambda = 1.5$ as an illustrative example), then a localized solution will initiate at the value of γ determined by our theoretical bifurcation condition. As soon as γ is increased above its critical value, the tube will snap-through to the *same* "two-phase" configuration that was encountered in the $\lambda = \lambda_{\text{min}}$ case. However, the proportion λ_L/λ of the bulged section will be different since we now have a different fixed value for the averaged axial stretch. In Fig. 5.10 (c), we display "two-phase" configurations of the tube when the averaged axial stretch is fixed to be λ_{min} and 1.5, and γ is increased to 9.

Numerical simulations, however, are not necessary to predict the fully non-linear bifurcation behaviour of the localized pattern. In-fact, such predictions can be completely obtained from our theoretical expressions for the primary axial tension deformation presented in section 3.3 of chapter 3. To elaborate, as was first elucidated by Clerk-Maxwell (1875) in the context of a liquid-gas two phase state (with pressure and volume being the dependent and independent variables, respectively), for any $\gamma > \gamma_{\text{min}}$ the stretches for each "phase" must satisfy the

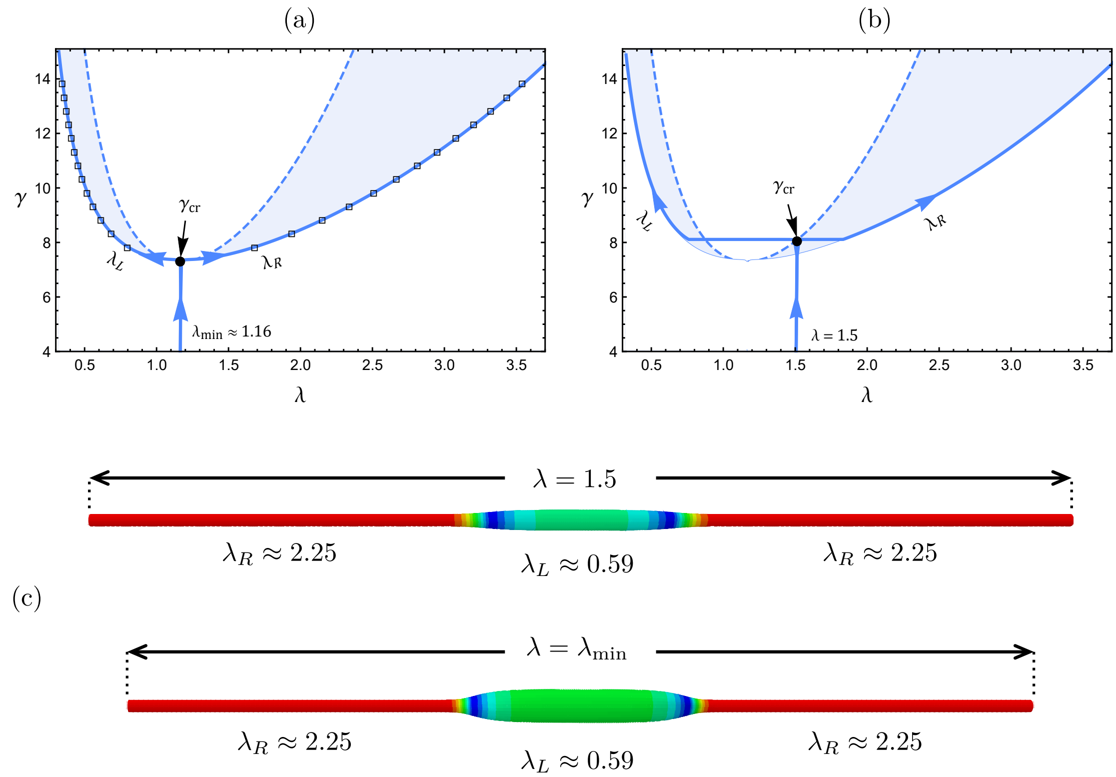

Figure 5.10: FEM simulation results (solid blue curve) for the Gent material model with $J_m = 100$, fixed inner radius $R_i = 0.4$, (a) fixed $\lambda = \lambda_{min}$ and (b) fixed $\lambda = 1.5$. The dashed blue curves represent the theoretical bifurcation condition, and the black squares give the relationship between the surface tension γ and stretches λ_L and λ_R determined from the equal area rule. The black dots mark the bifurcation point in each case given by the simulations. In (c), we present the "two-phase" configuration of the tube for fixed $\lambda = 1.5$ and λ_{min} when the surface tension has been increased beyond its bifurcation value to $\gamma = 9$. Both configurations consist of a bulged section with uniform axial stretch $\lambda_L \approx 0.59$, in-between two depressed sections with stretch $\lambda_R \approx 2.25$. The proportion of the bulged "phases" differ in each case due to the different averaged axial stretches.

following equal area rule:

$$\mathcal{N}_{MW} \equiv \mathcal{N}(\lambda_L) = \mathcal{N}(\lambda_R) \quad \text{and} \quad \int_{\lambda_L}^{\lambda_R} \mathcal{N} d\lambda = (\lambda_R - \lambda_L)\mathcal{N}(\lambda_L); \tag{5.62}$$

see Fig. 5.11 for a geometrical interpretation of (5.62). From (5.62), we can determine λ_L and λ_R as implicit functions of $\gamma > \gamma_{min}$. We observe in Fig. 5.10 (a) that these functions, plotted in the (λ, γ) plane (black squares), are in perfect agreement with the corresponding simulation results. The value $\mathcal{N}_{MW}$ is the so-called *Maxwell state*, which is invariant across the bulged and depressed "phases". However, the value of $\mathcal{N}_{MW}$ will increase as we increase γ beyond its bifurcation value.

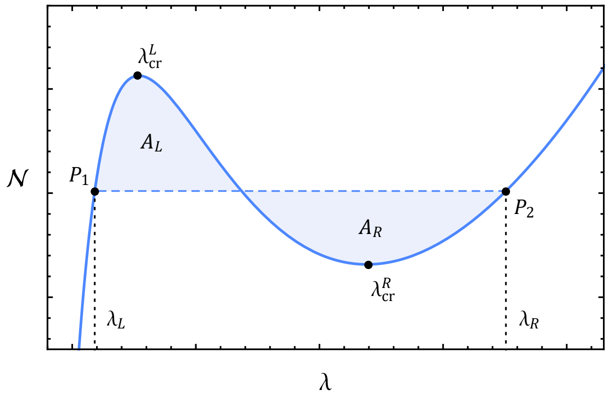

Figure 5.11: According to Maxwell's equal area rule, the stretch values λ_L and λ_R should be such that the magnitude of the areas between the horizontal line passing through P_1 and P_2 (dashed blue) and the $\mathcal{N} = \mathcal{N}(\lambda)$ curve (example shown in solid blue) above and below the line should be equal. That is, we must have $A_L = A_R$.

With λ_L and λ_R deduced, we can determine the evolution of the uniform radii of the bulged and depressed regions as γ is increased beyond its bifurcation value. This can be achieved by substituting $\lambda_L(\gamma)$ and $\lambda_R(\gamma)$ into the expression $r_\mathrm{o} = \sqrt{\lambda^{-1}(R_\mathrm{o}^2 - R_\mathrm{i}^2) + R_\mathrm{i}^2}$ for the outer deformed radius. In Fig. 5.12 (a), we consider the case $\lambda = \lambda_{\mathrm{min}} \approx 1.16$ with $R_\mathrm{i} = 0.4$ and $J_\mathrm{m} = 100$. In this case, a primary axial tension configuration is produced for $\gamma < \gamma_{\mathrm{min}}$ with outer radius $r_\mathrm{o} \approx 0.94$. As γ is increased above its bifurcation value γ_{min}, the radius of the bulged "phase" will increase continuously from 0.94, whilst the radius of the depressed "phase" will decrease continuously from 0.94. In other words, increasing surface tension will cause the bulged "phase" to get progressively thicker, whilst the depressed "phase" will get progressively thinner. This is also true for any $\lambda \neq \lambda_{\mathrm{min}}$, except the deviation of the bulged and depressed "phase" radii from the primary value of r_o at $\gamma = \gamma_{\mathrm{cr}}$ will not be continuous due to the aforementioned snap-through behaviour. In (b), we see that for $\lambda = \lambda_{\mathrm{min}}$, the proportion (half-length) of the bulged "phase" will decrease continuously from unity ($\lambda_{\mathrm{min}} L$) as γ is increased above γ_{min} (the proportion of the depressed "phase" will therefore increase in tandem). When $\lambda = 1.5$, say, the initial localized bulge will in contrast snap-through to a "two-phase" state with a bulged proportion of approximately 0.49 at $\gamma \gtrsim \gamma_{\mathrm{cr}}$; see (b). As γ is increased further beyond this threshold, the proportion of the bulged "phase" will decrease monotonically from this initial value.

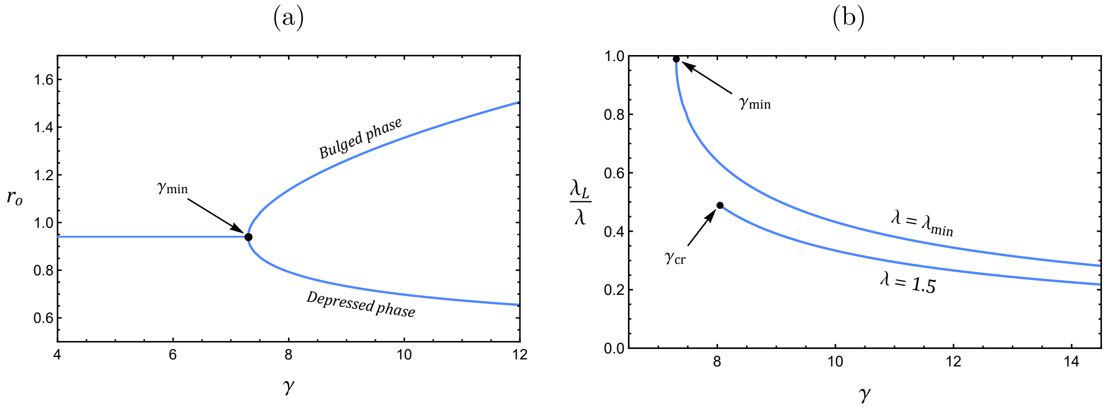

Figure 5.12: (a) A bifurcation diagram showing the uniform outer radii of the bulged and depressed "phases" against the control parameter γ for fixed $\lambda = \lambda_{\min}$, $R_{\rm i} = 0.4$ and $J_{\rm m} = 100$. (b) The corresponding variation of the proportion λ_L/λ of the bulged section in the "two-phase" state against γ for $\lambda = \lambda_{\min}$ and 1.5.

The post-bifurcation behaviour in the case of fixed γ and varying λ, or fixed $\mathcal{N}$ and increasing γ, is straight-forward to interpret. To illustrate, suppose again that $R_{\rm i} = 0.4$ and $J_{\rm m} = 100$, and that $\gamma = 7.5$ is fixed with $\mathcal{N} = 27.5$ initially. This produces an initial axial stretch $\lambda \approx 1.81$ from which to "unload". Once λ is decreased to the bifurcation value $\lambda_{\rm cr}^R \approx 1.33$, a localized bulge will initiate at the center of the tube. When decreasing λ slightly further from $\lambda_{\rm cr}^R$, the bulge will grow to a near maximum amplitude and then propagate in the axial direction to form a "two-phase" configuration. The latter consists of a bulged "phase" with uniform stretch $\lambda_L(7.5) \approx 0.912$ in between two depressed "phases" with stretch $\lambda_R(7.5) \approx 1.472$. The overall stretch of the "two-phase" configuration is $\lambda_{\rm cr}^R$ minus some small increment at this point. As the overall stretch λ is reduced further, the values of λ_L and λ_R (and hence $\mathcal{N}_{MW}$) will remain fixed since their argument γ is fixed. In tandem, the proportion λ_L/λ of the bulged "phase" will increase; once λ is reduced to $\lambda_L \approx 0.912$, a tube of uniform outer radius $r_{\rm o} = \sqrt{\lambda_L^{-1}(R_{\rm o}^2 - R_{\rm i}^2) + R_{\rm i}^2} \approx 1.04$ is returned. A similar interpretation can be made for the fixed $\mathcal{N}$ and increasing γ scenario.

5.4 Discussion

Through a weakly non-linear near-critical analysis, we have shown explicitly that the axi-symmetric zero wavenumber bifurcation mode encountered in the linear bifurcation analysis is associated with a localized pattern formation. For fixed γ and varying λ, the initial bifurcation solution was shown to be localized necking when "loading" from $\mathcal{N} = 0$ and localized bulging when "unloading" from some large value of $\mathcal{N}$. For fixed λ and increasing γ, we determined that localized necking will occur for $\lambda < \lambda_{\text{min}}$, whilst localized bugling will arise when $\lambda > \lambda_{\text{min}}$, where λ_{min} is the value of λ at the minimum of the bifurcation curve in the $(\lambda, \gamma_{\text{cr}})$ plane. For fixed $\mathcal{N} \geq 0$ and increasing γ, localized bulging was found to occur. In all of these scenarios, we showed explicitly that the initial localized solution arises subcritically. When $\lambda = \lambda_{\text{min}}$ and γ is increased, however, the bifurcation was shown to be supercritical instead. An appropriate rescaling of the analysis revealed the existence of a thin layer in a small neighbourhood either side of $\lambda = \lambda_{\text{min}}$ wherein a transition from the initial localized solution to a "two-phase" state takes place. At $\lambda = \lambda_{\text{min}}$, a two-phase deformation was shown to be the initial bifurcation behaviour as opposed to localization.

Our post-bifurcation analysis was focussed on the most challenging scenario of fixed λ and increasing γ. FEM simulations verified that, for fixed $\lambda = \lambda_{\text{min}}$ and increasing γ, a *continuous* transition to a "two-phase" state consisting of a bulged region with stretch λ_L and a depressed region with stretch λ_R takes place at $\gamma = \gamma_{\text{min}}$. For $\lambda \neq \lambda_{\text{min}}$, a localized bulging or necking solution was found to occur initially at $\gamma = \gamma_{\text{cr}}$. Beyond this point, a *snap-through* to the same "two-phase" state observed in the $\lambda = \lambda_{\text{min}}$ case was found to occur, however the proportion of the bulged section is different here due to the different overall axial stretch. We demonstrated how the stretches λ_L and λ_R of the two "phases" can be determined implicitly as functions of γ through Maxwell's Equal Area rule with the aid of the analytical expressions related to the primary axial tension deformation. Bifurcation diagrams constructed using these implicit functions demonstrated that, for larger values of γ above $\gamma_{\rm cr}$, the bulged and depressed regions of the "two-phase" state will get thicker and shorter, and thinner and longer, respectively. Our results illustrate the remarkable potential for describing the entire post-bifurcation behaviour of elastic localized pattern formations through analytical means.

5.A Appendix – Expressions for $p_1(R)$, $k_1(R)$ and $s_1(R)$

The function $p_1(R)$ in (5.13) is expressible as

$$p_1(R) = p_1^{(1)}\tilde{W}_d + p_1^{(2)}\tilde{W}_{dd} + p_1^{(3)}\tilde{W}_{ddd}, \tag{5.63}$$

where

$$\begin{aligned}
p_1^{(1)} &= -\frac{2R_{\rm i}^4(\lambda_{\rm cr}-1)}{r_{0\rm cr}^4R^3\lambda_{\rm cr}^3}\left\{R^2(2-\lambda_{\rm cr}) + r_{0\rm cr}^2\lambda_{\rm cr}\right\},\\
p_1^{(2)} &= -\frac{2R_{\rm i}^4(\lambda_{\rm cr}-1)^2}{r_{0\rm cr}^6R^5\lambda_{\rm cr}^5}\Big\{R_{\rm i}^6(\lambda_{\rm cr}-1)^2 - 2R^6(3\lambda_{\rm cr}^3+4\lambda_{\rm cr}^2+4\lambda_{\rm cr}+9)\\
&\quad -2R^4R_{\rm i}^2(2\lambda_{\rm cr}^4+\lambda_{\rm cr}^3+3\lambda_{\rm cr}-6) - R^2R_{\rm i}^4(2\lambda_{\rm cr}^5-2\lambda_{\rm cr}^4+\lambda_{\rm cr}^2-6\lambda_{\rm cr}+5)\Big\},\\
p_1^{(3)} &= \frac{4R_{\rm i}^4(\lambda_{\rm cr}-1)^4}{r_{0\rm cr}^8R^5\lambda_{\rm cr}^7}\Big\{R_{\rm i}^8(\lambda_{\rm cr}-1)^2(\lambda_{\rm cr}^2+\lambda_{\rm cr}+1) + 4R^8(\lambda_{\rm cr}^2+\lambda_{\rm cr}+1)^2\\
&\quad +2R^6R_{\rm i}^2(5\lambda_{\rm cr}^5+5\lambda_{\rm cr}^4+5\lambda_{\rm cr}^3-3\lambda_{\rm cr}^2-3\lambda_{\rm cr}-3) + 4R^4R_{\rm i}^4(2\lambda_{\rm cr}^6-2\lambda_{\rm cr}^3+\\
&\qquad \lambda_{\rm cr}^2+\lambda_{\rm cr}+2) + R^2R_{\rm i}^6(2\lambda_{\rm cr}^7-2\lambda_{\rm cr}^6-\lambda_{\rm cr}^4+5\lambda_{\rm cr}^3+\lambda_{\rm cr}-5)\Big\}.
\end{aligned} \tag{5.64}$$

The function $k_1(R)$ in (5.14) takes the form

$$k_1(R) = k_1^{(1)}\gamma + k_1^{(2)}\tilde{W}_d + k_1^{(3)}\tilde{W}_{dd}, \tag{5.65}$$

where $k_1^{(1)} = (R^2 - R_{\rm i}^2)/(4r_{0\rm cr}^2\lambda_{\rm cr})$ and

$$\begin{aligned}
k_1^{(2)} &= -\frac{1}{2R^2r_{0\rm cr}^4\lambda_{\rm cr}^3}\Big\{R_{\rm i}^4(\lambda_{\rm cr}-1)^2(R^2(1+2\lambda_{\rm cr}^3)-R_{\rm i}^2) + 2R^6(\lambda_{\rm cr}^3+1)\\
&\quad +2R^4(2\lambda_{\rm cr}^4-2\lambda_{\rm cr}^3+2\lambda_{\rm cr}-1)\Big\},\\
k_1^{(3)} &= -\frac{(\lambda_{\rm cr}-1)^2}{R^2r_{0\rm cr}^2\lambda_{\rm cr}^4}\Big\{2R^6(\lambda_{\rm cr}^2+\lambda_{\rm cr}+1)^2 + R_{\rm i}^6(\lambda_{\rm cr}^3-1) + 2R^4R_{\rm i}^2(2\lambda_{\rm cr}^5+2\lambda_{\rm cr}^4+\\
&\qquad 2\lambda_{\rm cr}^3-\lambda_{\rm cr}^2-\lambda_{\rm cr}-1) + R^2R_{\rm i}^4(2\lambda_{\rm cr}^6-\lambda_{\rm cr}^3+2\lambda_{\rm cr}^2+2\lambda_{\rm cr}+3)\Big\},
\end{aligned} \tag{5.66}$$

Finally, the function $s_1(R)$ in (5.15) is defined as

$$s_1(R) = \frac{R(R^2 - R_{\rm i}^2)}{r_{0\rm cr}^2 \lambda_{\rm cr}^2}. \tag{5.67}$$

5.B Appendix – Determining $\mathcal{P}(R)$ numerically

We discretize the radial domain $R_{\rm i} \leq R \leq R_{\rm o}$ with n evenly spaced node points R_j $(j = 1, 2, \ldots, n)$ such that $R_{\rm i} < R_1 < R_2 < \cdots < R_n = R_{\rm o}$. The n integrals $\int_{R_{\rm i}}^{R_j} p_1(t)dt$ are evaluated numerically using the *NIntegrate* command in *Mathematica*, and the function $\mathcal{P}_1(u) = \int_{R_{\rm i}}^{u} p_1(t)dt$ is then numerically defined through *Mathematica's Interpolation* command. The aim is to then repeat these steps until we obtain a numerically defined version of $\mathcal{P}(R)$. For instance, the next step would be to numerically compute the n integrals $\int_{R_{\rm i}}^{R_j} u\mathcal{P}_1(u)du$, and then construct the interpolation function $\mathcal{P}_2(v) = \int_{R_{\rm i}}^{v} u\mathcal{P}_1(u)du$. The study of Ye et al. (2020) for the analogous problem of localized bulging in internally inflated tubes showed that sufficient accuracy can be obtained by setting $n = 200$, and so we adopt this value in our computations.

5.C Appendix – Proof of the identity (5.25)

Using $(5.9)_1$, the left-hand side of (5.25) may be written as

$$\int_{R_{\rm i}}^{R_{\rm o}} \{g\mathcal{L}[f] - f\mathcal{L}[g]\}\, dR = \int_{R_{\rm i}}^{R_{\rm o}} \left\{ g\frac{\partial}{\partial R}\mathcal{B}_1[f] - f\frac{\partial}{\partial R}\mathcal{B}_1[g] \right\} dR. \tag{5.68}$$

By integrating by parts and then substituting $(5.9)_2$, the right-hand side of (5.68) can be shown to be equal to

$$[g\mathcal{B}_1[f] - f\mathcal{B}_1[g]]_{R_{\rm i}}^{R_{\rm o}} + \int_{R_{\rm i}}^{R_{\rm o}} \frac{f'}{R}\frac{\partial}{\partial R} R\tilde{W}_d\mathcal{B}_2[g]dR - \int_{R_{\rm i}}^{R_{\rm o}} \frac{g'}{R}\frac{\partial}{\partial R} R\tilde{W}_d\mathcal{B}_2[f]dR. \tag{5.69}$$

Finally, on evaluating the two integrals in (5.69) by parts and substituting $(5.9)_3$, the result (5.25) follows.

6

Localized pattern formation in soft solid cylinders: the effect of material compressibility

Contents

6.1 Introduction

Localized pattern formation in *incompressible* solid cylinders and hollow tubes is very well understood, but an incorporation of the effects of material *compressibility* into the analysis has yet to be undertaken analytically. In this chapter, we draw upon the analytical framework constructed by Fu et al. (2021) for the incompressible solid cylinder case, and by Emery and Fu (2021a,c) for the incompressible hollow tube case, to describe the entire bifurcation process in a compressible solid cylinder under elasto-capillary effects. After defining the primary axial tension deformation through an alternate stress-based formulation, we present a family of analytical bifurcation conditions for localized bulging or necking in terms of a general compressible strain-energy function. The effect of material compressibility and extensibility limits on the bifurcation points are examined, and comparisons with the corresponding numerically simulated bifurcation conditions of Dortdivanlioglu and Javili (2022) are made.

We then describe the entire post-bifurcation process using the equal area rule as in the previous chapter, and the effect of compressibility on the post-bifurcation behaviour is analyzed. Comparisons between our theoretical post-bifurcation results and the corresponding numerically simulated results of Dortdivanlioglu and Javili (2022) are presented, and the importance of our theoretical approach in guiding numerical studies of phase-separation-like phenomena is highlighted.

6.2 Primary deformation

Consider a *compressible*, isotropic, hyperelastic solid cylinder with a reference configuration $\mathcal{B}_0$ defined in terms of the cylindrical polar coordinates (R, Θ, Z), where

$$0 \leq R \leq R_{\rm o}, \quad 0 \leq \Theta \leq 2\pi, \quad |Z| < L. \tag{6.1}$$

The finitely deformed configuration $\mathcal{B}_e$ is in terms of the cylindrical polar coordinates (r, θ, z), and we assume that the solid cylinder undergoes a primary homogeneous deformation of the form

$$r = \lambda_\theta R, \quad \theta = \lambda_\theta \Theta, \quad z = \lambda Z, \tag{6.2}$$

where λ_θ and λ are the circumferential and axial stretches, respectively. Therefore, we have that

$$0 \leq r \leq \lambda_\theta R, \quad 0 \leq \theta \leq 2\pi, \quad |z| < \lambda L. \tag{6.3}$$

The primary deformation gradient F can then be written as

$$F = \lambda_\theta \left(\boldsymbol{e}_r \otimes \boldsymbol{E}_R + \boldsymbol{e}_\theta \otimes \boldsymbol{E}_\Theta \right) + \lambda \boldsymbol{e}_z \otimes \boldsymbol{E}_Z, \tag{6.4}$$

and the corresponding left Cauchy-Green strain tensor $B = FF^T$ takes the form

$$B = \lambda_\theta^2 \left(\boldsymbol{e}_r \otimes \boldsymbol{e}_r + \boldsymbol{e}_\theta \otimes \boldsymbol{e}_\theta \right) + \lambda^2 \boldsymbol{e}_z \otimes \boldsymbol{e}_z. \tag{6.5}$$

The three principal invariants of B are expressed through

$$I_1 = 2\lambda_\theta^2 + \lambda^2, \quad I_2 = \lambda_\theta^2 \left(2\lambda^2 + \lambda_\theta^2 \right), \quad I_3 = J^2 = \lambda_\theta^4 \lambda^2, \tag{6.6}$$

and we assume that the constitutive behaviour of the material is governed by a strain-energy function of the form

$$W = W(I_1, I_3). \tag{6.7}$$

In the computation of our results, we will predominantly specify W to the compressible Gent material model given by (2.64). However, to facilitate a comparison between our theory and the numerical results of Dortdivanlioglu and Javili (2022) (hereafter abbreviated as "DJ"), we will also consider the quadratic and logarithmic compressible neo-Hookean material models given respectively by (2.59) and (2.60).

6.2.1 Stress-based formulation

In order to provide an alternate perspective on the previous analysis of soft tubes, we present here a stress-based formulation for the compressible solid cylinder case. However, we note that the variational formulation in previous chapters can also easily be applied here. On substituting (6.7) into the expression (2.56) for the Cauchy stress tensor σ, and noting the relation $(6.6)_3$, we obtain

$$\sigma = 2JW_3 I + 2J^{-1} W_1 B. \tag{6.8}$$

From (6.8) and (6.5), we determine that the Cauchy stresses in the radial, circumferential and axial directions are given by

$$\sigma_{rr} = \sigma_{\theta\theta} = 2\lambda_\theta^2 \lambda W_3 + 2\lambda^{-2} W_1, \quad \sigma_{zz} = 2\lambda_\theta^2 \lambda W_3 + 2\lambda_\theta^{-2} W_1. \tag{6.9}$$

Since these stress components are constant, the equilibrium equations $\operatorname{div}\sigma = \mathbf{0}$ are automatically satisfied.

As in the hollow tube case previously, we assume that the solid cylinder is under the combined effect of a surface tension $\bar{\gamma}$ and a resultant axial force $\mathcal{N}$. We also continue to scale all lengths by $R_{\rm o}$ and all stresses by the ground state shear modulus μ such that $R_{\rm o}$ and μ are set equal to unity without loss of generality. We also introduce the non-dimensionalized surface tension $\gamma = \bar{\gamma}/(\mu R_{\rm o})$, which enters the analysis through the boundary condition

$$\sigma_{rr} = -\frac{\gamma}{\lambda_\theta R_{\rm o}}, \qquad r = \lambda_\theta R_{\rm o}; \tag{6.10}$$

see Fig. 6.1. On substituting (6.9) into (6.10), we obtain the following expression

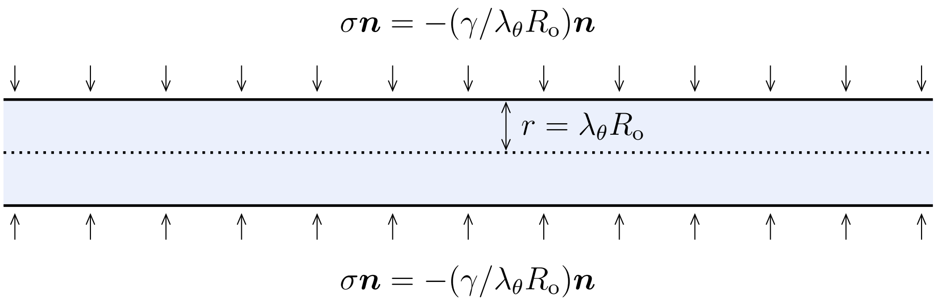

Figure 6.1: A schematic of the current configuration $\mathcal{B}_e$ of the solid cylinder and the associated boundary conditions on the lateral surface $r = R_{\rm o}\lambda_\theta$.

for γ in terms of λ_θ and λ:

$$\gamma = -2\lambda_\theta R_{\rm o}\left\{\lambda_\theta^2\lambda W_3 + 2\lambda^{-2}W_1\right\}. \tag{6.11}$$

The resultant axial force $\mathcal{N}$ is defined through

$$\begin{aligned}\mathcal{N} &= \int_{\theta=0}^{2\pi}\int_{r=0}^{\lambda_\theta R_{\rm o}} \sigma_{zz} r dr d\theta + \gamma\int_{\theta=0}^{2\pi}\lambda_\theta R_{\rm o} d\theta\\ &= 2\pi\lambda_\theta R_{\rm o}\left\{R_{\rm o}\lambda_\theta^3\lambda W_3 + R_{\rm o}\lambda_\theta^{-1}W_1 + \gamma\right\}.\end{aligned} \tag{6.12}$$

6.3 Bifurcation conditions for localized pattern formation

6.3.1 Fixed γ and varying $\mathcal{N}$

For any fixed $\gamma \geq 0$, we can define the circumferential stretch λ_θ as an implicit function of the axial stretch λ through (6.11). The bifurcation condition for localized pattern formation is then $d\mathcal{N}/d\lambda = 0$, where $\mathcal{N}$ is given in (6.12) and γ is fixed in the differentiation. This bifurcation condition takes the form

$$\begin{aligned}\gamma = &-\frac{2\lambda}{\lambda_{\theta\mathrm{d}}}W_{11} - \frac{\lambda_\theta^4}{\lambda_{\theta\mathrm{d}}}\left\{W_3 + 2\lambda(\lambda+1)W_{13} + 2\lambda_\theta^4\lambda^2 W_{33}\right\} \\ &- 4\lambda_\theta\left\{W_{11} + \lambda_\theta^2\lambda W_3 + \lambda_\theta^2\lambda(\lambda+\lambda_\theta^2)W_{13} + \lambda_\theta^6\lambda^3 W_{33}\right\},\end{aligned} \tag{6.13}$$

where $\lambda_{\theta\mathrm{d}} = d\lambda_\theta/d\lambda$, $W_{ij} = \partial^2 W/\partial I_i \partial I_j$ for $i, j = 1, 3$, and the right-hand side of (6.13) is evaluated at $\lambda = \lambda_{\mathrm{cr}}$. By differentiating equation (6.11) implicitly with respect to λ, the following explicit expression for $\lambda_{\theta\mathrm{d}}$ in terms of λ and λ_θ can be obtained:

$$\lambda_{\theta\mathrm{d}} = \lambda_\theta \frac{4W_1 - \lambda^2\{4W_{11} + \lambda_\theta^2\lambda W_3 + 2\lambda_\theta^6\lambda^3 W_{33} + 2\lambda_\theta^2(\lambda^3 + 2\lambda_\theta^2)W_{13}\}}{2\lambda W_1 + 8\lambda_\theta^2\lambda W_{11} + \lambda_\theta^2\lambda^3\{3\lambda W_3 + \lambda_\theta^4\lambda^3 W_{33} + 4\lambda_\theta^2(\lambda+2)W_{13}\}}. \tag{6.14}$$

For a given fixed γ, the critical axial stretches λ_{cr} can be determined numerically from (6.13). Then, with use of (6.12), the associated bifurcation values of the resultant axial force, $\mathcal{N}_{\mathrm{cr}} = \mathcal{N}(\lambda_{\mathrm{cr}})$, may be computed.

In Fig. 6.2, for the compressible Gent model (2.64) with $J_{\mathrm{m}} = 100$, we plot the resultant axial force $\mathcal{N}$ against λ for several fixed $\gamma \geq 0$ with (a) $\nu = 0.05$ and (b) $\nu = 0.25$. We observe that, as in the incompressible case, there exists a minimum value of γ, $\gamma_{\min}$, below which the $\mathcal{N} = \mathcal{N}(\lambda)$ curve is monotonic increasing and localized pattern formation cannot occur. The value of $\gamma_{\min}$ is dependent here on the value of ν. We see also that, in both the high and moderate compressibility cases considered, a larger fixed γ will both delay the expected onset of localized necking when "loading" from $\mathcal{N} = 0$, and make localized bulging occur more prematurely when "unloading" from a large value of $\mathcal{N}$.

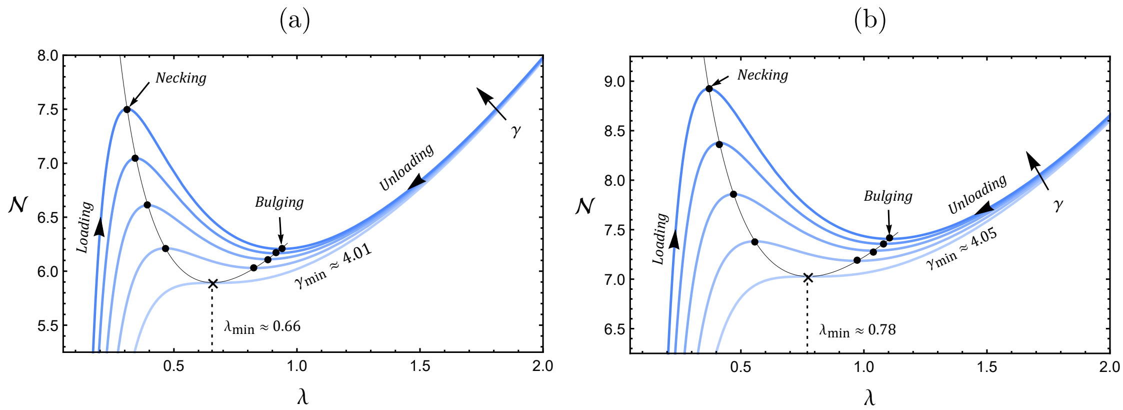

Figure 6.2: Plots of $\mathcal{N}$ against λ (blue curves) for the Gent material model (2.64) with $J_{\mathrm{m}} = 100$, $\gamma = \gamma_{\min}, 4.5, 5, 5.5, 6$ and (a) $\nu = 0.05$ and (b) $\nu = 0.25$. The black curves show the the bifurcation criterion $\mathcal{N}_{\mathrm{cr}} = \mathcal{N}(\lambda_{\mathrm{cr}})$, and the right-most arrows indicate the direction of parameter growth.

In Fig. 6.3 (a), we examine the variation of $\gamma_{\min}$ with respect to ν for the Gent material model (2.64) with several fixed values of J_{m}. We observe that $\gamma_{\min}$ increases with both ν and J_{m}. Thus, for materials with a greater level of compressibility (i.e. for values of ν closer to zero), or a lower level of extensibility, there is a greater range of values of γ for which localized pattern formation can occur. In (b), we plot this same relationship for the quadratic (solid dark blue curve) and logarithmic (solid light blue curve) neo-Hookean material models, and compare with the numerical simulation results presented in Fig. 6 (a) of DJ (squares). We note the exceptional agreement between both sets of results, and in the incompressible limit $\nu \to 1/2$, we recover the value $\gamma_{\min} = 4\sqrt{2}$ which was reported in Fu et al. (2021).

6.3.2 Fixed λ and increasing γ

When λ is fixed and γ is increased gradually from zero, the bifurcation condition for localized pattern formation is equivalent to (6.13), except the left-hand side is replaced with $\gamma = \gamma_{\mathrm{cr}}$, and the right-hand side is evaluated at the fixed axial stretch rather than λ_{cr}.

In Fig. 6.4, we plot γ_{cr} against (a) ν for $J_{\mathrm{m}} = 100$ and several fixed values of $\lambda \geq 1$ and (b) λ for $\nu = 0.4$ and several fixed values of J_{m}. In (a), we observe that highly compressible cylinders are the least susceptible to localized pattern

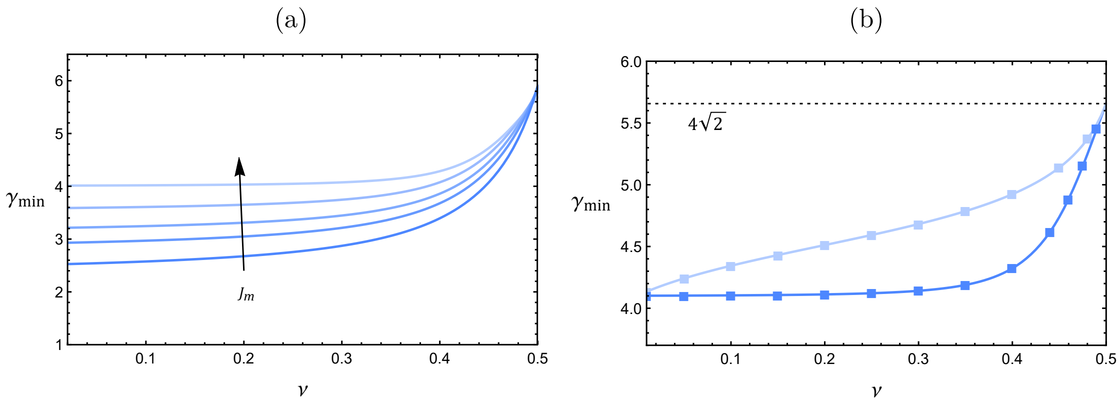

Figure 6.3: Plots of γ_{min} against ν for (a) the compressible Gent material model (2.64) with $J_{\text{m}} = 3, 5, 7.5, 15, 100$ and (b) the quadratic (dark blue) and logarithmic (light blue) neo-Hookean models. In (b), the solid lines represent our theoretical results, and the squares give numerical results from DJ.

formation. We also observe that there exists a threshold value of ν ($\nu \approx 0.43$ in the case presented) below which a greater fixed axial stretch delays localized pattern formation, and above which a greater fixed axial stretch encourages localized pattern formation. In (b), we show that there exists a threshold value of λ ($\lambda \approx 1.225$ in the case presented) below which a greater extensibility limit delays localized pattern formation, and above which a greater extensibility limit encourages localized pattern formation. We observe that γ_{cr} as a function of λ also possesses a minimum. Recall that this behaviour was similarly observed in the incompressible hollow tube case, and we showed that the initial bifurcation solution was localized necking (localized bulging) for $\lambda < \lambda_{\text{min}}$ ($\lambda > \lambda_{\text{min}}$). Here, the value of λ_{min} will vary with ν, and we plot this relationship in Fig. 6.5. We see generally that the value of λ_{min} increases with ν. Thus, for cylinders with a greater degree of compressibility, there is a larger range of values of fixed λ for which an initial localized bulging solution will emerge at $\gamma = \gamma_{\text{cr}}$. In Fig. 6.5 (b), we demonstrate the exceptional agreement between our theoretical results and the numerical simulation results in Fig. 6 (b) of DJ.

In Fig. 6.6, we plot the variation of γ_{cr} with respect to ν for the quadratic and logarithmic neo-Hookean models with $\lambda = 1$, and we note that there is exceptional agreement between our theoretical results (solid curves) and the numerical simulation results given in Fig. 5 of Dortdivanlioglu and Javili (2022) (squares).

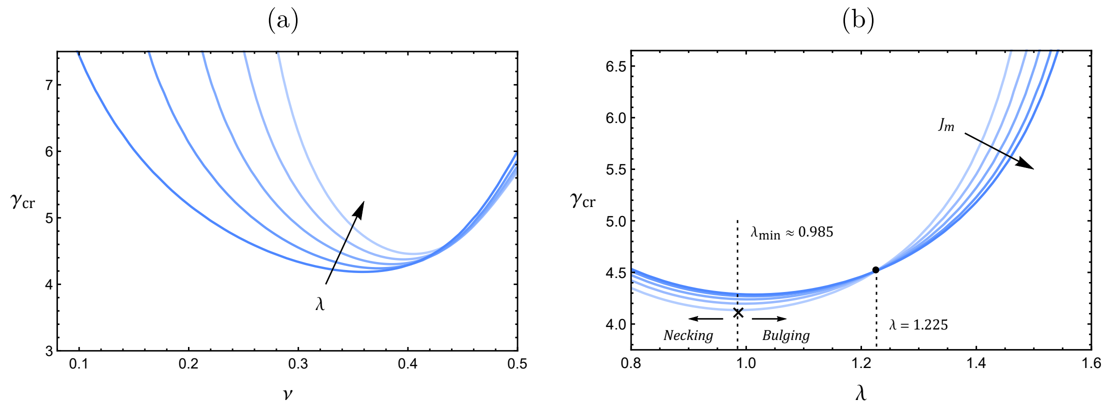

Figure 6.4: Plots of γ_{cr} against (a) ν and (b) λ corresponding to the Gent material model (2.64). In (a), we have $J_m = 100$ and $\lambda = 1, 1.05, 1.1, 1.15, 1.2$, and in (b) we have $\nu = 0.4$ and $J_m = 20, 30, 45, 70, 100$. Arrows indicate the direction of parameter growth.

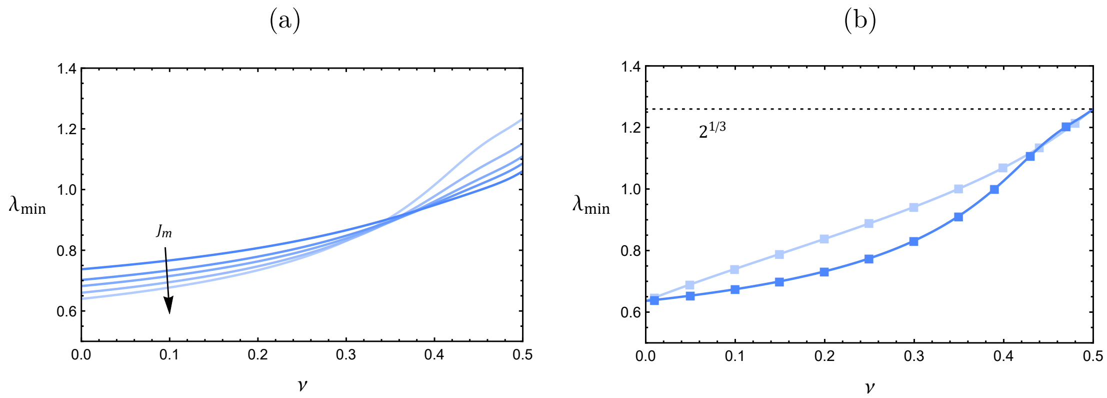

Figure 6.5: Plots of λ_{min} against ν corresponding to (a) the Gent material model (2.64) and (b) the quadratic (dark blue) and logarithmic (light blue) neo-Hookean material models. In (a), we fix $J_m = 3, 5, 7.5, 15, 100$, and the arrow indicates the direction of parameter growth. In (b), the solid curves give our theoretical results, and the squares give the numerical results of DJ. In the incompressible limit $\nu \to 1/2$, we recover the result $\lambda_{min} \to 2^{1/3}$ which was reported in Fu et al. (2021).

6.3.3 Fixed $\mathcal{N}$ and increasing γ

By making appropriate rearrangements in (6.12), the surface tension γ can be expressed explicitly in terms of λ_θ and λ for any fixed $\mathcal{N} \geq 0$ as follows:

$$\gamma = \frac{1}{2}\left\{\frac{\mathcal{N}}{\pi\lambda_\theta R_o} - 2R_o\lambda_\theta^3\lambda W_3 - 2R_o\lambda_\theta^{-1}W_1\right\}. \tag{6.15}$$

Then, we may subtract (6.15) from (6.11) and define λ_θ as an implicit function of λ from the resulting equation. The bifurcation condition for localized pattern

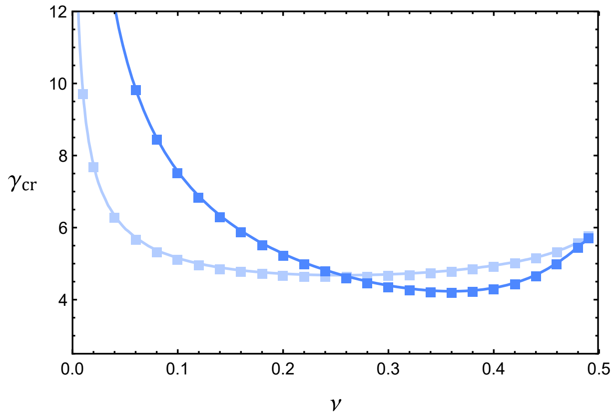

Figure 6.6: A plot of $\gamma_{\rm cr}$ against ν for the quadratic (dark blue) and logarithmic (light blue) compressible neo-Hookean models with $\lambda = 1$. The solid curves give our theoretical results, whilst the squares give numerical results from DJ.

formation is then $d\gamma/d\lambda = 0$, where γ is given in (6.15) and $\mathcal{N}$ is fixed in the differentiation. Explicitly, this condition is expressible as

$$\frac{\lambda_{\theta\rm d}\mathcal{N}}{2\pi R_{\rm o}^2} = \left\{W_1 - \lambda_\theta^2\left(4W_{11} + 3\lambda_\theta^2\lambda W_3 + 4\lambda_\theta^2\lambda\left((\lambda+\lambda_\theta^2)W_{13} + \lambda_\theta^4\lambda^2 W_{33}\right)\right)\right\}\lambda_{\theta\rm d}$$
$$- 2\lambda_\theta\lambda W_{11} - \lambda_\theta^5\left\{W_3 + 2\lambda\left((\lambda+1)W_{13} + \lambda_\theta^4\lambda W_{33}\right)\right\}, \tag{6.16}$$

and this equation is also evaluated at $\lambda = \lambda_{\rm cr}$. The expression for $\lambda_{\theta\rm d}$ can again be obtained by differentiating (6.11) implicitly with respect to λ. The left-hand side of the resulting equation will vanish since $d\gamma/d\lambda = 0$ is the bifurcation condition in this loading scenario, and we thus recover the relation presented in (6.14). Once the critical stretch $\lambda_{\rm cr}$ has been obtained from (6.16), we can substitute this value into the equation (6.11) to obtain the corresponding critical surface tension $\gamma_{\rm cr} = \gamma(\lambda_{\rm cr})$.

In Fig. 6.7, we plot the function $\gamma = \gamma(\lambda)$ given in (6.15) for (a) $\nu = 0.25$, $J_{\rm m} = 100$ and several fixed $\mathcal{N} \geq 0$, and (b) $\mathcal{N} = 8$, $J_{\rm m} = 100$ and several fixed ν. As in the purely incompressible case, there is seen in (a) to be a minimum value of $\mathcal{N}$, $\mathcal{N}_{\rm min}$, below which the curve $\gamma = \gamma(\lambda)$ is monotonic decreasing and localized pattern formation is prohibited. This minimum value of $\mathcal{N}$ will depend on the value of ν. Larger fixed $\mathcal{N}$ above this minimum value correspond to larger values of $\gamma_{\rm cr}$ (marked by the black dots), and so a greater fixed axial force will discourage localized bulging when the material is compressible. In (b), we find that there exists a maximum value of ν, $\nu_{\max}$, above which the $\gamma = \gamma(\lambda)$ curve becomes monotonic decreasing and localized bulging becomes impossible. The value of $\nu_{\max}$ will vary with the value of the fixed $\mathcal{N}$. We also observe that, for smaller values of ν (i.e. for materials with a greater level of compressibility), the associated value of $\gamma_{\rm cr}$ is larger. Hence, increased compressibility discourages the initiation of a localized bulge in this loading scenario.

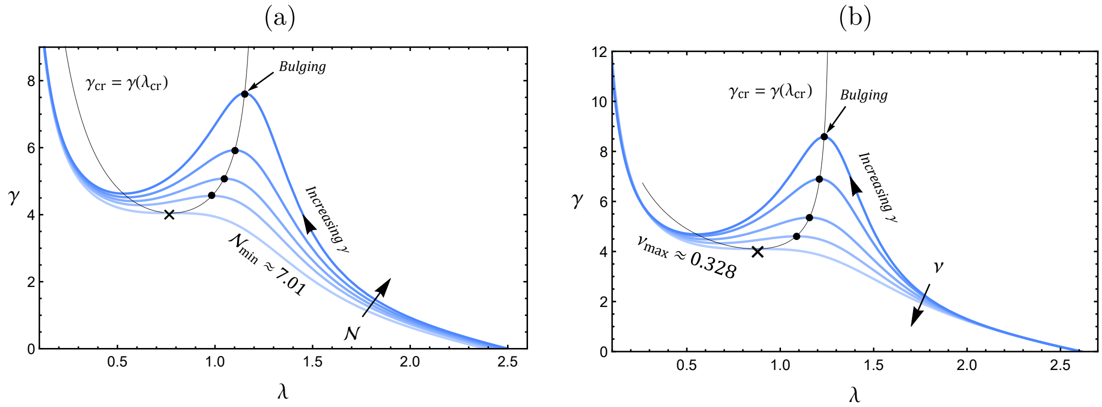

Figure 6.7: Plots of γ against λ (blue curves) corresponding to the Gent material model (2.64) with $J_{\rm m} = 100$. In (a) we fix $\nu = 0.25$ and $\mathcal{N} = \mathcal{N}_{\min}, 7.2, 7.3, 7.4, 7.5$, and in (b) we fix $\mathcal{N} = 8$ and $\nu = 0.29, 0.295, 0.305, 0.315, \nu_{\max}$, where $\mathcal{N}_{\min} \approx 7.03$ and $\nu_{\max} \approx 0.328$. The black curves give the associates bifurcation criterion $\gamma_{\rm cr} = \gamma(\lambda_{\rm cr})$, and the right-most arrows indicate the direction of parameter growth.

In Fig. 6.8, we plot the variation of (a) $\mathcal{N}_{\min}$ against ν and (b) $\nu_{\max}$ against $\mathcal{N}$ for several values of $J_{\rm m}$. In (a), for any given Poisson ratio ν, localized bulging is only possible if the fixed axial force $\mathcal{N}$ is greater than the value $\mathcal{N}_{\min}$ given by the relevant blue curve. The value of $\mathcal{N}_{\min}$ is seen to increase with both ν and $J_{\rm m}$. Thus, for materials with a greater degree of compressibility or a lower degree of extensibility, there is a greater range of values of fixed $\mathcal{N}$ for which localized bulging can occur. We note also that, in the incompressible limit $\nu \to 1/2$, we recover the result $\mathcal{N}_{\min} = 9\pi/2^{2/3}$ in the limit $J_{\rm m} \to \infty$ which was originally given in Fig. 5 (b) of Fu et al. (2021). In (b), for any given fixed value of $\mathcal{N}$, localized bulging is only possible provided the value of the Poisson's ratio is less than the value $\nu_{\max}$ on the blue curve of interest. We observe that, for each value of $J_{\rm m}$, there exists a threshold value of $\mathcal{N}$ below which localized bulging is impossible in cylinders with *any* level of compressibility. For instance, in the limit $J_\mathrm{m} \to \infty$, localized bulging is impossible in any compressible cylinder if $\mathcal{N} < 5.825$.

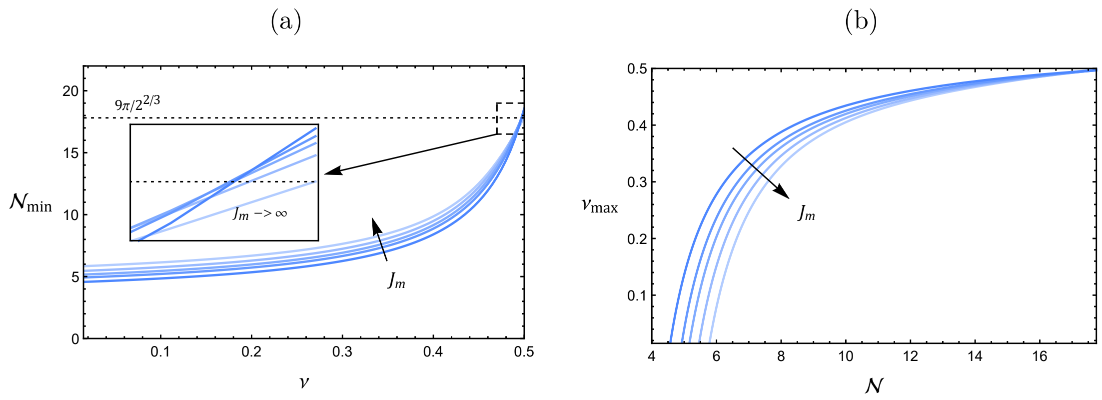

Figure 6.8: The variation of (a) $\mathcal{N}_{\min}$ against ν and (b) $\nu_{\max}$ against $\mathcal{N}$ for the Gent material model (2.64) with $J_\mathrm{m} = 3, 5, 7.5, 15$ and $J_\mathrm{m} \to \infty$. Arrows indicate the direction of parameter growth.

6.4 Post-bifurcation analysis

The numerically simulated post-bifurcation results presented in DJ can be examined and extended through the same analytical approach as presented in section 5.3 of chapter 5. For each $\gamma > \gamma_{\min}$, recall that we can define λ_θ implicitly as a function of λ from (6.11), and hence $\mathcal{N}$ as a function of λ through (6.12). Then, we may determine the values of the Maxwell stretches λ_L and λ_R associated with the final "two-phase" state from the equal area rule (5.62) as before.

We present in Fig. 6.9 (a) and (c) theoretical results for the bifurcation condition (dashed curve) and the Maxwell stretches (solid curve) in the (γ, λ) plane for the quadratic and logarithmic neo-Hookean models, respectively, with $\nu = 0.4$. The black stars are numerically simulated bifurcation points taken from Fig. 11 (d) of DJ, and we observe perfect agreement with our theory. However, the black dots, which are the numerically simulated Maxwell stretches for different values of γ from DJ, are at odds with our theoretical predictions. We have established that the "two-phase" state may only exist provided that the equal area rule is satisfied, and we show in Fig. 6.9 (b) and (d) that this requirement is not satisfied by the Maxwell stretches predicted in DJ. This highlights that the equal area rule should be applied to guide numerical simulation studies of elastic phase-separation-like phenomena, and to validate the results of such studies. As a further consistency check on our results, in Fig. 6.10 we take the limit $\nu \to 1/2$ and compare our values for the Maxwell stretches (solid blue curve) with corresponding FEM simulation results (black squares) in Fig. 13 (a) of Fu et al. (2021) for the incompressible case. We observe that there is perfect agreement between both sets of results.

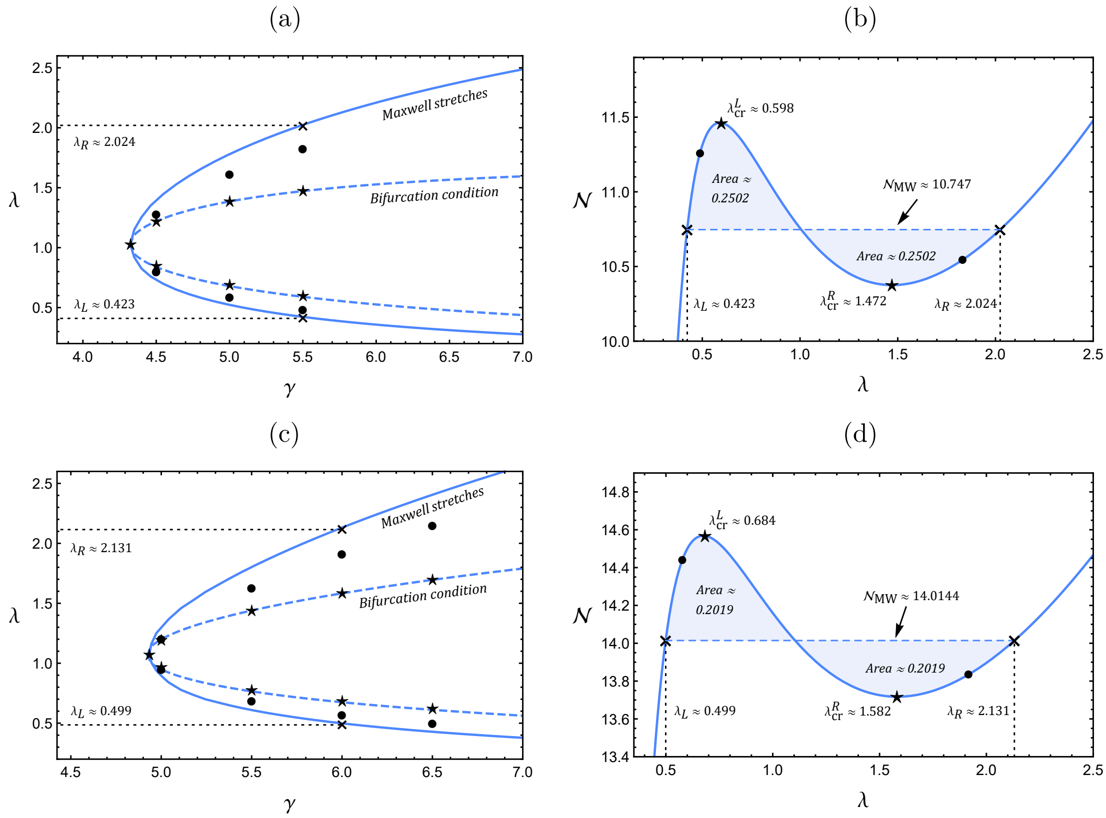

Figure 6.9: In (a) and (c), the critical stretches λ_{cr} from our theoretical bifurcation condition (dashed blue curve) and the Maxwell stretches λ_L and λ_R computed using the equal area rule (solid blue curve) are presented in the (λ, γ) plane for $\nu = 0.4$, and the quadratic and logarithmic neo-Hookean material models, respectively. The black stars and dots give the numerical simulation results from DJ for the bifurcation points and the Maxwell stretches, respectively. In (b) and (d), we superpose our theoretical bifurcation points and Maxwell stretches as well as the numerically determined values from DJ on the $\mathcal{N} = \mathcal{N}(\lambda)$ curve for $\gamma = 5.5$ and 6, respectively. This demonstrates that the theoretically determined Maxwell stretches satisfy the equal area rule, whereas the numerically simulated stretches don't.

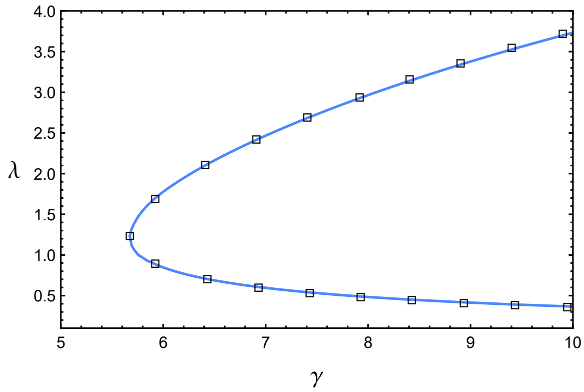

Figure 6.10: A comparison of the Maxwell stretches determined through the equal area rule in the limit $\nu \to 1/2$ (solid blue curve) and the corresponding FEM simulation results (black squares) for the incompressible case studied in Fu et al. (2021).

We then apply our determined values for the Maxwell stretches to investigate the evolution of the bulged and depressed "phases" beyond the bifurcation point. As an illustrative example, in Fig. 6.11 we fix $\lambda = \lambda_{\min}$ (solid curve) and $\lambda = 1.5 > \lambda_{\min}$ (dashed curve) with $\nu = 0.4$ and $J_{\rm m} = 100$, and we plot the circumferential stretch λ_θ against γ. Before the bifurcation point $\gamma_{\rm cr}$ in each case (marked by the black dots), we observe that λ_θ is monotonic decreasing function. This is a consequence of the compressibility effect. For $\lambda = \lambda_{\min}$ and $\lambda = 1.5$, the respective supercritical and snap-through transitions to the "two-phase" state beyond the associated bifurcation point are illustrated. The "bulged" and "depressed" bifurcation branches are determined by substituting $\lambda = \lambda_L$ and $\lambda = \lambda_R$, respectively, into our implicit function $\lambda_\theta = \lambda_\theta(\lambda)$.

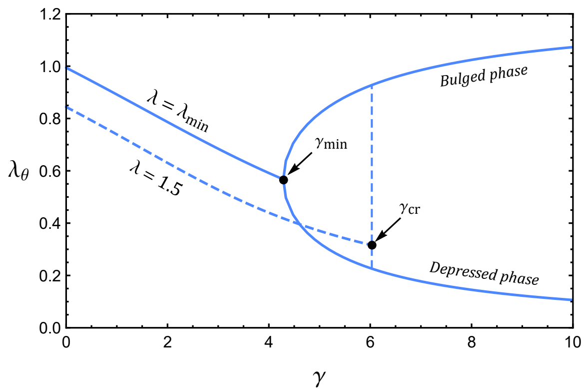

Figure 6.11: A bifurcation diagram showing the circumferential stretch λ_θ against the control parameter γ for fixed $\lambda = \lambda_{\min}$ (solid curve) and $\lambda = 1.5$ (dashed curve), with $\nu = 0.4$ and $J_{\rm m} = 100$.

In Fig. 6.12, we examine the effect of compressibility on the evolution of the thickness and length of the bulged and depressed "phases" when the averaged axial stretch is fixed at unity. In (a), we plot the proportion λ_L/λ of the bulged "phase" with respect to the overall length of the cylinder for $\nu = 0.2, 0.25$ and 0.3. The proportion of the bulged "phase" decreases with increasing γ for each value of ν considered, and it also decreases with *decreasing* ν. In other words, for any $\gamma > \gamma_{\text{cr}}$, a larger degree of compressibility will correspond to a smaller length of the bulged region in the "two-phase" state. In (b), we plot the difference in the scaled radii $r_{\text{max}} = \lambda_\theta(\lambda_L)/R_\text{o}$ and $r_{\text{min}} = \lambda_\theta(\lambda_R)/R_\text{o}$ of the bulged and depressed regions, respectively, against γ for $\lambda = 1$ and the same three values of ν. We observe that a greater degree of compressibility results in a lower value of $r_{\text{max}} - r_{\text{min}}$. Thus, cylinders with greater compressibility have a thinner (thicker) bulged (depressed) region for $\gamma > \gamma_{\text{cr}}$.

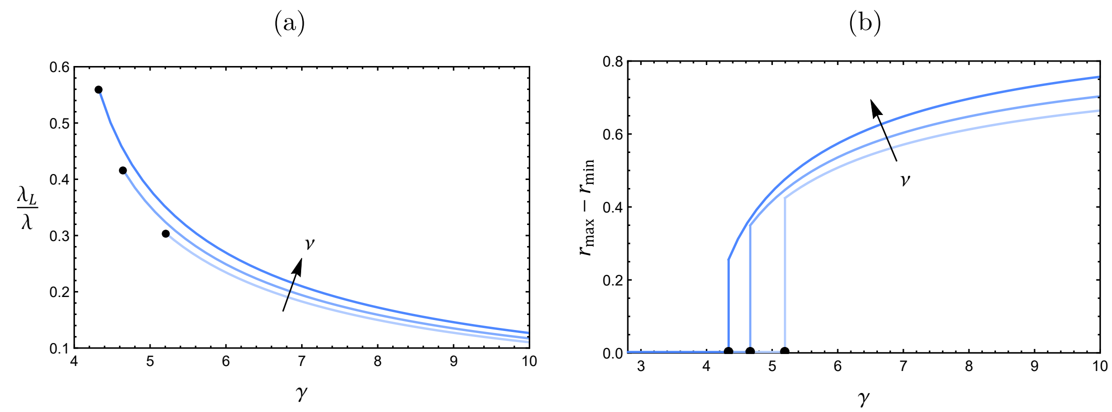

Figure 6.12: The variation of (a) the proportion λ_L/λ of the bulged "phase" and (b) the difference $r_{\text{max}} - r_{\text{min}} = (\lambda_\theta(\lambda_L) - \lambda_\theta(\lambda_R))/R_\text{o}$ in radii of the bulged and depressed "phases" against γ for $J_\text{m} = 100$, $\lambda = 1$ and $\nu = 0.2, 0.25$ and 0.3. The black dots mark the bifurcation points, and the arrows indicate the direction of parameter growth.

6.5 Discussion

The complete bifurcation behaviour of an incompressible solid cylinder or hollow tube under axial loading and surface tension is fully understood. However, with the exception of the numerical study of DJ, analogous studies when the cylinder is compressible are scarce. In this chapter, we have provided greater theoretical insights into localized pattern formation in compressible solid cylinders, as well as a source of comparison for existing and future numerical studies. By drawing upon results for the incompressible hollow tube case studied in the preceding chapters, we derived analytical bifurcation conditions for localized bulging or necking in compressible solid cylinders for three distinct loading scenarios in terms of a general compressible strain-energy function. For the quadratic and logarithmic neo-Hookean material models, we found perfect agreement between our theoretical bifurcation conditions and the numerical simulation conditions presented in DJ. The influence of material compressibility on the bifurcation points in each loading scenario considered is summarized in Table 6.1.

The Maxwell stretches λ_L and λ_R associated with the anticipated final "two-phase" state were again determined as functions of γ through the equal area rule. On comparing the results of the equal area rule approach with the corresponding numerical simulation results in Fu et al. (2021) and DJ, we found perfect agreement in the former case but disagreement in the latter. This highlighted that numerical studies of phase-separation-like phenomena don't always use the equal area rule as a consistency check on their results, and it is hoped that the work presented in this chapter will invoke change in this regard in future studies. We also demonstrated that, when $\lambda = 1$ is fixed, a greater level of material compressibility will result in a smaller bulged proportion in the "two-phase" state, as well as a smaller difference between the bulged and depressed radii, for each $\gamma > \gamma_{\mathrm{cr}}$.

Table 6.1: A summary of the results of the linear bifurcation analysis in section 4.3.

Fixed γ and varying $\mathcal{N}$	*Fixed λ and increasing γ*	*Fixed $\mathcal{N} \geq 0$ and increasing γ*
• A larger fixed γ delays (advances) localized necking (bulging) when loading (unloading) cylinders with both a high and moderate degree of compressibility • For cylinders with any degree of compressibility, there exists a minimum value of γ, $\gamma_{\min}$, below which localization cannot occur • $\gamma_{\min}$ increases with Poisson's ratio ν, so cylinders with greater compressibility can admit a localized pattern formation when subject to a wider range of fixed γ	• There exists a threshold value of ν below (above) which a greater (smaller) axial stretch λ will delay bifurcation • The regime of stretches in which a localized necking (bulging) solution is expected is larger (smaller) for cylinders with a greater degree of compressibility	• A larger degree of compressibility will delay the onset of localized necking • For each fixed $\mathcal{N} \geq 0$, there exists a maximum Poisson ratio, $\nu_{\max}$, above which localization is impossible • Below a certain fixed value of $\mathcal{N}$, localization is impossible in cylinders with *any* degree of compressibility

7

Crease formation in a compressed soft elastic material

Contents

7.1 Introduction

At a critical level of compression, the free surface of an incompressible, hyperelastic half-space will form a localized region of self-contact, and this phenomenon is typically termed “creasing”. An analytical bifurcation condition for crease formation has recently been presented for the first time in a ground-breaking work by Ciarletta and Truskinovsky (2019) (hereafter referred to as CT). However, the analysis is presented with such limited detail that a full comprehension and reproduction of the derivations is very challenging to achieve. The aim of this chapter is therefore to rephrase the analysis of CT in a self-contained and more rigorous manner in order to shed greater light on key steps in the analysis. Firstly, we present the primary uni-axial compression solution for a half-space in a state of plane strain. Then, we assume that the deformation field local to the crease corresponds to the mapping of a semi-circular half-space into a self-contacting whole-space, and this solution is derived explicitly. The effect of the creasing solution on the surrounding uni-axially compressed material sufficiently far away from the crease is then assumed to be equivalent to the action of a vertical concentrated force acting on the free surface. We provide a well-justified model for the evaluation of this concentrated force which is separate from the less well-justified approach taken by CT, and which in turn yields a different result. We also highlight explicitly that the calculation of this force is only a leading order approximation, and determine explicitly the incremental displacement field which it imposes onto the uni-axially compressed material surrounding the crease. The bifurcation condition is finally obtained through a conservation law given in terms of the *energy-momentum tensor* which matches the local creasing solution with the incremental field in a state of equilibrium. This bifurcation condition is found to be at odds with CT's counterpart, and the reason for this discrepancy is elucidated. Our analysis follows essentially the same idea as in CT, but it is hoped that our rephrasing will make the seminal work of CT more accessible and appreciated. It is also hoped that this will provide a springboard for future studies on this fundamentally important bifurcation problem.

7.2 The primary uni-axial compression

Consider an incompressible, isotropic, hyperelastic half-space whose reference configuration $\mathcal{B}_0$ is defined in terms of the Cartesian coordinates (X_1, X_2), where

$$-\infty < X_1 < \infty, \qquad 0 \leq X_2 < \infty. \tag{7.1}$$

We subject the half-space to a uni-axial compression at $X_1 = \pm\infty$, which maps $\mathcal{B}_0$ to a current configuration $\mathcal{B}_e$. Let $\boldsymbol{X}$ and $\boldsymbol{x}$ denote the position vectors of a representative material particle in $\mathcal{B}_0$ and $\mathcal{B}_e$, respectively, such that

$$\boldsymbol{X} = X_A\boldsymbol{E}_A, \qquad \boldsymbol{x} = x_i\boldsymbol{e}_i, \tag{7.2}$$

where $i, A = 1, 2$ and Einstein's summation convention over repeated indices is employed. Also, $(\boldsymbol{E}_1, \boldsymbol{E}_2)$ and $(\boldsymbol{e}_1, \boldsymbol{e}_2)$ are the standard orthonormal bases in $\mathcal{B}_0$ and $\mathcal{B}_e$, respectively. As is implied by our notation, the problem is taken to be one of plane strain, with zero displacement of the material body in the x_3 direction assumed.

The uni-axial compression can be described by the following transformations:

$$x_1 = \lambda X_1, \qquad x_2 = \lambda^{-1}X_2, \tag{7.3}$$

where $\lambda \in (0, 1]$ is the principal stretch in the horizontal direction; see Fig. 7.1. The deformation gradient $\bar{F}$ is then defined through $d\boldsymbol{x} = \bar{F}d\boldsymbol{X}$ and takes the form

$$\bar{F} = \lambda\, \boldsymbol{e}_1 \otimes \boldsymbol{E}_1 + \lambda^{-1}\boldsymbol{e}_2 \otimes \boldsymbol{E}_2; \tag{7.4}$$

we note that the incompressibility constraint $\det \bar{F} = 1$ is automatically satisfied. Throughout this chapter, we follow the convention that an overbar signifies association with primary deformation (7.3) and unbarred quantities correspond to a general deformation. From (7.4), we may compute the first principal invariant $\bar{I}_1$ of the left Cauchy-Green strain tensor $\bar{B} = \bar{F}\bar{F}^T$ as follows:

$$\bar{I}_1 = \operatorname{tr} \bar{B} = \lambda^2 + \lambda^{-2}. \tag{7.5}$$

We assume that the constitutive behaviour of the material is governed by a strain-energy function W of the form

$$W = W(I_1), \tag{7.6}$$

which is the most general form possible for an incompressible, isotropic, hyperelastic material in a state of plane strain. Given (7.6), the Cauchy stress tensor $\bar{\sigma}$ is defined through

$$\bar{\sigma} = 2\bar{W}_1\bar{B} - \bar{p}I, \tag{7.7}$$

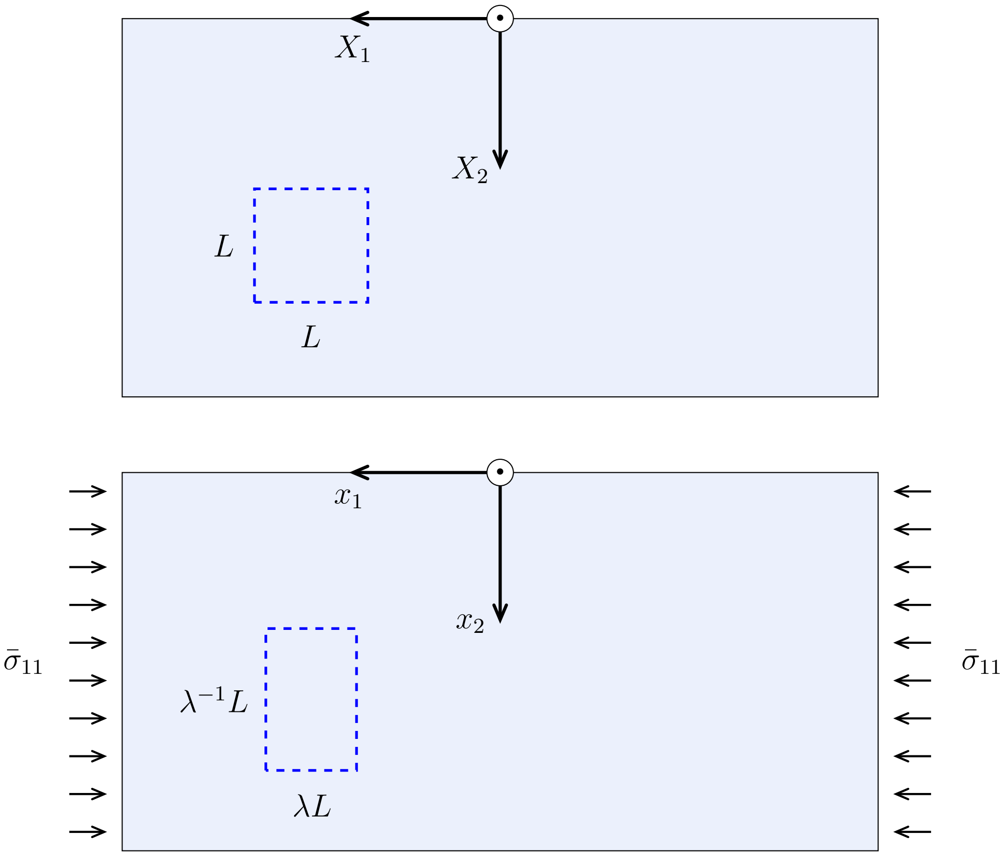

Figure 7.1: A schematic of the reference configuration $\mathcal{B}_0$ (top) and the primary uni-axially compressed configuration $\mathcal{B}_e$ (bottom).

where I denotes the identity tensor, $\bar{p}$ is the Lagrangian multiplier enforcing incompressibility in $\mathcal{B}_e$ and $\bar{W} = W(\bar{I}_1)$, $\bar{W}_1 = W'(\bar{I}_1)$, etc. The non-zero in-plane components of (7.7) are given by

$$\bar{\sigma}_{11} = 2\lambda^2\bar{W}_1 - \bar{p} \quad \text{and} \quad \bar{\sigma}_{22} = 2\lambda^{-2}\bar{W}_1 - \bar{p}. \tag{7.8}$$

Thus, the equilibrium equations $\operatorname{div}\bar{\sigma} = \mathbf{0}$ in $\mathcal{B}_e$ are automatically satisfied provided that $\bar{p}$ is a constant. We further assume that the free surface $x_2 = 0$ in $\mathcal{B}_e$ is traction-free, invoking the boundary condition

$$-\bar{\sigma}\boldsymbol{e}_2 = \mathbf{0}, \qquad x_2 = 0. \tag{7.9}$$

On substituting (7.8) into (7.9), the following constant expression for $\bar{p}$ is obtained:

$$\bar{p} = 2\lambda^{-2}\bar{W}_1. \tag{7.10}$$

Then, on substitution of this expression back into (7.8), we find that the controlled uni-axial compression is achieved solely through the horizontal stress given by

$$\bar{\sigma}_{11} = 2(\lambda^2 - \lambda^{-2})\bar{W}_1. \tag{7.11}$$

7.3 The folding solution

At a critical level of compression, a crease of arbitrarily small depth r_c forms on the free surface $x_2 = 0$ of the half-space. In this section, we assume that the formation of this crease is *locally* equivalent to the folding of a half-space into a whole-space.

Consider first a semi-circular reference configuration $\mathcal{B}_0^\star$ defined in terms of the cylindrical polar coordinates (R, Θ), where

$$0 \leq R \leq R_c, \qquad -\frac{\pi}{2} \leq \Theta \leq \frac{\pi}{2}. \tag{7.12}$$

Suppose then that this semi-circular region is folded into a circular region $\mathcal{B}_e^\star$ such that the surfaces OA and OB shown in Fig. 7.2 come into self-contact. This self-contacting circular region is defined in terms of the cylindrical polar

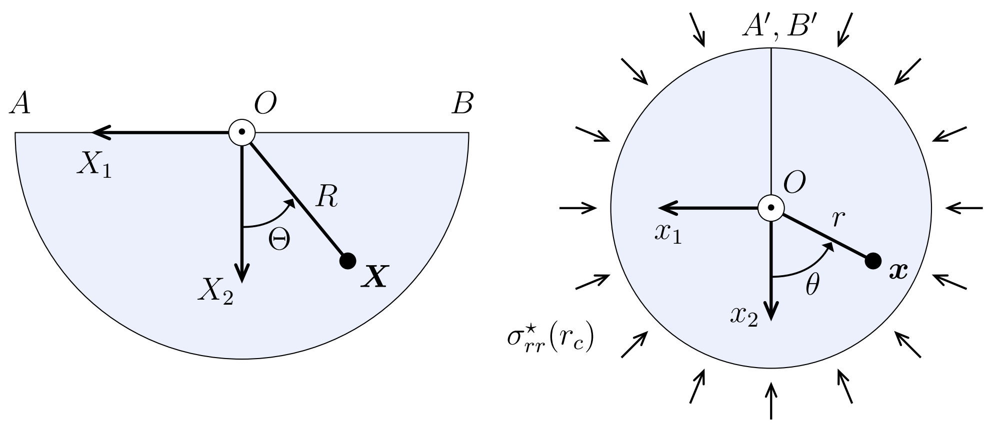

Figure 7.2: A schematic of the semi-circular reference configuration $\mathcal{B}_0^\star$ (left) and the folded circular configuration $\mathcal{B}_e^\star$ (right).

coordinates (r, θ), with

$$0 \leq r \leq r_c, \qquad -\pi \leq \theta \leq \pi. \tag{7.13}$$

That is, the self-contact occurs at $\theta = \pm\pi$ and $0 \le r \le r_c$. The position vectors of a representative material particle in $\mathcal{B}_0^\star$ and $\mathcal{B}_e^\star$ are given respectively by

$$\boldsymbol{X} = R\boldsymbol{E}_R, \qquad \boldsymbol{x} = r\boldsymbol{e}_r, \tag{7.14}$$

and the corresponding orthonormal bases $(\boldsymbol{E}_R, \boldsymbol{E}_\Theta)$ and $(\boldsymbol{e}_r, \boldsymbol{e}_\theta)$ are non-standard and expressible through

$$\boldsymbol{E}_R = -\sin\Theta\boldsymbol{E}_1 + \cos\Theta\boldsymbol{E}_2, \qquad \boldsymbol{E}_\Theta = -\cos\Theta\boldsymbol{E}_1 - \sin\Theta\boldsymbol{E}_2,$$

$$\boldsymbol{e}_r = -\sin\theta\boldsymbol{e}_1 + \cos\theta\boldsymbol{e}_2, \qquad \boldsymbol{e}_\theta = -\cos\theta\boldsymbol{e}_1 - \sin\theta\boldsymbol{e}_2. \tag{7.15}$$

This is because the polar coordinates θ and Θ here are non-standard by definition; they are their classical counterparts minus $\pi/2$. The basic vectors $\boldsymbol{E}_1$, $\boldsymbol{E}_2$, $\boldsymbol{e}_1$ and $\boldsymbol{e}_2$ presented in (7.15) have the same meaning as in section 7.2.

As shown by Silling (1991), the mapping $\mathcal{B}_0^\star \to \mathcal{B}_e^\star$ is enforced by the variable transformation

$$r = \frac{1}{\sqrt{2}}R, \qquad \theta = 2\Theta, \tag{7.16}$$

and hence we have the connection $r_c = R_c/\sqrt{2}$. The associated deformation gradient $F^\star$ is defined through $d\boldsymbol{x} = F^\star d\boldsymbol{X}$ and takes the form

$$F^\star = \frac{1}{\sqrt{2}}\boldsymbol{e}_r \otimes \boldsymbol{E}_R + \sqrt{2}\boldsymbol{e}_\theta \otimes \boldsymbol{E}_\Theta. \tag{7.17}$$

Here and hereafter, a superscript $\star$ signifies association with the creasing deformation (7.16). We note that, as with the primary uni-axial compression, the incompressibility constraint $\det F^\star = 1$ is automatically satisfied. The first principal invariant of the associated left Cauchy-Green strain tensor $B^\star = F^\star F^{\star T}$ takes the following constant value:

$$I_1^\star = \frac{5}{2}. \tag{7.18}$$

The non-zero in-plane components of the corresponding Cauchy stress tensor $\sigma^\star$ are

$$\sigma_{rr}^\star = W_1^\star - p^\star(r) \quad \text{and} \quad \sigma_{\theta\theta}^\star = 4W_1^\star - p^\star(r), \tag{7.19}$$

where $p^\star(r)$ is the Lagrangian multiplier enforcing incompressibility in $\mathcal{B}_e^\star$ and $W^\star = W(I_1^\star)$, $W_1^\star = W'(I_1^\star)$, etc. Given (7.19), only the equilibrium equation in the r direction remains unsatisfied, and this equation is expressed as

$$\frac{\partial \sigma_{rr}^\star}{\partial r} = \frac{1}{r}\left\{\sigma_{\theta\theta}^\star - \sigma_{rr}^\star\right\} \implies \frac{\partial}{\partial r}(r\sigma_{rr}^\star) = \sigma_{\theta\theta}^\star. \tag{7.20}$$

By substituting (7.19) into (7.20) and then integrating the resulting equation backwards from $r = r_c$, we obtain

$$p^\star(r) = -3W_1^\star \ln(r/r_c) + p^\star(r_c). \tag{7.21}$$

Then, on setting $r = r_c$ in $(7.19)_1$, we may determine that

$$p^\star(r_c) = W_1^\star - \sigma_{rr}^\star(r_c), \tag{7.22}$$

and hence

$$p^\star(r) = W_1^\star - 3W_1^\star \ln(r/r_c) - \sigma_{rr}^\star(r_c). \tag{7.23}$$

Thus, the folding solution is defined up to an additive constant $\sigma_{rr}^\star(r_c)$, which will be related to $\bar{\sigma}_{11}$ in section 7.5. For later use, we also record here the deformation gradient $F^\star$ and the nominal stress tensor $S^\star$ $(= F^{\star\,-1}\sigma^\star)$ at $\Theta = -\pi/2$ relative to the orthonormal bases $(\boldsymbol{E}_A)$ and $(\boldsymbol{e}_i)$:

$$F^\star = \sqrt{2}\,\boldsymbol{e}_1 \otimes \boldsymbol{E}_2 - \frac{1}{\sqrt{2}}\,\boldsymbol{e}_2 \otimes \boldsymbol{E}_1, \tag{7.24}$$

$$S^\star = -\sqrt{2}\,\{W_1^\star - p^\star(r)\}\,\boldsymbol{E}_1 \otimes \boldsymbol{e}_2 + \frac{1}{\sqrt{2}}\,\{4W_1^\star - p^\star(r)\}\,\boldsymbol{E}_2 \otimes \boldsymbol{e}_1. \tag{7.25}$$

7.4 The incremental field

Thus far, we have considered the uni-axial compression of a half-space which we term the "primary solution". Then, we assumed that the formation of a crease on the free surface of the half-space is *locally* equivalent to the folding of an infinitesimal semi-circular region into a self-contacting circular region, and we term this the

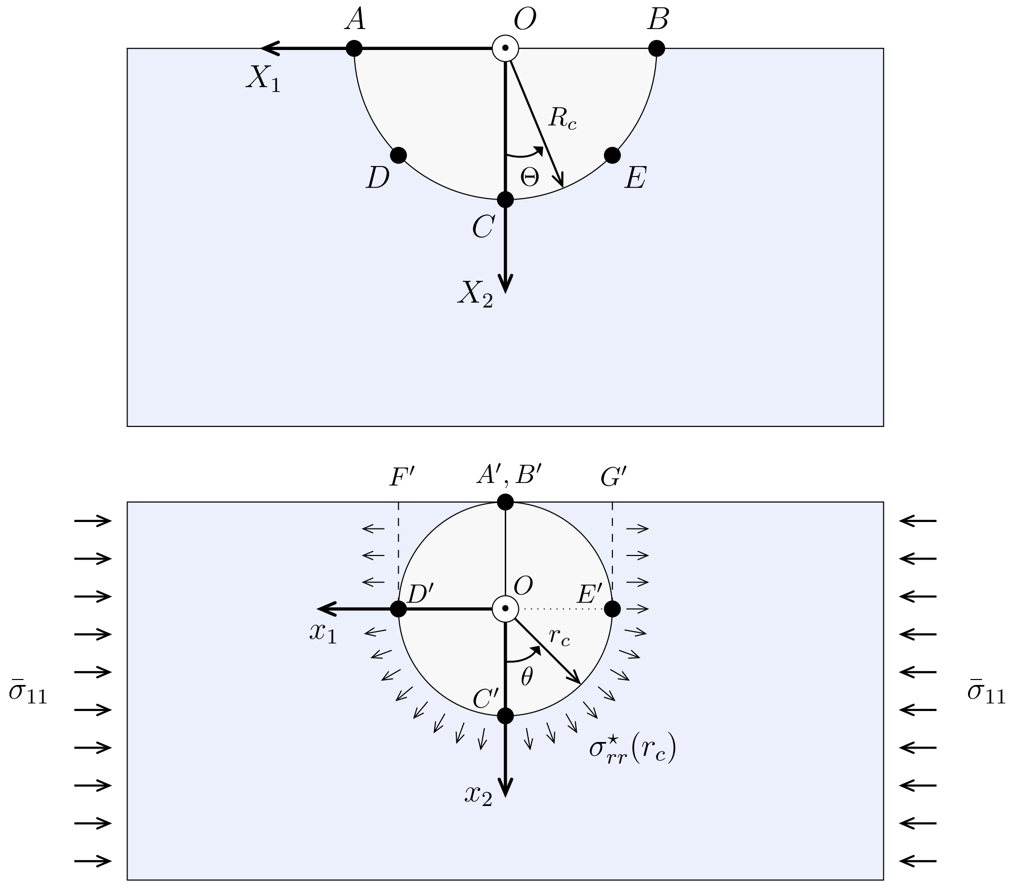

Figure 7.3: A simplified model to describe the effect of crease formation on the surrounding material. The upper and lower sketches show the creased domain in the reference configuration and the current configuration, respectively.

"folding solution". The question we now must ask ourselves is: what effect does the folding solution have on the primary solution, and vice versa?

Consider the simple model of creasing shown in Fig. 7.3 in which the semi-circular region $\mathcal{B}_0^\star$ described in the previous section would undergo a deformation given by (7.16) in the absence of constrictions of the surrounding material. Its image in the current configuration would be a circular domain with radius r_c as discussed earlier. We observe that, with constriction, the deformation in the creased region is very complicated. For instance, whereas the region near the crease tip O is undergoing a π-to-2π folding, the region near the end of the self-contact at points A' and B' is subjected to a π-to-$\pi/2$ bending deformation such that the surface outside the creased zone is horizontal again. It would seem impossible to give the deformation an exact description, and so the best we can do is propose a model which captures the leading order behaviour of the exact solution *in the limit* $r_c \to 0$.

To elaborate, we may think of the current creased configuration as the result of two consecutive deformations: firstly a π-to-2π folding around O as described above, and secondly a π-to-$\pi/2$ bending deformation around the points A' and B'. We assume that the crease formation has an $\mathcal{O}(r_c)$ effect on the deformation of the surrounding material, and conversely, the constriction of the surrounding material will induce an $\mathcal{O}(r_c)$ correction on the actual position of the curved surface $D'C'E'$ and the stress field on it. Thus, the leading order resultant force on $D'C'E'$ will be calculated with the aid of $\sigma^{\star}_{rr}$. However, the bending deformation around A' or B' has a more drastic effect on the stress field within the area bounded by $OE'G'B'A'F'D'$ (and even the locations of these points except O, A' and B' may deviate significantly from those shown in Fig. 7.3). In particular, equilibrium of the *infinitesimal* area $OB'G'E'$ implies that the resultant force on $G'E'$ must be horizontal under the assumption that OA' and OB' are in smooth, non-frictional contact. This in turn implies that the resultant force on OE' must be zero to leading order since $B'G'$ is traction-free. Finally, overall equilibrium of the rectangular domain defined by $x_1 < 0$, $x_2 < 0$ implies that the resultant on OB' is $-r_c\bar{\sigma}_{11}\boldsymbol{e}_1$.

Under the above assumptions, the tractions on the curved surface $D'C'E'$ are given by $\sigma^{\star}_{rr}(r_c)\boldsymbol{e}_r$, and have the following non-zero resultant:

$$\int_{-\pi/2}^{\pi/2} \sigma^{\star}_{rr}(r_c)\boldsymbol{e}_r r_c d\theta = r_c\sigma^{\star}_{rr}(r_c)\int_{-\pi/2}^{\pi/2}(-\sin\theta\boldsymbol{e}_1 + \cos\theta\boldsymbol{e}_2)d\theta = 2r_c\sigma^{\star}_{rr}(r_c)\boldsymbol{e}_2. \quad (7.26)$$

Since the resultant force on $D'F'$ is balanced by the force on $E'G'$ due to symmetry, the net force on the surface $F'G'E'C'D'F'$ is given by (7.26). It then follows that the effect of the creased region on the material sufficiently far away from the origin is given by the following equal yet opposite force $\delta\boldsymbol{f}$:

$$\delta\boldsymbol{f} = -2r_c\sigma^{\star}_{rr}(r_c). \quad (7.27)$$

The above force $\delta\boldsymbol{f}$ is of $\mathcal{O}(r_c)$ and hence infinitesimal. Thus, the resulting perturbation of the surrounding uni-axially compressed material should be infinitesimal, and it should also decay as we move far away from the crease tip. We now determine the small-amplitude perturbation imposed by the folding solution onto the surrounding material by applying the classical incremental equations of non-linear elasticity.

We assume that, in the limit $r_c \to 0$, the crease formation imposes a small-amplitude displacement onto the uni-axially compressed configuration $\mathcal{B}_e$, producing a resultant configuration $\mathcal{B}_t$. Let X_A, $x_i(X_A)$ and $\tilde{x}_i(X_A)$ be the components of the position vectors of a representative material particle in $\mathcal{B}_0$, $\mathcal{B}_e$ and $\mathcal{B}_t$, respectively. Then, the relation

$$\tilde{x}_i = x_i(X_A) + u_i(x_j), \tag{7.28}$$

is established, with $u_i(x_j)$ denoting the components of the small amplitude displacement associated with the deformation $\mathcal{B}_e \to \mathcal{B}_t$. With use of (7.28), the components of the deformation gradients $\bar{F}$ and $\tilde{F}$ mapping $\mathcal{B}_0 \to \mathcal{B}_e$ and $\mathcal{B}_e \to \mathcal{B}_t$ are given respectively as follows:

$$\bar{F}_{iA} = \frac{\partial x_i}{\partial X_A}, \qquad \tilde{F}_{iA} = \frac{\partial \tilde{x}_i}{\partial X_A} = (\delta_{ij} + u_{i,j})\bar{F}_{jA}, \tag{7.29}$$

where δ_{ij} is the Kronecker delta function defined in (2.3), and a tilde signifies association with the deformation $\mathcal{B}_0 \to \mathcal{B}_t$. Given $(7.29)_2$, the incompressibility constraint $\det \tilde{F} = 1$ for the deformation $\mathcal{B}_0 \to \mathcal{B}_t$ takes the form

$$u_{i,i} = 0. \tag{7.30}$$

We may also show, with the use of $(7.29)_2$ and (7.30), that the linearized first principal invariant of $\tilde{F}\tilde{F}^T$ is

$$\tilde{I}_1 = \operatorname{tr} \tilde{F}\tilde{F}^T = \lambda^2 + \lambda^{-2} + 2(\lambda^2 - \lambda^{-2})u_{1,1}. \tag{7.31}$$

We introduce the incremental stress tensor χ whose linearized components χ_{ij} are

$$\chi_{ij} = \mathcal{A}_{jilk} u_{k,l} + \bar{p} u_{j,i} - \delta p \, \delta_{ji}; \tag{7.32}$$

recall that $\mathcal{A}_{jilk}$ are the first-order instantaneous moduli, $\bar{p}$ is the pressure in $\mathcal{B}_e$ and δp is the incremental pressure associated with the deformation $\mathcal{B}_e \to \mathcal{B}_t$.

The incremental equilibrium equations take the simple form

$$\chi_{ij,j} = 0. \tag{7.33}$$

Given our assumption (7.6), we are able to express the instantaneous elastic moduli $\mathcal{A}_{jilk}$ in the reduced form given in (2.76). Through substitution of (7.32) into (7.33) and making use of (7.30), the incremental equilibrium equations reduce to

$$\mathcal{A}_{j1lk}u_{k,lj} - \delta p_{,1} = 0, \qquad \mathcal{A}_{j2lk}u_{k,lj} - \delta p_{,2} = 0. \tag{7.34}$$

A stream function $\phi = \phi(x_1, x_2)$ can then be introduced to satisfy the incompressibility constraint (7.30) exactly through the relations

$$u_1 = -\phi_{,2}, \qquad u_2 = \phi_{,1}. \tag{7.35}$$

We substitute the expressions (7.35) into (7.34). We then cross-differentiate $(7.35)_1$ and $(7.35)_2$, and subtract the latter resulting equation from the former in order to eliminate the term involving the incremental pressure. The following fourth-order partial differential equation is subsequently obtained:

$$\alpha\,\phi_{,1111} + 2\beta\,\phi_{,1122} + \gamma\,\phi_{,2222} = 0, \tag{7.36}$$

where the coefficients α, β and γ in this instance have the same meaning as in equation (4.7) of Dowaikh and Ogden (1990), and should not be confused with alternate definitions given in previous chapters. These coefficients take the following explicit form:

$$\alpha = 2\lambda^2\bar{W}_1, \qquad \beta = \frac{1}{\lambda^4}\left\{\lambda^2(\lambda^4+1)\bar{W}_1 + 2(\lambda^4-1)^2\bar{W}_{11}\right\}, \qquad \gamma = \lambda^{-4}\alpha. \tag{7.37}$$

We also assume that the surface $x_2 = 0$, $x_1 \neq 0$ is traction-free in the limit $r_c \to 0$, and this boundary condition takes the form

$$\chi_{12} = \chi_{22} = 0, \qquad x_2 = 0,\ x_1 \neq 0. \tag{7.38}$$

Finally, we assume that the perturbed field decays at a sufficiently large distance away from the crease tip such that

$$\lim_{|\boldsymbol{x}|\to\infty} (u_1, u_2) = \mathbf{0}. \tag{7.39}$$

To find a general solution to (7.36), we first rewrite it in the form

$$\Delta_1\Delta_2\phi = \Delta_2\Delta_1\phi = 0,$$
$$\Delta_1 = \omega^2\frac{\partial^2}{\partial x_1^2} + \omega^{-2}\frac{\partial^2}{\partial x_2^2}, \qquad \Delta_2 = \omega^2\lambda^2\frac{\partial^2}{\partial x_1^2} + \omega^{-2}\lambda^{-2}\frac{\partial^2}{\partial x_2^2}. \tag{7.40}$$

The scaling factor ω in the above expressions can be obtained by comparing the expansion of (7.40) with (7.36), and it may be defined through either of the following two relations:

$$2^{1/4}\omega = \left\{\kappa + \lambda^4 + 1 \pm \sqrt{\kappa^2 + 2\kappa(\lambda^4+1) + (\lambda^4-1)^2}\right\}^{1/4}, \tag{7.41}$$

where $\kappa = 2(\lambda^3 - \lambda^{-1})^2\bar{W}_{11}/\bar{W}_1$. We require a solution to (7.40) which admits the necessary singular behaviour at the origin resulting from the crease formation. Such a solution is a linear combination of the solutions to $\Delta_1\phi = 0$ and $\Delta_2\phi = 0$, and is given by

$$\phi = A_1 G(\omega^{-1}x_1, \omega x_2) + A_2 G(\omega\lambda^{-1}x_1, \omega^{-1}\lambda x_2), \tag{7.42}$$

where
$$G(x,y) = x\ln(x^2+y^2) + 2y\arctan\left(\frac{x}{y}\right), \tag{7.43}$$

and the constants A_1 and A_2 are to be determined. Note that the harmonic function $G(x,y)$ above is the real part of the analytical function $(z/2)\ln z$, $z = x + \mathrm{i}y$ (Barnett and Lothe, 1975).

With use of (7.32) and (7.35), the boundary conditions (7.38) are given respectively by

$$\phi_{,11} - \phi_{,22}, \qquad \frac{4}{\lambda^4}\left\{\lambda^2\bar{W}_1 - (\lambda^4-1)\bar{W}_{11}\right\}\phi_{,12} - \delta p = 0, \qquad x_2 = 0,\ x_1 \neq 0. \tag{7.44}$$

By solving $(7.34)_1$ for $\delta p_{,1}$ and substituting the resulting expression into the x_1 derivative of $(7.44)_2$, we obtain

$$\left\{2(\lambda^4-1)^2\bar{W}_{11} + \lambda^2(\lambda^4+2)\bar{W}_1\right\}\phi_{,112} + \lambda^2\bar{W}_1\phi_{,222} = 0, \quad x_2 = 0,\ x_1 \neq 0, \tag{7.45}$$

which is automatically satisfied by (7.42). Then, upon substitution of (7.42), we find that $(7.44)_1$ is satisfied provided the following relation holds:

$$A_1 = -\frac{A_2(\omega^4+\lambda^4)}{\omega^2(1+\omega^4)\lambda}. \tag{7.46}$$

Finally, we seek to determine the constant A_2. This is achieved by formulating a condition which ensures the balance of the resultant of incremental tractions in the negative x_2 direction sufficiently far away from the emerging crease tip with the opposing concentrated resultant force $\delta\boldsymbol{f}$ due to the crease formation. We consider a rectangular contour with sides at $x_1 = \pm l$ and $x_2 = h$, and calculate the resultant along it. Equilibrium then requires that

$$2\int_0^h \chi_{21}(l, x_2)dx_2 + 2\int_0^l \chi_{22}(x_1, h)dx_1 + \delta\boldsymbol{f}\cdot\boldsymbol{e}_2 = 0. \tag{7.47}$$

With use of (7.27) and the preceding derivations for the incremental field, we determine from (7.47) that A_2 takes the form

$$A_2 = \frac{r_c\lambda^3\omega^5(1+\omega^4)\sigma^\star_{rr}(r_c)}{2\pi\bar{W}_1\left\{\omega^{12}\lambda^2 - \lambda^8 + (\omega^8 - \omega^4\lambda^2)(2\lambda^2 - 1)\right\}}. \tag{7.48}$$

We observe that A_2, and hence A_1 by (7.46), is proportional to r_c. Thus, given (7.35) and (7.42) – (7.43), the incremental displacement of the primary solution due to crease formation is indeed of $\mathcal{O}(r_c)$. The incremental stress components χ_{ij} and the incremental displacement components u_i are presented in Appendix. 7.A.

7.5 Bifurcation condition

We have now considered a primary uni-axial compression solution, a creased solution encapsulated by the folding of a half-space into a whole-space and an incremental displacement field superposed by the latter onto the former. To obtain a bifurcation threshold for creasing, we must now determine the conditions under which all three of these solutions can coexist in a state of equilibrium. We identify that at this point in the analysis there are two remaining unknowns: the additive constant $\sigma^\star_{rr}(r_c)$ from the folding solution and the critical value of the stretch λ for crease initiation which we denote by λ_{cr}. To determine these unknowns, we make use of the two conservation laws corresponding to the stationarity of the total energy functional with respect to variations in $\boldsymbol{x}$ and $\boldsymbol{X}$, respectively. The first conservation law is simply the equilibrium condition in the current creased configuration, whereas the second is given in terms of the *energy-momentum tensor* through (2.119).

7.5.1 Determining $\sigma^\star_{rr}(r_c)$

We again refer to the simplified model shown in Fig. 7.3, and recall our assumption that the field within the lower half of the circular domain with radius r_c is the folding solution plus a perturbation of $\mathcal{O}(r_c)$, whereas the field below the horizonal line $x_2 = r_c$ is the primary uni-axial compression plus a perturbation of $\mathcal{O}(r_c)$. Also, the resultant on OB' has been determined to be $-r_c\bar{\sigma}_{11}\boldsymbol{e}_1$.

Consider the rectangular domain bounded by $x_1 = 0, l$ and $x_2 = -r_c, h$, where both l and h are sufficiently large positive constants. The balance of tractions on the boundary of this rectangular domain to leading order requires that

$$\int_{-r_c}^{h} \bar{\sigma}_{11}|_{x_1=l}dx_2 + \int_{h}^{r_c} \bar{\sigma}_{11}|_{x_1=0}dx_2 + \int_{r_c}^{0} \sigma^\star_{\theta\theta}|_{\theta=0}dr + \int_{0}^{-r_c} \bar{\sigma}_{11}|_{x_1=0}dx_2 = 0. \quad (7.49)$$

Through integrating $(7.20)_2$ between $r = 0$ and r_c, we can determine from (7.49) that

$$\sigma^\star_{rr}(r_c) = \bar{\sigma}_{11}. \quad (7.50)$$

7.5.2 Determining $\lambda_{\mathbf{cr}}$

Consider first the reference domain $\mathcal{B}_0' = \mathcal{B}_0 \cup \mathcal{B}_0^\star$ in Fig. 7.4 bounded by $X_1 = \pm L$ and $X_2 = 0, L$. We denote its boundary by $\partial\mathcal{B}_0'$ and travel along it in the anti-clockwise direction; see the blue contour in Fig. 7.4. Furthermore, we initially assume that L is a sufficiently large positive constant, but then we will take the limit $L \to \infty$.

As shown in section 2.5.2.2 of chapter 2, the stationarity of the total energy functional with respect to perturbations in $\boldsymbol{X}$ gives rise to the following conservation law (Chadwick, 1975) which must be satisfied by our solution:

$$\boldsymbol{\mathcal{J}} \equiv \int_{\partial\mathcal{B}_0'} \Sigma\boldsymbol{N}ds = \boldsymbol{0}, \quad (7.51)$$

where $\Sigma = WI - SF$ is the *energy-momentum tensor*, S is the nominal stress tensor corresponding to a *general* deformation, $\boldsymbol{N}$ is the unit normal to $\partial\mathcal{B}_0'$ and ds is an

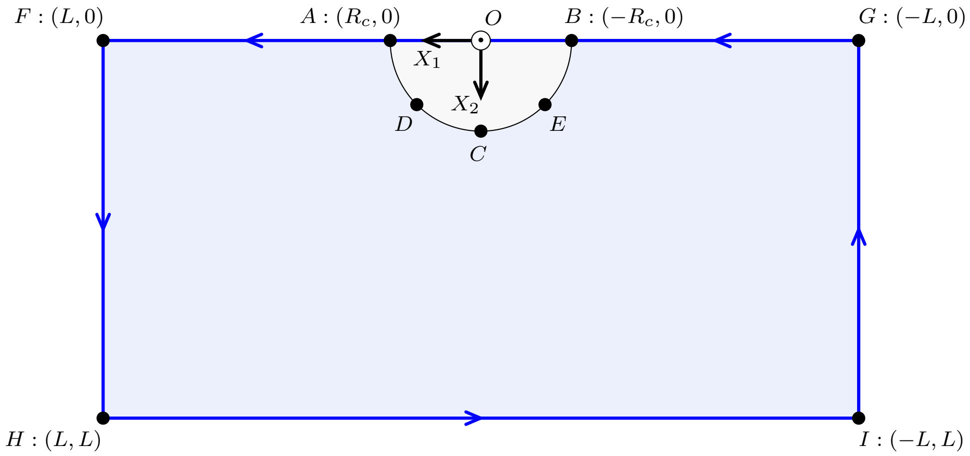

Figure 7.4: A schematic of the reference domain $\mathcal{B}_0' = \mathcal{B}_0 \cup \mathcal{B}_0^\star$ bounded by $X_1 = \pm L$ and $X_2 = 0, L$. We travel along the boundary $\partial\mathcal{B}_0'$ (shown in blue) in the anti-clockwise direction.

infinitesimal line element along $\partial\mathcal{B}_0'$. Having verified that $\boldsymbol{\mathcal{J}} \cdot \boldsymbol{E}_1$ is identically zero, our considered bifurcation condition is $\boldsymbol{\mathcal{J}} \cdot \boldsymbol{E}_2 = 0$. This condition is expressible as

$$\int_{\partial\mathcal{B}_0'} \{W N_2 - S_{2i} F_{iA} N_A\}\, ds, \tag{7.52}$$

where N_A are the components of $\boldsymbol{N}$.

We next consider the Taylor expansion of the left-hand side of the above equation around $r_c = 0$. The $\mathcal{O}(1)$ term is zero since it corresponds to the primary uni-axial compression before crease formation which already satisfies the equilibrium equations. The next term is of $\mathcal{O}(r_c)$, and it is by forcing the coefficient of r_c in this term to be equal to zero that the bifurcation condition for creasing is obtained.

On taking the limit $L \to \infty$, the $\mathcal{O}(r_c)$ contribution is restricted to the free surface $X_2 = 0$ since the decay condition (7.39) will cause the incremental displacement field to vanish at $X_1 = \pm L$ and $X_2 = L$. The bifurcation condition can then be expressed as a sum of contributions from the folding solution (between points B and A in Fig. 7.4) and the incremental field (between points G and B, and A and F in Fig. 7.4). Specifically, we have

$$2\int_0^{R_c} \{W^\star - S^\star_{2i} F^\star_{i2}\}\, dX_1 + 2\int_{R_c}^{L} \left\{\delta\tilde{W} - (\delta\tilde{S})_{2i}\bar{F}_{i2} - \bar{S}_{2i}(\delta\tilde{F})_{i2}\right\} dX_1 = 0, \tag{7.53}$$

where the integrands are evaluated at $X_2 = 0$, and $\delta\tilde{W}$, $\delta\tilde{S}$ and $\delta\tilde{F}$ are the $\mathcal{O}(r_c)$ terms in the expansions of $\tilde{W} = W(\tilde{I}_1)$, $\tilde{S}$ and $\tilde{F}$ (respectively) which will be computed shortly.

For the first integral on the left-hand side of (7.53), which is the contribution due to the folding solution, we may use (7.23), (7.24) and (7.25) to deduce that

$$S^\star_{2i}F^\star_{i2} = S^\star_{21}F^\star_{12} = 4W^\star_1 - p^\star\left(\frac{X_1}{\sqrt{2}}\right) = 3W^\star_1 + 3W^\star_1 \log\left(\frac{X_1}{\sqrt{2}}\right) + \sigma^\star_{rr}(r_c). \tag{7.54}$$

It then follows that

$$2\int_0^{R_c} \{W^\star - S^\star_{2i}F^\star_{i2}\}\, dX_1 = 2\sqrt{2}\, r_c \{W^\star - \sigma^\star_{rr}(r_c)\}\,, \tag{7.55}$$

where use has been made of the established relation $r_c = R_c/\sqrt{2}$.

We then move on to the second integral in (7.53), which pertains to the incremental field superposed onto the surrounding compressed material sufficiently far away from the crease tip. We note first that traction-free boundary conditions can be written as

$$\bar{S}_{2i} = \bar{F}^{-1}_{22}\bar{\sigma}_{2i} = 0, \qquad \delta\tilde{S}_{2i} = \bar{F}^{-1}_{22}\chi_{i2} = 0, \qquad X_2 = 0; \tag{7.56}$$

see (2.40). With the aid of (7.31), we may also deduce to $\mathcal{O}(\tilde{I}_1)$ that

$$\tilde{W} = \bar{W} + (\tilde{I}_1 - \bar{I}_1)\bar{W}_1 \implies \delta\tilde{W} = \tilde{W} - \bar{W} = 2(\lambda^2 - \lambda^{-2})u_{1,1}\bar{W}_1. \tag{7.57}$$

In the limit $L \to \infty$, the second integral in (7.53) therefore becomes

$$\begin{aligned} 2\lim_{L\to\infty}\int_{R_c}^{L} \delta\tilde{W}|_{X_2=0}dX_1 &= 4\,(\lambda - \lambda^{-3})\bar{W}_1 \lim_{L\to\infty}\int_{R_c}^{L} \left.\frac{\partial u_1}{\partial X_1}\right|_{X_2=0} dX_1, \\ &= 2\omega^4\lambda^2(\lambda^2-1)(\lambda-\lambda^{-3})\sigma^\star_{rr}(r_c)r_c\left\{\omega^8\lambda^2 + \lambda^6 + \omega^4(\lambda^4+2\lambda^2-1)\right\}^{-1}, \end{aligned} \tag{7.58}$$

where use has been made of the decay condition (7.39). On setting the sum of the two integrals (7.55) and (7.58) to zero, and making use of the relations (7.41) and (7.50), the bifurcation condition for crease formation is found to take the form

$$\begin{aligned} &\sqrt{2}\left\{\lambda^3(\lambda^6+\lambda^4+3\lambda^2-1)W^\star - 4\lambda(\lambda^4-1)^3\bar{W}_{11}\right\}\bar{W}_1 + 2\sqrt{2}\lambda^3(\lambda^4-1)^2W^\star\bar{W}_{11} \\ &- 2(\lambda^4-1)(\sqrt{2}\lambda^7 - \lambda^6 + \sqrt{2}\lambda^5 + \lambda^4 + 3\sqrt{2}\lambda^3 + \lambda^2 - \sqrt{2}\lambda - 1)\bar{W}_1^2 = 0. \end{aligned} \tag{7.59}$$

To illustrate (7.59), we adopt the Gent material model, which takes the following modified form in the case of plane strain deformations:

$$W(I_1) = -\frac{1}{2}\mu J_\mathrm{m} \ln\left(1 - \frac{I_1 - 2}{J_\mathrm{m}}\right). \tag{7.60}$$

On substituting (7.60) into (7.59), the bifurcation condition for creasing corresponding to the Gent material model is found to take the explicit form

$$\begin{aligned}
&\sqrt{2}\lambda_\mathrm{cr}^{11} + \lambda_\mathrm{cr}^{10} + \sqrt{2}(J_\mathrm{m}+1)\lambda_\mathrm{cr}^{9} + \sqrt{2}(J_\mathrm{m}-6)\lambda_\mathrm{cr}^{7} + (J_\mathrm{m}+2)(\lambda_\mathrm{cr}^{2} + 3\sqrt{2}\lambda_\mathrm{cr}+1)\lambda_\mathrm{cr}^{4} \\
&- (J_\mathrm{m}+3)(\lambda_\mathrm{cr}^{6} + \sqrt{2}\lambda_\mathrm{cr}+1)\lambda_\mathrm{cr}^{2} + \sqrt{2}\lambda_\mathrm{cr} + 1 - \frac{\lambda_\mathrm{cr}}{\sqrt{2}(\lambda_\mathrm{cr}^{4}-1)} \ln\left(1 - \frac{1}{2J_\mathrm{m}}\right) \times \\
&\Big\{\lambda_\mathrm{cr}^{14} - \lambda_\mathrm{cr}^{12} - (J_\mathrm{m}^2 + 2J_\mathrm{m} + 7)\lambda_\mathrm{cr}^{10} - (J_\mathrm{m}^2 - 8J_\mathrm{m} - 19)\lambda_\mathrm{cr}^{8} - 3(J_\mathrm{m}^2 + 4J_\mathrm{m} + 7)\lambda_\mathrm{cr}^{6} \\
&+ (J_\mathrm{m}^2 + 8J_\mathrm{m} + 13)\lambda_\mathrm{cr}^{4} - (2J_\mathrm{m}+5)\lambda_\mathrm{cr}^{2} + 1\Big\} = 0.
\end{aligned} \tag{7.61}$$

We plot in Fig. 7.5 the bifurcation condition (7.61), the bifurcation condition for wrinkling:

$$\lambda_\mathrm{cr}^{10} + (J_\mathrm{m}+1)\lambda_\mathrm{cr}^{8} + (J_\mathrm{m}-6)\lambda_\mathrm{cr}^{6} + 3(J_\mathrm{m}+2)\lambda_\mathrm{cr}^{4} - (J_\mathrm{m}+3)\lambda_\mathrm{cr}^{2} + 1 = 0, \tag{7.62}$$

as given in equation (4.14) of Destrade and Scott (2004), and the inextensible threshold $\bar{I}_1 - 2 = J_\mathrm{m}$ in the $(J_\mathrm{m}, \lambda_\mathrm{cr})$ plane. We see firstly that, according to our theory, creasing is only possible if $J_\mathrm{m} \geq 3.711$. Furthermore, as has been widely observed in experiments, creasing will occur earlier into the uni-axial compression than wrinkling for any value of $J_\mathrm{m} \geq 3.711$. For smaller values of $J_\mathrm{m} \geq 3.711$, the value of λ_cr on the upper branch is smaller. Thus, a lower level of extensibility of the material can delay the onset of crease formation. The black squares represent the corresponding FEM simulation results from Jin and Suo (2015), and we see that there is good agreement with our theory.

On taking the limit $J_\mathrm{m} \to \infty$ in (7.60), we obtain the plane strain counterpart of the neo-Hookean material model (2.58). The bifurcation condition for creasing pertaining to this model is the following polynomial equation:

$$\begin{aligned}
&4\lambda_\mathrm{cr}^{11} - \sqrt{8}\lambda_\mathrm{cr}^{10} + 3\lambda_\mathrm{cr}^{9} + \sqrt{8}\lambda_\mathrm{cr}^{8} + 7\lambda_\mathrm{cr}^{7} + \sqrt{32}\lambda_\mathrm{cr}^{6} - 11\lambda_\mathrm{cr}^{5} - \sqrt{32}\lambda_\mathrm{cr}^{4} - 11\lambda_\mathrm{cr}^{3} \\
&- \sqrt{8}\lambda_\mathrm{cr}^{2} + 4\lambda_\mathrm{cr} + \sqrt{8} = 0.
\end{aligned} \tag{7.63}$$

From (7.63) we determine that the critical stretch for crease formation in a neo-Hookean material is $\lambda_{\mathrm{cr}}^{\mathrm{nH}} = 0.64221$; this is in excellent agreement with the numerical predictions $\lambda_{\mathrm{cr}}^{\mathrm{nH}} = 0.6474$ and $\lambda_{\mathrm{cr}}^{\mathrm{nH}} = 0.646$ of Hohlfeld and Mahadevan (2012) and Jin and Suo (2015), respectively. However, our analytical prediction is at odds with CT, who reported a critical stretch $\lambda_{\mathrm{cr}}^{\mathrm{nH}} = 0.6362$. In the next section, we will note the differences between our analysis and that of CT, and locate the source of this discrepancy.

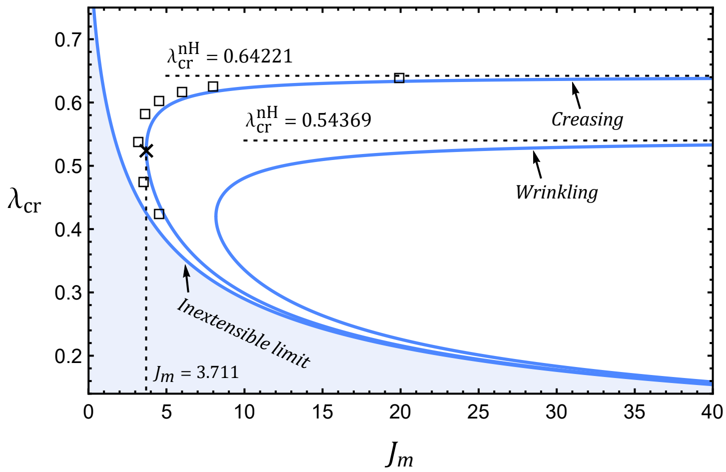

Figure 7.5: Plots of the bifurcation condition for creasing (7.61), the bifurcation condition for wrinkling (7.62) and the inextensible limit $\lambda^2 + \lambda^{-2} - 2 = J_{\mathrm{m}}$. The black squares are the FEM simulation results of Jin and Suo (2015) for the creasing bifurcation condition. The blue shaded region cannot be entered since the material becomes completely rigid at the inextensible limit curve.

7.6 Distinctions with Ciarletta and Truskinovsky (2019)

We first highlight that, on substituting the neo-Hookean material model into equation (3) of CT (which is their reported bifurcation condition for creasing), the critical stretch $\lambda_{\mathrm{cr}} = 0.7098$ is obtained. However, this is at odds with the value $\lambda_{\mathrm{cr}} = 0.6362$ presented on page 4 of the same paper. Through correspondence with CT, it was determined that the aforementioned equation (3) contains a typo. The correct version of CT's bifurcation condition is as follows:

$$2\sqrt{2}\left\{W^\star - 2\bar{W}_1(\lambda^2 - \lambda^{-2})\right\} + \frac{4\sqrt{2}\omega^4(\lambda^2-1)^3(\lambda^2+1)^2\bar{W}_1}{\omega^8\lambda^4 + \lambda^8 + \omega^4\lambda^2(\lambda^4+2\lambda^2-1)} = 0, \qquad (7.64)$$

where ω is as given in (7.41).

Of course, equation (7.64) is still at odds with our reported bifurcation condition (7.59); see Fig. 7.6. It can be shown that if the second term on the left-hand

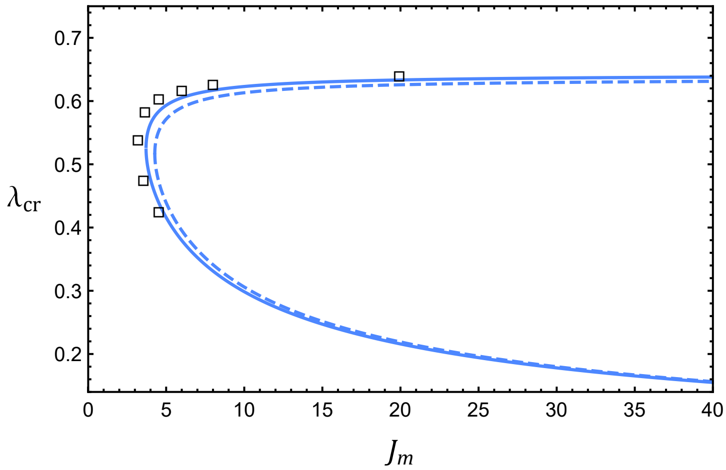

Figure 7.6: A comparison of the bifurcation conditions (7.61) (solid blue curve) and (7.64) specified to the Gent material model (7.60) (dashed blue curve). The black squares are the corresponding FEM simulation results of Jin and Suo (2015).

side of CT's condition (7.64) is divided by $\sqrt{2}\lambda$, our reported bifurcation condition (7.59) is obtained. This discrepancy appears to materialize through the alternate approaches taken in calculating the concentrated force $\delta \boldsymbol{f}$. On page 2 of CT, the following expression for $\delta \boldsymbol{f}$ is given in terms of our notation:

$$\delta \boldsymbol{f} = -4\bar{W}_1(\lambda^2 - \lambda^{-2})R_c. \qquad (7.65)$$

However, equation (S7) in the supplementary material of CT, which is their equivalent of our equation (7.48), can only be true if the right-hand side of (7.65) is multiplied by λ. Thus, we suspect that the reported expression (7.65) is a typo. If we divide the "corrected" form of (7.65) by the discrepancy factor $\sqrt{2}\lambda$, our concentrated force (7.27) is recovered under the relation $r_c = R_c/\sqrt{2}$. We have also determined through correspondence with CT that equations $(S4)$ – $(S6)$, $(S8)_{1,4}$

and ($S9$) in CT's supplementary material contain typos, although these typos do not seem to have been carried through to the actual analysis.

The approach of CT in calculating $\delta\boldsymbol{f}$ is justified using the argument: "*The opposite sides of the self-contact must be pulled together by forces distributed on the reference surface with the normal* $-\boldsymbol{E}_2$". From this argument, and through brief correspondence with CT, we gather that their approach is centred around "pulling back" the tractions along the self-contact lines OA' and OB' to the reference configuration by imposing a prescribed distribution of normal tractions along OA and OB. These tractions are then "pushed forward" to the uni-axially compressed configuration. Whilst the validity of CT's argument is uncertain to us, we believe that our approach to calculating $\delta\boldsymbol{f}$ is well-justified and self-consistent. Furthermore, we observe in Fig. 7.65 that our bifurcation condition is in better agreement with the FEM simulations of Jin and Suo (2015) than the condition of CT, lending further credence to our approach.

7.7 Discussion

An analytical study of crease formation in a compressed hyperelastic half-space based on the seminal work of Ciarletta and Truskinovsky (2019) (referred to as CT) has been presented in this chapter. Our main intent was to provide a more rigorous rephrasing of CT's paper (which was notably lacking in terms of detailed derivations) in order to make the exceptional idea more accessible to the wider community and to encourage further analytical work to be undertaken on this extremely challenging yet enticing problem. Although our general approach was well aligned with CT, we presented a different yet well-justified model which approximates the action of the emerging crease on the surrounding compressed material through a concentrated force argument. The corresponding approach of CT is less well-justified, provokes a certain level of scepticism and leads to a slightly different expression for the aforementioned concentrated force (and in turn the bifurcation condition). We demonstrated that our reported bifurcation condition for creasing is in better agreement with the FEM simulations of Jin and Suo (2015) than the bifurcation condition of CT, lending support for our approach. Nevertheless, it is remarkable how well CT's analysis was able to describe the numerical simulation results of Jin and Suo (2015). For instance, not only can it predict the bifurcation value of λ_{cr} for crease initiation for all values of J_{m} to a high degree of accuracy, it can also describe the second bifurcation value at which a fully developed crease disappears. This excellent agreement seems to indicate that our reported bifurcation condition (7.59) might be exact, despite its derivation involving leading order approximations as previously explained.

7.A Appendix – Incremental displacements and stresses

The incremental displacement components u_1 and u_2 can be expressed through the following relations:

$$\begin{aligned}
\tilde{\omega} u_1 &= \omega^2(\omega^4+\lambda^4)\arctan\left(\frac{x_1}{\omega^2 x_2}\right) - \omega^2(\omega^4+1)\lambda^2\arctan\left(\frac{\omega^2 x_1}{\lambda^2 x_2}\right)\\
\tilde{w} u_2 &= 2(\omega^8-\lambda^4) + (\omega^8+\omega^4)\log\left(\frac{\omega^2 x_1^2}{\lambda^2}+\frac{\lambda^2 x_2^2}{\omega^2}\right) - (\omega^4+\lambda^4)\log\left(\frac{x_1^2}{\omega^2}+\omega^2 x_2^2\right),\\
\tilde{\omega} &= \frac{2\pi \bar{W}_1}{\omega^2\lambda^2 r_c \sigma^{\star}_{rr}(r_c)}\Big\{\omega^{12}\lambda^2 - \lambda^8 + \omega^4(\omega^4-\lambda^2)(2\lambda^2-1)\Big\}. \qquad (7.66)
\end{aligned}$$

An expression for the incremental pressure δp can be determined in the following manner. Firstly, we integrate the incremental equation $(7.34)_2$, say, with respect to x_2 to obtain the expressions

$$\begin{aligned}
\bar{W}_1 \tilde{f}\delta p = &-2\omega^2(\omega^4\lambda^{-2}+1)r_c\sigma^{\star}_{rr}(r_c)x_2\Big\{2\omega^4(\lambda^4-1)(\lambda^4 x_2^2 - x_1^2)\bar{W}_{11}\\
&+\lambda^2(\omega^4(1+\lambda^4)x_1^2 + \omega^8\lambda^4 x_2^2 + \lambda^8 x_2^2)\Big\} + \bar{W}_1\tilde{f}\tilde{C}(x_2),\\
\tilde{f}(x_1,x_2) = &\ \pi(x_1^2+\omega^4 x_2^2)(\omega^4 x_1^2 + \lambda^4 x_2^2)(\omega^8\lambda^2 + \lambda^6 + \omega^4(\lambda^4 + 2\lambda^2 - 1)), \qquad (7.67)
\end{aligned}$$

where $\tilde{C}$ is an arbitrary function of x_2. On substituting the expressions (7.67) into the boundary condition $(7.44)_2$, we find that the function $\tilde{C}(x_2)$ must necessarily be zero. Then, an expression for δp can be explicitly obtained from (7.67), and the incremental stress components χ_{11}, χ_{12}, χ_{21} and χ_{22} can then be defined through

$$\begin{aligned}
\tilde{f}\chi_{11} &= 2\,\lambda^{-2}\bar{W}_1^{-1}\omega^2(\omega^4+\lambda^2)r_c\sigma^\star_{rr}(r_c)x_2\Big\{\lambda^2(\omega^8\lambda^4x_2^2+\lambda^8x_2^2\\
&\qquad +\omega^4(\lambda^4+1)(2x_1^2-\lambda^4x_2^2))\bar{W}_1+2\omega^4(\lambda^4-1)^2(x_1^2-\lambda^4x_2^2)\bar{W}_{11}\Big\},\\
\tilde{f}\chi_{12} &= 2\,\omega^2(\omega^4+1)(\omega^4+\lambda^2)(\omega^4+\lambda^4)r_c\sigma^\star_{rr}(r_c)x_1x_2^2,\\
\tilde{f}\chi_{21} &= 2\,\omega^2(\omega^4+\lambda^2)r_c\sigma^\star_{rr}(r_c)x_1\Big\{\omega^4(\lambda^4-1)x_1^2+\lambda^4(2\omega^4+\omega^8+\lambda^4)x_2^2\Big\},\\
\tilde{f}\chi_{22} &= 2\,\omega^2(\omega^4+\lambda^2)r_c\sigma^\star_{rr}(r_c)x_2\Big\{\omega^4(\lambda^4-1)x_1^2+\lambda^4(2\omega^4+\omega^8+\lambda^4)x_2^2\Big\},
\end{aligned} \tag{7.68}$$

8

Conclusions, perspectives and future work

Contents

8.1 Conclusions and perspectives

We have previously stated that, whilst the study of stress-induced *periodic* pattern formation in elastic materials is highly popular and well understood, research surrounding *localized* pattern formation as a bifurcation problem has only recently begun to prosper. In this thesis, we endeavoured to show that, although localized pattern formation problems are largely more challenging to tackle, much analytical progress can be made in describing the partial or complete bifurcation process. We have specifically focussed on understanding theoretically the bifurcation behaviour of localized bulging, necking and creasing in elastic materials under effects such as surface tension, material compressibility and mechanical loading.

The first part of this thesis was centred around axi-symmetric localized pattern formations in soft incompressible hollow tubes under several elasto-capillary-based boundary conditions and loading scenarios. A study of this problem was noted in chapter 1 to have several physiological motivations; our contributions to this topic can be summarized as follows:

- Analytical bifurcation conditions for localized pattern formation were derived based on known results for the prototypical problem of localized bulging in a hollow tube under internal inflation. These conditions were given in terms of expressions for the surface tension γ and the resultant axial force $\mathcal{N}$ pertaining to the primary axial tension deformation. They have been shown in chapter 3 to be equivalent to the condition for an axi-symmetric bifurcation mode with zero wavenumber to exist, or the condition for zero to become a triple eigenvalue of the associated spectral problem. Thus, we have provided evidence that there exists a strong unification between a range of elastic localized pattern formation problems; we hope that our work will further pave the way for the development of simple analytical bifurcation conditions for unexplored localized pattern formation problems.

- A linear analysis investigated the competition between localized patterns associated with zero wavenumber and periodic patterns in the axial or circumferential direction. We found that the choice of boundary conditions had a significant influence on the type of pattern formation which is preferred. For an internally supported tube (case 2), localized pattern formation is preferred and circumferential buckling modes are physically implausible. In contrast, if the internal support is removed (case 1), then the tube becomes highly sensitive to circumferential buckling modes, and localized pattern formation is unfavourable. When the tube is externally supported (case 3), the type of loading employed has a marked effect. For example, we demonstrated for the fixed λ and increasing γ scenario that there exists a threshold value of λ below which circumferential buckling is preferred and above which localized pattern formation is preferred. Thus, our results not only demonstrate where localized pattern formation is favoured, but highlight that pattern selection in tubes under surface tension can be achieved by an appropriate choice of boundary conditions and loading approaches.

- A weakly non-linear analysis first confirmed our expectations that the zero wavenumber mode is associated with a subcritical localized solitary wave bifurcation solution. The choice of loading scenario was shown to greatly influence whether this localized solution was necking or bulging. In this sense, the treatment of localization as a bifurcation solution with zero wavenumber was beneficial, since the non-zero wavenumber approach would be unable to describe the effect of these various loading conditions. The initiation, growth and propagation of the localized pattern into a final “two-phase” Maxwell state was also described analytically in a small neighbourhood of $\lambda = \lambda_{\text{min}}$. For any fixed $\lambda \neq \lambda_{\text{min}}$, FEM simulations confirmed that the transition beyond $\gamma = \gamma_{\text{cr}}$ from localized pattern to Maxwell state will be a *snap-through*. For $\lambda = \lambda_{\text{min}}$, localized pattern formation is instead non-existent, and a supercritical transition to a “two-phase” state occurs instead. This supercritical bifurcation solution was again determined analytically through our weakly non-linear analysis.

- It was then evidenced that the evolution of final Maxwell state in the fully non-linear regime can be fully understood analytically, and hence that a sole reliance on numerical simulations in predicting post-bifurcation behaviour is unnecessary in this context. For instance, the Maxwell stretches of each “phase” were determined implicitly as functions of γ through the equal area rule. From this, we determined completely the evolution of the amplitude and proportion of the bulged “phase” for multiple loading scenarios. Exceptional agreement between our theory and simulations was witnessed.

It is noteworthy that the higher order role of axial curvature has been shown to influence the dynamic selection and evolution of patterns. For instance, Pandey et al. (2021) demonstrated that dynamically evolved configuration of coexisting cylindrical and spherical beads can exist in sufficiently soft elastic cylinders.

Extensions to our work on the incompressible hollow tube case in chapters 3 through 5 were made in chapter 6 to study the effect of material compressibility on localized pattern formation in soft solid cylinders. We again set out to illustrate that much analytical progress can be made in constructing bifurcation conditions and describing post-bifurcation behaviour. The verification of newly emerged numerical simulation results (Dortdivanlioglu and Javili, 2022) through theoretical means was also a key motivation. The contribution in this area was twofold:

- Analytical bifurcation conditions for localized pattern formation were formulated in a similar manner to in the hollow tube case, and the effect of the Poisson ratio ν on the bifurcation threshold was assessed. For fixed λ and increasing γ, we demonstrated that cylinders with higher levels of compressibility are less susceptible to localized pattern formation. In contrast, for fixed γ (fixed $\mathcal{N}$) and monotonically varying $\mathcal{N}$ (increasing γ), there is a larger range of values of fixed γ (fixed $\mathcal{N}$) for which localized pattern formation is possible in cylinders with a greater level of compressibility. We demonstrated perfect agreement between our theoretical bifurcation conditions and the corresponding numerical simulation results of Dortdivanlioglu and Javili (2022).

- We highlighted that the numerically simulated Maxwell stretches of Dortdivanlioglu and Javili (2022) do not conform to the equal area rule, and presented corrected theoretical counterparts. This served to illustrate that the equal area rule should be used as a consistency check in numerical post-bifurcation studies of phase-separation-like phenomena. A greater degree of compressibility was seen to lower the proportion and amplitude of the bulged section in the final "two-phase" state.

Lastly, we confronted the problem of crease formation in a compressed elastic half-space analytically. Despite there existing many agreeable numerical studies on this problem, theoretical works are few and far between since creasing, being a characteristically non-linear phenomenon, cannot be captured by the standard approach of a linear bifurcation analysis. We presented a re-phrasing of the notably ground-breaking theoretical study of Ciarletta and Truskinovsky (2019), complete with derivations possessing greater detail and rigour. A new approach to calculating the effect of the crease formation on the surrounding compressed material (which we believe is better justified than the associated approach of CT) was proposed. This lead to an analytical bifurcation condition for crease formation which is in slightly better agreement with FEM simulation results compared with the bifurcation condition derived by CT. It is hoped that our rephrasing of CT's analysis will provide both a greater appreciation of the seminal idea and a platform from which a completely convincing argument for the analytical derivation of the bifurcation condition can be formulated.

8.2 Future work

The research presented in this thesis presents several natural avenues for future work. We believe that further inspiration can be taken from the analytical framework for the inflation problem to determine analytical bifurcation conditions for more complicated localized pattern formations. For instance, the consideration of torsion and surface tension effects on soft cylinders could shed greater light on the beading of axons which have been twisted due to rotational head injuries, say. In this case, there would exist an additional force parameter in the resultant moment $\mathcal{M}$, and we anticipate that bifurcation conditions for moment-control-induced localized pattern formation can be easily formulated by setting the derivative of this function with respect to the axial stretch to zero. A transition from localized bulging to a "two-phase" Maxwell state has also been observed in dielectric tubes under internal pressure and an electric field; see Fig. 8.1. Analytical bifurcation conditions for localized bulging in this context have been determined under the membrane assumption (Lu et al., 2015), and the axi-symmetric bifurcation behaviour of a arbitrarily thick tube has been studied in Dorfmann and Ogden (2019), with attention focussed on *periodic* modes. A complete theoretical understanding of the associated localized pattern formation behaviour in arbitrarily thick tubes does not

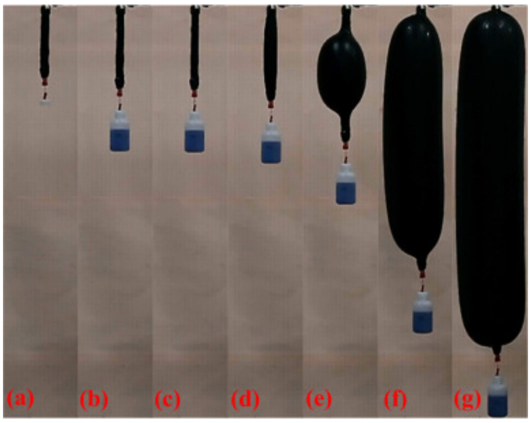

Figure 8.1: Experimental observations of the initiation, growth and propagation of a localized bulge in a membrane tube under axial loading, internal pressure and an electric field (Lu et al., 2015).

yet seem to have been established. We believe that the analytical tools employed in this thesis can be transferred to understanding this problem completely.

Many extensions to the work presented in chapter 7 can be considered. For instance, the formation of creases on the surface and at the interface of soft elastic bilayers has been observed experimentally; see Fig. 8.2. It would be of great interest to investigate whether the seminal idea of Ciarletta and Truskinovsky (2019) can be extended to study this problem. Whether the crease appears on the free surface or the interface is thought to be heavily influence by the thickness and shear modulus ratios of the two layers; the question of whether the threshold values of these ratios at which surface creases become impossible can be determined analytically is highly intriguing.

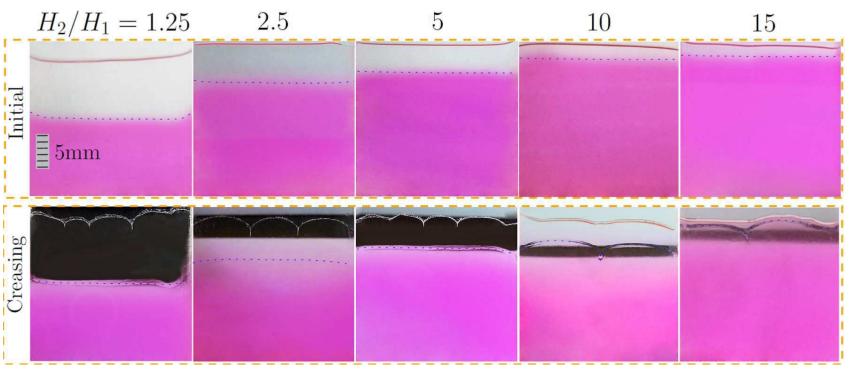

Figure 8.2: Evidence of creasing on the surface and interface of a compressed hydrogel bilayer (Zhou et al., 2017).

Bibliography

Abaqus, 2013. ABAQUS Analysis Users Manual, version 6.13. Dassault Systems, Providence, RI, USA.

Alexander, H., 1971. Tensile instability of initially spherical balloons. Int. J. Eng. Sci. 9, 151–160.

Althobaiti, A., 2022. Effect of torsion on the initiation of localized bulging in a hyperelastic tube of arbitrary thickness. Z. Angew. Math. Phys. 73, 1–11.

Balbi, V., Destrade, M., Goriely, A., 2020. Mechanics of human brain organoids. Phys. Rev. E 101, 022403.

Bar-Ziv, R., Moses, E., 1994. Instability and "pearling" states produced in tubular membranes by competition of curvature and tension. Phys. Rev. Lett. 73, 1392.

Barnett, D., Lothe, J., 1975. Line force loadings on anisotropic half-spaces and wedges. Phys. Norv. 8, 13–22.

Batchelor, G.K., 1967. An introduction to fluid dynamics. Cambridge University Press.

Ben Amar, M., Bordner, A., 2017. Mimicking cortex convolutions through the wrinkling of growing soft bilayers. J. Elast. 129, 213–238.

Bico, J., Reyssat, É., Roman, B., 2018. Elastocapillarity: When surface tension deforms elastic solids. Annu. Rev. Fluid Mech. 50, 629–659.

Biot, M., 1963. Surface instability of rubber in compression. Appl. Sci. Res. 12, 168–182.

Bridges, T.J., 1999. The orr–sommerfeld equation on a manifold. Proc. R. Soc. A 455, 3019–3040.

Bush, J.W., Hu, D.L., 2006. Walking on water: biolocomotion at the interface. Annu. Rev. Fluid Mech. 38, 339–369.

Cao, Y., Hutchinson, J.W., 2011. From wrinkles to creases in elastomers: the instability and imperfection-sensitivity of wrinkling. Proc. R. Soc. A 468, 94–115.

Carew, T.E., Vaishnav, R.N., Patel, D.J., 1968. Compressibility of the arterial wall. Cir. Res. 23, 61–68.

Carroll, M.M., 2004. A representation theorem for volume-preserving transformations. Int. J. Non-Linear Mech. 39, 219–224.

Chadwick, P., 1975. Applications of an energy-momentum tensor in non-linear elastostatics. J. Elast. 5, 249–258.

Chadwick, P., 1999. Continuum Mechanics: Concise Theory and Problems. Courier Corporation.

Chen, D., Cai, S., Suo, Z., Hayward, R.C., 2012. Surface energy as a barrier to creasing of elastomer films: An elastic analogy to classical nucleation. Phys. Rev. Lett 109, 038001.

Chen, D., Hyldahl, R.D., Hayward, R.C., 2015. Creased hydrogels as active platforms for mechanical deformation of cultured cells. Lab Chip 15, 1160–1167.

Chiao, R.Y., Garmire, E., Townes, C.H., 1965. Self-trapping of optical beams. Phys. Rev. Lett. 14, 1056.

Chippada, U., Yurke, B., Langrana, N.A., 2010. Simultaneous determination of young's modulus, shear modulus, and poisson's ratio of soft hydrogels. J. Mater. Res. 25, 545–555.

Ciarletta, P., 2011. Generating functions for volume-preserving transformations. Int. J. Non-Linear Mech. 46, 1275–1279.

Ciarletta, P., 2013. Surface instability of a gel disc in swelling. Eur. Phys. J. E 36, 1–4.

Ciarletta, P., 2018. Matched asymptotic solution for crease nucleation in soft solids. Nat. Commun. 9, 496.

Ciarletta, P., Balbi, V., Kuhl, E., 2014. Pattern selection in growing tubular tissues. Phys. Rev. Lett. 113, 248101.

Ciarletta, P., Ben Amar, M., 2012a. Papillary networks in the dermal–epidermal junction of skin: a biomechanical model. Mech. Res. Commun. 42, 68–76.

Ciarletta, P., Ben Amar, M., 2012b. Peristaltic patterns for swelling and shrinking of soft cylindrical gels. Soft Matter 8, 1760–1763.

Ciarletta, P., Fu, Y.B., 2015. A semi-analytical approach to biot instability in a growing layer: Strain gradient correction, weakly non-linear analysis and imperfection sensitivity. Int. J. Non-Linear Mech. 75, 38–45.

Ciarletta, P., Truskinovsky, L., 2019. Soft nucleation of an elastic crease. Phys. Rev. Lett. 122, 248001.

Clerk-Maxwell, J., 1875. On the dynamical evidence of the molecular constitution of bodies. J. Chem. Soc 28, 493–508.

Conte, S.D., 1966. The numerical solution of linear boundary value problems. SIAM Rev. 8, 309–321.

Cooke, M.E., Jones, S.W., Ter Horst, B., Moiemen, N., Snow, M., Chouhan, G., Hill, L.J., Esmaeli, M., Moakes, R.J., Holton, J., et al., 2018. Structuring of hydrogels across multiple length scales for biomedical applications. Adv. Mater. 30, 1705013.

Cox, H.L., 1940. Stress analysis of thin metal construction. Aeronaut. J. 44, 231–282.

Datar, A., Ameeramja, J., Bhat, A., Srivastava, R., Mishra, A., Bernal, R., Prost, J., Callan-Jones, A., Pullarkat, P.A., 2019. The roles of microtubules and membrane tension in axonal beading, retraction, and atrophy. Biophys. J. 117, 880–891.

Davey, A., 1983. An automatic orthonormalization method for solving stiff boundary-value problems. J. Comput. Phys. 51, 343–356.

De Gennes, P.G., Brochard-Wyart, F., Quéré, D., et al., 2004. Capillarity and wetting phenomena: drops, bubbles, pearls, waves. volume 315. Springer.

Dervaux, J., Ben Amar, M., 2012. Mechanical instabilities of gels. Annu. Rev. Condens. Matter Phys. 3, 311–332.

Destrade, M., Scott, N.H., 2004. Surface waves in a deformed isotropic hyperelastic material subject to an isotropic internal constraint. Wave Motion 40, 347–357.

Dorfmann, A., Ogden, R.W., 2005. Nonlinear electroelasticity. Acta Mech. 174, 167–183.

Dorfmann, L., Ogden, R.W., 2019. Instabilities of soft dielectrics. Philos. Trans. R. Soc. A 377, 20180077.

Dortdivanlioglu, B., Javili, A., 2022. Plateau rayleigh instability of soft elastic solids. effect of compressibility on pre and post bifurcation behavior. Extreme Mech. Lett. 55, 101797.

Dowaikh, M.A., Ogden, R.W., 1990. On surface waves and deformations in a pre-stressed incompressible elastic solid. IMA J. Appl. Math. 44, 261–284.

Emery, D.R., 2023. Elasto-capillary necking, bulging and maxwell states in soft compressible cylinders. Int. J. Non-Linear Mech. 148, 104276.

Emery, D.R., Fu, Y.B., 2021a. Localised bifurcation in soft cylindrical tubes under axial stretching and surface tension. Int. J. Solids Struct. 219, 23–33.

Emery, D.R., Fu, Y.B., 2021b. Elasto-capillary circumferential buckling of soft tubes under axial loading: existence and competition with localised beading and periodic axial modes. Mech. Soft Mater. 3.

Emery, D.R., Fu, Y.B., 2021c. Post-bifurcation behaviour of elasto-capillary necking and bulging in soft tubes. Proc. R. Soc. A 477, 20210311.

Ericksen, J.L., 1975. Equilibrium of bars. J. Elast. 5, 191–201.

Eshelby, J., 1975. The elastic energy-momentum tensor. J. Elast. 5, 321–335.

Fong, H., Chun, I., Reneker, D.H., 1999. Beaded nanofibers formed during electrospinning. Polymer 40, 4585–4592.

Fu, Y.B., 1993. On the instability of inextensible elastic bodies: nonlinear evolution of non-neutral, neutral and near-neutral modes. Proc. R. Soc. A 443, 59–82.

Fu, Y.B., 1999. Buckling of an elastic half-space with surface imperfections, in: Proceedings of the 1st Canadian Conference on Nonlinear Solid Mechanics, The University of Victoria. pp. 99–107.

Fu, Y.B., 2001. Nonlinear stability analysis, in: Fu, Y.B., Ogden, R.W. (Eds.), Nonlinear elasticity: Theory and Applications. Cambridge University Press, Cambridge.

Fu, Y.B., Dorfmann, L., Xie, Y., 2018. Localized necking of a dielectric membrane. Extreme Mech. Lett. 21, 44–48.

Fu, Y.B., Jin, L., Goriely, A., 2021. Necking, beading, and bulging in soft elastic cylinders. J. Mech. Phys. Solids 147, 104250.

Fu, Y.B., Liu, J.L., Francisco, G.S., 2016. Localized bulging in an inflated cylindrical tube of arbitrary thickness–the effect of bending stiffness. J. Mech. Phys. Solids 90, 45–60.

Fu, Y.B., Ogden, R.W., 1999. Nonlinear stability analysis of pre-stressed elastic bodies. Contin. Mech. Thermodyn. 11, 141–172.

Fu, Y.B., Ogden, R.W., 2001. Nonlinear Elasticity: Theory and Applications. Cambridge University Press.

Fu, Y.B., Pearce, S.P., Liu, K.K., 2008. Post-bifurcation analysis of a thin-walled hyperelastic tube under inflation. Int. J. Non-Linear Mech. 43, 697–706.

Fu, Y.B., Rogerson, G.A., 1994. A nonlinear analysis of instability of a pre-stressed incompressible elastic plate. Proc. R. Soc. A 446, 233–254.

Geissler, E., Hecht, A.M., Horkay, F., Zrinyi, M., 1988. Compressional modulus of swollen polyacrylamide networks. Macromolecules 21, 2594–2599.

Gent, A., Cho, I., 1999. Surface instabilities in compressed or bent rubber blocks. Rubber Chem. Technol. 72, 253–262.

Gent, A.N., 1996. A new constitutive relation for rubber. Rubber Chem. Technol. 69, 59–61.

Ghatak, A., Das, A.L., 2007. Kink instability of a highly deformable elastic cylinder. Phys. Rev. Lett. 99, 076101.

Giudici, A., Biggins, J.S., 2020. Ballooning, bulging and necking: an exact solution for longitudinal phase separation in elastic systems near a critical point. Phys. Rev. E 102, 033007.

Goriely, A., 2017. The mathematics and mechanics of biological growth. volume 45. Springer.

Goriely, A., Vandiver, R., Destrade, M., 2008. Nonlinear euler buckling. Proc. R. Soc. A 464, 3003–3019.

Green, A.E., Rivlin, R.S., Shield, R.T., 1952. General theory of small elastic deformations superposed on finite elastic deformations. Proc. R. Soc. A , 128–154.

Gurtin, M.E., Murdoch, A.I., 1975. A continuum theory of elastic material surfaces. Arch. Ration. Mech. Anal. 57, 291–323.

Hannezo, E., Prost, J., Joanny, J.F., 2012. Mechanical instabilities of biological tubes. Phys. Rev. Lett. 109, 018101.

Haragus, M., Iooss, G., 2010. Local bifurcations, center manifolds, and normal forms in infinite-dimensional dynamical systems. Springer Science & Business Media.

Haughton, D.M., Ogden, R.W., 1979a. Bifurcation of inflated circular cylinders of elastic material under axial loading—i. membrane theory for thin-walled tubes. J. Mech. Phys. Solids 27, 179–212.

Haughton, D.M., Ogden, R.W., 1979b. Bifurcation of inflated circular cylinders of elastic material under axial loading—ii. exact theory for thick-walled tubes. J. Mech. Phys. Solids 27, 489–512.

Haughton, D.M., Orr, A., 1995. On the eversion of incompressible elastic cylinders. Int. J. Non-linear Mech. 30, 81–95.

Hazel, A.L., Heil, M., 2005. Surface-tension-induced buckling of liquid-lined elastic tubes: a model for pulmonary airway closure. Proc. R. Soc. A. 461, 1847–1868.

Hemphill, M.A., Dauth, S., Yu, C.J., Dabiri, B.E., Parker, K.K., 2015. Traumatic brain injury and the neuronal microenvironment: a potential role for neuropathological mechanotransduction. Neuron 85, 1177–1192.

Henann, D.L., Bertoldi, K., 2014. Modeling of elasto-capillary phenomena. Soft Matter 10, 709–717.

Hohlfeld, E., 2013. Coexistence of scale-invariant states in incompressible elastomers. Phys. Rev. Lett. 111, 185701.

Hohlfeld, E., Mahadevan, L., 2012. Scale and nature of sulcification patterns. Phys. Rev. Lett. 109, 025701.

Hong, W., Zhao, X., Suo, Z., 2009. Formation of creases on the surfaces of elastomers and gels. Appl. Phys. Lett. 95, 111901.

Horgan, C.O., Saccomandi, G., 2004. Constitutive models for compressible nonlinearly elastic materials with limiting chain extensibility. J. Elast. 77, 123–138.

Huang, Z., Wang, J.x., 2006. A theory of hyperelasticity of multi-phase media with surface/interface energy effect. Acta Mech. 182, 195–210.

Hunt, G.W., Peletier, M.A., Champneys, A.R., Woods, P.D., Wadee, M.A., Budd, C.J., Lord, G.J., 2000. Cellular buckling in long structures. Nonlin. Dynam. 21, 3–29.

Javili, A., Steinmann, P., 2009. A finite element framework for continua with boundary energies. part i: The two-dimensional case. Comput. Methods Appl. Mech. Eng. 198, 2198–2208.

Javili, A., Steinmann, P., 2010. A finite element framework for continua with boundary energies. part ii: The three-dimensional case. Comput. Methods Appl. Mech. Eng. 199, 755–765.

Jin, L., Suo, Z., 2015. Smoothening creases on surfaces of strain-stiffening materials. J. Mech. Phys. Solids 74, 68–79.

Kilinc, D., Gallo, G., Barbee, K.A., 2009. Interactive image analysis programs for quantifying injury-induced axonal beading and microtubule disruption. Comput. Methods Programs Biomed. 95, 62–71.

Kirchgässner, K., 1982. Wave-solutions of reversible systems and applications. J. Diff. Eqns 45, 113–127.

Koiter, W.T., 1945. On the stability of elastic equilibrium. dissertation, delft, the netherlands. an english translation is available in 1967. Tech. Trans. F 10, 833.

Korteweg, D.J., De Vries, G., 1895. On the change of form of long waves advancing in a rectangular canal, and on a new type of long stationary waves. Phil. Mag. 39, 422–443.

Kyriakides, S., Yu-Chung, C., 1990. On the inflation of a long elastic tube in the presence of axial load. Int. J. Solids Struct. 26, 975–991.

Lang, G.E., Waters, S.L., Vella, D., Goriely, A., 2017. Axonal buckling following stretch injury. J. Elast. 129, 239–256.

Lange, C.G., Newell, A.C., 1971. The post-buckling problem for thin elastic shells. SIAM J. Appl. Math. 21, 605–629.

Levich, V., Krylov, V., 1969. Surface-tension-driven phenomena. Annu. Rev. Fluid Mech. 1, 293–316.

Lindsay, K.A., Rooney, C.E., 1992. A note on compound matrices. J. Comput. Phys. 103, 472–477.

Liu, J.L., Feng, X.Q., 2012. On elastocapillarity: A review. Acta. Mech. Sin. 28, 928–940.

Liu, T., Jagota, A., Hui, C.Y., 2017. A closed form large deformation solution of plate bending with surface effects. Soft Matter 13, 386–393.

Liu, Y., 2018. Axial and circumferential buckling of a hyperelastic tube under restricted compression. Int. J. Non-Linear Mech. 98, 145–153.

Liu, Y., Ye, Y., Althobaiti, A., Xie, Y.X., 2019. Prevention of localized bulging in an inflated bilayer tube. Int. J. Mech. Sci. 153, 359–368.

Lu, T., An, L., Li, J., Yuan, C., Wang, T., 2015. Electro-mechanical coupling bifurcation and bulging propagation in a cylindrical dielectric elastomer tube. J. Mech. Phys. Solids 85, 160–175.

Ma, L., Peng, J., Wu, C., He, L., Ni, Y., 2017. Sphere-to-tube transition toward nanotube formation: a universal route by inverse plateau–rayleigh instability. ACS nano 11, 2928–2933.

Mallock, A., 1891. Ii. note on the instability of india-rubber tubes and balloons when distended by fluid pressure. Proc. R. Soc. 49, 458–463.

Markin, V.S., Tanelian, D.L., Jersild Jr, R.A., Ochs, S., 1999. Biomechanics of stretch-induced beading. Biophys. J. 76, 2852–2860.

Matsuo, E.S., Tanaka, T., 1992. Patterns in shrinking gels. Nature 358, 482–485.

Ménager, C., Meyer, M., Cabuil, V., Cebers, A., Bacri, J.C., Perzynski, R., 2002. Magnetic phospholipid tubes connected to magnetoliposomes: pearling instability induced by a magnetic field. Eur. Phys. J. E 7, 325–337.

Mooney, M., 1940. A theory of large elastic deformation. J. Appl. Phys. 11, 582–592.

Mora, S., Abkarian, M., Tabuteau, H., Pomeau, Y., 2011. Surface instability of soft solids under strain. Soft matter 7, 10612–10619.

Mora, S., Phou, T., Fromental, J.M., Pismen, L.M., Pomeau, Y., 2010. Capillarity driven instability of a soft solid. Phys. Rev. Lett. 105, 214301.

Ng, B.S., Reid, W.H., 1979a. An initial value method for eigenvalue problems using compound matrices. J. Comput. Phys. 30, 125–136.

Ng, B.S., Reid, W.H., 1979b. A numerical method for linear two-point boundary-value problems using compound matrices. J. Comput. Phys. 33, 70–85.

Ng, B.S., Reid, W.H., 1985. The compound matrix method for ordinary differential systems. J. Comput. Phys. 58, 209–228.

Noether, E., 1918. Nachr. d. könig. gesellsch. d. wiss. zu göttingen, math. Phys. Kl 2, 235.

Ogden, R.W., 1972. Large deformation isotropic elasticity–on the correlation of theory and experiment for incompressible rubberlike solids. Proc. R. Soc. A 326, 565–584.

Ogden, R.W., 1997. Non-linear elastic deformations. Courier Corporation.

Ogden, R.W., 2007. Incremental statics and dynamics of pre-stressed elastic materials, in: Waves in nonlinear pre-stressed materials. Springer, pp. 1–26.

Pandey, A., Kansal, M., Herrada, M.A., Eggers, J., Snoeijer, J.H., 2021. Elastic rayleigh–plateau instability: dynamical selection of nonlinear states. Soft matter 17, 5148–5161.

Pandurangi, S.S., Akerson, A., Elliott, R.S., Healey, T.J., Triantafyllidis, N., 2022. Nucleation of creases and folds in hyperelastic solids is not a local bifurcation. J. Mech. Phys. Solids 160, 104749.

Papastavrou, A., Steinmann, P., Kuhl, E., 2013. On the mechanics of continua with boundary energies and growing surfaces. J. Mech. Phys. Solids 61, 1446–1463.

Park, H.S., Wang, Q., Zhao, X., Klein, P.A., 2013. Electromechanical instability on dielectric polymer surface: Modeling and experiment. Comput. Methods Appl. Mech. Eng. 260, 40–49.

Peletier, L.A., Troy, W.C., 2001. Spatial Patterns: Higher Order Models in Physics and Mechanics. volume 45. Springer Science & Business Media.

Pipkin, A.C., Rivlin, R.S., 1961. Small deformations superposed on large deformations in materials with fading memory. Arch. Ration. Mech. Anal. 8, 297–308.

Plateau, J., 1873. Statique expérimentale et théorique des liquides soumis aux seules forces moléculaires. volume 2. Gauthier-Villars.

Potier-Ferry, M., 1987. Foundations of elastic postbuckling theory, in: Buckling and Post-buckling. Springer, pp. 1–82.

Pucci, E., Saccomandi, G., 2002. A note on the gent model for rubber-like materials. Rubber Chem. Technol. 75, 839–852.

Qiu, Y., Zhang, E., Plamthottam, R., Pei, Q., 2019. Dielectric elastomer artificial muscle: materials innovations and device explorations. Acc. Chem. Res. 52, 316–325.

Rayleigh, L., 1892. On the instability of a cylinder of viscous liquid under capillary force. Phil. Mag 34, 145–154.

Razavi, M.J., Pidaparti, R., Wang, X., 2016. Surface and interfacial creases in a bilayer tubular soft tissue. Phys. Rev. E 94, 022405.

Riccobelli, D., 2021. Active elasticity drives the formation of periodic beading in damaged axons. Phys. Rev. E 104, 024417.

Riccobelli, D., Bevilacqua, G., 2020. Surface tension controls the onset of gyrification in brain organoids. J. Mech. Phys. Solids 134, 103745.

Rivlin, R.S., 1948. Large elastic deformations of isotropic materials. i. fundamental concepts. Philos. T. R. Soc. A 240, 459 – 490.

Rooney, F.J., Carroll, M.M., 1984. Generating functions for plane or axisymmetric isochoric deformations. Q. Appl. Math. 42, 249–253.

Russell, J.S., 1845. Report on Waves: Made to the Meetings of the British Association in 1842-43.

Sattler, R., Wagner, C., Eggers, J., 2008. Blistering pattern and formation of nanofibers in capillary thinning of polymer solutions. Phys. Rev. Lett. 100, 164502.

Sawyers, K.N., Rivlin, R.S., 1982. Stability of a thick elastic plate under thrust. J. Elast. 12, 101–125.

Seow, C.Y., Wang, L., Paré, P.D., 2000. Airway narrowing and internal structural constraints. J. Appl. Physiol. 88, 527–533.

Sheppard, S., Elliott, F., 1918. The reticulation of gelatine. Ind. Eng. Chem. Res. 10, 727–732.

Shimizu, T., Ding, W., Kameta, N., 2020. Soft-matter nanotubes: a platform for diverse functions and applications. Chem. Rev. 120, 2347–2407.

Shivapooja, P., Wang, Q., Orihuela, B., Rittschof, D., López, G.P., Zhao, X., 2013. Bioinspired surfaces with dynamic topography for active control of biofouling. Adv. Mater. 25, 1430–1434.

Shyer, A.E., Tallinen, T., Nerurkar, N.L., Wei, Z., Gil, E.S., Kaplan, D.L., Tabin, C.J., Mahadevan, L., 2013. Villification: how the gut gets its villi. Science 342, 212–218.

Silling, S., 1991. Creasing singularities in compressible elastic materials. J. Appl. Mech. 58, 70–74.

Steigmann, D.J., Ogden, R.W., 1997. Plane deformations of elastic solids with intrinsic boundary elasticity. Proc. R. Soc. A 453, 853–877.

Steigmann, D.J., Ogden, R.W., 1999. Elastic surface—substrate interactions. Proc. R. Soc. A 455, 437–474.

Style, R.W., Jagota, A., Hui, C.Y., Dufresne, E.R., 2017. Elastocapillarity: Surface tension and the mechanics of soft solids. Ann. Rev. Cond. Matter. Phys 8, 99–118.

Swift, J., Hohenberg, P.C., 1977. Hydrodynamic fluctuations at the convective instability. Phys. Rev. A 15, 319.

Taffetani, M., Ciarletta, P., 2015a. Beading instability in soft cylindrical gels with capillary energy: weakly non-linear analysis and numerical simulations. J. Mech. Phys. Solids 81, 91–120.

Taffetani, M., Ciarletta, P., 2015b. Elastocapillarity can control the formation and the morphology of beads-on-string structures in solid fibers. Phys. Rev. E 91, 032413.

Tallinen, T., Biggins, J.S., Mahadevan, L., 2013. Surface sulci in squeezed soft solids. Phys. Rev. Lett. 110, 024302.

Tanaka, T., Sun, S.T., Hirokawa, Y., Katayama, S., Kucera, J., Hirose, Y., Amiya, T., 1987. Mechanical instability of gels at the phase transition. Nature 325, 796.

Treloar, L.R.G., 1944. Stress-strain data for vulcanized rubber under various types of deformation. Rubber Chem. Technol. 17, 813–825.

Truesdell, C., Noll, W., 2004. The non-linear field theories of mechanics, in: The non-linear field theories of mechanics. Springer, pp. 1–579.

Trujillo, V., Kim, J., Hayward, R.C., 2008. Creasing instability of surface-attached hydrogels. Soft Matter 4, 564–569.

Tsafrir, I., Sagi, D., Arzi, T., Guedeau-Boudeville, M.A., Frette, V., Kandel, D., Stavans, J., 2001. Pearling instabilities of membrane tubes with anchored polymers. Phys. Rev. Lett. 86, 1138.

Veranič, P., Lokar, M., Schütz, G.J., Weghuber, J., Wieser, S., Hägerstrand, H., Kralj-Iglič, V., Iglič, A., 2008. Different types of cell-to-cell connections mediated by nanotubular structures. Biophys. J. 95, 4416–4425.

Von Karman, T., Tsien, H.S., 1939. The buckling of spherical shells by external pressure. J. Aeronaut. Sci. 7, 43–50.

Wang, C., Sim, K., Chen, J., Kim, H., Rao, Z., Li, Y., Chen, W., Song, J., Verduzco, R., Yu, C., 2018. Soft ultrathin electronics innervated adaptive fully soft robots. Adv. Mater. 30, 1706695.

Wang, J., Althobaiti, A., Fu, Y.B., 2017. Localized bulging of rotating elastic cylinders and tubes. J. Mech. Mater. Struct. 12, 545–561.

Wang, J., Fu, Y.B., 2018. Effect of double-fibre reinforcement on localized bulging of an inflated cylindrical tube of arbitrary thickness. J. Eng. Math. 109, 21–30.

Wang, L., 2020. Axisymmetric instability of soft elastic tubes under axial load and surface tension. Int. J. Solids Struct. 191, 341–350.

Wang, M., Fu, Y., 2021. Necking of a hyperelastic solid cylinder under axial stretching: Evaluation of the infinite-length approximation. Int. J. Eng. Sci. 159, 103432.

Wang, Q., Liu, M., Wang, Z., Chen, C., Wu, J., 2021. Large deformation and instability of soft hollow cylinder with surface effects. J. Appl. Mech. 88.

Wang, S., Guo, Z., Zhou, L., Li, L., Fu, Y.B., 2019. An experimental study of localized bulging in inflated cylindrical tubes guided by newly emerged analytical results. J. Mech. Phys. Solids 124, 536–554.

Wilkes, E.W., 1955. On the stability of a circular tube under end thrust. Q. J. Mech. Appl. Math. 8, 88–100.

Wineman, A., 2005. Some results for generalized neo-hookean elastic materials. Int. J. Non-Linear. Mech. 40, 271–279.

Wolfram Research Inc., 2021. Mathematica 12.3.1. URL: `https://www.wolfram.com/mathematica`. champaign, IL.

Xu, B., Hayward, R.C., 2013. Low-voltage switching of crease patterns on hydrogel surfaces. Adv. Mater. 25, 5555–5559.

Xuan, C., Biggins, J., 2016. Finite-wavelength surface-tension-driven instabilities in soft solids, including instability in a cylindrical channel through an elastic solid. Phys. Rev. Lett. 94, 023107.

Xuan, C., Biggins, J., 2017. Plateau-rayleigh instability in solids is a simple phase separation. Phys. Rev. E 95, 053106.

Yang, P.F., Fang, Y.P., Yuan, Y.N., Meng, S., Nan, Z.H., Hu, H., Imtiaz, H., Liu, B., Gao, H.J., 2021. A perturbation force based approach to creasing instability in soft materials under general loading conditions. J. Mech. Phys. Solids 151, 104401.

Ye, Y., Liu, Y., Fu, Y.B., 2020. Weakly nonlinear analysis of localized bulging of an inflated hyperelastic tube of arbitrary wall thickness. J. Mech. Phys. Solids 135, 103804.

Yin, W.L., 1977. Non-uniform inflation of a cylindrical elastic membrane and direct determination of the strain energy function. J. Elast. 7, 265–282.

Yoon, J., Kim, J., Hayward, R.C., 2010. Nucleation, growth, and hysteresis of surface creases on swelled polymer gels. Soft Matter 6, 5807–5816.

Yu, X., Fu, Y., 2022. An analytic derivation of the bifurcation conditions for localization in hyperelastic tubes and sheets. Z. Angew Math. Phys. 73, 1–16.

Zhou, L., Wang, S., Li, L., Fu, Y.B., 2018. An evaluation of the gent and gent-gent material models using inflation of a plane membrane. Int. J. Mech. Sci. 146, 39–48.

Zhou, Z., Li, Y., Wong, W., Guo, T., Tang, S., Luo, J., 2017. Transition of surface–interface creasing in bilayer hydrogels. Soft Matter 13, 6011–6020.